Identification of signalling pathways regulating autophagy in response to cellular stress

Reham Alsaadi

Thesis submitted to the University of Ottawa in partial fulfillment of the requirements for the Doctorate in Philosophy degree in Cellular and Molecular Medicine.

Department of Cellular and Molecular Medicine

Faculty of Medicine

University of Ottawa

February 2025

Dedication

To my late grandmother, Khadra Saud, who spent countless hours listening to me talk about the stories of great scientists yet never had the chance to hear my own.

Acknowledgments

They say a PhD is a marathon, not a sprint. Well, this marathon included a few detours (like that time I Googled “how to quit a PhD” at 3 a.m.), some unexpected hurdles (hello, peer reviews), and at least one point where I considered lying down on the track. But here are the people who handed me water bottles, yelled “you’re almost there!” (Even when we all knew it was a lie) and basically carried me across the finish line. You’re the real MVPs. I would like to express my very heartfelt appreciation to the people who have supported me through these years, because let’s be honest, I wouldn’t have survived without you.

First and foremost, a standing ovation goes to my thesis supervisor, Dr. Ryan Russell, who deserves a medal for putting up with me. This journey would not have been possible without his unwavering support, expertise, and patience. It is hard to overstate my gratitude to Dr. Russell, who put tremendous effort into explaining things clearly and simply. The opportunity you gave me has changed my life, and I will always be grateful for the time and work I have done in your lab. I thoroughly enjoyed my stay, thank you for everything.

I would like to extend my sincere gratitude to the Thesis Advisory Committee, Dr. Mary-Ellen Harper, Dr. Damien D'Amours, and Dr. Lynn Megeney for their constructive feedback and guidance, your insights have greatly contributed to the success of this work.

I am especially grateful to lab mates, Wensheng Tian thank you for being the Watson to my Sherlock (or maybe the other way around, depending on who actually solved the problems). Knowing you has been a true blessing, both in my academic life and during our video gaming adventures. Your friendship is one of the greatest gifts I have received on this journey. Dr. Damian Gatica, I feel incredibly fortunate to have had the opportunity to work alongside a scientist as talented and inspiring as you. Over the years, you’ve been not only an exceptional mentor but also

a cherished friend, guiding me with wisdom and kindness. My dear lab mate and friend Karyn King, thank you for the countless times you stayed late with me to squeeze in “just one more experiment.” may your coffee always be strong and your gels forever perfect. Chenxuan Zhu (Charlotte) your joy and positivity were absolutely contagious, and I’m so grateful for the time we spent together, both in the lab and outside of it. Thank you for teaching me more about China and for introducing me to the wonderful world of mahjong. I am incredibly thankful to all my past and present lab members for creating such a vibrant, fun, and supportive environment where I’ve been able to learn, grow, and thrive.

To my parents, who have earned a lifetime achievement award for their endless patience, boundless love, and heroic ability to tolerate my chaos. To my mother, Aisha Saleh, the most incredible woman I know, thank you for sacrificing your own dreams to help us achieve ours. Your unwavering faith in my goals and your steadfast support in every decision I’ve made have been my greatest strength. You are my role model in life, not only for your endless love but also for your kindness toward others. This accomplishment is as much yours as it is mine. To my father, Musaibeh Muaad, thank you for pushing me to study hard for the past 17 years. You are the reason I fell in love with school, and especially with science, and also the reason I can function on three hours of sleep. Your belief in my dreams and your unwavering guidance have been the foundation of everything I’ve accomplished. There truly aren’t enough words to express my gratitude to you both.

To my incredible siblings Abeer, Ahlam, Nawal, Maram, Muhammed, Khaled, Abdallah, Ziyad, and Rawah thank you for being the ultimate dream team. You have been my personal cheerleaders, therapists, and occasional comedians, and I am not sure how I would have survived without your endless support (and tolerance for my complaining). You are the best gift life has ever given me,

and I am so lucky to have you in my corner. Nawal, you deserve a special shoutout for being my Canadian survival guide since day one. Your help has been more invaluable than Wi-Fi in a dead zone, and I'm so grateful to have you here with me, seriously, you're the human equivalent of a 'Ctrl + Z' for my life mistakes. To all of you, I want to say: thank you for being the most amazing support system I could ever ask for. I love you all, and I am endlessly thankful for your presence in my life.

To my friends, Esraa, Javiera, Joyce Mortimer, Charles King, Radha, Antoine, and Kadambari thank you for all the incredible times we have shared, the miles we have traveled together, and the endless laughter. I'm so grateful for the countless times you listened to me complain about, well, pretty much everything. Your support and friendship mean the world to me.

Abstract

Macroautophagy (hereafter referred to as autophagy) is a key cellular degradative process that plays an important role in maintaining cellular homeostasis. Defects in autophagy are linked to a range of health conditions, including but not limited to metabolic disorders, inflammatory bowel diseases, and cancer. Despite decades of research, measurement of autophagy dynamics in rare cell populations and *in vivo* remains challenging due to the inherent limitations of existing tools. We developed a novel approach for autophagy measurement by monitoring the phosphorylation of ATG16L1 on serine 278 (pATG16L1^{s278}). We found that phospho-ATG16L1 is exclusively localized to nascent autophagosomes, and that its detection is not confounded by prolonged cellular stress or late-stage autophagy impairments, which often obscure autophagic analyses. We have developed and characterized a monoclonal antibody capable of specifically detecting endogenous phospho-ATG16L1 in mammalian cells. This highly versatile antibody enables its use in Western blotting, immunofluorescence, and immunohistochemistry assays for autophagy measurement.

In the context of metabolic disorders, we investigated the impact of chronic iron overload on the autophagy pathway. Iron overload is a clinical hallmark of metabolic syndrome, which is a collection of conditions often associated with insulin resistance and is known to lead to increased risk of developing cardiovascular disease and type 2 diabetes. We discovered that chronic iron overload induced major autophagy disruptions, as evidenced by the accumulation of defective autolysosomes and a significant depletion of free lysosomes in skeletal muscle cells. The autophagy defects, in turn, led to impairment of insulin-stimulated glucose uptake and disrupted insulin signaling. Mechanistically, we demonstrated that iron overload affected Akt-mediated suppression of tuberous sclerosis complex 2 (TSC2) and reduced Rheb-dependent activation of

mechanistic target of rapamycin complex 1 (mTORC1) on autolysosomes. This dysregulation inhibited the autophagic-lysosome regeneration, thereby contributing to the development of insulin resistance. Notably, restoring mTORC1 signaling to the autophagy machinery on mature autophagosomes, or removing excess iron, significantly replenished lysosomal pools and restored insulin sensitivity. This discovery uncovers the potential therapeutic pathways that could be targeted to improve insulin sensitivity in metabolic syndrome.

Additionally, we examined the process of ER-phagy, which is the selective degradation of the endoplasmic reticulum (ER) by autophagy. ER-phagy is critical for maintaining cellular homeostasis and is frequently targeted by pathogens to create a more favourable cellular environment for infection. We discovered that *Salmonella* Typhimurium utilizes a mechanism to inhibit ER-phagy by targeting the ER-phagy receptor FAM134B. This inhibition prevents FAM134B oligomerization, a key step in the ER-phagy pathway, leading to increased intracellular bacterial load post-invasion. In FAM134B knockout mice, we observed increased susceptibility to *Salmonella* infection, characterized by severe intestinal damage and elevated bacterial loads. Furthermore, we identified the bacterial effector SopF as the primary mediator of FAM134B inhibition, shedding light on how intracellular bacteria such as *Salmonella* could subvert innate immune defenses.

Together, these studies provide a comprehensive understanding of the complex regulatory networks that govern autophagosome biogenesis, maturation, and functionality. They also highlight the critical role of environmental factors in modulating autophagic activity and maintaining cellular homeostasis, revealing the dynamic interplay between intracellular mechanisms and external stimuli in the regulation of autophagy. Identifying novel therapeutic

targets, such as phospho-ATG16L1 and FAM134B, offers promising avenues for developing interventions to restore autophagy and mitigate disease progression.

Table of Contents

List of Abbreviations

EM	Electron microscopy
ATGs	Autophagy related genes
CMA	Chaperone-mediated autophagy
Hsc70	Heat shock 70 kDa protein 8
LAMP2A	Lysosomal-associated membrane protein 2A
ULK1	unc-51-like kinase 1
FIP200	Focal adhesion kinase family interacting protein of 200 kD
RB1CC1	Retinoblastoma 1-inducible coiled-coil 1
ATG13L	Autophagy-related gene 13L
ATG101	Autophagy-related gene 101
C12orf44	Chromosome 12 open reading frame 44
VPS34	Vacuolar protein sorting 34
PIK3C3	Phosphatidylinositol 3-kinase catalytic subunit type 3
VPS15	Vacuolar protein sorting 15
beclin-1	Bcl-2 interacting protein
ATG14L	Autophagy-related gene 14L
UVRAG	Ultraviolet radiation resistance-associated gene
PtdIns3P	Phosphatidylinositol 3-phosphate
WIPI	WD-repeat protein Interacting with PhosphoInositides
DFCP1	Double FYVE domain-containing protein 1
LC3	microtubule-associated protein light chain 3
ATG13	Autophagy-related gene 13
mTORC1	mammalian target of rapamycin complex 1
PI3P	Phosphatidylinositol 3-phosphate
ATG16L1	Autophagy-related gene 16L

PE	phosphatidylethanolamine
AMPK	AMP-activated protein kinase
mLST8	mammalian lethal with SEC13 protein 8
PIKK	Phosphatidylinositol 3-kinase-related kinases
Rheb	Ras homolog enriched in brain
TSC2	tuberous sclerosis complex 2
ALR	autophagic lysosome reformation
LKB1	Liver Kinase B1
AMBRA1	activating molecule in Beclin1-regulated autophagy protein 1
BECN1	the gene that encodes the protein Beclin-1
SNARE	soluble N-ethylmaleimide-sensitive factor attachment protein receptor
STX17	syntaxin 17
VAMP8	vesicle-associated membrane protein 8
LIR	LC3-interacting region
SQSTM1/p62	sequestosome 1
NBR1	neighbor of BRCA1 gene 1
NDP52	nuclear dot protein 52 kDa
PTMs	post-translational modifications
OPTN	optineurin
FAM134B	member of the family with sequence similarity 134
ER	endoplasmic reticulum
SEC62	SEC62 homolog, preprotein translocation factor
ATL3	atlastin GTPase 3
TEX264	testis expressed 264
RETREG1	reticulophagy regulator 1
IRGM	immunity-related GTPase M
NOD2	nucleotide-binding oligomerization domain 2

TLR4	Toll-like receptor 4
TF	transferrin
CFP	cyan fluorescence protein
IRE	iron response element
PGSK	phen green SK
FTH	ferritin heavy chain
FTL	ferritin light chain
TSC	tuberous sclerosis complex

List of Manuscripts

1. An Antibody for Analysis of Autophagy Induction

Wensheng Tian[1], **Reham Alsaadi[1¥]**, Zhihao Guo[1¥], Alena Kalinina[1], Micaël Carrier[2], Marie-Eve Tremblay[2], Baptiste Lacoste[1,3,4], Diane Lagace[1] and Ryan C. Russell[1,5* ¥]

Published in **Nature Methods** - DOI: 10.1038/s41592-019-0661-y

2. Iron overload inhibits late stage autophagy flux leading to insulin resistance.

James Won Suk Jahng[1]*, **Reham Musaibeh Alsaadi[2]***, Palanivel Rengasamy[1], Erfei Song1, Victoria Emily Barbosa Hipolito[3], Hye Kyoung Sung1, Roberto Jorge Botelho[3], Ryan Charles Russell[2#], Gary Sweeney[1#] * Co-First authors, these two authors contributed equally to this work.

Published in **EMBO reports** - DOI: 10.15252/embr.201947911

3. The ER-phagy receptor FAM134B is targeted by *Salmonella* Typhimurium to promote infection

Damián Gatica[1*], **Reham M. Alsaadi[1*]**, Rayan El Hamra[2], Boran Li[3], Rudolf Mueller[4], Makoto Miyazaki[5], Qiming Sun[3,6], Subash Sad[2] & Ryan C. Russell[1,7,8] *Co-first authors, these authors contributed equally to this work

Published in **Nature Communications**- DOI: 10.1038/s41467-025-58035-7

Chapter 1: General Introduction

1.1 A Brief History of Autophagy

The term autophagy (from Greek meaning "self-eating") was coined by Christian de Duve in 1963, after electron microscopy (EM) analysis of cells revealed that the newly discovered degradative vesicles (lysosomes) degraded components of both extra- and intra-cellular origins[1]. In 1966, Palade and Farquhar discovered the autophagosome, the double membraned vesicles that drove the autophagy pathway; previously, they were simply known as pre-lysosomes[2]. In the 1980s, cell biologists started using *Saccharomyces cerevisiae* as a model to study the process of cellular cargo transport to and from the vacuole, a process which was closely related to autophagy. In a yeast genetic screen under nitrogen starvation, Yoshinori Ohsumi identified the first autophagy related genes (ATGs), which coded proteins that participated in the autophagic process and demonstrated that nutrient deficiency stimulated autophagic degradation in yeast[3,4]. Identification of mammalian homologs for yeast ATG genes followed soon after[5]. To date, over 40 ATG genes have been identified. The process of autophagy has been further sub-classified based on the manner in which intracellular materials are delivered to lysosomes for degradation: macroautophagy, chaperone-mediated autophagy (CMA), and microautophagy [6]. Autophagosomes engulf and deliver their cargo to the lysosome for degradation in macroautophagy. Whereas microautophagy requires the lysosomal membrane to directly engulf small portions of the cytoplasm. In CMA, substrate proteins are recognized through a pentapeptide consensus motif KFERQ by the chaperone protein

Heat shock 70 kDa (Hsc70), then delivered directly to the lysosome through interactions with lysosomal transmembrane protein Lysosome-associated membrane protein 2 (LAMP2A)[7] (Fig.1).

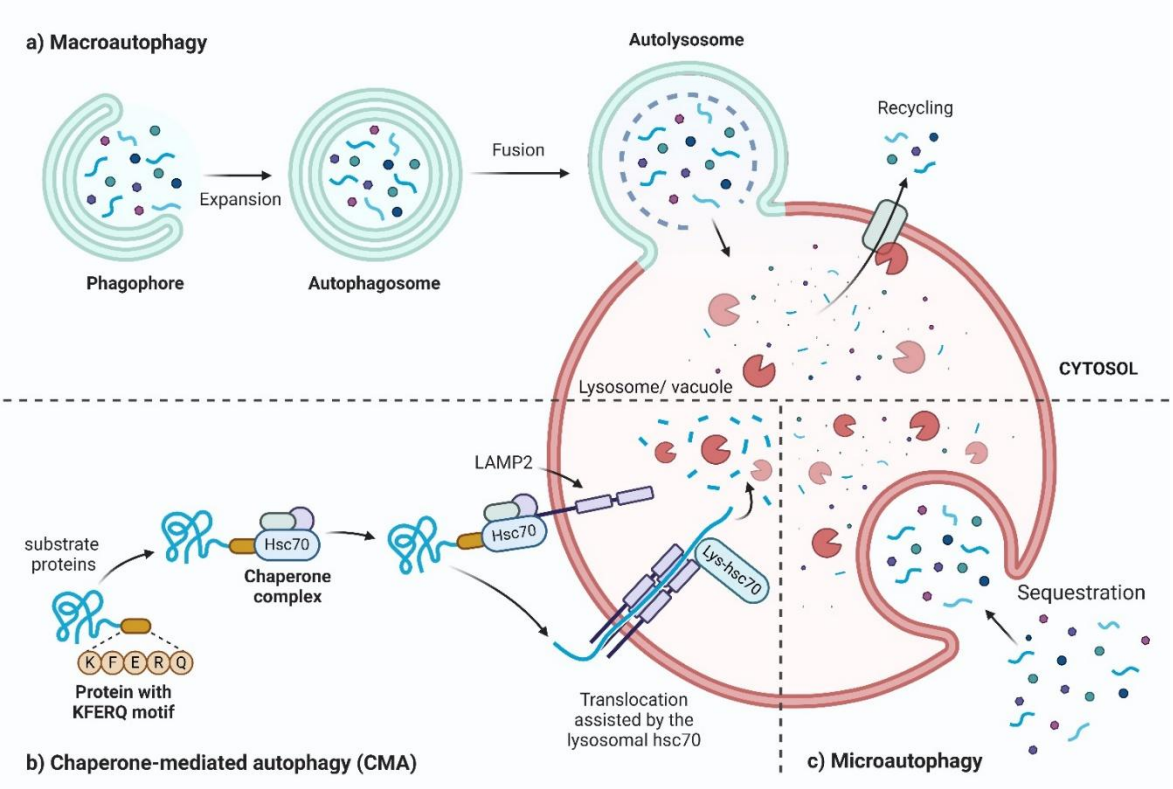

Figure 1: **Autophagic pathways in mammals**: The three main autophagic pathways—macroautophagy (a), CMA (b) and microautophagy (c) all play a role in lysosomal degradation. However, they differ in their regulatory mechanisms, the type of cargo targeted for degradation, and the processes involved in targeting the cargo to the lysosomal compartment.

In macroautophagy, the engulfment of cytoplasmic components begins with the formation of the phagophore, a small double-membraned structure acting as a recruitment platform for early autophagic proteins. The recruited autophagic proteins promote additional signalling, resulting in the expansion of the phagophore membrane around autophagic cargo, eventually forming an enclosed mature autophagosome and fully sequestering the cargo within. The autophagosome then

fuses with the lysosome, resulting in the formation of the autolysosome and the degradation of the sequestered cargo[8] (Fig.2). Autophagy can be activated under a range of stresses, such as the presence of protein aggregates, damaged organelles, invading pathogens and nutrient starvation[9,10,11]. Autophagy supports cellular homeostasis in response to a changing cellular environment by clearing harmful intracellular elements and providing basic nutrients by degradation of complex macromolecules such as lipids carbohydrates and proteins.

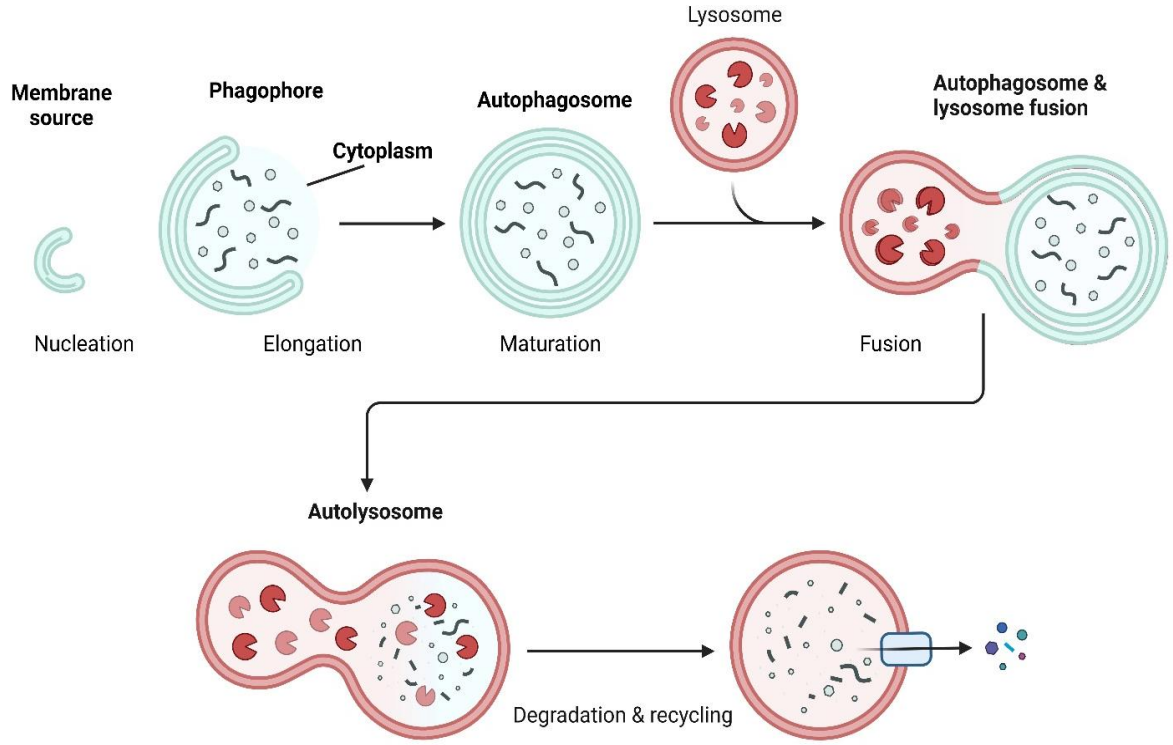

Figure 2: **Autophagy Process.** Portions of cytosol and organelles are sequestered into a double-membrane vesicle, an autophagosome, and delivered into an autolysosome for degradation and recycling by the lysosomal hydrolysis.

1.2 Molecular Mechanisms of Autophagy

In the decades after the discovery of ATG genes, extensive research has led to the characterization of six functional groups of proteins that play major roles in autophagosome biogenesis. Ordered based on their hierarchical ranking in autophagy signaling: first, the Unc-51-like kinase 1 (ULK1) kinase complex, comprised of ULK1, focal adhesion kinase family interacting protein of 200 kD (FIP200), (also known as RB1CC1), ATG13L, and ATG101 (also known as C12orf44); second, the acuolar protein sorting 34 (VPS34), (also known as PIK3C3) kinase complex, including VPS34, VPS15, Bcl-2 interacting protein (beclin-1), ATG14L or UVRAG (two populations of VPS34 complexes exist containing either ATG14L or UVRAG); third, proteins recruited by phosphatidylinositol 3-phosphate (PI3P), such as WD-repeat protein Interacting with PhosphoInositides (WIPI) and Double FYVE-containing protein 1 (DFCP1); fourth, the ATG16L1/ATG5-12 E3-like complex and upstream proteins of the ATG5-12 ubiquitin-like conjugation system; fifth, the microtubule-associated protein 1-light chain 3 (LC3) phosphatidylethanolamine conjugation system; and sixth, transmembrane protein ATG9. Collectively, these six groups of proteins make up the "core" autophagy proteins and promote autophagosome formation in response to activating signals, usually in the form of stresses.

Mammals have two homologues of yeast ATG1, ULK1 and ULK2, which are serine/threonine kinases complexes that are mostly functionally redundant in promoting autophagy activation (ULK1 and ULK2 will be referred to as ULK hereafter) [12]. As part of the ULK complex ATG13 binds to ULK and mediates the interaction between ULK and another subunit, FIP200. In addition, the binding of ATG13 stabilizes and activates ULK, resulting in the phosphorylation of FIP200 by ULK[13,14]. ATG13 is also thought to recruit ATG101 to the ULK-ATG13-FPI200 complex at the phagophore, which then promotes the recruitment of downstream factors[14]. Under basal

conditions, ULK activity is suppressed by the mammalian target of rapamycin complex 1 (mTORC1) through inhibitory phosphorylation[15]. However, nutrient starvation, a well-known inducer of autophagy, inhibits mTORC1 and thereby releases its inhibition of ULK. Upon activation, ULK directly phosphorylates a number of downstream autophagy proteins, several of which are components of the pro-autophagic ATG14-containing VPS34 complexes[16,17]. ULK complex activity is essential for the phosphorylation and recruitment of the PI3KC3 complex, which results in the production of phosphatidylinositol 3-phophate (PI3P) and phagophore formation[18,16]. PI3P functions as an important effector molecule recruiting downstream components of the autophagy pathway, including the ATG16L1/5-12 complex, to the phagophore to facilitate its growth into a mature autophagosome. Under basal conditions, VPS34 activity is inhibited by the direct phosphorylation of the lipid kinase subunit ATG14L by mTORC1, which acts to block unnecessary autophagy initiation[19]. PI3P recruits PI3P-binding proteins WD-repeat protein interacting with phosphoinoside (WIPI) to the formation of phagophore. WIPI2 binds to ATG16L1 and recruits the ATG16L1 to ATG5-ATG12, which is critical for the conjugation of LC3 protein to phosphatidylethanolamine (PE) in the growing autophagosome membrane[20,21]. Conjugation of LC3 onto the autophagosomal membrane is a key event in autophagosome biogenesis, required for recruitment of serval autophagy specific cargo and autophagosome maturation[22,23].

1.3 Upstream regulators of autophagy – mTORC and AMPK

Nutrient starvation is one of the earliest established and most well-studied inducers of autophagy[24]. Two major cellular energy-sensing kinases, the mechanistic target of rapamycin complex 1 (mTORC1) and the AMP-activated protein Kinase (AMPK) are integral for coupling autophagy rates to nutrient availability.

Mammals have two slightly different mTORCs: mTORC1 and mTORC2, with mTORC1 being sensitive to nutrient signaling while mTORC2 is involved in growth factor signaling. mTORC1 can sense a range of stresses such as nutrient starvation, hypoxia, or DNA damage, and controls cellular growth. mTORC1 consists of three core components: mTOR, Raptor (regulatory associated protein of mTOR), and mLST8 (mammalian lethal with Sec13 protein 8). mTOR is a member of the PIKK (phosphatidylinositol-kinase-related kinase) family of serine and threonine kinases, while Raptor functions as a scaffold protein recruiting canonical mTOR substrates. mTORC kinase activity is regulated by insulin and growth factor signaling, as well as specific amino acids and their derivatives. When a cellular amino acid is abundant, mTORC1 is active and localizes to the lysosomal membrane. mTORC1 is also regulated by the small GTPase Ras homolog enriched in brain (Rheb), Rheb is sensitive to the change in GTP and GDP levels. When the cellular GTP:GDP ratio is high, Rheb is activated and stimulates mTORC1 kinase activity. Conversely, the GTPase activating protein Tuberous sclerosis complex 2 (TSC2) converts GTP to GDP bound by Rheb, and leads to the inactivation of mTORC.

mTORC exerts its inhibition of autophagy by phosphorylating a multitude of autophagy (ATG) proteins, including members of the ULK1 complex, the class III PI3K complex I, and WIPI2. By associating to and phosphorylating ULK on serines 758, 638, and ATG13 on serine 258[25], mTORC inhibits the kinase activity of ULK, rendering it inable to promote autophagy initiation signaling. Only when the cell experiences nutrient starvation, mTORC becomes inactive and dissociates from ULK, relieving its inhibitory effect[13]. Similarly, phosphorylations by mTORC on the class III PI3K complex I and WIPI2 both inhibit their autophagy-promoting functions, leading to autophagy inhibition[26].

Importantly, mTORC also phosphorylates UV radiation resistance-associated gene (UVRAG), a member of the VPS34 complex that is mutually exclusive to ATG14. The population of UVRAG-containing VPS34 complex is known to regulate autophagosome lysosome reformation (ALR), the recycling autophagosomal membrane to lysosome. This is to maintain cellular lysosome homeostasis as lysosomes are used up from fusion with autophagosomes during autophagy. By phosphorylating UVRAG, mTORC promotes ALR through activating the UVRAG-containing VPS34 complexes[27].

AMPK is a serine/threonine protein kinase found as a heterotrimetric complex, including a catalytic α-subunit, a scaffolding β-subunit and a regulatory γ-subunit[28]. The upstream regulator of AMPK, the tumour suppressor LKB1 (also called serine/threonine kinase 11), phosphorylates AMPK α catalytic subunit at Thr172 under nutrient starvation[29]. This phosphorylation is essential for AMPK kinase activity. AMPK activity maintains cellular energy homeostasis in response to stresses, such as nutrient starvation, hypoxia and infection[30].

AMPK is upregulated in response to cellular ATP/AMP ratio changes through direct and indirect interactions with AMP and ADP[31,32]. Activation of AMPK turns on the catabolic pathway to produce ATP and prevents consumption of ATP by halting the synthetic pathways that utilize ATP[31,32]. AMPK can induce autophagy activation through the major autophagy inducing kinase ATG1 (ULK) in three ways: (1) AMPK indirectly activates tuberous sclerosis 2 (TSC2) by phosphorylating TSC2 at Ser1345[33,34]. (2) AMPK phosphorylates ULK at Ser317/777 to induce its activation and autophagy induction[35,36]. (3) AMPK inhibits mTORC1 directly through inhibitory phosphorylation of Raptor in Ser792/722. mTORC1, a downstream target of AMPK is another major energy-sensing kinase and a key regulator of cell growth and metabolism[36].

1.4 Autophagosome Biogenesis

1.4.1 Nucleation and phagophore formation

The initial membrane structure in autophagy, called a phagophore, may utilize several membrane sources, including the Golgi apparatus [37], endoplasmic reticulum [38], mitochondria [39], and endosomal compartments [40]. A defining feature of phagophore membranes is their high membrane curvature, which facilities the assembly of the autophagy-related class III phosphatidylinositol 3-kinase (PtdIns3K) complex, composed of subunits VPS34, VPS15, beclin-1 and ATG14 [41]. The localization of the PtdIns3K complex onto phagophores is achieved through the ability of ATG14 to associate with highly curved membranes [42]. PtdIns3K assembly also requires the dissociation of Beclin1 and AMBRA1 (the activating molecule in BECN1-regulated autophagy protein 1) from their inhibitory regulator, Bcl-2[43]. Upon assembly onto nascent autophagosomal membranes, this complex catalyzes the formation of phosphatidylinositol-3-phosphate, which is a key lipid signalling molecule that acts as a platform for the recruitment of a multitude of effector ATG proteins to the nascent phagophore membrane. This sequential recruitment of molecular machinery led to the development of the assembly and expansion of the phagophore structure[19].

1.4.2 Autophagosome Formation and Elongation

Autophagosome biogenesis requires two distinct ubiquitin-like conjugation systems, composed of ATG proteins. The first conjugation system contains ATG7 and ATG10, which mediates the covalent conjugation of ATG12 to ATG5[44]. The ATG12-ATG5 complex subsequently associates with ATG16L1, forming a functional complex that acts as the E3-like enzyme in the second ubiquitin-like conjugation system[45]. In the second system, ATG8 (LC3) undergoes sequential

processing mediated by ATG4, ATG7, and ATG3, culminating in its conversion to the lipidated form LC3-II by the ATG12-5-16 complex. Lipidation of LC3 occurs through conjugation to phosphatidylethanolamine groups embedded in the phagophore membrane[45]. The activities of these two conjugation systems drive LC3 lipidation, phagophore membrane expansion and eventual closure, completing cargo sequestration. After autophagosome formation, the majority of ATG proteins dissociate and are recycled to the cytosol[45]. Notably, removal of lipidated LC3-II by ATG4 protease activity only occurs on the cytosol facing outer membrane, while luminal LC3-II remains as the sole ATG protein marker associated with the mature autophagosomal membrane, serving as a crucial indicator of autophagic activity[45,46].

1.4.3 Fusion and degradation

The maturation of autophagosomes into functional degradative vesicles involves a specific membrane fusion mechanism. Once enclosed and fully formed, the soluble N-ethylmaleimide-sensitive factor attachment protein receptor (SNARE) protein STX17 (syntaxin 17) localizes to the outer membrane of mature autophagosomes, where it then recruits another SNARE protein Synaptosomal-associated protein 29 (SNAP29)[47]. Together STX17-SNAP29 interact with the lysosomal SNARE protein vesicle-associated membrane protein 8 (VAMP8) to facilitate the fusion of autophagosomes with lysosomes to form the mature hydrolytic organelle[47]. Following this fusion, proton pumps and hydrolytic enzymes are added to the autophagosomes for the formation of the autolysosome, enabling cargo acidification and hydrolysis for effective degradation of cellular components[47].

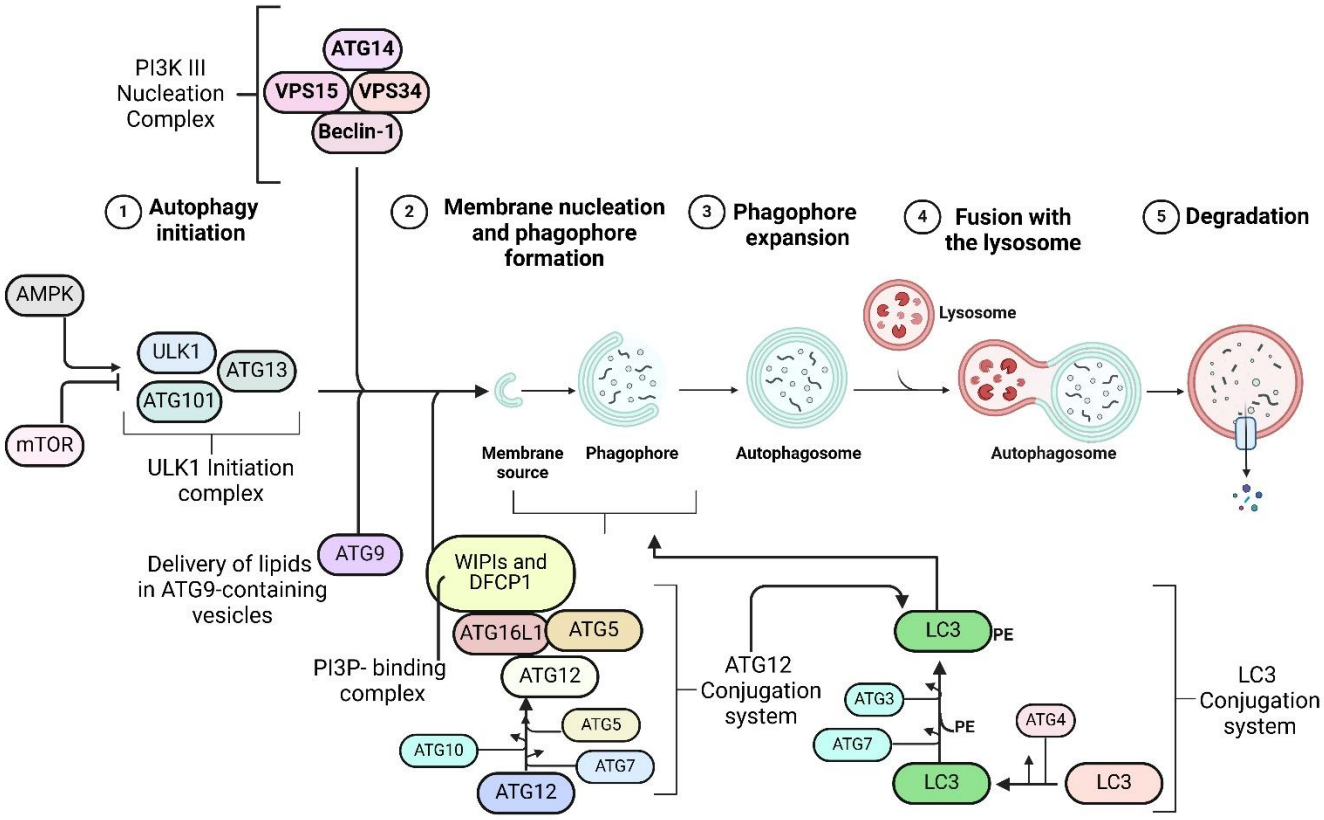

Figure 3. A schematic describing the process and main regulatory machinery of autophagy. A schematic of macroautophagy (autophagy) illustrates its key regulatory mechanisms. mTOR acts as an inhibitor, while AMP-activated kinase (AMPK) acts as an activator. The process begins with the formation of a phagophore, which engulfs cytoplasmic material. This leads to the formation of autophagosomes that fuse with lysosomes to form autolysosomes for degradation. Autophagy involves five main steps: (1) initiation, (2) membrane nucleation and phagophore formation, (3) phagophore expansion, (4) fusion with lysosomes, and (5) degradation. This process is regulated by autophagy-related proteins (ATGs) that assemble into complexes, including the ULK1 initiation complex and the class III PI3K nucleation complex. The ATG12 conjugation system,

where ATG12 binds to ATG5 and ATG16L1, facilitates LC3 conjugation. LC3 interacts with cargo receptors, and membrane expansion is supported by ATG9 vesicles.

1.5 Autophagy Cargo Receptor

Autophagy cargo receptor proteins refer to a class of proteins that assist the autophagic capture of cargo by providing physical linkage between potential autophagic cargo and the LC3 moieties of the autophagosomes. Polyubiquitination of cargo facilitates its recruitment to autophagosomes through cargo adaptors, which have two key domains: a ubiquitin-binding domain (UBD) and an LC3-interacting region (LIR) domain which allow the cargo adaptor to bind both the ubiquitined target and autophagosome[48,49,50,51]. In addition to functions in cargo recruitment to the autophagosome, cargo receptor also provide a means to target specific cellular components for degradation, such as large protein aggregates, mitochondria, or intracellular bacteria[52].

1.6 Measurement of autophagy

Since its discovery in the 1990's, multiple methods to accurately measure autophagic activity have been developed. The following section explains two modes of autophagy measurement that most modern autophagy assays are based upon.

1.6.1 LC3-Turnover Assay

Measuring the turnover of autophagosomes (autophagic flux) is a straightforward way to assess the ongoing rate of autophagy. The most widely used method for quantifying autophagic flux is monitoring the turnover dynamics of ATG8 proteins and their mammalian homologs, LC3 and GABARAP family proteins [53,54]. Initially synthesized as a cytosolic form (LC3-I), LC3-I is covalently conjugated through its C terminal glycine residue to phosphatidylethanolamine within

the phagophore and autophagosomal membranes during autophagosome formation[54]. The lipidated form is termed LC3-II. LC3-II is present on both the outer and inner autophagosomal membranes and is therefore widely used as a marker for autophagosomes, as its cellular abundance roughly correlates to the quantity of autophagosomes present[22]. After fusion with lysosomes, LC3-II on the outer membrane is increasingly deconjugated and recycled, while those on the inner membrane are degraded, which enables the measurement of autophagic activity by monitoring LC3 turnover[22]. LC3 turnover can be easily measured by common laboratory assays, such as immunofluorescent microscopy, where LC3-positive vesicles appear as distinct puncta[55]. Western blotting is also widely used to monitor LC3 lipidation, as the lipidated (LC3-II) and unlipidated (LC3-I) forms of LC3 migrate at slightly different locations by SDS-PAGE, providing an easy readout for measuring the state of LC3 lipidation[56,55].

Inducing autophagy, such as during starvation, typically leads to an increase in both the number of autophagosomes and the levels of ATG8-II. To effectively monitor autophagic flux, it is crucial to assess the degradation of ATG8-II within lysosomes, which can be achieved by treating the cells with lysosomal inhibitors to measure the turnover of ATG8-II . A higher difference in ATG8-II levels between these two groups indicates enhanced autophagic flux, while a negligible difference suggests inhibited flux.

For example, during nutrient starvation in many cell types, inhibiting lysosomal function results in an increase in ATG8-II levels, indicating a higher autophagic flux. Conversely, if inhibition of the lysosome does not alter ATG8-II levels, it indicates low autophagic activity, even when baseline levels of ATG8-II are high[56].

1.6.2 Degradation of LC3-Binding Substrates

Autophagic flux can also be evaluated by monitoring the degradation of selective autophagy adaptors. These adaptors are typically recognized and bind to LC3 proteins in autophagosomes. A commonly detected autophagy adaptor is SQSTM1/p62 [57]. Decrease in SQSTM1 level can be interpreted as autophagy activation, while the opposite could indicate autophagy blockage (and accumulation of substrates)[57]. However, changes in protein level could also be a result of overproduction due to stresses such as oxidative stress[57]. Therefore, to ensure that changes in the adaptor protein level are not due to transcriptional changes, it is important to measure the mRNA levels. Alternatively, pulse-labeling of p62 tagged with a fluorescent marker, such as HaloTag, can help avoid this issue, as this method allows the tracking of a population of p62 protein made within a specific period of time and measurement of its turnover rate, which is indicative of the turnover rate of autophagosomes[58].

1.6.3 Other methods to measure autophagy

Cyto-ID

The Cyto-ID fluorescence spectrophotometric assay enables the estimation of autophagy flux by measuring Cyto-ID-stained autophagic compartments. As a live-cell compatible dye, Cyto-ID offers an alternative to mRFP-GFP-LC3 systems for monitoring autophagy using live-cell imaging techniques. As claimed by the manufacturer, Cyto-ID offers greater sensitivity and reduced variability in quantifying autophagic compartments and flux when compared to traditional markers [59].

mRFP-GFP-LC3 Tandem Fluorescent Protein Quenching Assay

GFP (pKa=5.9) fluorescence quenches in acidic compartments, such as lysosomes (pH 4-5), while mRFP (pKa=4.5) can remain stable in lysosomes. The mRFP-GFP-LC3 probe exploits this pH sensitivity to provide a visible readout for tracking autophagosome (yellow, GFP and mRFP) to autolysosome (red, mRFP only) conversion. Increased yellow and red puncta indicate autophagy induction, while yellow-only accumulation suggests late-stage blockade. RFP-only puncta require both GFP quenching and RFP stability, so their increase may reflect either enhanced flux or reduced lysosomal degradation. The mTagRFP-mWasabi-LC3 variant improves detection as mWasabi (pKa=6.5) quenches more efficiently than GFP[60].

1.7 Cargo Selectivity of Autophagy

Autophagy can be defined into two types based on cargo selection. The first is non-selective bulk autophagy, which indiscriminately sequesters and degrades parts of the cytoplasm. Alternatively, the cell can promote selective autophagy specifically degrades cellular components, such as mitochondria[61], endoplasmic reticulum[62], invasive pathogens[63,64], aggregated proteins[65] and many other cytosolic components[52].

1.7.1 Non-selective Autophagy (Bulk Autophagy)

Initial characterization of autophagy identified its role as a bulk degradation pathway activated in response to nutrient starvation. This non-selective form, termed bulk autophagy, primarily serves to recycle cellular macromolecules during nutrient deprivation through the relatively non-selective degradation of cytoplasmic components (cargos). Through this mechanism, cells can maintain essential metabolic processes and survive acute periods of nutritional stress by recycling existing cellular materials[66,67,68], metabolically active cells such as rat hepatocytes have been observed to

turn over around 2%-3% of the cytosol per hour through autophagy[24]. This process is particularly crucial during development, as different ATG protein knockouts usually result in neonatal lethality, or death shortly after birth in mice.

1.7.2 Selective Autophagy

Selective autophagy refers to the targeted autophagic degradation of specific cellular cargos, in contrast to bulk autophagy, which degrades portions of the cytosol without distinguishing the content within. Some common types of selective autophagy include degradation of the mitochondria (mitophagy), lysosomes (lysophagy), ER (ER-phagy), protein aggregates (aggrephagy), invading pathogen (xenophagy) and many more[61,69,70]. Selective autophagy signaling can be categorized into two major classes based on their targeting mechanisms: ubiquitin-dependent and ubiquitin-independent pathways[71]. Both mechanisms utilize receptor proteins to achieve the selectivity in cargo capture.

1.7.2.1 Ubiquitin-dependent autophagy

Ubiquitin-dependent pathways require first the ubiquitination of the target substrates. Once the substrate is ubiquitinated, receptors such as p62, NBR1, NDP52, etc., recognize and bind to these ubiquitin modifications. In addition to ubiquitin binding, these receptors also contain a LC3 interacting region (LIR) and therefore bridge the ubiquitinated cargo to the lipidated LC3 present on the forming autophagosomes. facilitating selective cargo degradation[71,72] (Fig.4). In addition to recognition of ubiquitinated cargo, the selective autophagy receptors are also regulated through PTMs. For example, p62 can be ubiquitinated on lysine residues 7 and 420, these ubiquitination events both enhance the cargo-targeting ability of p62 and serve to promote selective autophagy.

Similarly, phosphorylation of mitophagy receptors NDP52 and OPTN also enhance their ability to bind ubiquitin chains present of damaged mitochondria, positively regulating mitophagy[73,74,75].

1.7.2.2 Ubiquitin-independent autophagy

Selective autophagy can also degrade cargos independent of ubiquitin. This is done with the help of specific cargo-recognizing receptors linking the cargo to the autophagosome through binding both the cargo and lipidated LC3 proteins, facilitating the formation of the autophagosomal membrane around the cargo[76]. Example of an ubiquitin-independent selective autophagy pathway is ER-phagy through the ER-phagy receptor FAM134B. FAM134B is an ER transmembrane protein with a C-terminal LIR domain, therefore capable of recruiting ER fragments to autophagosomes. FAM134B have been found to be crucial in maintaining ER homeostasis through its regulation of ER-phagy. Another common mode of cargo-recognition in ubiquitin-independent selective autophagy is through the detection of surface lipid and sugar moieties. For example, glycoproteins exposed through damaged salmonella containing vesicles are recognized by galectin-8, which are in turn detected by NDP52, leading to salmonella being targeted and degraded by the xenophagy machinery.

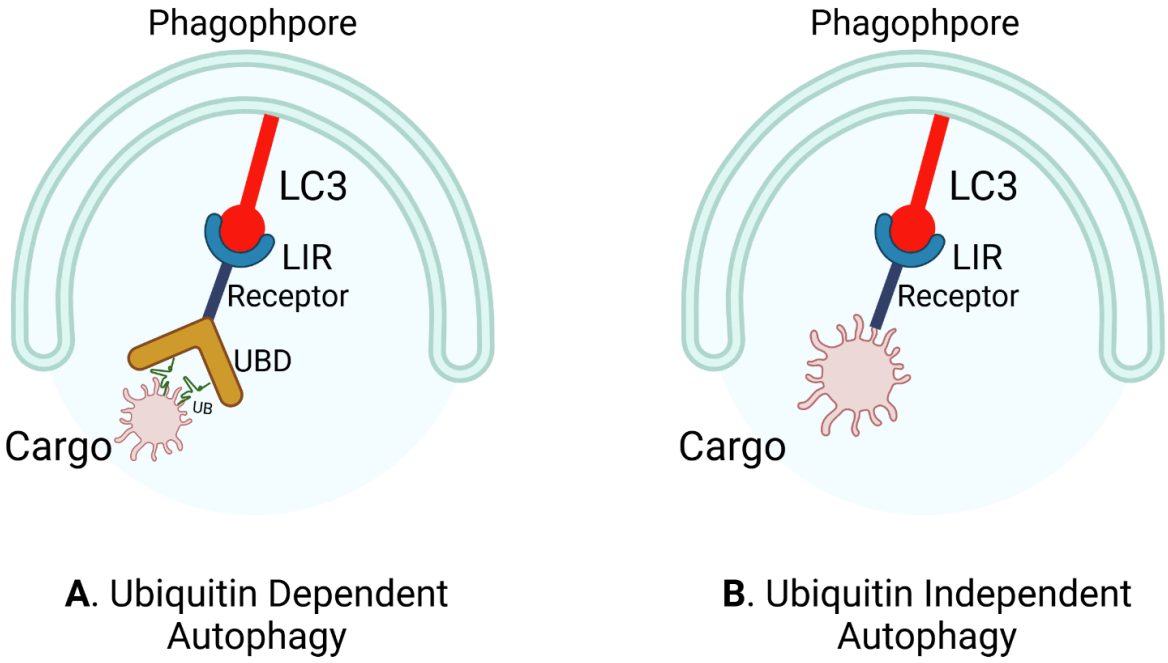

Figure 4. **Selective autophagy Ubiquitin-Dependent and Independent Pathways.** In the ubiquitin-dependent mechanism (A), the target organelle interacts with receptors through a polyubiquitinated chain (UB). The receptor protein attaches to the Ub chain on the damaged organelle through its ubiquitin-binding domain (UBD) and binds to the LC3-II protein of the autophagosome via LC3-interacting regions (LIR). In contrast, the ubiquitin-independent mechanism (B) involves receptors on the damaged organelle that directly bind the cargo to LC3 on the autophagosome.

This thesis will focus on the mechanistic diversity of selective autophagy pathways in mammalian systems, with a specific focus on two forms of autophagy: xenophagy: the selective autophagic degradation of intracellular pathogens, and ER-phagy: the targeted elimination of endoplasmic reticulum components.

1.8 Xenophagy

The fundamental role of innate immunity as a self-defence system in all eukaryotes begins with recognition of invading pathogens through pathogen recognition receptor proteins with the ability

to bind to pathogen components, which then trigger downstream innate immunity signaling. There has been a growing appreciation for the contribution of autophagy to the innate immune pathways. Autophagy can serve as a part of the innate immune responses by degradation of intracellular pathogens. The targeting of bacterial and viral pathogens by autophagy is called xenophagy (from Greek for eating of others)[77] Bacterial invasion of a mammalian cell stimulates xenophagy and lead to the formation of autophagosomes around targeted bacteria, then the autophagosome delivers the bacteria to the lysosome for degradation[78].

The first observation of autophagy triggered by microbial infection was made in 1984 when Rikihisa observed increased rate of autophagosome formation in polymorphonuclear leukocytes of guinea pigs under Rickettsiae infection. Pathogen degradation by autophagy was first observed in a study with a mutant strain of *Listeria monocytogenes* (delta Acta), where the mutant bacteria were observed to be captured in autophagosomes for degradation[79]. The ability of autophagy to target and eliminate wildtype bacteria was first demonstrated for *Streptococcus pyogenes*, also known as group A *Streptococcus* (GAS). In nonphagocytic cells that were infected with GAS, the bacteria escaped from the initial uptake vesicle to the cytosol and were then surrounded by autophagosome-like structures called GAS-containing autophagosome-like vacuoles (GcAVs)[80]. Additionally, a study by Gutierrez et al., showed that autophagy induction restrains intracellular survival of *Mycobacterium tuberculosis*, however, as a survival mechanism, M. *tuberculosis* have been shown to block autophagosome maturation when infecting macrophages [81]. Since this discovery, many studies also observed that pathogenic bacteria have evolved strategies to escape or subvert xenophagic activity by inhibiting autophagy pathways at various stages. Some of the bacteria that have been shown to inhibit autophagy include, *Salmonella*, *Mycobacteria*, *Shigella*, *Listeria monocytogenes*, and *Rickettsia conorii*. These strategies usually include bacterial removal

of post-translational modifications which promote targeting to the autophagosome [82,83,84], or blockage of autophagosome-lysosome fusion[85].

1.9 ER-phagy

The endoplasmic reticulum (ER) is an essential and dynamic organelle that plays a crucial role in the synthesis, folding, and modification of secretory and membrane proteins, calcium homeostasis, and innate immunity[86,87,88]. It is composed of a contiguous structure of interconnected network of smooth tubules and rough sheets[89]. To maintain its homeostasis, the ER can mark regions for degradative turn-over by ER-phagy or impede misfolded protein accumulation via activation of the unfolded protein response[90]. ER-phagy is promoted by ER-phagy receptors, which interact with both the ER and LC3 family members on the autophagosomal membrane to activate self-digestion programs [91,92]. This form of selective autophagy is crucial for maintaining ER homeostasis and preventing the accumulation of damaged or excess ER, which can lead to cellular stress and disease [93].

The selectivity of autophagic degradation of the ER is determined by ER-phagy receptors, including the family with sequence similarity 134 member B (FAM134B), SEC62 homolog, preprotein translocation factor (SEC62), reticulon 3 (RTN3), cell cycle progression 1 (CCPG1), atlastin GTPase 3 (ATL3), and testis expressed 264 (TEX264)[94]. These proteins are responsible for coupling ER fragments to autophagic membranes, which ultimately leads to the turnover of the ER in response to stress, as well as the degradation of ER protein aggregates by the lysosome[94].

This process is mediated by specific ER-phagy receptors in response to specific stresses [94,95]. The first and most well-characterized ER-phagy receptor in mammals is FAM134B, also known as Reticulophagy Regulator 1 (RETREG1)[96]. FAM134B is an ER membrane protein that localizes to

ER sheets and contains two domains: the reticulon homology domain (RHD) and the LC3 interaction domain (LIR)[97] .The RHD enhances the binding of the ER membrane, while the LIR stabilizes LC3 or GABARAP to autophagic vesicles, LC3/GABARAP proteins are involved in cargo recruitment, engulfment and autophagosome closure[98]. This unique structure is essential for FAM134B to regulate ER-phagy activity effectively[99].

1.10 Autophagy and human health

Over the past two decades, autophagy research has become a rapidly expanding field. In particular, much enthusiasm has been directed toward understanding autophagy defects in disease. Autophagy defects have now been linked to multiple diseases, including cancer[100], neurodegeneration[101], cardiovascular diseases[102] and immune diseases[103].

1.10.1 Autophagy in metabolic syndromes

Metabolic syndrome is generally defined as a cluster of metabolically related health conditions, including abdominal obesity, high blood pressure, elevated blood sugar, high triglycerides, and low High-density lipoprotein (HDL) cholesterol that occur together, increasing the risk of heart disease, stroke, and type 2 diabetes. It is primarily driven by insulin resistance, poor diet, lack of physical inactivity, and genetics. Diagnosis requires at least three of these risk factors[104]. Defects in autophagy can exacerbate metabolic derangements, leading to insulin resistance and contributing to conditions such as type-II diabetes and obesity[105]. Insulin resistance is a pathological state characterized by diminished cellular responsiveness to insulin in key metabolic tissues—primarily skeletal muscle, adipose tissue, and liver—leading to dysregulated glucose and lipid metabolism.[106]. In muscle, impaired insulin signaling reduces GLUT4-mediated glucose uptake, while adipose tissue releases excess free fatty acids (FFAs) and proinflammatory cytokines

(e.g., TNF-α, IL-6) that further disrupt insulin receptor signaling and promote ectopic fat deposition[107]. Molecular mechanisms involve defects in the PI3K/Akt/mTOR pathway, mitochondrial dysfunction, and chronic inflammation.

Metabolic syndrome-like conditions have been observed in autophagy-deficient mice put under an over-nutrition diet, which were far more likely to develop insulin resistance, liver steatosis, expansion of adipose tissue, and a much higher body weight when compared with wild-type mice[105]. It is understood that chronic excessive calorie intake in these mice led to glucolipotoxicity, which induced metabolic stress in the pancreatic β-cells, the liver, and adipose tissue, often in the form of mitochondrial dysfunction, ER stress, and oxidative stress[105]. The same stressors that autophagy responds to. Therefore, autophagy impairment results in the accumulation of damaged organelles and protein aggregates, leading to the inability to maintain a homeostatic cellular environment [102]. When manifested at the tissue or organ level, this results in reduced insulin secretion in pancreatic β-cells, adipocyte dysfunction, and the onset of non-alcoholic fatty liver disease due to increased lipid deposits in the liver[105]. All these conditions contribute to the development of insulin resistance, which would then exacerbate glucolipotoxicity, creating a detrimental feedback loop. While normal autophagy activity would act to reduce the aforementioned metabolic stressors, thereby preventing the formation of the detrimental feedback loop[105].

1.10.2 Autophagy in gut health

Autophagy in the intestinal tissues have been shown to be important in the regulation of inflammatory responses and defence against pathogenic bacteria[108]. In an environment rife with microbiota, normal autophagy activity has been shown to keep inflammation in check by suppressing pro-inflammatory T-cell signaling. Inflammatory bowel disease (IBD) is a chronic

syndrome that affects the intestinal tract, influenced by both genetic and environmental factors. Autophagy have been shown to be strongly linked to the pathogenesis of IBDs such as Crohn's disease and ulcerative colitis[108, 109].

Crohn's disease (CD) is a chronic inflammatory bowel disease usually affecting various separate segments of the gastrointestinal tract, with a greatly heterogeneous symptom profile. At any time between early childhood and late adulthood, the onset of the disease can occur. Both genetic and environmental factors are involved in the development of the disease. The current model of Crohn's disease pathogenesis suggests that intestinal microbiota-based stimulation in genetically predisposed individuals results in defective inflammatory responses, which leads to chronic inflammation of the gastrointestinal tract. Therefore, investigating pathogen-host interactions and the complex network of signalling cascades would be important in the search for new treatment options. Genome-wide association studies (GWAS) have detected high susceptibility regions of the genome that are associated with or contribute to CD pathogenesis.[108]. Several of the proteins involved in xenophagy induction (ATG16L1and IRGM) and pathogen detection (NOD2 and TLR4) were among the genes detected[108]. As the gut microbiota becomes more extensively researched, multiple studies have highlighted the importance of autophagy in maintaining intestinal health and shaping microbiota composition.[108]. Research has shown that mice with dysregulated autophagy have altered gut microbial diversity, leading to a reduction of beneficial bacteria species such as *Akkermansia muciniphila*[110]. Conversely, gut microbiota have also been shown to influence autophagy activity in various organs of the body through secreted metabolites.[108]. Shedding new light onto the previously unknown pathway of autophagy regulation.

1.11 Statement of Research Problem, Rationale, and Hypothesis

Autophagy is a critical cellular process that maintains cellular homeostasis by eliminating damaged organelles, misfolded proteins, and pathogens. Dysregulation of autophagy has been implicated in a wide range of diseases, including metabolic syndrome, bacterial infections, and neurodegenerative disorders. Due to limitations in existing tools, accurate measurement of autophagy induction remains challenging, particularly in rare cell populations or *in vivo* conditions. Additionally, autophagy has long been implicated in playing important roles in metabolic regulation and pathogen defence, as perturbations such as iron overload or bacterial infections lead to disruption in autophagy pathways, resulting in disease progression. Understanding the details of these mechanisms could provide new therapeutic targets for conditions such as insulin resistance and bacterial infections.

Hypothesis:

We hypothesize that the phosphorylation of ATG16L1 serves as a reliable and specific biomarker for autophagy induction, enabling accurate measurement of autophagy rates in diverse physiological and pathological contexts. Furthermore, we propose that chronic iron overload disrupts autophagy by inhibiting mTORC1-UVRAG signaling, leading to impaired autophagic-lysosome regeneration and contributing to insulin resistance in metabolic syndrome. Additionally, we hypothesize that bacterial pathogens, such as *Salmonella Typhimurium*, evade host innate immunity by targeting the ER-phagy receptor FAM134B, thereby inhibiting ER-phagy and promoting intracellular survival.

Chapter 2: An Antibody for Analysis of Autophagy Induction

Published in Nature Methods - DOI: 10.1038/s41592-019-0661-y

Wensheng Tian[1], **Reham Alsaadi[1¥]**, Zhihao Guo[1¥], Alena Kalinina[1], Micaël Carrier[2], Marie-Eve Tremblay[2], Baptiste Lacoste[1,3,4], Diane Lagace[1] and Ryan C. Russell[1,5*]

2.1 Statement of Author Contributions

WT and RCR wrote the manuscript. WT was primarily responsible for data production in all figures except IF and IHC panels in figures 2 and 4. **RM** assisted with IF experiments and data analysis. ZH was responsible for optimizing pATG16L1 antibody protocols for IF and IHC. AK and DL provided the mice used for the study and assisted with IHC experimental planning and tissue staining. MC and MET imaged EM samples. BL provided expertise and guidance for EM sample preparation. RCR oversaw manuscript planning and conceived of the study.

An Antibody for Analysis of Autophagy Induction

Wensheng Tian[1], Reham Alsaadi[1¥], Zhihao Guo[1¥], Alena Kalinina[1], Micaël Carrier[2], Marie-Eve Tremblay[2], Baptiste Lacoste[1,3,4], Diane Lagace[1] and Ryan C. Russell[1,5*]

[1]Department of Cellular and Molecular Medicine, University of Ottawa, 451 Smyth Road, Ottawa, Ontario K1H 8M5, Canada.

[2] Axe neurosciences, Centre de recherche du CHU de Québec , Université Laval, Québec, QC, Canada

[3]University of Ottawa Brain and Mind Research Institute

[4]Neuroscience Program, Ottawa Hospital Research Institute, Ottawa, ON, Canada

[5]University of Ottawa Center for Infection, Immunity and Inflammation

[¥] Denotes equal contribution

*Address for correspondence: 451 Smyth Rd, Ottawa, Ontario, K1H 8M5, Canada.

E-mail: ryan.russell@uottawa.ca

2.2 Abstract

Autophagy is a degradative program that maintains cellular homeostasis. Autophagy defects have been described in numerous diseases. However, analysis of autophagy rates can be challenging, particularly in rare cell populations or *in vivo*, due to limitations in currently available tools for measuring autophagy induction. Here, we describe a novel method to monitor autophagy by measuring phosphorylation of the protein ATG16L1. We developed and characterized a monoclonal antibody that can detect phospho-ATG16L1 endogenously in mammalian cells. Suitable for Western blot, immune-fluorescence and IHC, phospho-ATG16L1 levels directly correspond to autophagy rates. Importantly, phospho-ATG16L1 is only present on newly-forming autophagosomes. Therefore, its levels are not affected by prolonged stress or late-stage autophagy blocks, which can confound autophagy analysis. Moreover, we show ATG16L1 phosphorylation is a conserved signalling pathway activated by numerous autophagy-inducing stressors. Taken together, this phospho-antibody represents an exciting new tool to study autophagy induction.

2.3 MAIN

Macroautophagy (hereafter referred to as autophagy) is a degradative pathway that is potently upregulated in response to intrinsic or extrinsic cellular stressors.[1]. Autophagy is driven by the formation of a double-membraned vesicle called an autophagosome. Autophagosomes can sequester harmful elements in the cytoplasm and deliver them to the lysosome for degradation.[1]. Starvation also potently increases autophagosome formation, recycling macromolecules to fund essential biosynthetic pathways. [2,3]. Autophagosome formation is driven by a highly conserved set of autophagy-related (ATG) proteins, including a serine/threonine kinase and a ubiquitin-like E3 enzyme.[4]. Study of the autophagy pathway often involves analysis of outputs that are downstream of these two enzymes.[1].

UNC-51-like kinase (ULK1), a serine/threonine kinase, serves as the catalytic component of the autophagy-promoting protein kinase complex consisting of ATG13L, FIP200 (or RB1CC1) and ATG101[5-10]. Mammals possess two ULK homologs, ULK1 and ULK2, which have largely overlapping targets and roles in promoting autophagy[11]. Hereafter, ULK1 and ULK2 will collectively be referred to as ULK. In the absence of stress, ULK complexes are inhibited through direct phosphorylation by the mammalian target of rapamycin complex 1 (mTORC1)[8-10]. Under stress, ULK is released from mTORC1-inhibition and acts by phosphorylating downstream targets to promote the first steps of autophagosome formation[8-10]. Recruitment of the E3-like enzyme consisting of ATG16L1/ATG5-12 to the autophagosomal membrane is dependent on the FIP200 subunit of the ULK complex[12,13]. The ATG16L1 subunit is responsible for targeting the enzyme complex to nascent autophagosomes[14], while ATG5-12 recruits microtubule-associated protein 1-light chain (LC3) to the complex. ATG16L1-containing complexes are essential for autophagy and

are referred to as E3-like due to the mechanistic similarities in the conjugation of LC3 to phosphatidylethanolamine (PE) with the ubiquitin conjugation cascade.

LC3B is the most studied member of the LC3/GABARAP family[15,16]. Functionally, LC3B is involved in cargo recruitment, engulfment and autophagosome closure. However, LC3B is best known for its use to monitor autophagy rates[17]. This is due to the fact that lipidated LC3B is readily identifiable as a lower migrating band by western blot or a punctate structure by immunofluorescence (IF). The ability to measure autophagosomes through lipidated LC3B (hereafter referred to as LC3B-II) has resulted in the inclusion of LC3B-II measurement in the majority of studies on the autophagy pathway[17]. However, analysis of the autophagy pathway using LC3B-II must be performed carefully as decreases in autophagosome clearance often result in increased LC3B-II levels, which incorrectly indicates an elevation of autophagy rates[17]. Conversely, under stress conditions rapidly degraded LC3B-II sometimes fails to accumulate, thereby masking increased autophagy rates[17]. To overcome these obstacles, LC3B-II analysis is often performed in the presence of inhibitors of autophagosome clearance[18]. However, use of such drugs can be problematic *in vivo*, or introduce confounding effects if used for an extended duration *in vitro*. Despite these drawbacks, LC3B-based autophagy analysis has enabled a tremendous expansion of our knowledge of the autophagy pathway to date.

Analysis of autophagy adaptors is another common approach to examine autophagy rates[18]. Autophagy adaptors recruit specific cargo to the autophagosomal membrane through interaction with LC3B[18] and, as a result, are degraded along with the cargo. The best characterized autophagy adaptor is p62 (also known as sequestosome-1), which is rapidly cleared by autophagy in response to several stressors[18]. However, autophagy analysis using p62 comes with important caveats: 1) p62 is transcriptionally regulated by stress[19,20] and in disease states[21,22], affecting protein levels

independently of autophagy flux, 2) different stressors can preferentially utilize specific autophagy adaptors[23-25], which can be problematic if the adaptor is not known, and 3) after an initial decrease, the levels of autophagy adaptors remain lowered under continued stress and provide limited information about changes in prolonged autophagy rates. Despite these limitations, analysis of autophagy adaptors has been a very useful tool for autophagy researchers, which is often performed with LC3B-II analysis.

In addition to analysis of LC3B and autophagy adaptors, other methods have been developed to monitor mammalian autophagy including: electron microscopy[26], turn-over of long lived proteins[27], BHMT cleavage[28], or the use of specialized dyes or probes[29,30]. However, analysis of p62 and LC3B remain the most commonly used methods to monitor autophagy. Their popularity, despite the above-mentioned limitations, is largely due to their ease of use and the availability of high-quality reagents that can be applied to multiple assays. We propose that an ideal method to monitor autophagy would couple these beneficial qualities but would also be specifically tied to autophagosome formation itself, rendering it insensitive to the accumulation of dysfunctional autophagosomes or skewing by the duration of autophagy activation. An assay with these properties would address several of the most pressing deficiencies. However, for comprehensive analysis of the autophagy pathway multiple lines of analysis will remain best practice.

We identified a stress-sensitive signalling event that may be tied to newly forming autophagosomes. We found that ULK phosphorylates ATG16L1 in response to infection at a conserved serine (S278)[31]. Both ATG16L1 and ULK are essential for autophagy initiation in nearly all conditions, unlike individual members of LC3/GABARAP family or autophagy adaptors that have functional redundancies. Therefore, the newly-discovered mechanistic link between ULK and the LC3-lipidating machinery may represent a common signalling event that is

stimulated upon autophagy induction, regardless of the stress or cargo. Previous reports have shown that FIP200, an essential cofactor for ULK-kinase activity, can bind to ATG16L1[13,32]. This binding requires amino acids 229-242 of ATG16L1, which are not phosphorylated by ULK[31]. However, FIP200 binding with ATG16L1 may promote phosphorylation by the ULK-complex. To study this pathway, we partnered with Abcam to create a monoclonal antibody capable of detecting ATG16L1 phosphorylation on serine 278 (hereafter referred to as pATG16L1^{s278}). Hybridomas were first screened by ELISA, then positive clones were tested in our lab for specificity and functionality in several assays. After two years of development, involving multiple rounds of hybridoma fusions and clonal screens, we identified a monoclonal antibody capable of detecting endogenous levels of the phospho-protein across multiple assays, which is now available to the research community.

2.4 RESULTS

Phosphorylation of ATG16L1 following bacterial infection has been shown to play a role in the defects related to Crohn's-associated mutations of ATG16L1[31,33]. IKKα has been shown to phosphorylate ATG16L1 *in vitro* at serine 278 (S278). However, *in vivo* ULK, not IKK□ is responsible for ATG16L1 phosphorylation[31]. To further characterize this signaling, we developed a monoclonal antibody against pATG16L1^{s278}. Using ATG16L1 knockout (KO) or Wildtype (WT) cells we tested the specificity of pATG16L1^{s278} antibody in response to amino acid starvation, a potent inducer of autophagy. pATG16L1^{s278} was stimulated by starvation and could be detected endogenously by western blot in WT, but not KO cells (Fig. 1A). Mutation of the S278, deletion of key autophagy genes, or pharmacological blockage of autophagy all disrupted ATG16L1 phosphorylation, underscoring the specificity of the antibody (S1A-D).

Figure 1

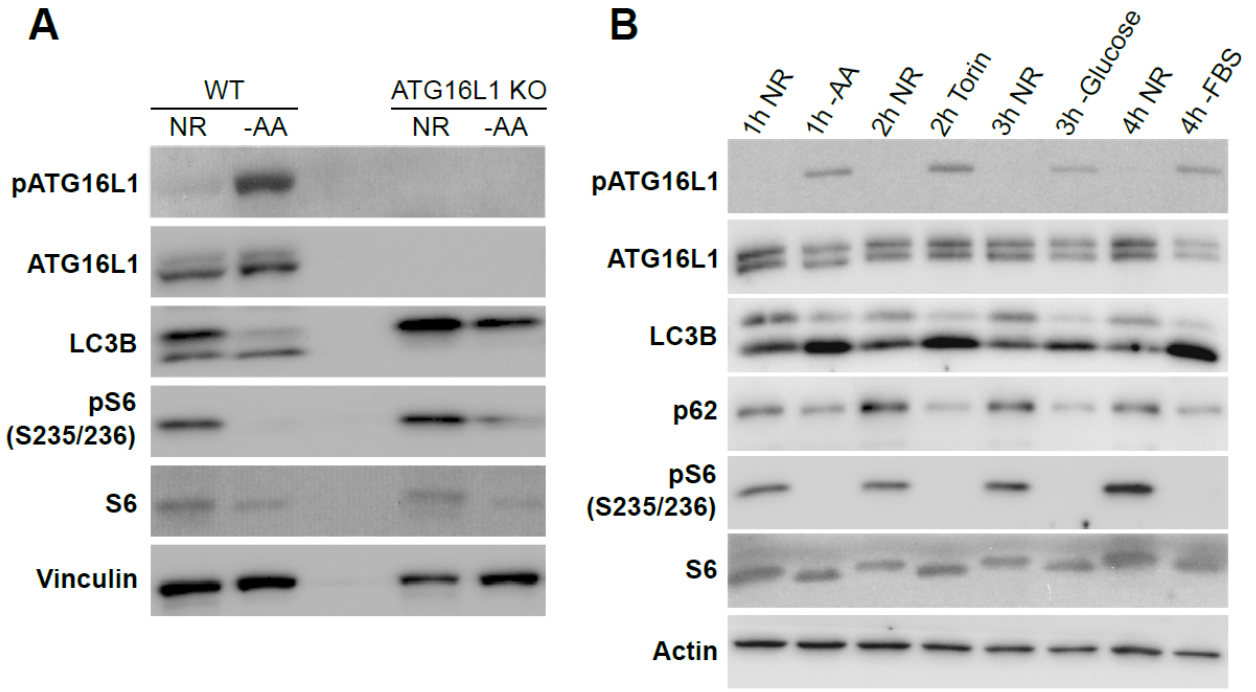

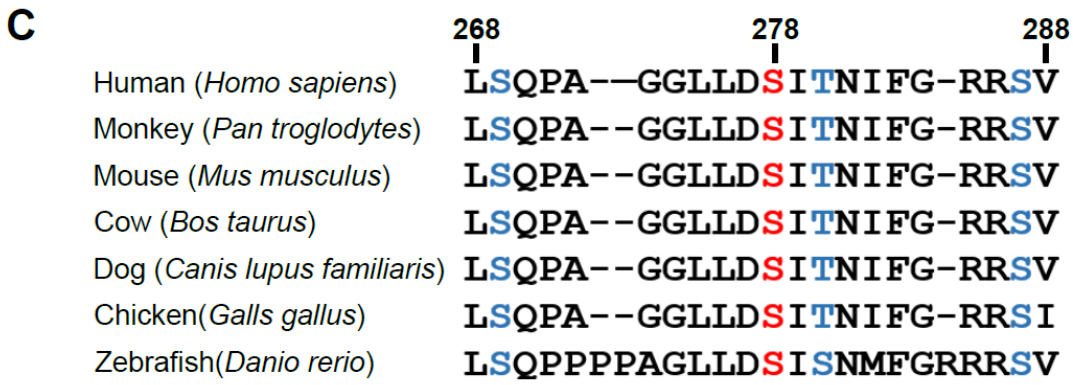

Fig.1 **Phosphorylation of ATG16L1 is a conserved indicator of autophagy induction, which is activated by multiple stimuli.** a, Immunoblot of WT and ATG16L1 KO HCT116 cells either kept in nutrient-rich complete medium (NR) or starved with DMEM deficient in amino acids (-AA) for 3 h. An empty lane demarcates WT and KO cell lines. Experiment was repeated three times (n = 3) independently with similar results. b, Representative immunoblot of Q7 mouse brain striatal cell lysates treated as indicated. Experiment was repeated three times (n = 3) independently with similar results. c, Amino acid sequence proximal to serine 278 of human ATG16L1 aligned to indicated species displaying high degree of conservation. The 278 serine residue is marked in red. Additional conserved serine and threonine residues are marked in blue.

We next tested whether ATG16L1 phosphorylation is induced by autophagy-inducing stressors in addition to infection and amino acid withdrawal[31]. We observed increased ATG16L1 phosphorylation in response to *i)* mTOR-inhibition, *ii)* glucose withdrawal, *iii)* cytokine depletion, *iv)* reactive oxygen species, and *v)* mitochondrial uncoupling (Fig. 1B and S1E-F). Increased pATG16L1^{s278} levels correlated with autophagy induction, confirmed by p62 clearance, and increased LC3B-II (Fig. 1B). As this antibody was generated from a highly-conserved region of ATG16L1 (Fig. 1C), it was capable of detecting ATG16L1 phosphorylation in 8 cell lines of different species and tissue origins (Fig. S1G). The induction of pATG16L1^{s278} in multiple cell types under diverse stressors lead us to further determine if pATG16L1^{s278} levels could be used as a method to measure autophagy induction.

We next sought to determine if our antibody was suitable for IF and how it compared to other established autophagy markers. Specificity of our antibody was verified by the absence of pATG16L1^{s278} staining in cells: treated with VPS34 inhibitor, with ATG16L1 deleted, reconstituted with ATG16L1(S278A) (Fig. 2A, S2A). While WT-cells showed strong pATG16L1^{s278} staining that colocalized almost completely (97%) with total-ATG16L1. Strikingly, we found that pATG16L1^{s278} was almost exclusively punctate when compared to diffuse and punctate pattern of total ATG16L1 (Fig. 2A). We postulated that pATG16L1^{s278} may be selectively associated with autophagosomes due to its exclusive punctate staining. To verify our hypothesis, we analyzed pATG16L1^{s278} colocalization with LC3B and its sensitivity to starvation. Co-staining of endogenous pATG16L1^{s278} and LC3B revealed a partial colocalization and upregulation of puncta with both antibodies (Fig. 2B, S2B).

Figure 2

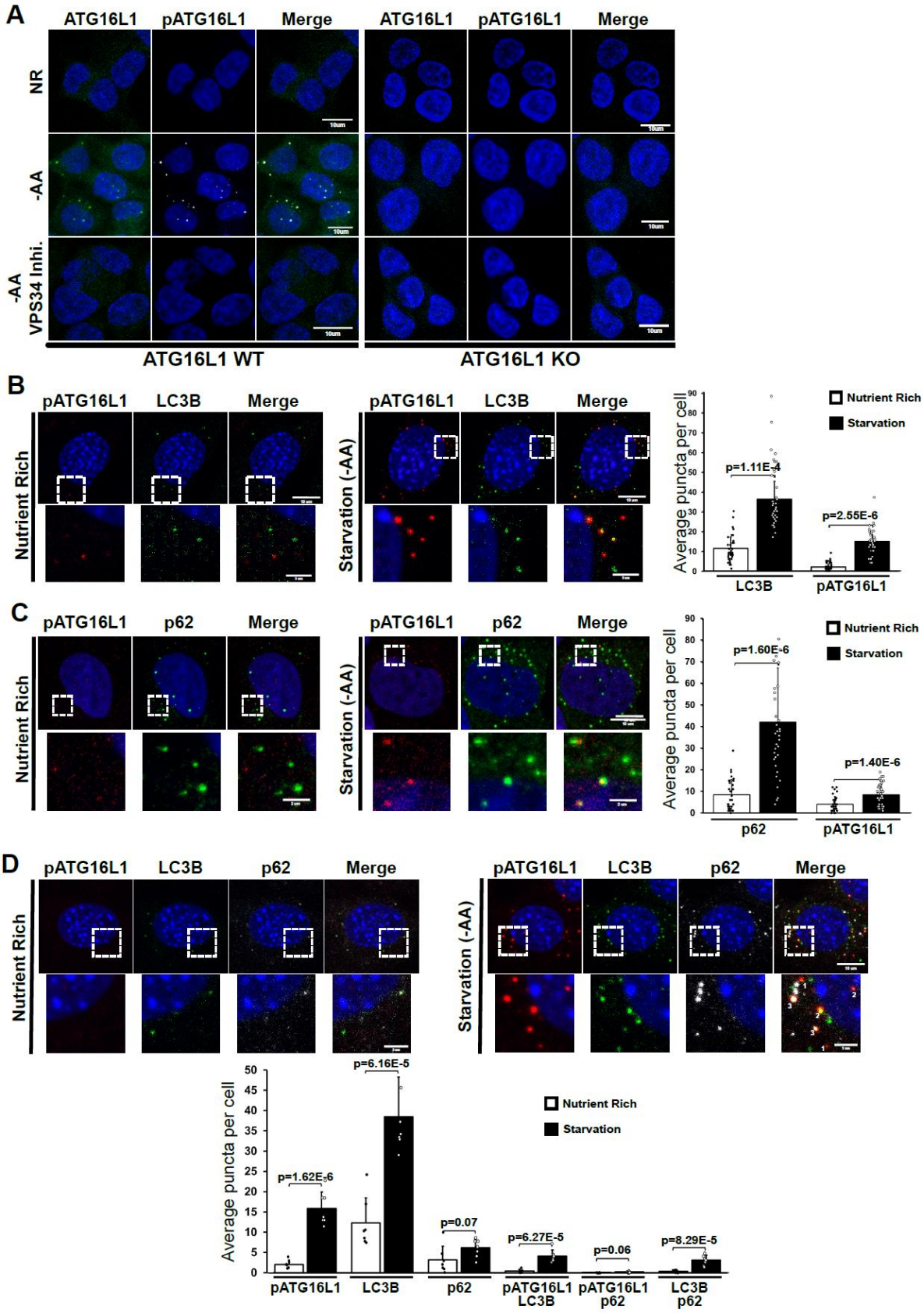
A
ATG16L1
pATG16L1
Merge
NR
-AA
-AA VPS34 Inhi.
ATG16L1 WT
ATG16L1 KO
B
pATG16L1
LC3B
Nutrient Rich
Starvation (-AA)
Average puncta per cell
Nutrient Rich
Starvation
p=1.11E-4
p=2.55E-6
LC3B
pATG16L1
C
p62
p=1.60E-6
p=1.40E-6
D
p=6.16E-5
p=1.62E-6
p=0.07
p=6.27E-5
p=0.06
p=8.29E-5
pATG16L1
LC3B
p62
pATG16L1 LC3B
pATG16L1 p62
LC3B p62

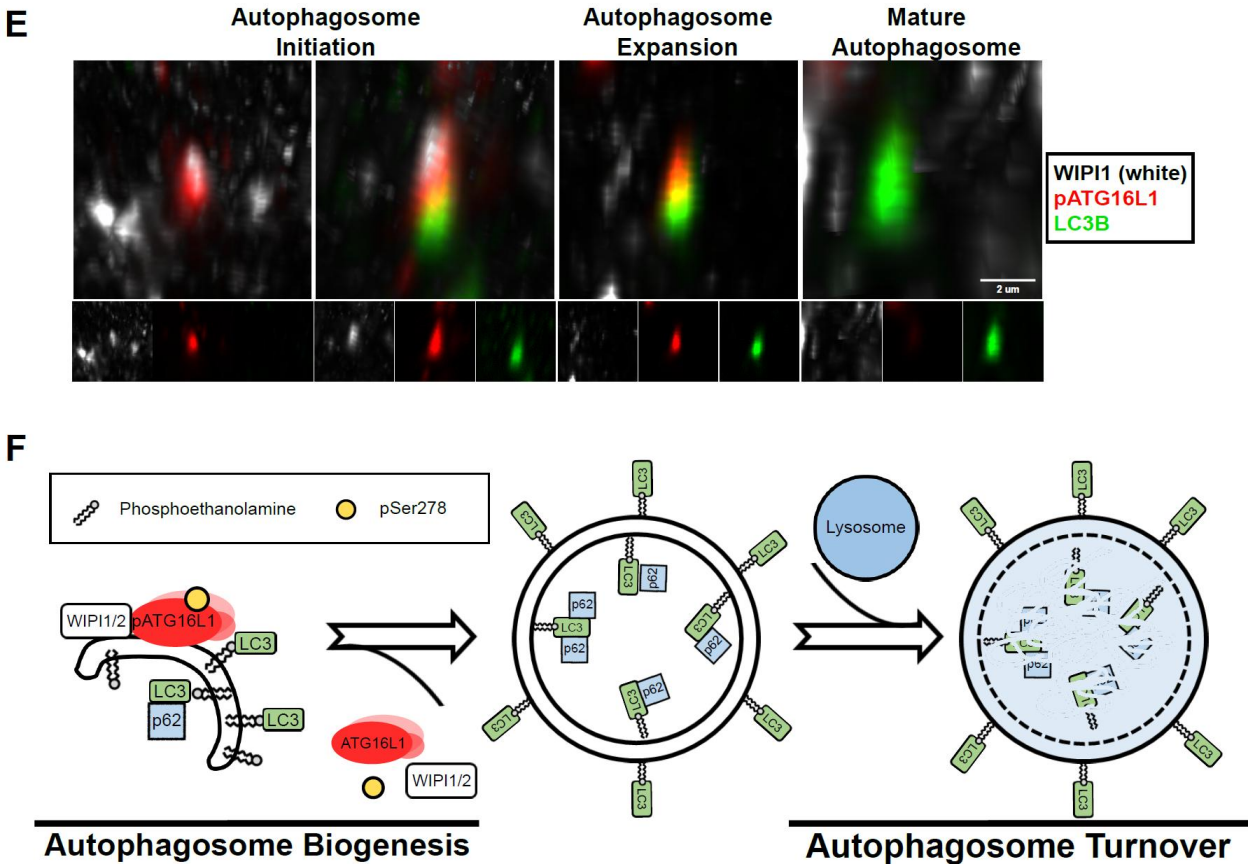

Fig. 2: **pATG16L1 can be analyzed by immunofluorescence and is recruited to the expanding autophagosomal membrane**. a, HCT116 WT and ATG16L1 KO cells were treated with the indicated treatments for 2 h. Endogenous ATG16L1 (green), pATG16L1 (white) and DNA (blue) were stained. Representative images are shown (scale bars, 10 µm). b, Endogenous pATG16L1 (red), LC3B (green) and DNA (blue) were stained in Q7 cells incubated in either complete medium or amino acid-deficient DMEM for 1 h. Representative images are shown (scale bars, top row, 10 µm; bottom row, 3 µm). Quantification of one representative experiment is shown, independently repeated three times (n = 3) with similar results. Measure of center represents mean value and error bars represent standard deviation. Statistical analysis was performed using two-sided Student's t-test; asterisks denote $P < 0.05$. c, Endogenous pATG16L1 (red), p62 (green) and DNA (blue) were stained in Q7 cells incubated in either complete medium or amino acid-deficient DMEM for 1 h. Representative images are shown (scale bars, top row, 10 µm; bottom row, 2 µm). Quantification of one representative experiment is shown, independently repeated three times (n = 3) with similar results. Measure of center represents mean value and error bars represent standard deviation. Statistical analysis was performed using two-sided Student's t-test; asterisks denote $P < 0.05$. d, Endogenous pATG16L1 (red), LC3B (green), p62 (white) and DNA (blue) were stained in Q7 cells incubated in either complete medium or amino acid-deficient DMEM for 1 h. Representative images are shown (scale bars, top row, 10 µm; bottom row, 3 µm). Quantification

of one representative experiment is shown, independently repeated three times (n = 3) with similar results. Measure of center represents mean value and error bars represent standard deviation. Statistical analysis was performed using two-sided Student's t-test; asterisks denote $P < 0.05$. e, MEFs transiently expressing GFP-tagged WIPI1 were incubated in either complete medium or amino acid-deficient DMEM for 1 h. Endogenous pATG16L1 and LC3B were stained and analyzed along with GFP by AiryScan high-resolution fluorescent microscopy. Four representative images corresponding to different stages of autophagosome expansion are shown. Experiment was repeated three times (n = 3) with similar results. For consistency pATG16L1 was pseudocolored red, LC3B green and GFP-WIPI1 white (scale bars, 2 μm). f, Simplified schematic of autophagosome biogenesis with respect to the roles of WIPI1/2, ATG16L1, LC3 and p62.

To confirm the autophagosomal nature of pATG16L1^{s278} puncta, we also analyzed colocalization between pATG16L1^{s278} and p62. Consistent with our previous observations, we detected pATG16L1^{s278}/p62 double-positive puncta primarily in amino acid starved cells (Fig. 2C, S2C). Triple staining revealed a higher degree of colocalization between p62 and LC3B than either protein had for pATG16L1^{s278} (Fig. 2D, S2D). As p62 and LC3B remain on fully formed autophagosomes this raises the possibility that pATG16L1^{s278} associates with the autophagic membrane prior to autophagosome closure. The possibility of selective localization of pATG16L1^{s278} to newly-forming autophagosomes is particularly interesting as these structures could provide a direct readout for the rate of autophagy initiation.

To decipher the stage at which pATG16L1^{s278} promotes autophagosome biogenesis, we performed high-resolution confocal microscopy on cells transiently expressing GFP-WIPI1. GFP-WIPI1 was previously found exclusively on expanding autophagosomal structures and not on mature autophagosomes[34]. We were able to observe distinct patterns of co-staining, which may be attributed to different stages of autophagosome biogenesis. For example, we observed puncta that exhibited colocalization between pATG16L1^{s278}/WIPI1, pATG16L1 ^{s278}/LC3B, and

pATG16L1^{s278}/WIPI1/LC3B (Fig. 2E). However, we did not observe any WIPI1/LC3B in the absence of pATG16L1 ^{s278} (Fig. 2E).

To look at pATG16L1^{s278} on autolysosomes we co-stained lysosomal marker LAMP1 with pATG16L1^{s278}, but found very little lysosomal localization of pATG16L1^{s278} (Fig. S2E). Similar observation was made in eGFP-mCherry-LC3B reporter cells (Fig. S2F). Taken together these data suggest a working model of autophagosomal initiation where pATG16L1^{s278} is targeted to newly forming autophagosomes, promoting LC3B-lipidation and dissociating along with WIPI-proteins upon autophagosomal maturation (Fig. 2F).

Interestingly, ATG16L1 phoshporylation is not required for autophagy induction. In mutant ATG16L1 reconstituted cells, we observed similar autophagy induction (Fig. S2G) and no difference in total ATG16L1 colocalization with GFP-WIPI2 (Fig. S2H). However, this does not relate to the utility of pATG16L1^{s278} to monitor autophagy, as both LC3B and p62 are similarly not essential for autophagy[35,36].

The localization of pATG16L1^{s278} to newly-forming autophagosomes indicates that it should be insensitive to blockages in autophagosome clearance. A persistent problem in autophagy research is that blockade of autophagosomal turnover leads to accumulation of LC3B-positive vesicles, resembling a potent induction of autophagy[17]. To test if pATG16L1^{s278} levels are altered by accumulation of mature autophagosomes, we treated cells with bafilomycin A1 (Baf A1), an inhibitor of autophagosome turnover, under nutrient rich conditions and analyzed LC3B and pATG16L1^{S278} using IF. As expected, LC3B puncta were dramatically increased under Baf A1 treatment, despite no increase in the overall rate of autophagy (Fig. 3A). However, we observed that pATG16L1^{s278} staining was indistinguishable between Baf A1 treated cells and untreated, consistent with the actual rate of autophagy induction under nutrient rich conditions (Fig. 3A).

pATG16L1^{s278} levels by western blot similarly did not increase with Baf A1 (Fig. S3A). Together, these findings indicate that pATG16L1^{s278} can discriminate between autophagy induction and autophagosome accumulation.

Figure 3

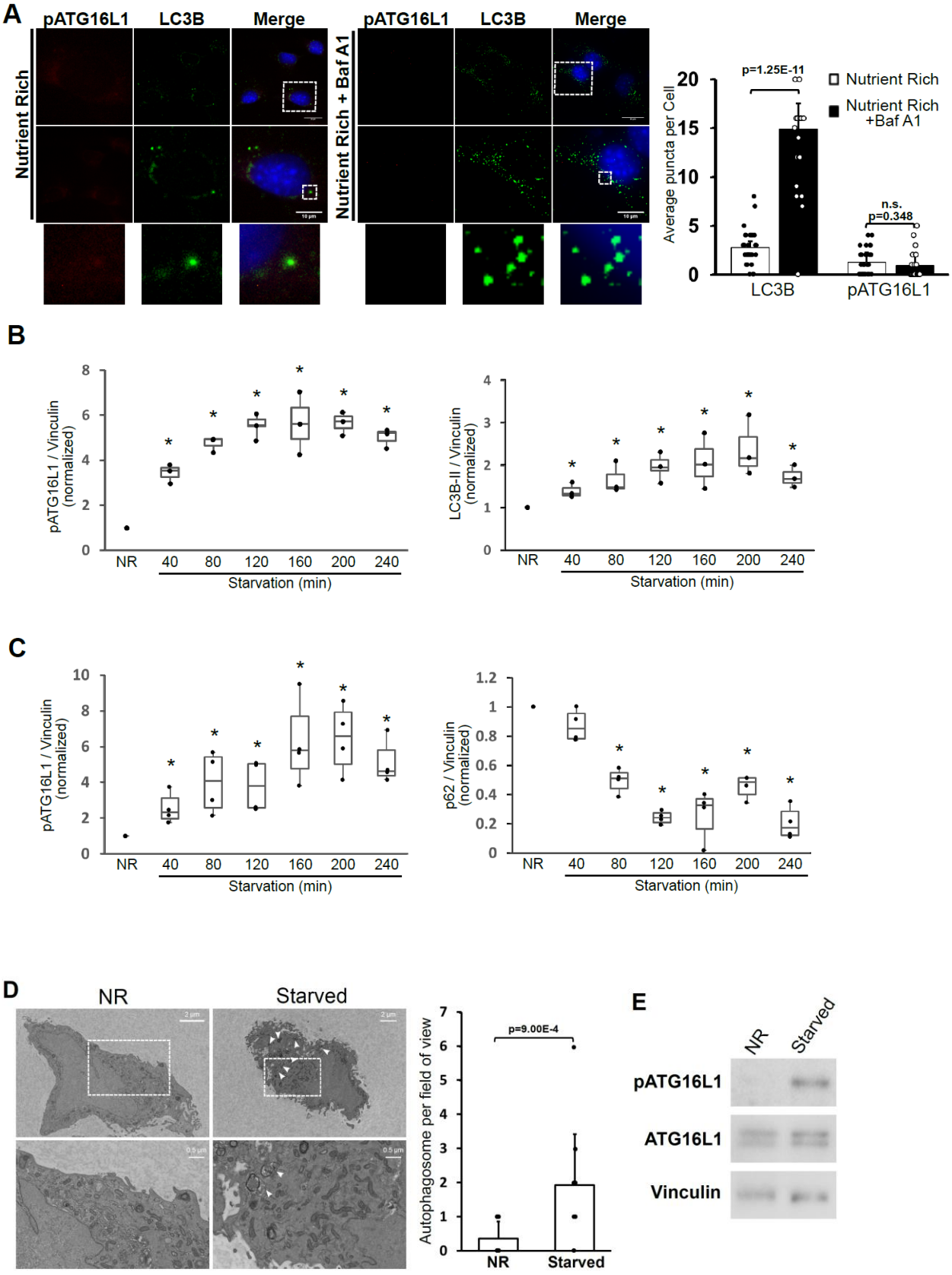
A
pATG16L1
LC3B
Merge
Nutrient Rich
Nutrient Rich + Baf A1
Average puncta per Cell
p=1.25E-11
n.s.
p=0.348
Nutrient Rich
Nutrient Rich +Baf A1
LC3B
pATG16L1
B
pATG16L1 / Vinculin (normalized)
LC3B-II / Vinculin (normalized)
NR
40
80
120
160
200
240
Starvation (min)
C
pATG16L1 / Vinculin (normalized)
p62 / Vinculin (normalized)
Starvation (min)
D
NR
Starved
Autophagosome per field of view
p=9.00E-4
E
NR
Starved
pATG16L1
ATG16L1
Vinculin

Fig. 3: pATG16L1 level provides a reliable measurement of autophagy rates independent of late-stage autophagy block and directly reflects autophagic vesicle formation. a, Q7 cells were incubated in complete medium in the presence or absence of Baf A1. pATG16L1, LC3B and DNA were stained and analyzed by immunofluorescence. Representative images are shown (scale bars, top row, 20 µm; bottom row, 10 µm). Quantification of one representative experiment is shown, independently repeated three times (n = 3) with similar results. Measure of center represents mean value and error bars represent standard deviation. Statistical analysis was performed using two-sided Student's t-test; asterisk denotes $P < 0.05$. b, Q7 cells were incubated in either complete medium or HBSS in the presence of Baf A1. Cell lysates were collected at the time points indicated and immunoblotted. Quantification of western blot protein relative intensities normalized against the NR sample from three independently repeated experiments (n = 3) is shown. Measure of center represents mean value and error bars represent standard deviation. Statistical analysis was performed using two-sided Student's t-test; asterisk denotes $P < 0.05$. c, Q7 cells were incubated in either complete medium or HBSS. Cell lysates were collected at the time points indicated and immunoblotted. Quantification of western blot protein relative intensities normalized against the NR sample from four independently repeated experiments (n = 4) is shown. Measure of center represents mean value and error bars represent standard deviation. Statistical analysis was performed using two-sided Student's t-test; asterisk denotes $P < 0.05$. d, Q7 cells were incubated in either complete DMEM or HBSS for 240 min. Cells were then fixed, agarose-embedded, sectioned and analyzed by electron microscopy. White arrows denote autophagosomes. Scale bars, top row, 2 µm; bottom row, 0.5 µm. Quantification of one representative experiment is shown, independently repeated three times (n = 3) with similar results. Measure of center represents mean value and error bars represent standard deviation. Statistical analysis was performed using two-sided Student's t-test; asterisk denotes $P < 0.05$. e, Representative immunoblot from duplicate set of cells treated with the same conditions as Fig. 2d. Experiment was independently repeated three times (n = 3) with similar results.

To compare the kinetics of pATG16L1^{s278} induction to established markers of autophagy flux we performed western blot measuring LC3B-II and pATG16L1 levels under starvation with inhibitors. We constantly observed a correlation between the peak signals for LC3B-II and pATG16L1 (Fig. 3B, S3B), indicating that analysis of ATG16L1 phosphorylation could be used as a substitute to LC3B-II analysis with flux inhibitors. Repeated in the absence of Baf A1 to measure the clearance of p62, we observed a potent decrease in p62 protein levels and a concomitant increase in ATG16L1 phosphorylation, consistent with autophagy induction (Fig. 3C, S3C). However, these two methods of monitoring autophagy gave slightly different information at early and late time

points. After 40min starvation we observed a dramatic increase in pATG16L1^{s278} levels and a statistically insignificant reduction in p62 levels (Fig. 3C, S3C). This is consistent with an early point in the autophagic flux, where several new autophagosomes are being formed (pATG16L1^{s278} high) but only few have fused with the lysosome to degrade p62 (Fig. 2F). However, beyond 120min starvation p62 levels remain low making it difficult to determine changes in autophagy flux after the initial clearance of autophagy adaptors. As a consequence, the increase we see pATG16L1^{s278} and LC3B-II levels around 3-4 hours (Fig. 3B-C) is not observable by p62 clearance. Moreover, stress-induced degradation of p62 has been described to correlate with an upregulation of its transcription[37], potentially confounding autophagy analysis unlike phosphorylation/dephosphorylation, which is rapid and reversible making it the ideal indicator for autophagic activity. These data indicate the potential for a unique advantage of analyzing autophagy through phosphorylation of ATG16L1, which is not sensitive to the duration of starvation.

We next analyzed autophagosome formation at the time points with peak pATG16L1^{S278} levels using fluorescent LC3B-reporter lines (Fig. S3D), endogenous pATG16L1^{s278} staining (Fig. S3E), and an autophagosome-specific live cell stain CytoID^{tm} (Fig. S3F), which showed that autophagosome formation correlated with pATG16L1^{S278} levels. Next, we analyzed pATG16L1^{s278} levels from duplicated samples using western blot and electron microscopy (EM) under starvation. We observed an increase in autophagic vesicles in EM images (Fig. 3D), which correlated with an increase in pATG16L1^{s278} levels by western blot (Fig. 3E). Together, our findings establish pATG16L1^{s278} as a robust indicator of autophagic rate, independent of late stage autophagy block, with the potential to provide a more accurate readout and/or simpler readout of autophagy induction than widely-used markers such as p62 and LC3B.

We also examined the possibility of using other mTORC1 and ULK targets as potential readouts of autophagy induction. mTORC1-mediated S6K phosphorylation was rapidly lost after starvation, rendering it much less informative than pATG16L1^{s278} (Fig. S4A). mTORC1 assays were also more vulnerable to disruption by other factors than pATG16L1^{s278} (Fig. S4B). ULK phosphorylation of ATG13 was induced under starvation; however, it was far less consistent in measuring autophagy when compared to pATG16L1^{s278} (Fig. S4C).

We next asked if pATG16L1^{s278} levels could be monitored *in vivo* from histological sections. Mice were either fed *ad libitum* or starved for 16 hours, which was previously shown to activate autophagy in skeletal muscle[38]. Cryopreserved muscle sections showed punctate pATG16L1^{s278} staining when compared to secondary antibody alone, indicating immunoreactivity (Fig. 4A). More importantly, we observed that the number of puncta per cell increased significantly in starved muscles indicating that pATG16L1^{s278}-induction is detectable by IHC (Fig. 4A, S5A). LC3B-staining in cryopreserved samples was increased across starvation samples but did not achieve statistical significance (Fig. 4A, S5A). Consistent with the cryopreserved samples, paraffin-formalin samples displayed pATG16L1^{s278} as a punctate pattern that was absent in controls (Fig. 4B). Additionally, punctate pATG16L1 staining was increased in starved sections compared to controls (Fig. 4B, S5B). LC3B staining was also increased in starved samples (Fig. 4B, S5B). Notably, using this protocol LC3B staining gave more reliable staining than cryopreserved samples consistent with a previously report describing optimal LC3B immunohistological staining[39]. While we are using an LC3B antibody that has previously been validated for IHC, other antibodies may give improved results or require alternate tissue preparation protocols. We next sought to determine if pATG16L1^{s278} was suitable for IHC of liver or brain. Successful IHC of the brain and liver required transcardial perfusion with PBS and PFA to reduce background staining and

allow interpretation of pATG16L1^{s278} staining. We found that staining of both liver and hippocampal sections yielded a specific and punctate staining pattern for ATG16L1^{s278} (Fig. 4C-D). We then stained pATG16L1^{S278} in fixed slices of the hippocampus from adult *Atg5*$^{flox/flox}$ mice. As previously described Atg5 was specifically removed from dividing NPCs in the hippocampus of the *Atg5*$^{flox/flox}$ mice[40]. Staining of these sections showed that the Atg5-null NPCs were void of pATG16L1 when compared to the surrounding tissue (Supplementary Video 1). Taken together, these results show that pATG16L1^{s278} staining is compatible for autophagy analysis using immunohistochemistry.

Figure 4

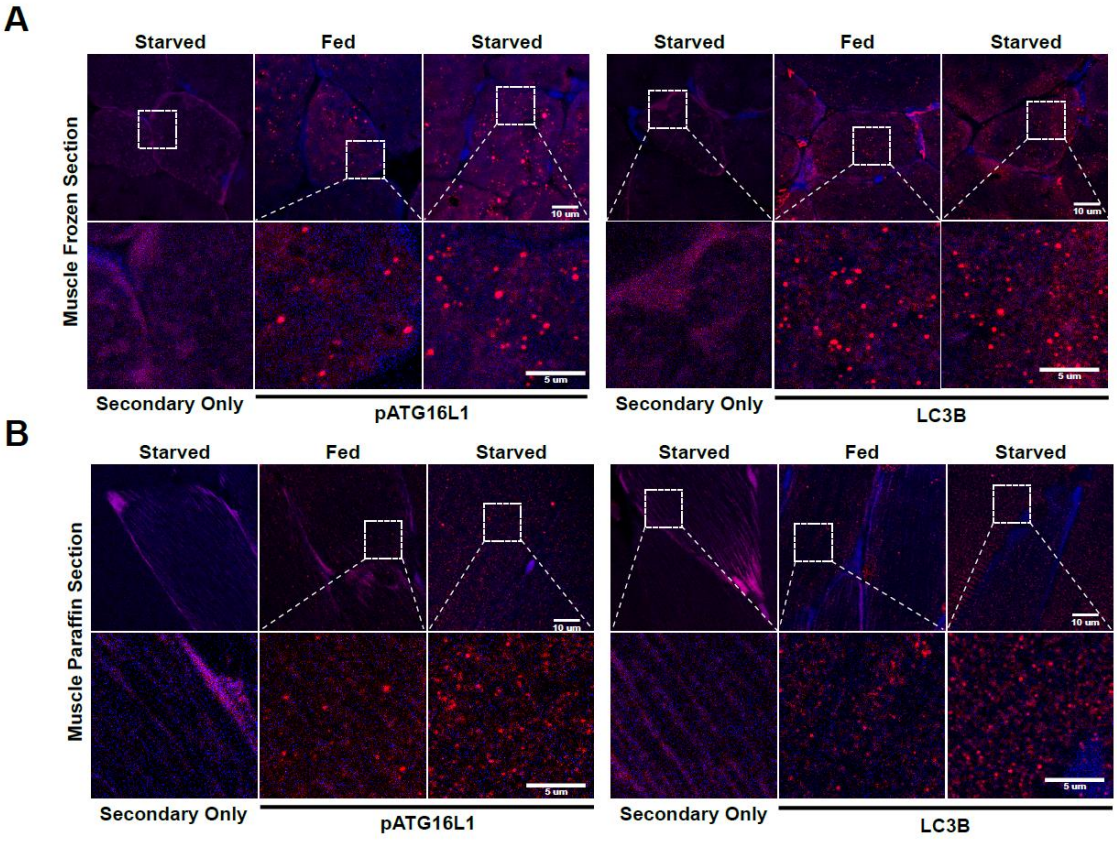
A
Starved
Fed
Starved
Starved
Fed
Starved
Muscle Frozen Section
10 um
5 um
Secondary Only
pATG16L1
Secondary Only
LC3B
B
Starved
Fed
Starved
Starved
Fed
Starved
Muscle Paraffin Section
10 um
5 um
Secondary Only
pATG16L1
Secondary Only
LC3B
C
Secondary Only
With DAPI
pATG16L1
With DAPI
Liver
10 um
5 um
D
Secondary Only
With DAPI
pATG16L1
With DAPI
Brain
10 um
5 um

Fig. 4: pATG16L1 is compatible with IHC staining of tissue samples to measure autophagic activities in vivo. a, Tissue sections from quadriceps of either fed or starved mice were cryopreserved and sectioned into 10-µm-thick slices. Staining was done using the indicated primary antibodies, followed by incubation with fluorophore-conjugated secondary antibody. Samples stained with secondary antibody alone are shown to provide a baseline of background fluorescence. Representative confocal microscopy images from a total of three biological replicates (n = 3) are shown (scale bars, 10 µm). b, Tissue sections from quadriceps of either fed or starved mice were fixed with 10% formalin, paraffin embedded and sectioned into 4-µm-thick slices. Staining was performed using the indicated primary antibodies, followed by incubation with fluorophore-conjugated secondary antibody. Samples stained with secondary antibody alone are shown to provide a baseline of background fluorescence. Representative confocal microscopy images from a total of five biological replicates (n = 5) are shown (scale bars, 10 µm). c, Mouse liver tissue sections were stained with pATG16L1 antibody. Secondary-only images are shown to distinguish specific pATG16L1 staining. Representative images are shown from a total of five biological replicates (n = 5) (scale bars, top row, 10 µm; bottom row, 5 µm). d, Mouse brain hippocampus tissue sections were stained with pATG16L1 antibody. Secondary-only images are shown to distinguish specific pATG16L1 staining. Representative images are shown from a total of four biological replicates (n = 4) (scale bars, top row, 10 µm; bottom row, 5 µm).

2.5 Discussion

Here, we identified a novel method for monitoring mammalian autophagy utilizing measurement of the direct signalling between two essential enzymes involved in autophagosome formation. The selective presence of pATG16L1^{s278} on newly-forming autophagosomes indicates this signalling event is tightly tied to the biology of autophagosome formation, and therefore to the rate of autophagy induction. In a well-defined system, pATG16L1^{s278} levels largely follow the rate of LC3B-II. However, in the absence of lysosomal inhibitors pATG16L1^{s278} consistently yielded a more reliable result, likely due to the closer relationship between pATG16L1^{s278} and autophagy induction than LC3B-II. The reliability of this assay will likely be of even greater benefit in more technically challenging experimental systems, where target cells may be rare, or drugs impractical. The monoclonal pATG16L1^{s278} antibody characterized here is capable of endogenously detecting

autophagy induction in multiple tissues and species across several common assays making it a robust method that can be easily adopted in most experimental situations.

Additionally, the analysis of pATG16L1^{s278} may open new avenues for research into the mechanisms of autophagy induction and regulation. pATG16L1^{s278} analysis may aid in demarcating the mechanisms and stages of autophagosomal membrane expansion. Moreover, we identified a single phosphorylation site in a conserved stretch of serine and threonine residues on a region of ATG16L1 that has not been well characterized. Based on high throughput mass spectrometry data that have been deposited, we have found that other sites in region are also phosphorylated. It is quite possible that other regulatory events, either activating or inhibiting, are acting in this region of ATG16L1 and controlling the rate of autophagy initiation.

Lastly, we must reiterate that the use of pATG16L1^{s278} alone has the potential to be misleading in specific conditions that we have not yet determined, but likely exist. Therefore, employment of multiple methods of autophagy analysis will remain the best approach to study of the autophagy pathway. However, the use of pATG16L1^{s278} nonetheless represents an exciting new tool for autophagy researchers to utilize in the continued interrogation of the autophagy pathway.

2.6 Materials and Methods

Cell Culture

HeLa, RPE1, COS-7, Q7, L6, HCT116, MEF and MDCK cells were obtained from American Type Culture Collection (ATCC; Rockville, MD). Cells were cultured at 37°C in a humidified 5% CO2 atmosphere. HCT116 ATG16L1 knockouts were generated using CRISPR/Cas9 targeting exon 1. Guide RNA sequence: 5’ AAACCCGCTGGAAGCGCCACATCTC 3’. HCT116 ATG16L1 KO reconstituted cells were generated using the same guides. WT2 cells were

generated by stable reconstitution of VHL in the 786-0 background as previously described41. ATG5 and ATG7 knockout MEFs were generated using CRISPR/Cas9 and has been previously described42. FIP200 knockout MEFs were a generous gift from Jun-Lin Guan (University of Cincinnati). All cell lines were maintained in Dulbecco's modified Eagle's medium (DMEM) supplemented with 10% Bovine Calf Serum (BCS - VWR Life Science Seradigm), with the exception of L6 cells which were grown in alpha modified Eagle's medium (AMEM) supplemented with 10% heat-inactivated fetal bovine serum (FBS). eGFP-mCherry-LC3B stable MEF cells was generated from infection of wild-type MEFs with a lentivirus containing the transgene. A stable polyclonal population was obtained through puromycin (1 □g/ml) selection for stable integration of the transgene.

Mammalian expression plasmids

GFP-WIPI2 DNA plasmid was a gift from Dr. Proikas-Cezanne and has been described previously43. Transfection was performed with polyethylenimine (PEI, 4:1 v/w ratio to DNA) and cells were used for experiment 48 hours post transfection.

Phospho-antibody development

Phospho-peptide flanking S278 of ATG16L1 was used to immunize 4 rabbits. Sera were screened against in vitro phosphorylated ATG16L1. Hybridomas were made from the most reactive rabbit. Hybridoma supernatants were screened for reactivity against phospho-peptide, recombinant phospho-protein, and endogenous phospho protein. Clones that were successful in all phases of screening were then tested for reactivity in IF. A single clone (211) from the second hybridoma fusion was reactive in all assays. This antibody has now been cloned and is commercially available (ab195242).

Antibodies

Anti-phospho-S6 (4858), S6 (2317), phospho-S6 kinase (108D2), were purchased from Cell Signalling Technology. Anti-ATG16L1 (ab187617), anti-ATG13 (ab201467), anti-S6 kinase (ab32529) were purchased from Abcam. Anti-LC3B (NB100-2220) was from Novus Biological. Anti-p62 (GP62-C) was obtained from Progen Biotechnik. Anti-β-actin (A5441), vinculin (V9131) were from Sigma-Aldrich. Anti-phospho-ATG13 was a custom antibody obtained from Millennium Pharmaceuticals. For immunofluorescence microscopy, anti-LAMP1 (ab25630) was purchased from Abcam, anti-LC3B (PM036), anti-p62 (M162-3) and anti-ATG16L1 (PM040) were purchased from MBL. For immunohistochemistry, anti-LC3B (PM036) from MBL was used to stain LC3B.

Autophagy induction & inhibition

Cells were plated at desired confluence the night before treatment. At 1 hour prior to starvation treatment, cells were replenished with fresh media. Starvation was performed using HBSS media (Multicell #311-513-CL), DMEM without amino acid, DMEM without glucose, or DMEM without serum. Torin-1 (200nM, Tocris Bioscience) was added to cells for 2 hours to achieve mTORC inhibition. H2O2 (75μM, Fisher H325-500) was added to cells for 1 hour to induce ATG16L1 phosphorylation. Carbonyl cyanide m-chlorophenylhydrazone (CCCP. 100μM, Abcam ab141229) was added to cells for 5 hours to induce ATG16L1 phosphorylation. For samples treated with bafilomycin A1 (200nM, Cayman Chemicals), bafilomycin A1 was applied 15 minutes before treatment with stressors. VPS34 inhibitor (100nm, Calbiochem 5326280001) was added to cells for 2hours (IF) to 3 hours(WB) to achieve inhibition of autophagy.

Western blot

Cells were lysed directly with 1x Laemmil sample buffer. Samples were boiled at 95˚C for 10 minutes and then resolved by SDS-PAGE on 6%-18% gradient polyacrylamide gels. After transferring onto a PVDF membrane, the portions containing pATG16L1 were blocked with blocking solution (Ab126587) diluted in 1x PBS for 30 minutes. All other membranes were blocked with 5% skim milk dissolved in TBST for 30 minutes. Earlier pATG16L1 blots in this manuscript used 5% skim milk as the blocking agent, but had significantly higher background. Use of Ab126587 is strongly recommended. pATG16L1 was detected with overnight incubation in primary antibody diluted at 1:2000 with 2.5% BSA at 4°C, followed by 5x TBST washes and incubation in 1:15000 diluted anti-rabbit HRP conjugated secondary antibody at room temperature for 45 minutes.

Immunofluorescence (IF) microscopy

IF was performed on IBIDI-treated coverslips, cut to 1cm2 (ibidi, cat. 10814) which were deposited into 6 or 12 well plates. Cells were seeded onto coverslips 16 hours before treatment. After treatment, cells were rinsed with PBS then fixed in 4% paraformaldehyde in PBS for 15 minutes. Cells were then permeabilized with 50 µg/mL of digitonin in PBS for 10 minutes. Blocking was performed in 1% BSA and 2% serum in PBS for 30 minutes. Cells were then incubated with primary antibodies in the blocking buffer for 1 hour at room temperature. Slides were then washed 3x with PBS, then incubated with secondary antibodies in blocking buffer for 30 minutes. Slides were then washed 3x with PBS and mounted onto glass microscope slides with ProLong gold anti-fade (Invitrogen). Epifluorescent images were captured with inverted Zeiss AxioObserver.Z1. High-resolution images were captured using Zeiss LSM 880 AxioObserverZ1 Confocal Microscope with AiryScan. Images were deconvoluted with AutoQuant x3.1 and 3D structures were constructed using Imaris.

Quantification of Immunofluorescence microscopy

Colocalization and average numbers of puncta per cell were determined by blinded manual counting of puncta from representative epifluorescent images. Quantification was performed on 3 independent experiments with at least 30 cells counted per treatment condition. Statistical analysis was performed with student's T-test.

Cyto-ID Autophagy Detection Kit assay

Cells were plated on ibidi 8 well □-Slide (Ibidi, cat. 80826) overnight and subjected to the indicated treatments. Cells were then incubated in DMEM without phenol red containing Cyto-ID autophagy detection stain (Enzo, ENZ-KIT175-0050) for 30 minutes, then washed with PBS, reincubated with either complete DMEM without phenol red or HBSS. Images were acquired and deconvolved using an environmental chamber control microscope (DeltaVision Elite-Olympus IX-71 with FemtoJet Microinjector).

Immunohistochemistry (IHC)

Mice and tissue extraction

Muscle samples were harvested from CD1 wildtype mice that were either fed ad libitum or starved for 16 hours. Both groups of mice were provided with drinking water. Mice were sacrificed in the following morning after 16 hours; quadriceps muscle were harvested and immediately processed as described in the following sections.

Brain and liver samples were from mice fed ad libitum. These organs were harvested from mice perfused with PFA. Mice were anesthetized and transcardially perfused with cold phosphate buffered saline (PBS, pH7.4) followed by 4% paraformaldehyde in PBS. Brains were removed

and post fixed for 1 hour in 4% paraformaldehyde and then transferred in cryoprotectant solution of 30% sucrose with 0.1% sodium azide in PBS. For brain section preparation brains were sectioned coronally into 30µm slices on a freezing microtome and stored in PBS with 0.1% sodium azide.

Tissue processing

Tissue samples were either: 1) Directly embedded in optimal cutting temperature compound (OCT) and snap frozen in liquid nitrogen-cooled isopentane bath. The frozen samples were sectioned into 10µm thick slices and mounted onto glass slides. Samples were then rinsed once with PBS and fixed in 4% PFA for 25 minutes. 2) Fixed in 10% formalin for 2 days. Then rinsed 3 times with 30% sucrose 3 times. The samples were then dehydrated and paraffin embedded, sectioned into 4µm thick slices, and mounted onto glass microscope slides. Prior to staining, samples were rehydrated and deparffinized. Antigen-retrieval for both groups was performed in pH 9.0 EDTA solution, at 110°C for 12 minutes in a microwave processor (Histo5, Milestone).

Antibody staining

Samples were rinsed 3 times with PBS; treated with 3% H2O2 (in PBS) for 10 minutes; washed 3 times with TbT; blocked with 5% BSA for 2 hours; stained with primary antibody overnight at 4˚C (LC3 1:1000, p62 1:1000, pATG16L1 1:300); washed 3 times with TbT, incubated with secondary antibody (Alexa Fluor 555 anti-rabbit cat. A31572, 1:1000) for 1 hour; washed once with TbT; stained with DAPI (2mg/mL, Roche Diagnostics) for 10 minutes; washed 3 times with TbT; cover slip mounted with Fluoromount-G mounting solution (Invitrogen, 00-4958-02). All treatments were done at room temperature unless otherwise stated.

Image acquisition for IHC

IHC Images were acquired using Zeiss LSM 800 AxioObserverZ1 Confocal Microscope. Video was made by the 3D reconstruction function.

Quantification of Immunohistochemistry

Average numbers of puncta per cell were determined by blinded manual counting of puncta from representative images. Quantification was performed across at least 3 unique field of views and at least 15 cells counted per treatment condition.

Electron Microscopy

Q7 cells were treated with the indicated treatments then fixed with EM grade 4% paraformaldehyde and 3.5% glutaldehyde overnight. The cells were then washed with PBS 3 times and embedded in 4% agarose. The agarose embedded cells were sectioned into 50□m thick sections on a vibratome, then silver-enhanced for EM imaging. Quantifications of autophagosomes numbers were done by blinded manual counting from at least 14 unique field of views and at least 7 cells were counted per sample.

Statistics

All error bars in the bar graphs represented standard deviation. The error bars of the whisker plot in Fig. 3B and 3C represented max and min data points. Statistical significance were determined by two tailed, two-sided Student's t-test, with p values < 0.05 defined as significant (denoted by asterisks in graphs) and $p > 0.05$ defined as not significant (n.s.).

Data Availability Statement

The data that support the findings of this study are available from the corresponding author upon reasonable request.

Ethics compliance

All experiments including animals were approved by the University of Ottawa Animal Care Committee and are in accordance with the Guidelines of the Canadian Council on Animal Care.

Acknowledgement

We would like to thank the uOttawa PALM-Histology Core Facility for processing the IHC tissue samples, the Cell Biology and Image Acquisition Core (CBIA) for assistance in 3D reconstruction and rendering of brain imaging, technical assistance in electron microcopy by Nathalie Vernoux, John A. Lunde for technical assistance in harvesting mice skeletal muscle samples, and members of the Russell laboratory for advice and critical reading of this manuscript. This work was supported by a Canadian Institutes of Health Research (CIHR) Project Grant awarded to RCR (#PJT153034), Canada Foundation for Innovation to CBIA core, and Canada Research Chair Tier 2 to MT.

2.7 Supplementary Information

Supplemental figure 1

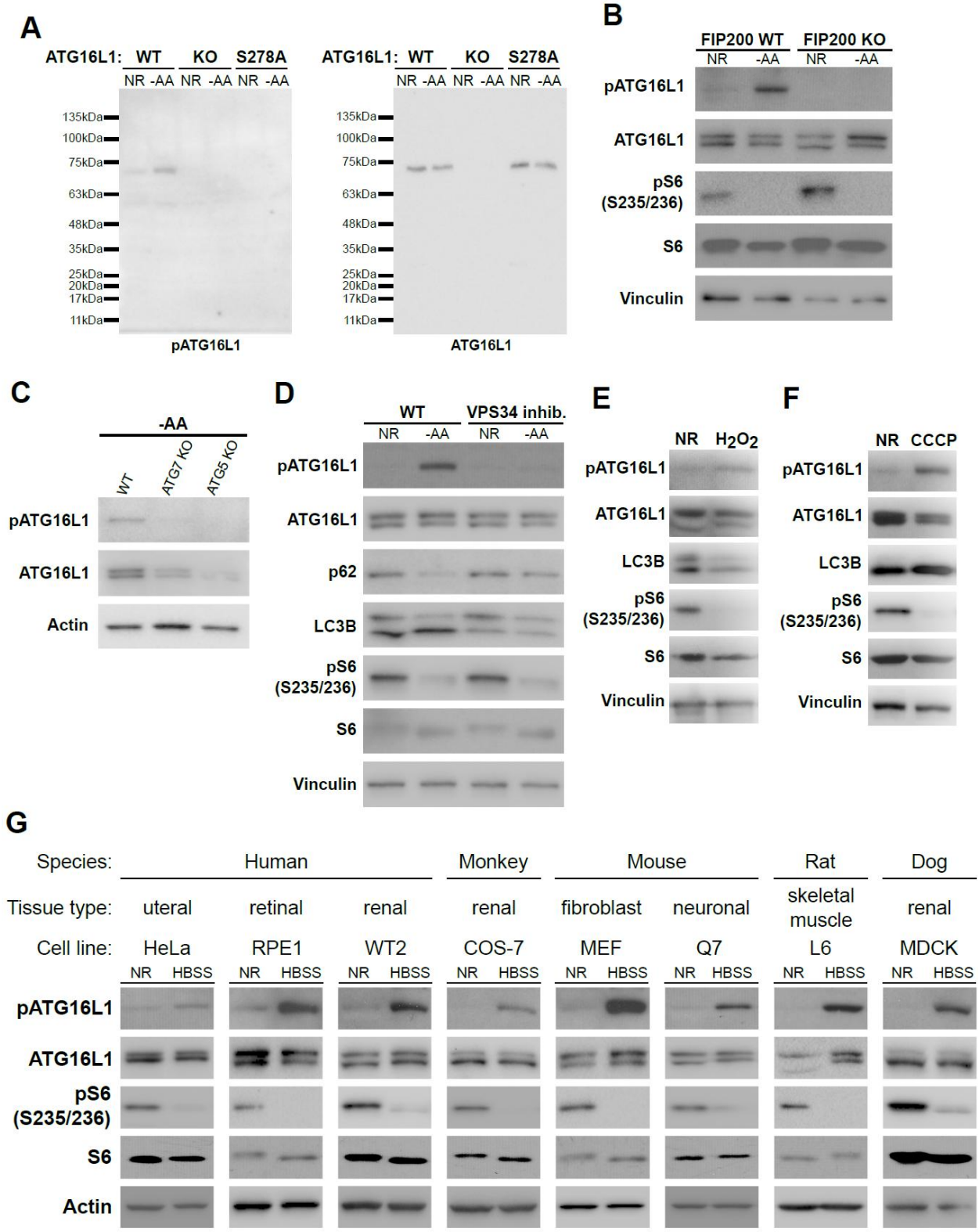

Supplementary Figure 1. **pATG16L1 is ULK-dependent, sensitive to upstream disturbance autophagy and can be detected across a range of species by western blot.** (A) Representative full length immunoblots of HCT116 cells of the indicated genotype incubated in the indicated treatments for 3 hours. Experiment was repeated 3 times (n=3) independently with similar results. (B) Immunoblot of FIP200 knockout or wild-type mouse embryonic fibroblasts (MEFs) incubated in the indicated treatments for 3 hours. Experiment was repeated 3 times (n=3) independently with similar results. (C) Immunoblot of L6 cells incubated in the indicated treatments for 1 hour. Experiment was repeated 3 times (n=3) independently with similar results. (D) Immunoblot of L6 cells WT2 cells incubated in complete media in the presence or absence of carbonyl cyanide mchlorophenylhydrazone (CCCP) for 5 hours. Experiment was repeated 3 (n=3) times independently with similar results. (E) Immunoblot of wild-type, ATG5 knockout, and ATG7 knockout MEFs incubated in the indicated treatments for 3 hours. Experiment was repeated 3 times (n=3) independently with similar results. (F) Immunoblot of wild-type MEFs incubated in the indicated media, in the presence or absence of VPS34 inhibitor (Calbiochem, 100nm) for 3 hours. Cell lysates were resolved by SDS-PAGE and immunoblotted using the indicated antibodies. Experiment was repeated 3 times (n=3) independently with similar results. (G) Immunoblot of 8 cell lines of different species and/or tissue origins, as labeled, were incubated in indicated treatment for 2 to 4 hours. Experiment was repeated 3 times (n=3) independently with similar results.

Supplemental figure 2

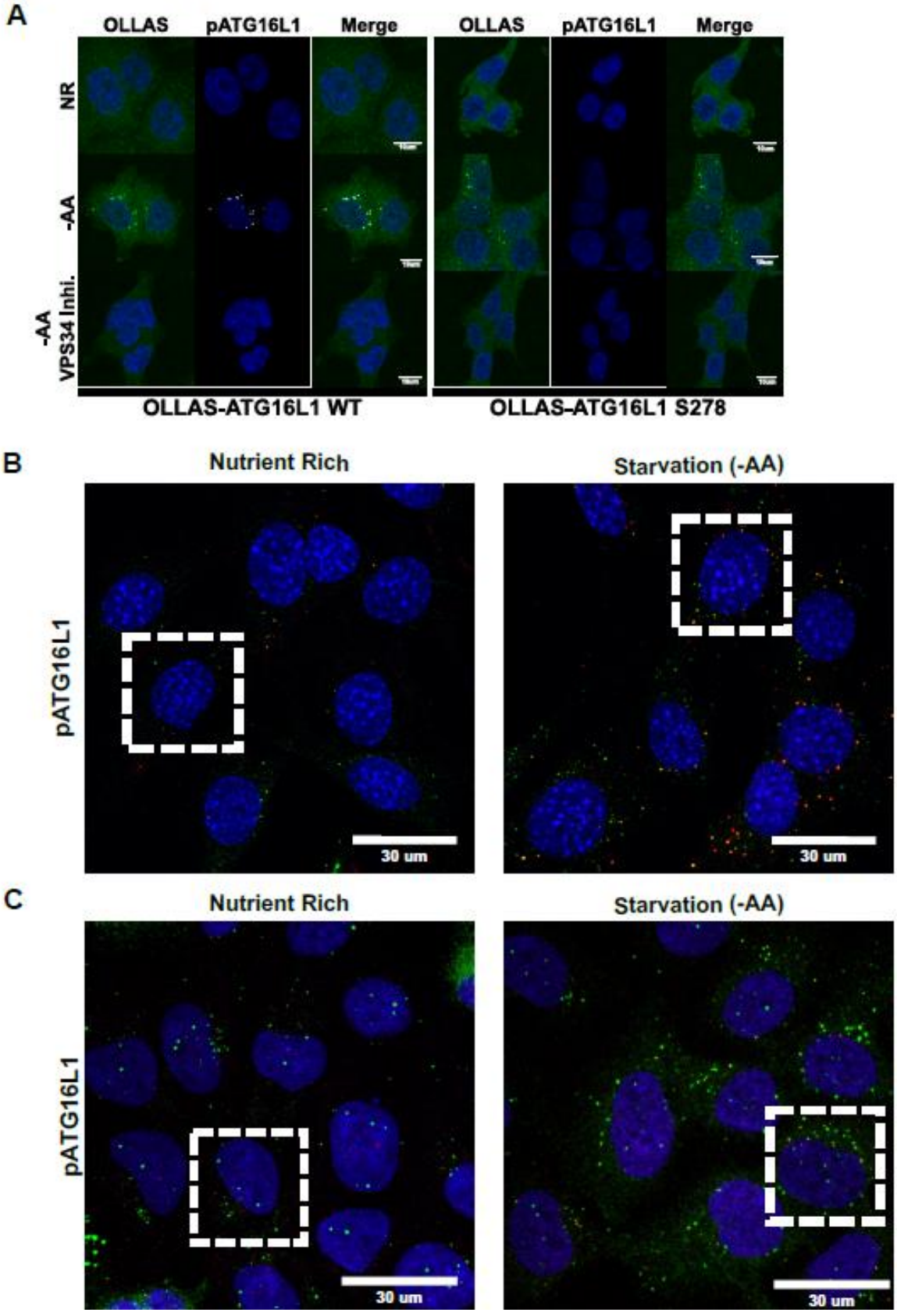

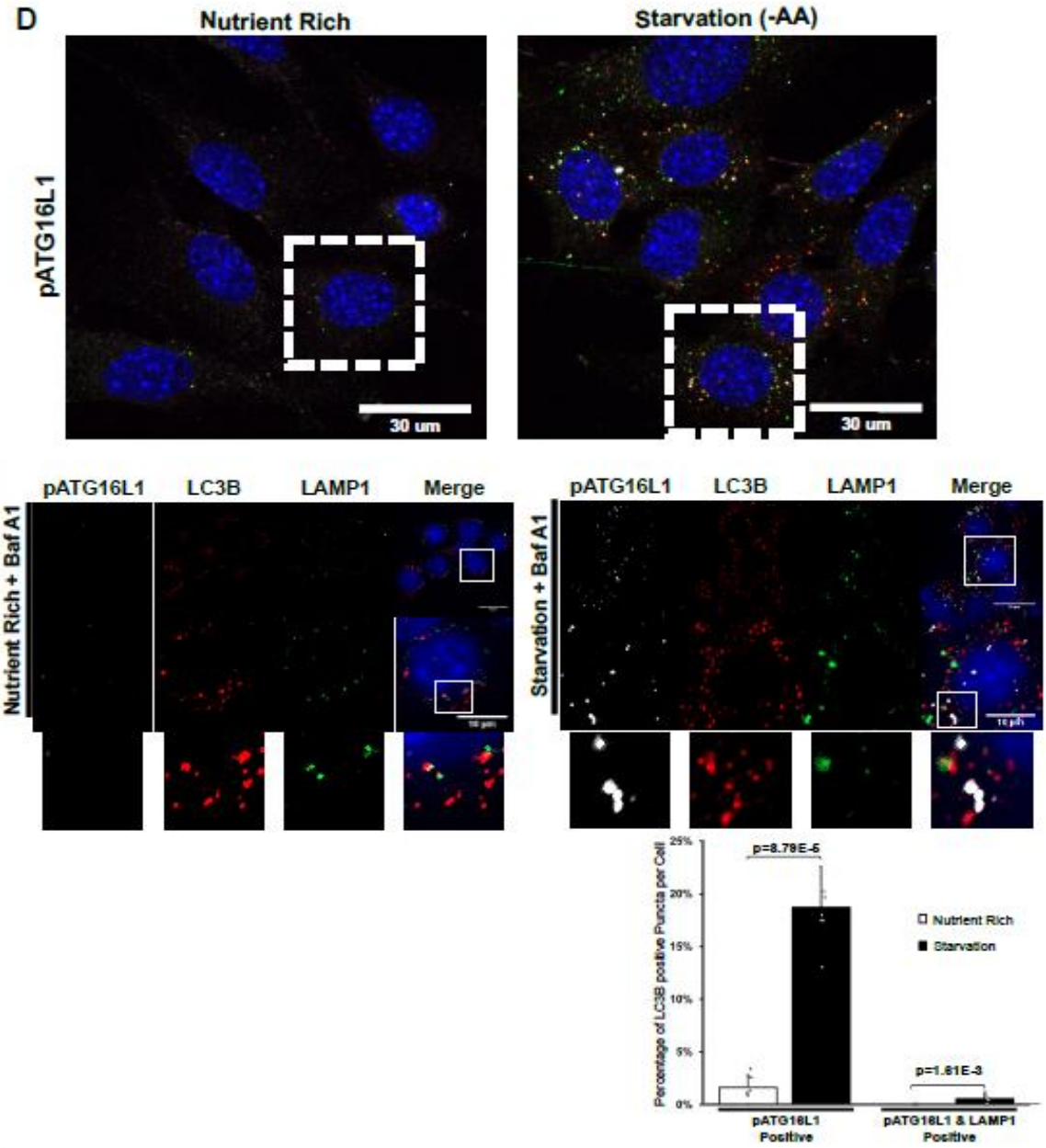
D
Nutrient Rich
Starvation (-AA)
pATG16L1
30 um
30 um
E
pATG16L1
LC3B
LAMP1
Merge
Nutrient Rich + Baf A1
Starvation + Baf A1
Percentage of LC3B positive Puncta per Cell
p=8.78E-6
p=1.61E-3
Nutrient Rich
Starvation
pATG16L1 Positive
pATG16L1 & LAMP1 Positive
F
mCherry-eGFP-LC3
eGFP
mCherry
pATG16L1
Merge
Starvation
pATG16L1-positive puncta per cell
p=8.61E-8
Autolysosome
Autophagosome

Supplementary Figure 2. **pATG16L1 is not present on autolysosomes and not essential for autophagy.** (A) HCT116 ATG16L1 knock-out cells reconstituted with either OLLAS tagged wild-type or S278A ATG16L1 were treated with the indicated treatments for 2 hours. OLLAS (green), pATG16L1 (white) and DNA (blue) were stained. Representative images are shown (scale bars: 10μm). Experiment was repeated 3 times (n=3) independently with similar results. (B) Enlarged multicell view of Fig. 2B showing all channels merged. Experiment was independently repeated 3 times (n=3) with similar results (C) Enlarged multicell view of Fig. 2C showing all channels merged. Experiment was independently repeated 3 times (n=3) with similar results. (D) Enlarged multicell view of Fig. 2D showing all channels merged. Experiment was independently repeated 3 times (n=3) with similar results. (E) Wild-type MEFs were incubated in DMEM or amino acid deficient media for 2 hours in the presence of Bafilomycin A1 (200nm). The specified proteins were stained and representative immunofluorescent images are shown. Quantification of one representative experiment is shown, independently repeated 3 (n=3) times with similar results. Measure of center represent mean value and error bars represent standard deviation. Statistical analysis was performed using two-sided Student's T-test, asterisk denote $p<0.05$. (F) mCherry-eGFP-LC3 knockin MEFs were incubated in complete DMEM or amino acid deficient media for 240 minutes. pATG16L1 (white) was stained and representative immunofluorescent images are shown. White arrows in enlarged view #1 indicate autolysosomes (mCherry singlepositive puncta) absent of pATG16L1 signal. White arrows in enlarged view #2 indicate autophagosomes (mCherry-eGFP double-positive puncta) colocalized with pATG16L1. Quantification of one representative experiment is shown, independently repeated 4 (n=3) times with similar results. Measure of center represent mean value and error bars represent standard deviation. Statistical analysis was performed using two-sided Student's T-test, asterisk denote $p<0.05$. (G) Wild-type and ATG16L1 S278A mutant HCT116 cells were incubated in DMEM or amino acid deficient media for 2 hours. LC3B was stained and representative immunofluorescent images are shown. Quantification of one representative experiment is shown, independently repeated 3 times with similar results. Measure of center represent mean value and error bars represent standard deviation. Statistical analysis was performed using two-sided Student's Ttest, asterisk denote $p<0.05$. (H) GFP-WIPI2 was transiently expressed in HCT116 cells stably expressing either wild-type or S278A mutant ATG16L1. Cells were starved in amino acid deficient media for 2 hours. ATG16L1 (red) was stained and analyzed with GFP signal (green). Representative immunofluorescent images are shown. Quantification of one representative experiment is shown, independently repeated 3 times (n=3) with similar results. Measure of center represent mean value and error bars represent standard deviation. Statistical analysis was performed using two-sided Student's T-test, asterisk denote $p<0.05$.

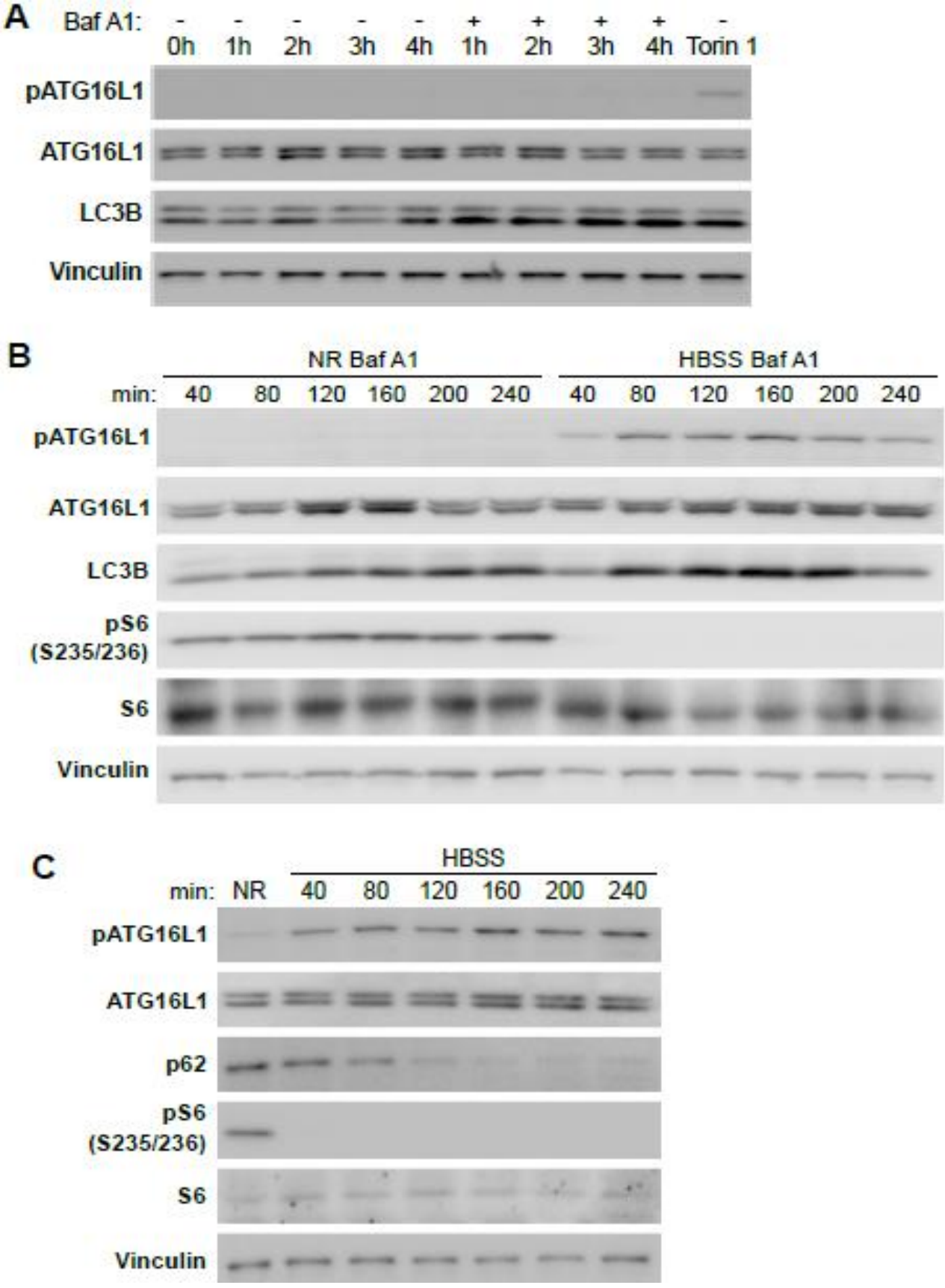
A
Baf A1: - - - - - + + + + -
0h 1h 2h 3h 4h 1h 2h 3h 4h Torin 1
pATG16L1
ATG16L1
LC3B
Vinculin
B
NR Baf A1
HBSS Baf A1
min: 40 80 120 160 200 240 40 80 120 160 200 240
pATG16L1
ATG16L1
LC3B
pS6 (S235/236)
S6
Vinculin
C
HBSS
min: NR 40 80 120 160 200 240
pATG16L1
ATG16L1
p62
pS6 (S235/236)
S6
Vinculin

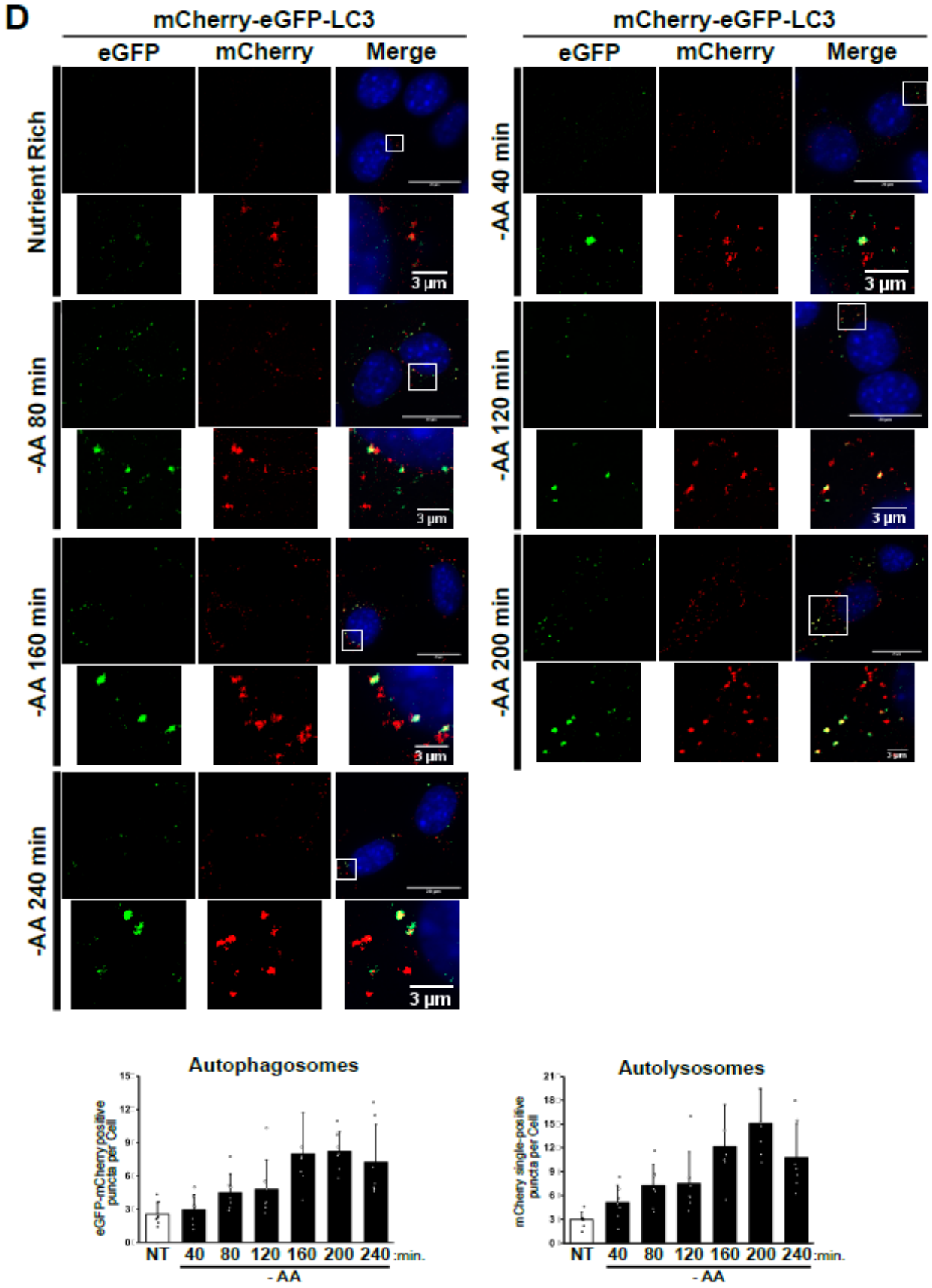
D
mCherry-eGFP-LC3
eGFP
mCherry
Merge
Nutrient Rich
-AA 40 min
-AA 80 min
-AA 120 min
-AA 160 min
-AA 200 min
-AA 240 min
3 µm
Autophagosomes
eGFP-mCherry positive puncta per Cell
NT 40 80 120 160 200 240 :min.
- AA
Autolysosomes
mCherry single-positive puncta per Cell
NT 40 80 120 160 200 240 :min.
- AA

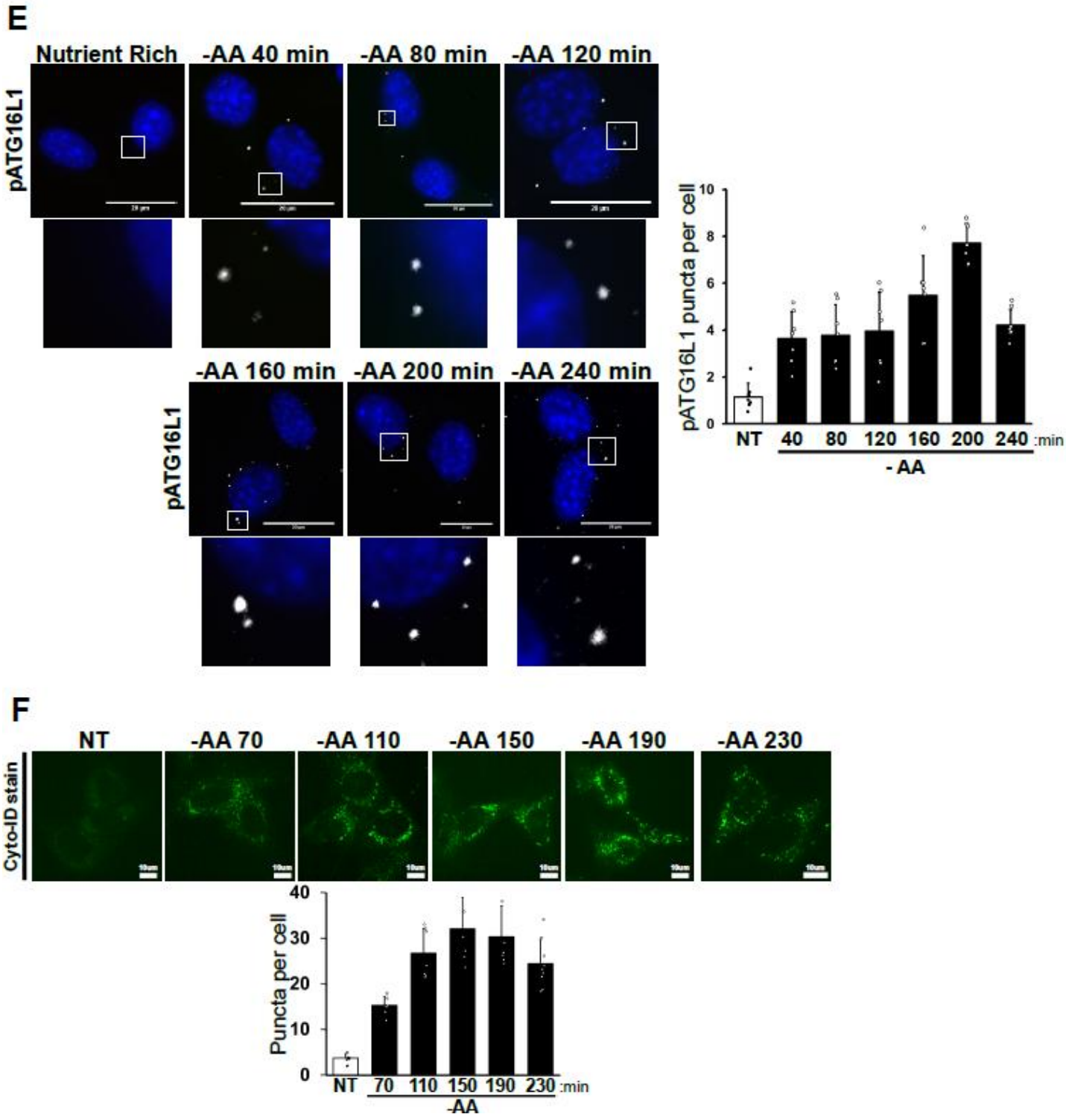
E
Nutrient Rich
-AA 40 min
-AA 80 min
-AA 120 min
pATG16L1
-AA 160 min
-AA 200 min
-AA 240 min
pATG16L1
pATG16L1 puncta per cell
NT
40
80
120
160
200
240
:min
- AA
F
NT
-AA 70
-AA 110
-AA 150
-AA 190
-AA 230
Cyto-ID stain
Puncta per cell
NT
70
110
150
190
230
:min
-AA

Supplementary Figure 3. **pATG16L1 level provides a reliable measurement of autophagy rates independent of late stage autophagy block and directly reflects autophagic vesicle formation.**

(A) Immunoblot of Q7 cells incubated in complete media in the presence or absence of Baf A1. Cell lysates were collected at the time points indicated. Cells were treated with Torin-1 for 2 hours as a positive control for induction of ATG16L1 phosphorylation. Experiment was repeated 3 times independently with similar results. (B) Q7 cells were incubated in either complete media or HBSS in the presence of Baf A1. Cell lysates were collected at the time points indicated and immunoblotted. Representative immunoblot is shown, experiment was independently repeated 3 times. (C) Q7 cells were incubated in either complete media or HBSS without Baf A1. Cell lysates were collected at the time points indicated and immunoblotted. Representative immunoblot is shown, experiment was independently repeated 4 times. (D) mCherry-eGFP-LC3 knockin MEFs were incubated in DMEM or amino acid deficient media for the specified time. mCherry (red) and GFP (green) signals were analyzed and representative immunofluorescent images are shown. The number of autophagosomes (GFP, mCherry dual-positives) and autolysosomes (mCherry signal only) per timepoint were quantified separately from one representative experiment, repeated 3 times with similar results. Measure of center represent mean value and error bars represent standard deviation. Statistical analysis was performed using two-sided Student's T-test, asterisk denote $p<0.05$. (E) mCherry-eGFP-LC3 knockin MEFs were incubated in DMEM or amino acid deficient media for the specified time. Endogenous pATG16L1 (white) was stained and representative immunofluorescent Representative images are shown. The number pATG16L1 puncta per timepoint was quantified from one representative experiment, repeated 3 times with similar results. Measure of center represent mean value and error bars represent standard deviation. Statistical analysis was performed using two-sided Student's T-test, asterisk denote $p<0.05$. (F) Wild-type MEFs were incubated in either complete DMEM or HBSS and stained at specified timepoints with Cyto-ID Autophagy Detection Kit 2.0 (Enzo).. Representative live cell images are shown. The number of stained vesicles (green) for each timepoint were quantified from one representative experiment, repeated 2 times with similar results. Measure of center represent mean value and error bars represent standard deviation. Statistical analysis was performed using two-sided Student's T-test, asterisk denote $p<0.05$.

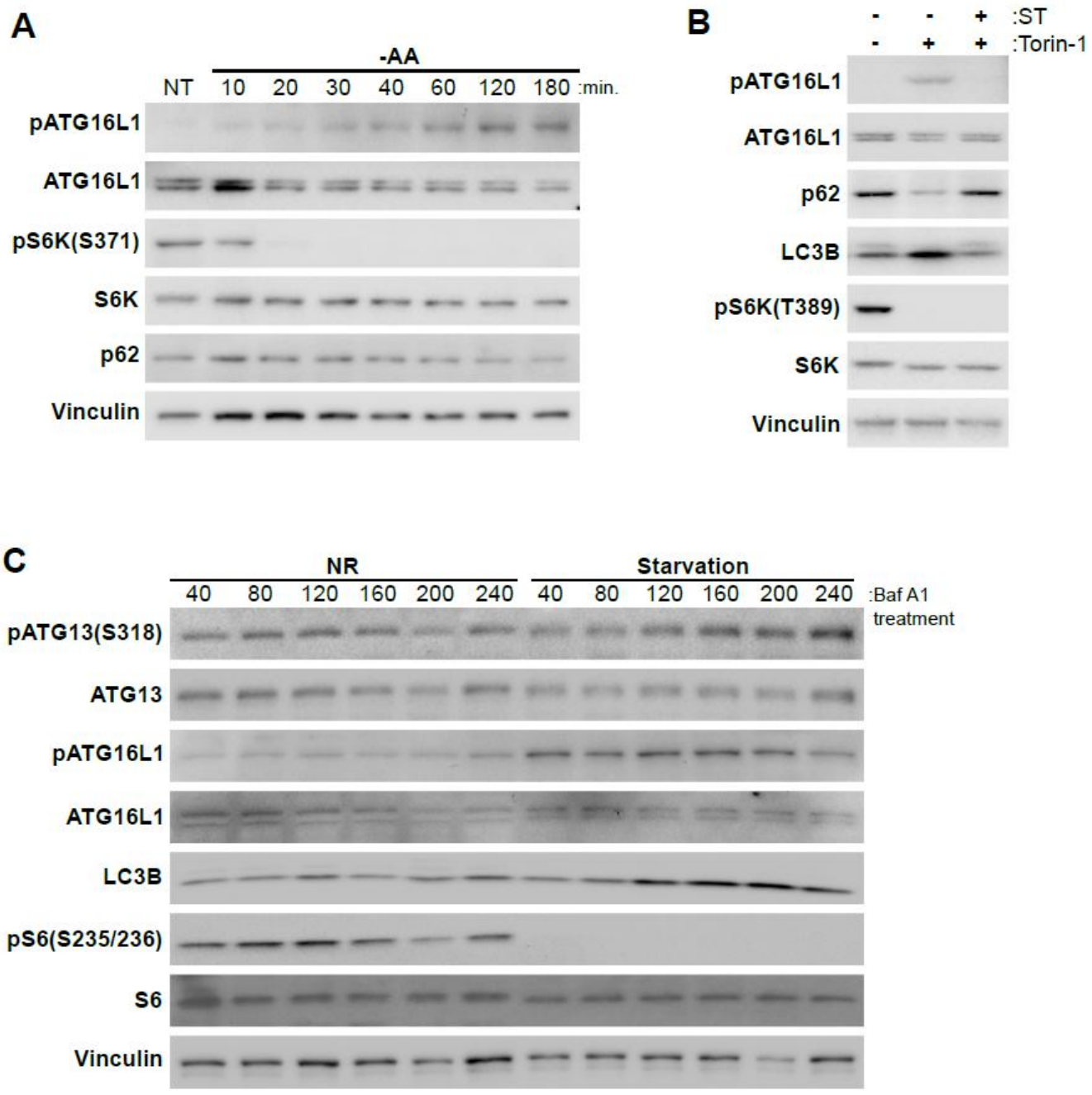

Supplementary Figure 4. **pATG16L1 is a better marker of autophagy than general readouts of mTOR or ULK activity**. (A) Immunoblot of wild-type MEFs incubated in DMEM (NT) or Hank's Balanced Salt Solution (HBSS) for the indicated period of time. Experiment was independently repeated 3 times with similar results. (B) Immunoblot of wild-type MEFs incubated in DMEM and treated with salmonella (ST) and/or Torin-1 (200nm) as indicated for 1 hour. Experiment was independently repeated 3 times with similar results. (C) Immunoblot of wild-type MEFs incubated in DMEM (NR) or Hank's Balanced Salt Solution (HBSS) with Bafilomycin A1

(Baf A1, 200nm) for the indicated period of time. Experiment was independently repeated 3 times with similar results.

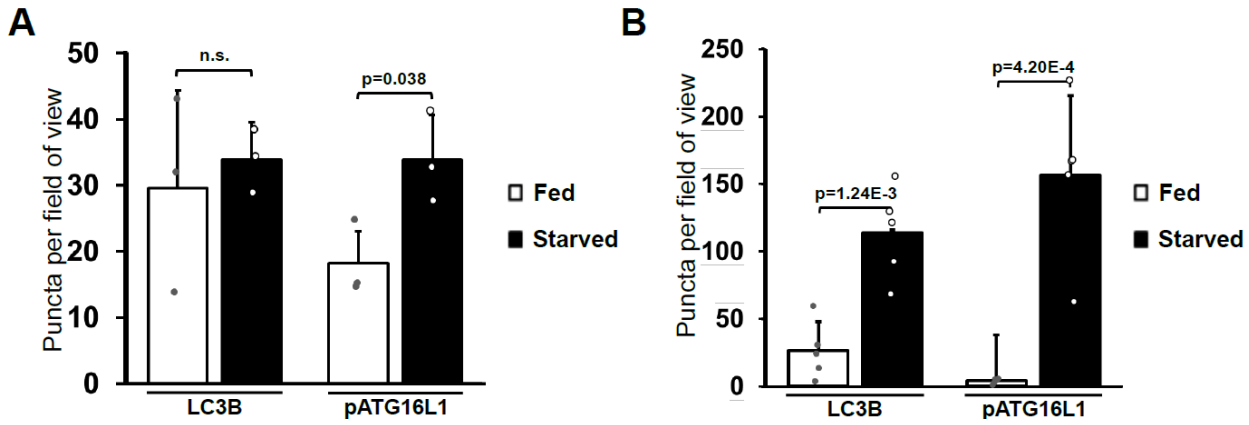

Supplementary Figure 5. **pATG16L1 is compatible with immunohistochemistry staining of tissue samples to measure autophagic activities in vivo.** (A) Quantification of LC3B and pATG16L1 puncta for Fig. 4A. n=3/group. Statistical analysis was performed using twosided Student's T-test with $p<0.05$. (B) Quantification of LC3B and pATG16L1 puncta for Fig. 4B. n=5/group. Statistical analysis was performed using two-sided Student's T-test with $p<0.05$.

Supplementary Video 1 **Brain hippocampus tissue sections of wildtype and Atg5flox/flox mice were stained with pATG16L1S278**. GFP and RFP signals were enhanced with anti-GFP/RFP antibodies. GFP expression is indicative of cells knocked out of Atg5. 3D model of the cell was constructed using the 3D reconstruction function in Imaris based on GRP and RFP signals. N=2 animals/group. Representative cell from one conditional Atg5 KO mouse sample is shown in the video.

Chapter 3: Iron overload inhibits late stage autophagy flux leading to insulin resistance.

Published in EMBO reports - DOI: 10.15252/embr.201947911

James Won Suk Jahng1*, **Reham Musaibeh Alsaadi2***, Palanivel Rengasamy1, Erfei Song1, Victoria Emily Barbosa Hipolito3, Hye Kyoung Sung1, Roberto Jorge Botelho3,

Ryan Charles Russell2#, Gary Sweeney1#

Co-First authors * These two authors contributed equally to this work

3.1 Statement of Author Contributions

JWSJ and **RMA** performed majority of experiments and contributed to manuscript writing. RP, ES, VEBH, and HKS made substantial experimental contributions. RJB designed lysosome dynamics experiments and edited the final manuscript. RCR and GS initiated and developed the project, discussed planning of experiments and interpretation of data, and wrote final manuscript.

Iron overload inhibits late stage autophagy flux leading to insulin resistance.

James Won Suk Jahng[1*], Reham Musaibeh Alsaadi[2*], Palanivel Rengasamy[1], Erfei Song[1], Victoria Emily Barbosa Hipolito[3], Hye Kyoung Sung[1], Roberto Jorge Botelho[3], Ryan Charles Russell[2#], Gary Sweeney[1#]

[1]Department of Biology, York University, Toronto, Canada

[2]Department of Cellular and Molecular Medicine, University of Ottawa, Ottawa, Canada

[3]Department of Chemistry and Biology and the Molecular Science Graduate Program, Ryerson University, Toronto, Canada

Running title: mTORC1-UVRAG autophagy defect impairs insulin sensitivity

* These two authors contributed equally to this work

[#]Co-corresponding authors: GS: Department of Biology, York University, 4700 Keele St, Toronto, M3J 1P3, Ontario, Canada. Tel: (1) 416-736-2100 (ext. 66635), E-mail: gsweeney@yorku.ca and ryan.russell@uottawa.ca

3.2 Abstract

Iron overload, a common clinical occurrence, is implicated in the metabolic syndrome although the contributing pathophysiological mechanisms are not fully defined. We show that prolonged iron overload results in an autophagy defect associated with accumulation of dysfunctional autolysosomes and loss of free lysosomes in skeletal muscle. These autophagy defects contribute to impaired insulin-stimulated glucose uptake and insulin signaling. Mechanistically, we show that iron overload leads to a decrease in Akt-mediated repression of tuberous sclerosis complex (TSC2) and Rheb-mediated mTORC1 activation on autolysosomes, thereby inhibiting autophagic-lysosome regeneration. Constitutive activation of mTORC1 or iron withdrawal replenishes lysosomal pools via increased mTORC1-UVRAG signaling, which restores insulin sensitivity. Induction of iron overload via intravenous iron-dextran delivery in mice also results in insulin resistance accompanied by abnormal autophagosome accumulation, lysosomal loss, and decreased mTORC1-UVRAG signaling in muscle. Collectively, our results show that chronic iron overload leads to a profound autophagy defect through mTORC1-UVRAG inhibition and provides new mechanistic insight into metabolic syndrome-associated insulin resistance.

3.3 Introduction

Iron is an essential element involved in multiple cellular processes such as erythropoiesis, mitochondrial respiration, and growth/differentiation [1]. The total amount of labile iron must be precisely regulated and in circulation iron typically exists bound to transferrin (TF) [4]. However, when iron exceeds TF capacity, iron homeostasis becomes imbalanced [6] and non-TF bound iron contributes to pathophysiological processes, including insulin resistance and diabetes [7]. Interventions to reduce iron have been reported to improve insulin sensitivity and delay the onset of type 2 diabetes mellitus (T2DM). These include use of chelators [11], blood-letting [14], and iron restriction diet [17]. However, the molecular mechanisms linking iron overload (IO) to T2D are poorly understood. Cellular labile iron, which contains chelatable redox-active Fe2+/Fe3+, has been implicated in iron-mediated cellular toxicity by increasing oxidative stresses. Excess accumulation of intracellular iron leads to the generation of reactive oxygen species (ROS) and tissue damage [2].

We have previously shown that autophagy plays an important role in regulating insulin sensitivity and metabolism in skeletal muscle [19.] Autophagy is a stress-sensitive cellular degradative process capable of clearing and recycling potential substrates such as damaged mitochondria and protein aggregates [20]. Indeed, autophagy is generally considered to play a protective role against T2D, recycling nutrients to maintain energy homeostasis and remove damaged organelles [21]. IO has been described to regulate the activity of both AMP-activated protein kinase (AMPK) and mTOR complex 1 (mTORC1) [23], which are both established upstream regulators of the autophagy pathway [25]. However, the potential mechanisms linking IO-mediated autophagy to insulin resistance remain to be elucidated.

Here, we established in vitro and in vivo models to examine direct effects of IO on autophagy flux in skeletal muscle and its significance in insulin resistance. We describe a mechanistic link between chronic IO and autophagy dysfunction, which alters insulin sensitivity in skeletal muscle. We identified the regulation of mTORC1 by IO as a double-edged sword that initially leads to transient autophagy activation, but ultimately causes an autophagy defect through loss of autophagic-lysosome regeneration (ALR), a newly discovered membrane recycling mechanism that to date has not been identified as a contributor to pathophysiology [27]. The data presented here provide new mechanistic knowledge to enhance our understanding of the pathogenic mechanisms of IO, which may have widespread consequences in insulin resistance, metabolic dysfunction, and beyond.

3.4 Results

Iron overload (IO) induced insulin resistance in L6 cells

Skeletal muscle is a primary consumer of glucose, yet the effects of IO on glucose uptake and insulin sensitivity are not known. Therefore, we first sought to determine whether IO induces insulin resistance in rat L6 skeletal myoblasts. An experimental model of IO was established by treating cells with ferrous labile iron for up to 24 h. The extent of IO was then determined via dose and temporal analysis using biochemical intracellular iron measurement (Fig 1A). The concentration selected for subsequent use, 250 μM, is intended to mimic IO and is consistent with iron concentrations used in the literature for other cell types 28. Conventional iron overload response 5 by skeletal muscle cells was monitored by using an iron response element (IRE)-driven reporter construct tagged with cyan fluorescence protein (CFP) transfected in L6 cells as well as the use of fluorescence-based indicators of iron levels (IP-1). We observed that iron treatment for 24 h increased the expression of CFP and fluorescence of iron probe 1 (IP-1) without adversely affecting viability (Figs 1B and EV1A). Analyzing increased intracellular iron via quenching of

the iron-sensitive fluorescent probe phen green SK (PGSK), we confirmed elevated iron in our model and that it could be effectively blocked by the iron chelator, 2,2′ di-pyridyl (DPD; Fig 1C). We further tested iron-responsive transcription by performing qPCR against ferritin (FTH and FTL, H-heavy and L-light chain), ferroportin (SLC40A1), and Tfr1 (transferrin receptor 1, TFRC). Iron treatment for 24 h significantly increased the expression of ferritins and ferroportin and decreased the expression of Tfr1 (Fig 1D). Transcriptional changes aligned with protein levels indicating that iron treatment significantly increased ferritin heavy chain and decreased TfR1 expression (Fig 1E). Together, these results indicate that our in vitro IO model in skeletal muscle line recapitulates the key hallmarks of IO 30. We next analyzed insulin sensitivity after IO by measuring glucose uptake and phosphorylation of insulin signaling molecules (IRS-1 Y612 and AKT T308) after insulin stimulation. Iron treatment for 24 h significantly reduced glucose uptake following insulin stimulation (Fig 1F). Additionally, insulin-stimulated phosphorylation of IRS-1 and AKT was significantly reduced after 24-h iron treatment (Fig 1G). Furthermore, we determined that insulin resistance was due to intracellular iron accumulation since DPD significantly reduced the intracellular iron accumulation at 24-h iron treatment and restored insulin-stimulated glucose uptake and insulin signaling phosphorylation (Fig EV1B–E). Taken together, our results indicate that IO directly caused insulin resistance in skeletal muscle.

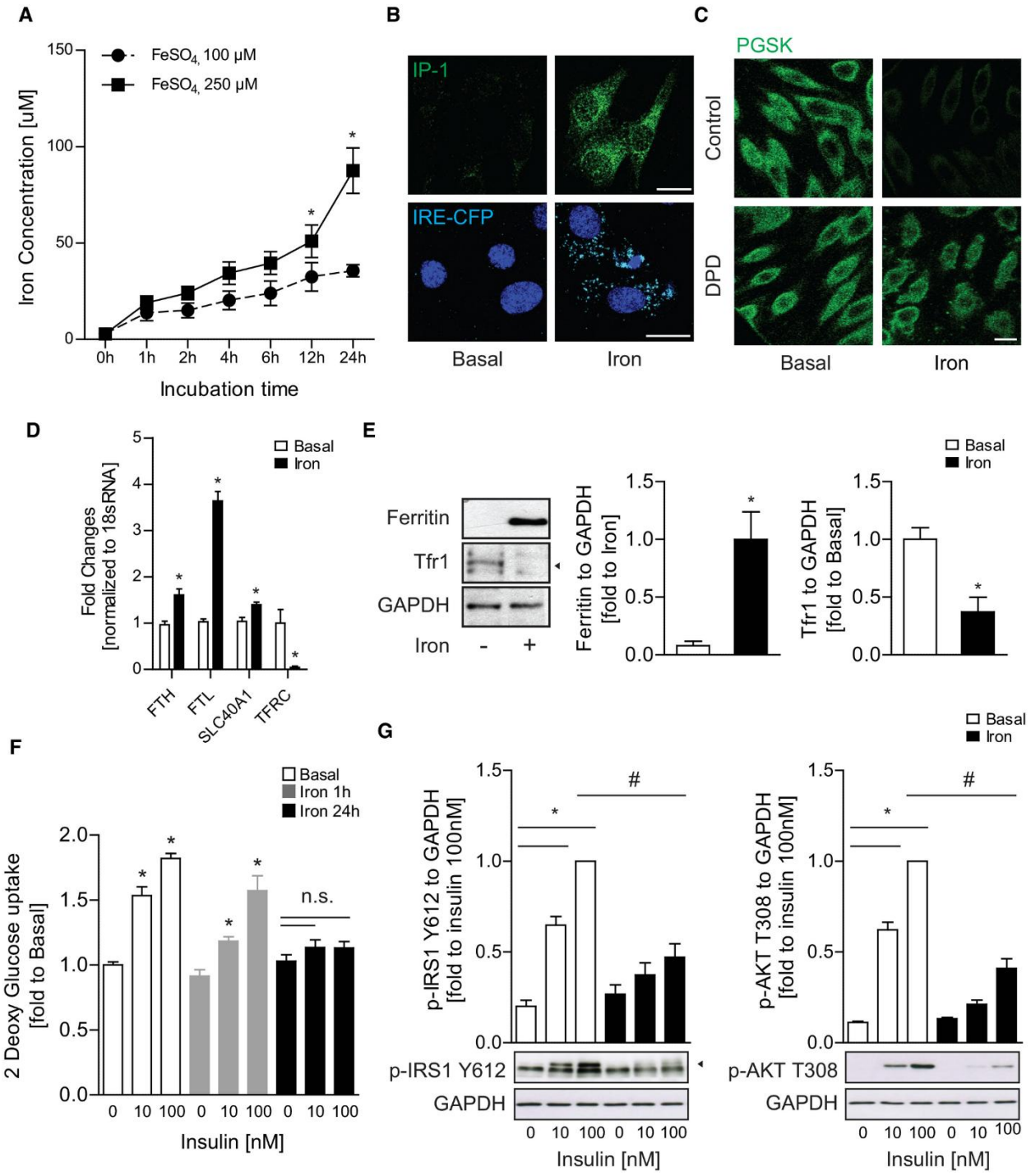

Figure 1. Validation of iron overload (IO) model and insulin resistance induction after IO in L6 muscle cells. A. Ferrozine-based intracellular iron concentration measurement in L6 cells after temporal analysis of iron treatment at 100 or 250 µM for multiple time points. *$P < 0.05$ (unpaired

Student's *t*-test versus each time points with $FeSO_4$, 100 μM). **B.** Representative confocal microscope images of L6 cells stained with IP-1 (iron probe 1) or transfected with IRE-CFP (iron regulatory element) reporter after iron treatment ($FeSO_4$, 250 μM) for 24 h. **C.** Representative confocal images of L6 cells using iron-sensitive fluorescent PGSK dye after iron treatment (250 μM, 24 h) with iron chelator DPD (500 μM). **D.** Relative gene expressions—ferritin heavy chain (FTH), ferritin light chain (FTL), ferroportin (SLC40A1, transferrin receptor 1 (tfr1, TFRC)—normalized to 18S rRNA expression after iron treatment ($FeSO_4$, 250 μM) for 24 h. $*P < 0.05$ (unpaired Student's *t*-test versus basal). **E.** Representative Western blot images and quantification of ferritin (heavy chain) and Tfr1 (indicated with arrowhead) over GAPDH after iron treatment (250 μM, 24 h). $*P < 0.05$ (unpaired Student's *t*-test versus basal). **F.** Glucose uptake of L6 cells with insulin stimulation (10 or 100 nM, 20 min) after iron treatment (250 μM, 1 or 24 h). $*P < 0.05$ (one-way ANOVA with multiple comparisons). **G.** Representative Western blot images and quantification of phospho-IRS1 (Y612) and phospho-AKT (T308) over GAPDH with insulin stimulation (10 or 100 nM, 5 min) after iron treatment (250 μM, 24 h). $*P < 0.05$ (one-way ANOVA with multiple comparisons). $^{\#}P < 0.05$ (unpaired Student's *t*-test versus iron with insulin 100 nM).

Data information: All experiments were repeated five times. Data are expressed as means ± SEM. Scale bar = 20 μm.

Prolonged iron treatment causes autophagy flux defects in skeletal muscle cells

We have previously established that autophagy is an important regulator of insulin sensitivity in skeletal muscle [19]. Thus, we analyzed the temporal effect of iron treatment on autophagosome production and fusion with lysosomes by imaging L6 cells stably expressing LC3B-eGFP-mCherry. In this assay, eGFP fluorescence was quenched by low pH after autophagosome fusion with the lysosome, whereas mCherry is not [31]. We observed a rapid increase in the number of autophagosome puncta after iron treatment, which was corroborated by Western blot analysis of LC3B that showed the lipidated form of LC3B (LC3-II) was significantly increased after iron treatment (Figs 2A and B, and EV2A). Consistent with our analysis of LC3B, we found that p62 puncta formation and protein clearance were rapidly increased by iron treatment (Figs 2C, and EV2B and C). Surprisingly, while we observed p62 protein levels decreased significantly at early time points after iron treatment, we found they were significantly stabilized at 24 h posttreatment (Fig 2C). p62 stabilization under prolonged iron treatment potentially indicates a blockage of autophagic flux at later time points. To further analyze autophagy flux, we quantified the accumulation of lipidated LC3B in the presence of a late-stage autophagy inhibitor (CQ, chloroquine). At 4 h after iron treatment, LC3-II significantly increased with CQ, indicating an induction in autophagy (Fig 2D). However, 24 h after iron treatment LC3-II levels were elevated but unchanging, indicating a lack of autophagy flux despite the presence of a large pool of autophagosomes (Fig 2E). We also observed autophagosomes under prolonged IO were morphologically abnormal, with a mean diameter nearly three times those in the untreated samples (Fig 2F and G). Enlarged LC3-positive vesicles are often observed in autophagy-deficient backgrounds including cells with knock outs in ULK1/2 (Fig EV2D and E), Beclin-1 [32], FIP200 [33], and ATG14L1 [34]. We next performed live cell imaging to analyze autophagosome mobility that, in

addition to autophagosome number, is positively correlated with autophagic flux [35]. As expected, amino acid starvation increased autophagosome motility to 78 nm/s compared to 44 nm/s in untreated samples indicating an increase in autophagy rates. In contrast, autophagosomes observed in cells with IO were nearly static, moving an average of 6.4 nm/s (Fig 2H, Movie EV1). Ultrastructural analysis by transmission electron microscopy (TEM) showed that chronic IO resulted in a striking accumulation of enlarged vesicles, characteristic of autolysosomes (Fig 2I). To further characterize the blockage of autophagy that accompanies insulin resistance under chronic IO, we sought to determine whether lysosomal fusion with autophagosomes was inhibited at this time point [31]. We immuno-stained for endogenous LC3B and LAMP1 and observed large dual positive structures, which indicated that lysosomal fusion was not inhibited in the accumulated autolysosomes under prolonged IO (Fig 2J). This was confirmed by additional markers for both autophagosomes and lysosomes (Fig EV2F). Moreover, we found that chronic IO did not inhibit the proteolytic activity of lysosomal enzymes (β-glucosidase and cathepsin B) that were still active in autolysosomes under chronic IO, indicating that autophagy defects were not caused by an inhibition of lysosomal fusion or lysosomal enzyme activity (Fig EV2G–I). However, we also observed that under IO there was a precipitous loss of "free" lysosomes (defined as LAMP1-positive, LC3B-negative), with nearly all LAMP1 staining detected on autophagosomes (Figs 2J, and EV3A and B). Taken together, our data indicate that IO overload results in a temporary increase in autophagy rates, followed by an accumulation of non-functional autolysosomes and autophagy inhibition.

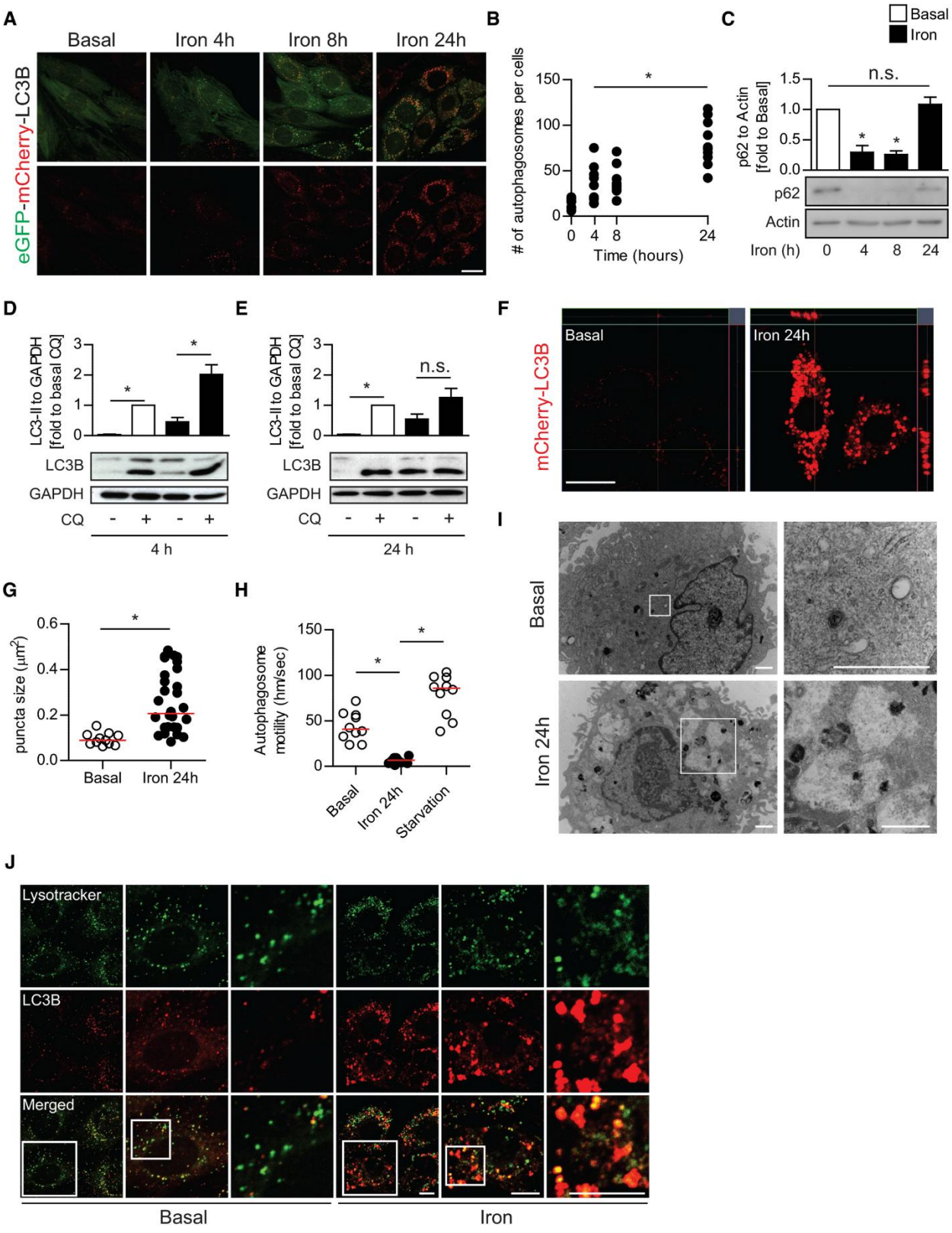
A
Basal
Iron 4h
Iron 8h
Iron 24h
eGFP-mCherry-LC3B
B
# of autophagosomes per cells
Time (hours)
C
Basal
Iron
p62 to Actin [fold to Basal]
n.s.
p62
Actin
Iron (h)
D
LC3-II to GAPDH [fold to basal CQ]
LC3B
GAPDH
CQ
4 h
E
n.s.
24 h
F
mCherry-LC3B
Basal
Iron 24h
G
puncta size (μm²)
Basal
Iron 24h
H
Autophagosome motility (hm/sec)
Basal
Iron 24h
Starvation
I
Basal
Iron 24h
J
Lysotracker
LC3B
Merged
Basal
Iron

Figure 2. Iron treatment transiently induced autophagy yet led to flux inhibition at 24-h iron treatment

A. Representative confocal microscope image of L6 cells stably expressing tandem fluorescent-eGFP-mCherry LC3B treated with iron ($FeSO_4$, 250 μM) for the indicated time points (4, 8, 24 h). **B.** Quantification of mean LC3B puncta per cell from (A). Experiments were repeated three times, and one representative experiment is presented here. *$P < 0.05$ (one-way ANOVA with Dunnett's *post hoc* test versus basal). **C.** Representative Western blot images and quantification of p62 to actin in L6 cells after iron treatment ($FeSO_4$, 250 μM) at multiple time points. *$P < 0.05$ (multiple unpaired Student's *t*-test versus basal). **D.** Representative Western blot images and quantification of LC3B-II to GAPDH in L6 cells after 4-h iron treatment stimulated with chloroquine (CQ, 30 μM). *$P < 0.05$ (unpaired Student's *t*-test versus control, basal, or iron without CQ). **E.** Representative Western blot images and quantification of LC3B-II to GAPDH in L6 cells after 24-h iron treatment stimulated with CQ 30 μM. *$P < 0.05$ (unpaired student's *t*-test versus control, basal, or iron without CQ). **F.** Representative confocal microscope z-stack image of mCherry-LC3B L6 cells after iron treatment (250 μM, 24 h). **G.** Quantification of LC3B puncta size from (F). Experiments were performed three times, and one representative experiment is presented here. *$P < 0.05$ (unpaired Student's *t*-test compared to basal). **H.** Quantification of autophagosome motility from live cell microscopy (Movie EV1) from mCherry-LC3B L6 cells under basal, iron (250 μM, 24 h), and starvation (amino acid free) condition. Experiments were performed three times, and one representative experiment is presented here. *$P < 0.05$ (unpaired Student's *t*-test compared to iron 24 h). **I.** Representative TEM images of autophagosome and autolysosomes in L6 cells after iron treatment (250 μM, 24 h). **J.**Representative confocal microscope images of eGFP-mCherry-LC3B L6 cells with LysoTracker Deep Red after iron treatment (250 μM, 24 h).

Data information: Data are expressed as means ± SEM. Western blot and confocal image analysis were performed three times. Scale bar (confocal microscope) = 10 μm. Scale bar (electron microscope) = 1 μm.

IO inhibits reactivation of mTOR following autophagosome degradation

The nature of the lysosomal and autophagosomal defects described above could be consistent with attenuation of the recently described membrane recycling event termed ALR [37]. ALR is essential to sustain prolonged periods of autophagic induction [37]. ALR is an mTOR-dependent process where membrane from the spent autophagosome is extruded, followed by scission to form protolysosomes that then mature into new lysosomes. mTORC1 promotes this scission after being activated by nutrients generated from the degradation of autophagic cargo. Importantly, this function of mTORC1 acts to promote autophagy under prolonged stress through the production of lysosomes and is independent of the autophagy-suppressive effects mTORC1 exerts under basal conditions [37]. Therefore, we next sought to monitor mTORC1 activity in iron-treated samples. Temporal analysis of mTORC1 target phosphorylation (p-S6K T389 and p-ULK1 S757) upon FBS withdrawal showed a partial rescue at 8 h that was absent in the iron-treated samples (Fig 3A and B). This result indicates that IO may prevent reactivation of mTORC1 from nutrients generated by the autolysosomes.We next tested whether maintenance of mTORC1 activation under chronic IO was sufficient to rescue the autophagic defects observed. To do so, L6 cells were transiently transfected with a Myc-tagged RHEB (Ras homolog enriched in brain) GTPase, which contained the Q64L mutation to remain GTP bound and can directly maintain mTORC1 activity [39]. Transfected cells were treated with iron for 24 h and then stained with anti-LC3B antibodies to identify autophagosomal aggregates and anti-Myc antibodies to mark cells transfected with Myc-RHEB mutant. We found that cells with forced activation of mTORC1 exhibited a dramatic absence of large autolysosome accumulation under chronic iron treatment (Fig 3C, Box1) when compared to cells that were not transfected under the same conditions (Fig 3C, Box2). We next generated stable cell lines over expressing RHEB mutant (RHEB Q64L L6) and compared to wt

(wild-type) cells after treating with iron. As a control, we tested intracellular iron levels in RHEB Q64L and wt cells after 24-h iron treatment and found them comparable (Fig 3D). After 24-h iron treatment, wt cells developed autophagosomal aggregates and compromised LC3B-free lysosomal pools as previously observed. Conversely, RHEB Q64L cells did not accumulate large autophagosomes and total lysosomal content was comparable with/without iron treatment (Fig 3E and F). Ultrastructure analysis by TEM further confirmed that RHEB Q64L stable cells did not develop abnormal autophagosomal structures after iron treatment, when compared to control (Fig 3G). To examine the functional significance of these observations, we tested if maintenance of mTORC1 activity affected IO-induced insulin resistance. In RHEB Q64L cells, we observed improved insulin signaling (p-IRS-1 Y612 and p-AKT T308) under IO (Fig 3H and I). Taken together, these data suggest that loss of mTORC1 activity during chronic IO is responsible for autophagy defects and insulin resistance.

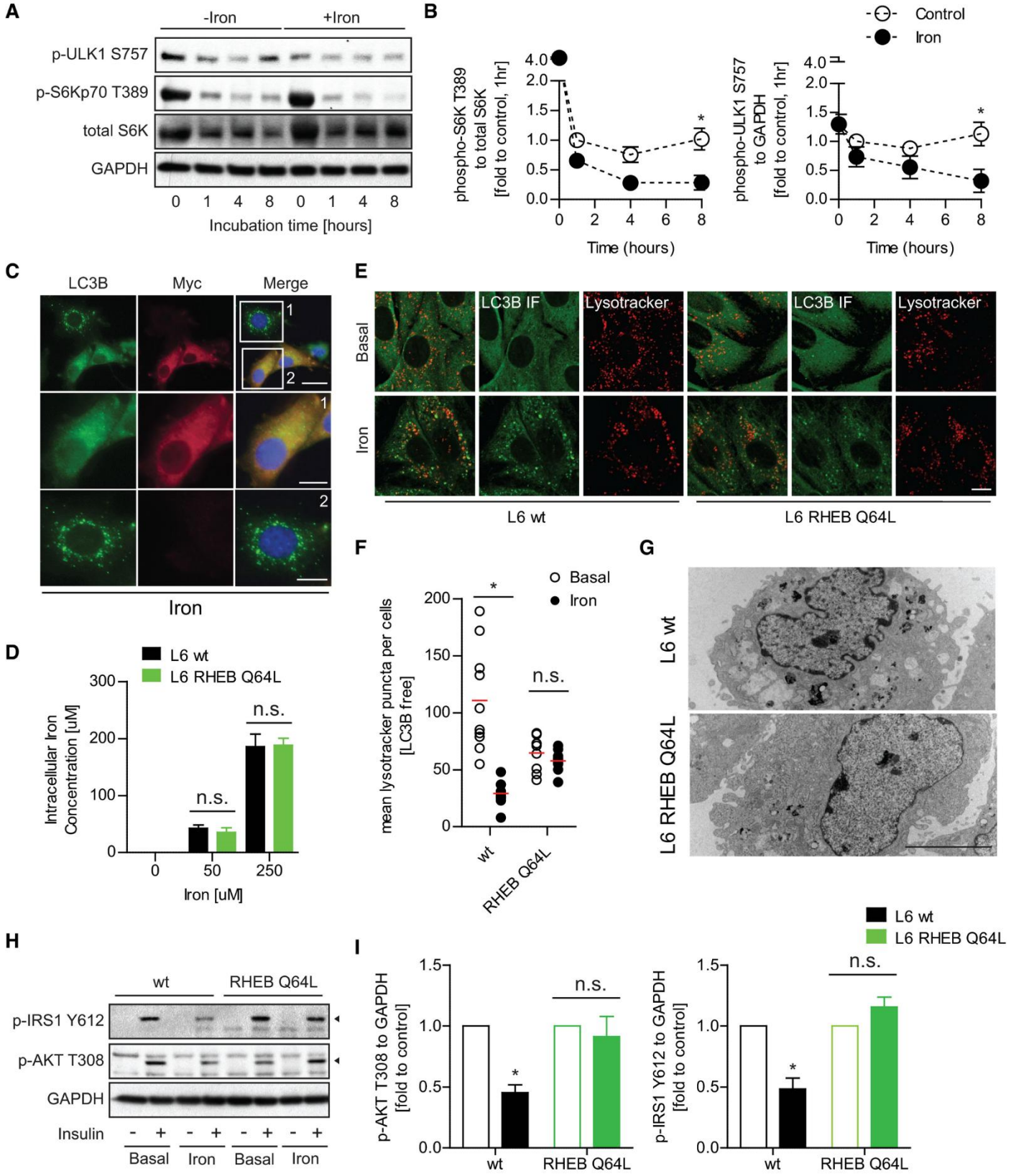
A
-Iron
+Iron
p-ULK1 S757
p-S6Kp70 T389
total S6K
GAPDH
0 1 4 8 0 1 4 8
Incubation time [hours]
B
Control
Iron
phospho-S6K T389 to total S6K [fold to control, 1hr]
Time (hours)
phospho-ULK1 S757 to GAPDH [fold to control, 1hr]
Time (hours)
C
LC3B
Myc
Merge
Iron
D
L6 wt
L6 RHEB Q64L
Intracellular Iron Concentration [uM]
n.s.
n.s.
Iron [uM]
E
Basal
Iron
LC3B IF
Lysotracker
L6 wt
L6 RHEB Q64L
F
Basal
Iron
mean lysotracker puncta per cells [LC3B free]
n.s.
wt
RHEB Q64L
G
L6 wt
L6 RHEB Q64L
H
wt
RHEB Q64L
p-IRS1 Y612
p-AKT T308
GAPDH
Insulin
Basal
Iron
Basal
Iron
I
L6 wt
L6 RHEB Q64L
p-AKT T308 to GAPDH [fold to control]
n.s.
wt
RHEB Q64L
p-IRS1 Y612 to GAPDH [fold to control]
n.s.
wt
RHEB Q64L

Figure 3. Iron treatment impaired mTOR restoration following autophagosome degradation and enforced mTOR reactivation reversed autophagy defects and insulin resistance

A. Representative Western blot images of phospho-ULK1 (S757), phospho-S6Kp70 (T389), total S6K, and GAPDH after iron treatment ($FeSO_4$, 250 μM) for multiple time points. **B.** Quantification of mTORC1 activity analyzed through phosphorylation of S6K T389 to total S6k and ULK1 S757 to GAPDH after iron treatment ($FeSO_4$, 250 μM) for multiple time points. *$P < 0.05$ (multiple unpaired Student's *t*-test versus control at each time point). **C.** Representative epi-immunofluorescent images of L6 cells transfected with myc-RHEB Q46L and immuno-stained against LC3B and myc after iron treatment (FeSO4, 250 μM) for 24 h. **D.** Ferrozine-based colorimetric measurement of intracellular iron in wild-type (wt) L6 and RHEB-Q64L L6 cells after iron treatment (50 or 250 μM) for 24 h. **E.** Representative confocal images of wt L6 and RHEB-Q64L L6 cells pulsed with LysoTracker Deep Red and immuno-stained against LC3B after iron treatment (250 μM, 24 h). **F.** Quantification of LC3B-free lysosome numbers in (E). Experiments were repeated three times, and one representative experiment is presented here. *$P < 0.05$ (multiple unpaired Student's *t*-test versus basal in wt and RHEB Q64L cells). **G.** Representative TEM images of wt L6 and RHEB-Q64L cells after iron treatment (250 μM, 24 h). **H, I.** Representative Western blot images and quantifications of phospho-IRS1 (Y612, indicated by arrowhead) and AKT (T308, indicated by arrowhead) to GAPDH in wt and RHEB-Q64L L6 cells stimulated with insulin (100 nM, 5 min) after iron treatment (250 μM, 24 h). *$P < 0.05$ (multiple unpaired Student's *t*-test versus basal in wt and RHEB Q64L cells).

Data information: All experiments were performed three times. Data are expressed as means ± SEM. Scale bar (confocal microscope) = 10 μm, (electron microscope) = 5 μm, and (epi-immunofluorescent microscope) = 25 and 5 μm.

IO-induced insulin resistance and autophagy defects are reversed upon iron withdrawal

In the clinic, IO-induced insulin resistance can be improved by iron-restricted diets or iron chelation therapy [17]. Therefore, we examined whether IO-induced insulin resistance could be rescued by withdrawing iron from treatment medium following iron treatment for 24 h. 24-h withdrawal resulted in alleviation of IO, by significantly reducing intracellular iron levels as indicated by PGSK and ferrozine-based colorimetric assay (Fig 4A and B). The recovery from IO occurred concurrently with insulin sensitivity restoration. Phosphorylation of insulin signaling molecules after insulin stimulation significantly recovered after 24-h withdrawal (Fig 4C and D). We next analyzed the effects of iron withdrawal after iron overload on autophagosome and lysosomal populations. We observed that iron withdrawal after chronic IO resulted in clearance of accumulated autolysosomes and a restoration of LC3B-negative lysosomes (Fig 4E and F). Iron overload has been described to inhibit the targeting of ferritin to autophagosomes. Therefore, we looked at ferritin protein levels under IO and after iron wash off. As expected, ferritin was stabilized by chronic IO consistent with a block in autophagic clearance and was cleared significantly by 24 h after media replacement without excess iron (Fig 4G). Taken together, our data show that iron removal results in clearance of abnormal autophagosomes, restoration of lysosomes, and increased insulin sensitivity.

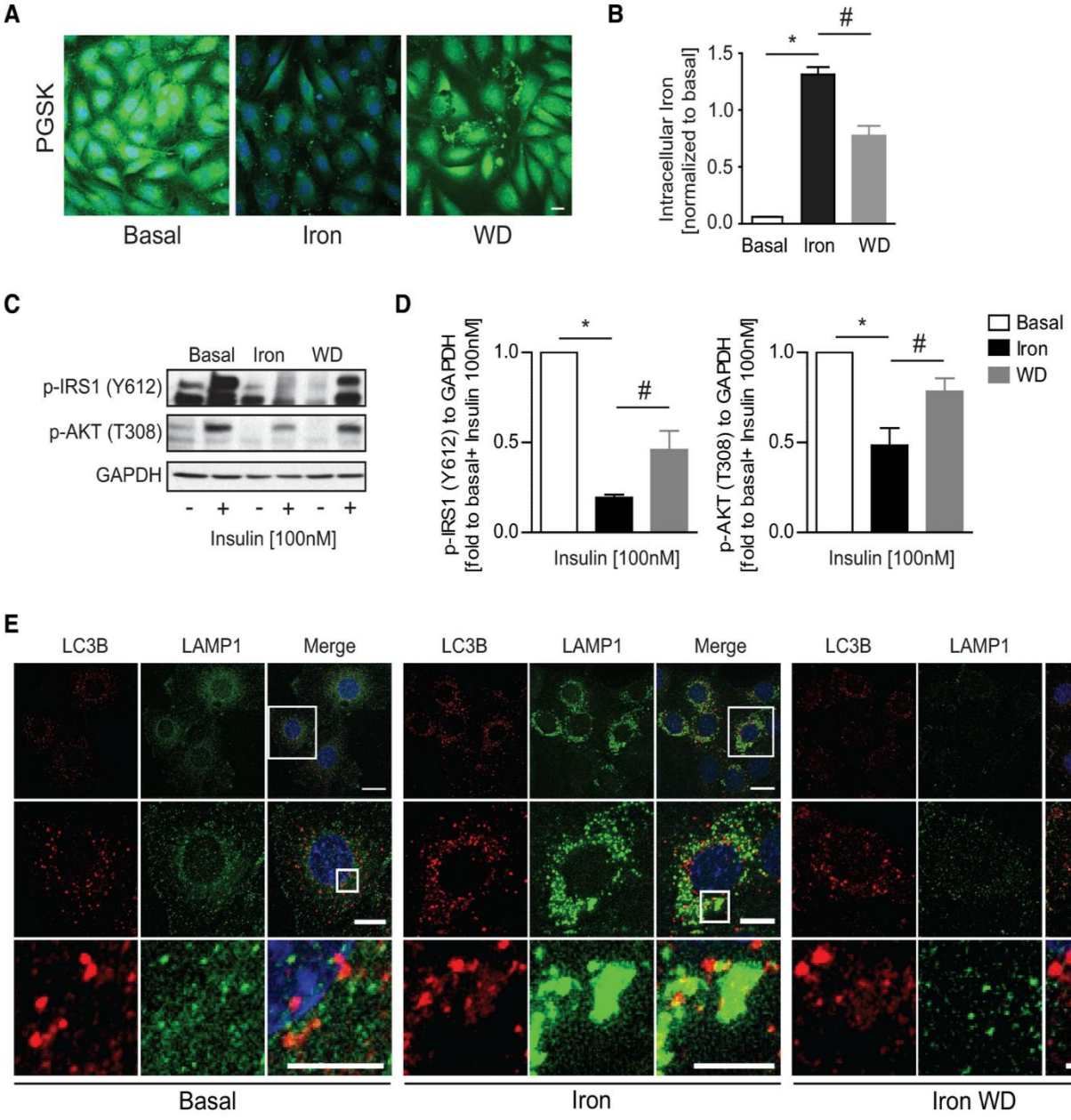
A
PGSK
Basal
Iron
WD
B
Intracellular Iron [normalized to basal]
1.5
1.0
0.5
0.0
*
#
Basal Iron WD
C
Basal Iron WD
p-IRS1 (Y612)
p-AKT (T308)
GAPDH
- + - + - +
Insulin [100nM]
D
p-IRS1 (Y612) to GAPDH [fold to basal+ Insulin 100nM]
p-AKT (T308) to GAPDH [fold to basal+ Insulin 100nM]
Insulin [100nM]
Basal
Iron
WD
E
LC3B
LAMP1
Merge
Basal
Iron
Iron WD
F
LC3B negative LAMP1 positive puncta per cells
40
30
20
10
0
Basal Iron WD
G
Ferritin to Vinculin [fold to Iron]
n.s.
Ferritin
Vinculin
WD (h) 0 4 24
Iron (h) 0 24 24 24

Figure 4. Restoration of lysosomal pools following iron withdrawal reversed insulin resistance A. Representative confocal microscope images of L6 cells pulsed with PGSK dye after iron treatment (250 μM, 24 h) followed by 24-h iron withdrawal. **B.** Ferrozine-based colorimetric measurement of intracellular iron in L6 cells after iron treatment (250 μM, 24 h) followed by 24-h withdrawal. $*P < 0.05$, $^{\#}P < 0.05$ (multiple unpaired Student's *t*-test versus basal or iron). **C, D.** Representative Western blot images and quantification of phospho-IRS1 (Y612) and phospho-AKT (T308) to GAPDH in L6 cell iron treatment (250 μM, 24 h) followed by 24-h withdrawal. $*P < 0.05$, $^{\#}P < 0.05$ (multiple unpaired Student's *t*-test versus basal or iron). **E.** Representative epi-immunofluorescent microscope images of L6 cells immuno-stained against LC3B and LAMP1 after iron treatment (250 μM, 24 h) followed by 3-h withdrawal. **F.** Quantification of autophagosome-free lysosomes in (E). Experiments were performed three times, and one representative experiment is presented here. Red line indicates median. $*P < 0.05$, $^{\#}P < 0.05$ (multiple unpaired Student's *t*-test versus basal or iron). **G.** Representative Western blot images and quantification of ferritin to vinculin in L6 cells after iron treatment (250 μM, 24 h) followed by withdrawal for 4 or 24 h. $*P < 0.05$, $^{\#}P < 0.05$ (multiple unpaired Student's *t*-test versus basal or iron).

Data information: All experiments were performed three times. Data are expressed as means ± SEM. Scale bar = (confocal microscope, A) 10 μm and (epi-immunofluorescent microscope) = 20, 10, and 5 μm.

Chronic IO blocks mTORC1 reactivation on autolysosomes and signaling to UVRAG

We next sought to determine the mechanism underlying IO-induced autophagic defects. We previously determined that forced mTORC1 activation was sufficient to block autolysosome accumulation (Fig 3C and G). Therefore, we first sought to characterize the effects of prolonged IO on regulatory phosphorylation of mTORC1. L6 cells were treated with iron for 24 h or 24 h plus iron withdrawal. mTORC1 was monitored by phosphorylation at S2448, which correlates with mTORC1 activity [42]. We observed mTORC1 phosphorylation was greatly diminished at 24-h IO and recovered after 4 h of iron withdrawal (Fig 5A). mTORC1 phosphorylation at S2448 is dependent on localization to the lysosome or autolysosome for activation by the RHEB-GTPase activity, which is in turn regulated by tuberous sclerosis complex (TSC)-AKT signaling [44]. We stained cells for endogenous mTOR and LC3B and found that mTOR was localized to autolysosomes under prolonged IO, indicating localization defects are likely not the cause of mTORC1 activity loss (Fig EV4A). Therefore, we next looked at the effect of IO on AKT-mediated inhibition of TSC2. We observed a decrease in inhibitory phosphorylation of TSC2 under IO, which was dramatically reversed upon wash off (Fig 5B). However, when iron withdrawal media was supplemented with AKT inhibitor, mTORC1 was not re-activated upon iron removal (Fig 5B). Together, these data demonstrate that IO results in a decrease in AKT-mediated repression of TSC2, resulting in a potent repression of RHEB and mTORC1.The lysosomal loss, mTORC1 inhibition, and autophagy defect we observe under IO are all consistent with a defect in ALR. mTORC1 promotes ALR through scission of the autolysosome activity via direct phosphorylation of UVRAG, a component of the VPS34 lipid kinase complex [38]. Phospholipid production by UVRAG-containing VPS34 complexes is essential for the scission of the autolysosomal membrane. mTORC1-mediated phosphorylation of UVRAG on serine S550 was

monitored in L6 cells transfected with FLAG-UVRAG that were treated with iron as indicated followed by immunoprecipitation of FLAG-UVRAG-containing VPS34 complexes (Fig 5C). Interestingly, at 4-h iron treatment we saw a slight increase in mTORC1-mediated UVRAG phosphorylation, which indicates that mTORC1 can be activated at the autolysosome even when global mTORC1 activity (as measured by S6K phosphorylation) is low (Fig 3A). This is consistent with the relatively normal functioning of autophagosomes and lysosomes that we observe at this time point (Fig 2C and D). However, at 24-h iron treatment we observed a dramatic loss in mTORC1-mediated phosphorylation of UVRAG (Fig 5C), indicating mTORC1 is incapable of efficiently promoting ALR under chronic iron treatment despite an overabundance substrate (mature autolysosomes). Additionally, the removal of iron resulted in a partial recovery of mTORC1-mediated UVRAG phosphorylation, indicating that IO-induced stress was responsible for the loss of ALR signaling (Fig 5C). We then used Torin1, a well-established mTOR inhibitor [46], and found that in its presence recovery of UVRAG signaling was completely abolished, confirming that mTORC1 ALR signaling is regulated by IO (Fig 5D). Based on the recovery of mTORC1 signaling to UVRAG upon iron withdrawal, we hypothesized that treatment of cells with Torin1 would be sufficient to block lysosomal recovery following iron withdrawal. To validate our hypothesis, we monitored lysosomal number and trafficking using cells transfected with RFP-LAMP1 to determine whether inhibition of mTORC1 was sufficient to ablate the rescue of lysosomes upon iron withdrawal after chronic IO. RFP-LAMP1 was present on enlarged autolysosomes similar to endogenous LAMP1 (Fig EV4B). Under basal conditions, the number of lysosomes ranged from 100 to 300 per cell, and continuously trafficked and underwent fusion events (Fig 5E). On the other hand, iron treatment significantly reduced the number of lysosomes (Fig 5E) and the motility of LAMP1 particles was reduced significantly (Fig 5F and G, Movie

EV2). The lysosomal pools were significantly recovered near basal levels after 4-h withdrawal. However, as predicted the addition of Torin1 abolished recovery of lysosomal pools and lysosomal motility following iron withdrawal (Fig 5E and F). Collectively, these data demonstrate that prolonged IO results in lysosomal loss due to ablation of mTORC1 reactivation on autolysosomes caused by alterations in AKT-TSC-RHEB signaling (Fig 5H).

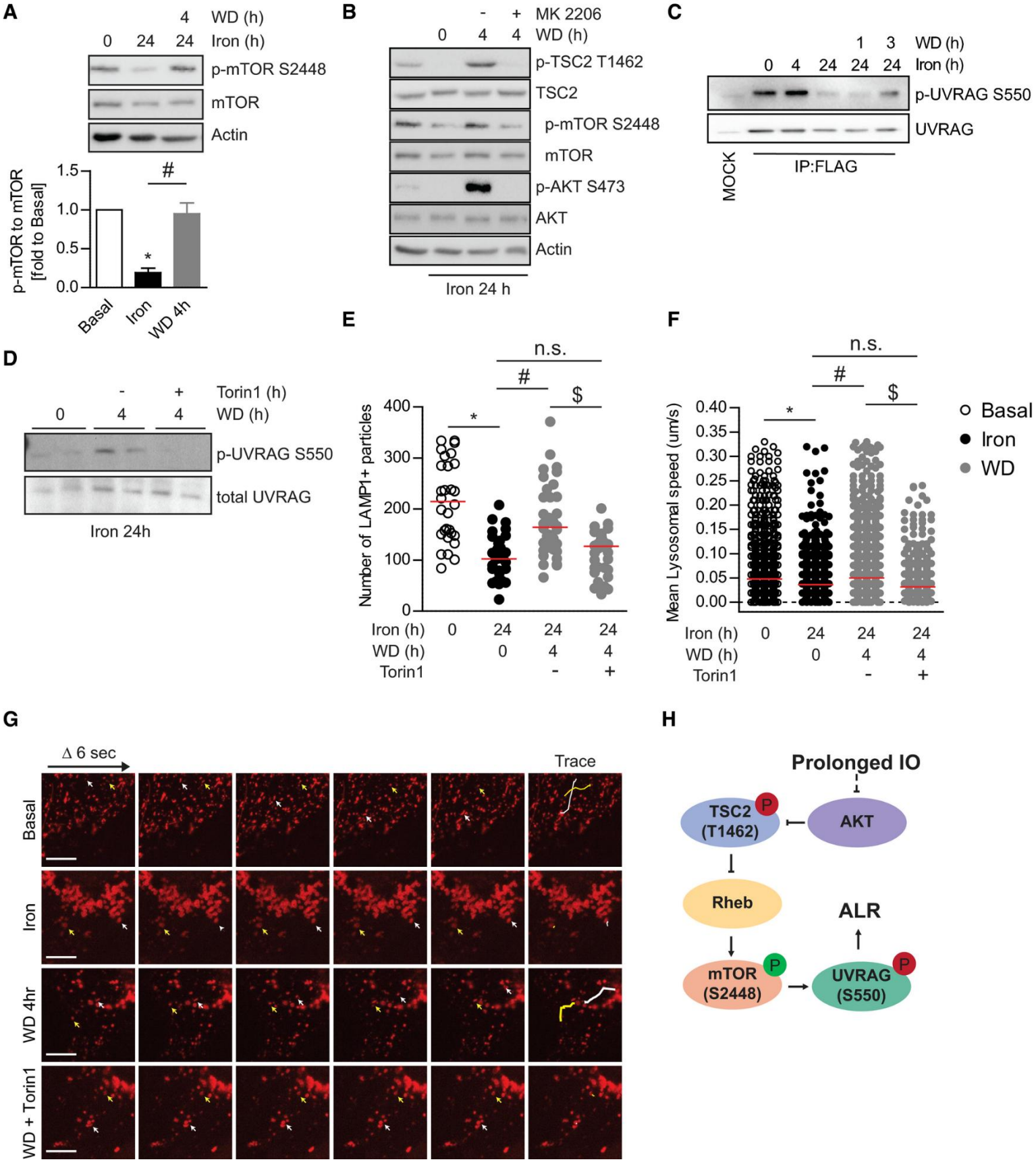
A
4 WD (h)
0 24 24 Iron (h)
p-mTOR S2448
mTOR
Actin
p-mTOR to mTOR [fold to Basal]
1.5
1.0
0.5
0.0
#
*
Basal
Iron
WD 4h
B
- + MK 2206
0 4 4 WD (h)
p-TSC2 T1462
TSC2
p-mTOR S2448
mTOR
p-AKT S473
AKT
Actin
Iron 24 h
C
1 3 WD (h)
0 4 24 24 24 Iron (h)
p-UVRAG S550
UVRAG
MOCK
IP:FLAG
D
- + Torin1 (h)
0 4 4 WD (h)
p-UVRAG S550
total UVRAG
Iron 24h
E
n.s.
#
$
*
Number of LAMP1+ particles
400
300
200
100
0
Iron (h) 0 24 24 24
WD (h) 0 4 4
Torin1 - +
F
n.s.
#
$
*
Mean Lysosomal speed (um/s)
0.40
0.35
0.30
0.25
0.20
0.15
0.10
0.05
0.00
Iron (h) 0 24 24 24
WD (h) 0 4 4
Torin1 - +
Basal
Iron
WD
G
Δ 6 sec
Trace
Basal
Iron
WD 4hr
WD + Torin1
H
Prolonged IO
TSC2 (T1462)
P
AKT
Rheb
ALR
mTOR (S2448)
P
UVRAG (S550)
P

Figure 5. Molecular mechanisms underlying IO-induced mTOR activity suppression

A. Representative Western blot images and quantification of phospho-mTOR S2448, total mTOR, and actin in L6 cells after iron treatment (250 μM, 24 h) followed by withdrawal for 4 h. Experiments were performed three times. $^{*}P < 0.05$, $^{\#}P < 0.05$ (multiple unpaired Student's *t*-test versus basal or iron). **B.** Representative Western blot images of phospho-mTOR S2448, total mTOR phospho-TSC2 T1462, total TSC2, phospho-AKT S473, total AKT, and actin in L6 cells after iron treatment (250 μM, 24 h) followed by withdrawal for 4 h with or without MK2206 (AKT inhibitor). **C.** Representative Western blot images of phospho-UVRAG S550 and total UVRAG in L6 cells transfected with FLAG-UVRAG and FLAG pulldown after iron treatment (250 μM, 4 and 24 h) followed by withdrawal for 1 and 3 h. **D.** Representative Western blot images of endogenous phospho-UVRAG S550 and total UVRAG expression in L6 cells after iron treatment (250 μM, 24 h) followed by withdrawal for 4 h with or without torin1 (200 nM). **E, F.** Live cell imaging analysis of L6 cells transfected with LAMP1-RFP from Movie EV2: lysosomal number (E) and speed (F) in L6 cells after iron treatment (250 μM, 24 h) followed by withdrawal for 4 h with or without Torin1 (200 nM). Experiments were performed three times, and all biological and technical replicates are plotted here. Red line indicates median. $^{*}P < 0.05$, $^{\#}P < 0.05$, $^{\$}P < 0.05$ (one-way ANOVA with multiple comparisons). **G.** Representative confocal images of time-lapse captures of lysosomes at 6-s intervals for 30 s. White and yellow arrows mark positions of two representative LAMP1 puncta over 30 s, and the traces of puncta were shown as lines in final panel. **H.** Schematic diagram of mTOR signaling regulation by IO.

Data information: Data are presented as mean ± SEM. Scale bar = 10 μm.

Induction of IO in mice and development of insulin resistance following IO

As in previous studies which have adopted injections to induce IO [48], we delivered iron intravenously at 15 mg/kg, a dose with minimal toxicity [50], via three injections at 2-h intervals (Fig 6A). Twenty-four hours after first administration, animals were sacrificed, and tissue iron accumulation examined with Perls Prussian Blue Staining. As expected, a robust increase in hepatic iron staining and more modest increase in skeletal muscle iron content was apparent (Fig 6B). Western blotting indicated that skeletal muscle ferritin levels increased while TfR1 levels decreased significantly in IO mice (Fig 6C and D). IO mice exhibited signs of peripheral insulin resistance, as shown upon examination of glucose handling via insulin and glucose tolerance tests (Fig 6E–H). To directly investigate changes in skeletal muscle insulin sensitivity, we examined insulin-stimulated phosphorylation of IRS-1 (Y612) and AKT (T308) and observed significantly attenuated insulin-induced phosphorylation in IO mice (Fig 6I and J). Collectively, these data indicate that our intravenous iron injection regimen recapitulated key aspects of iron-induced insulin resistance in skeletal muscle from our L6 cell culture model.

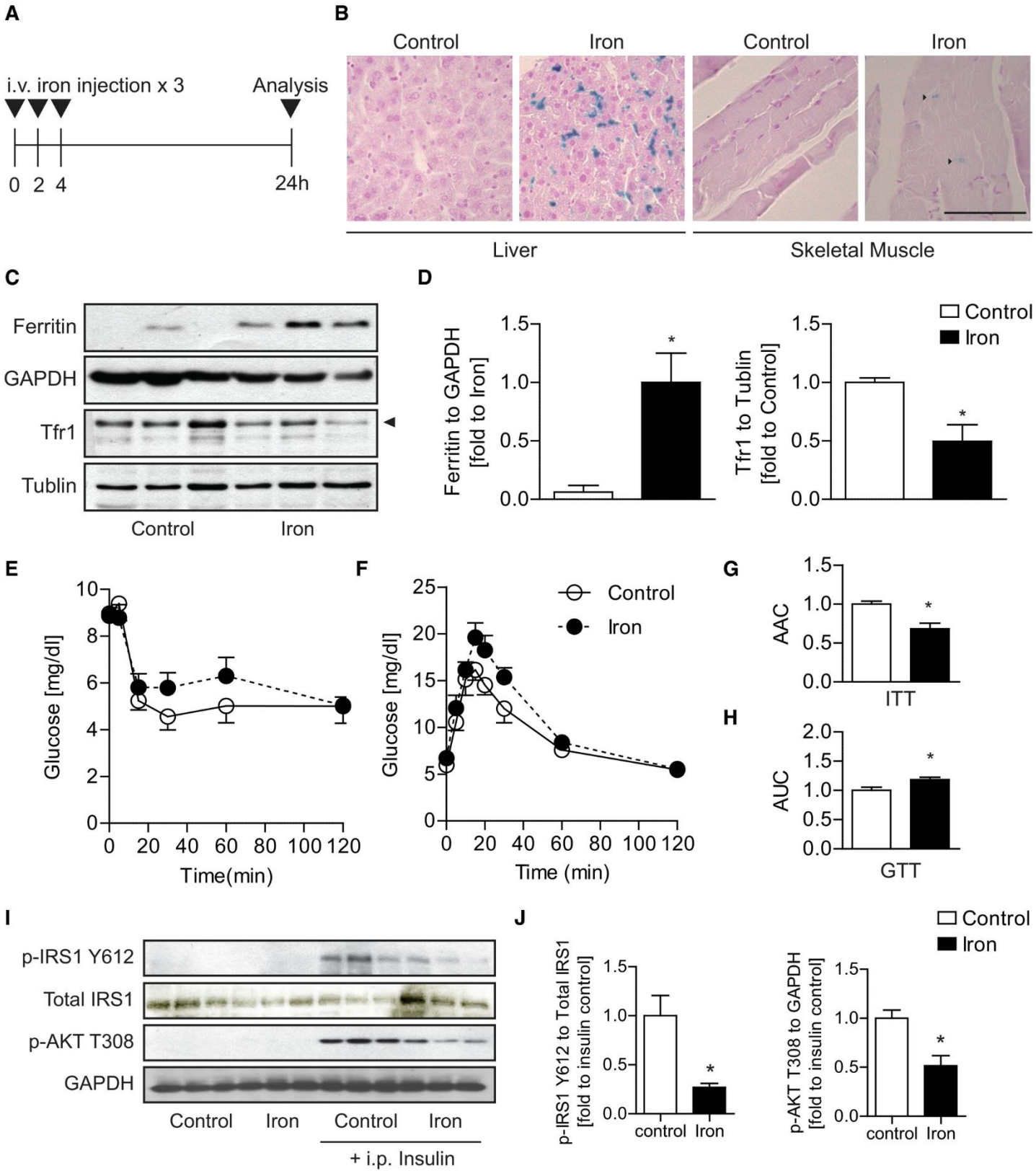
A
i.v. iron injection x 3
Analysis
0 2 4
24h
B
Control
Iron
Control
Iron
Liver
Skeletal Muscle
C
Ferritin
GAPDH
Tfr1
Tublin
Control
Iron
D
Ferritin to GAPDH [fold to Iron]
Tfr1 to Tublin [fold to Control]
Control
Iron
E
Glucose [mg/dl]
Time(min)
F
Glucose [mg/dl]
Time (min)
Control
Iron
G
AAC
ITT
H
AUC
GTT
I
p-IRS1 Y612
Total IRS1
p-AKT T308
GAPDH
Control
Iron
Control
Iron
+ i.p. Insulin
J
p-IRS1 Y612 to Total IRS1 [fold to insulin control]
p-AKT T308 to GAPDH [fold to insulin control]
control
Iron
Control
Iron

Figure 6. Development of acute iron overload (IO) *in vivo* model and validation of IO and insulin resistance in skeletal muscle

A. Schematic diagram of iron-dextran injections' experimental plan. **B.** Prussian Perl blue staining in liver and skeletal muscle after iron injections. **C, D.** Representative Western blot images and quantification of ferritin and Tfr1 (indicated by arrowhead) to tubulin in skeletal muscles 24 h after iron injections. *$P < 0.05$ (unpaired Student's *t*-test versus control). **E.** Insulin tolerance test 24 h after iron injections. **F.** Glucose tolerance test (GTT) 24 h after iron injections. **G.**Quantification of area under curve in ITT (E). *$P < 0.05$ (unpaired Student's *t*-test versus control). **H.** Quantification of area under curve for panel (F). *$P < 0.05$ (unpaired Student's *t*-test versus control). **I, J.** Representative Western blot images and quantification of phospho-IRS1 (Y612) and phospho-AKT (T308) to GAPDH in skeletal muscles 24 h after iron injection followed by i.p. insulin injection. *$P < 0.05$ (unpaired Student's *t*-test versus control).

Data information: Results are presented as mean ± SEM. $n = 6$ males for ITT and GTT. $n = 3$ males for Western blot analysis. Scale bar = 50 μm.

IO caused reduced lysosomal pools with reduced UVRAG signaling and inhibited autophagy flux

To measure ALR events *in vivo*, we performed LC3B and LAMP1 immunofluorescence on tissue sections and observed a pronounced difference between the control and IO groups (Fig 7A). In control mice, there was a minimal complement of autophagosomes (LC3B puncta) yet numerous lysosomes (LAMP1 puncta), quantitatively 200–300 puncta per field of view (Fig 7B). In IO mice, the number of autophagosomes increased while the number of lysosomes decreased significantly to less than 100 puncta per field of view. TEM analysis of muscle tissue from the control group confirmed the predominant appearance of lysosomes as single membrane clear structures, with occasional observation of autophagosomes (Fig 7C). On the other hand, TEM analysis of muscle from iron group showed very sparse lysosomal content, with much smaller size than lysosomal structures observed in the control group. Also present in IO samples were tubular projections that are characteristic of reduced activity of UVRAG-containing VPS34 complexes [38] (Fig 7C). We further analyzed autophagy flux and ALR by Western blotting of UVRAG phosphorylation, LC3B, and p62 expression. In iron-treated mice, phosphorylation of UVRAG at S550 significantly decreased (Fig 7D), matching *in vitro* data (Fig 5C and D). Moreover, both LC3B-II expression and p62 expression in the IO group increased, indicating impaired autophagy flux, compared to the control groups (Fig 7E and F). These changes were also observed in liver, indicating that IO-induced ALR defects are not limited to skeletal muscle and may have widespread highly significant pathophysiological implications (Fig EV5). Taken together, we have identified that IO induces an mTORC1 reactivation defect in skeletal muscle which leads to an ALR defect (Fig 8). This represents a new mechanistic link connecting disturbed iron homeostasis to insulin resistance and metabolic dysfunction.

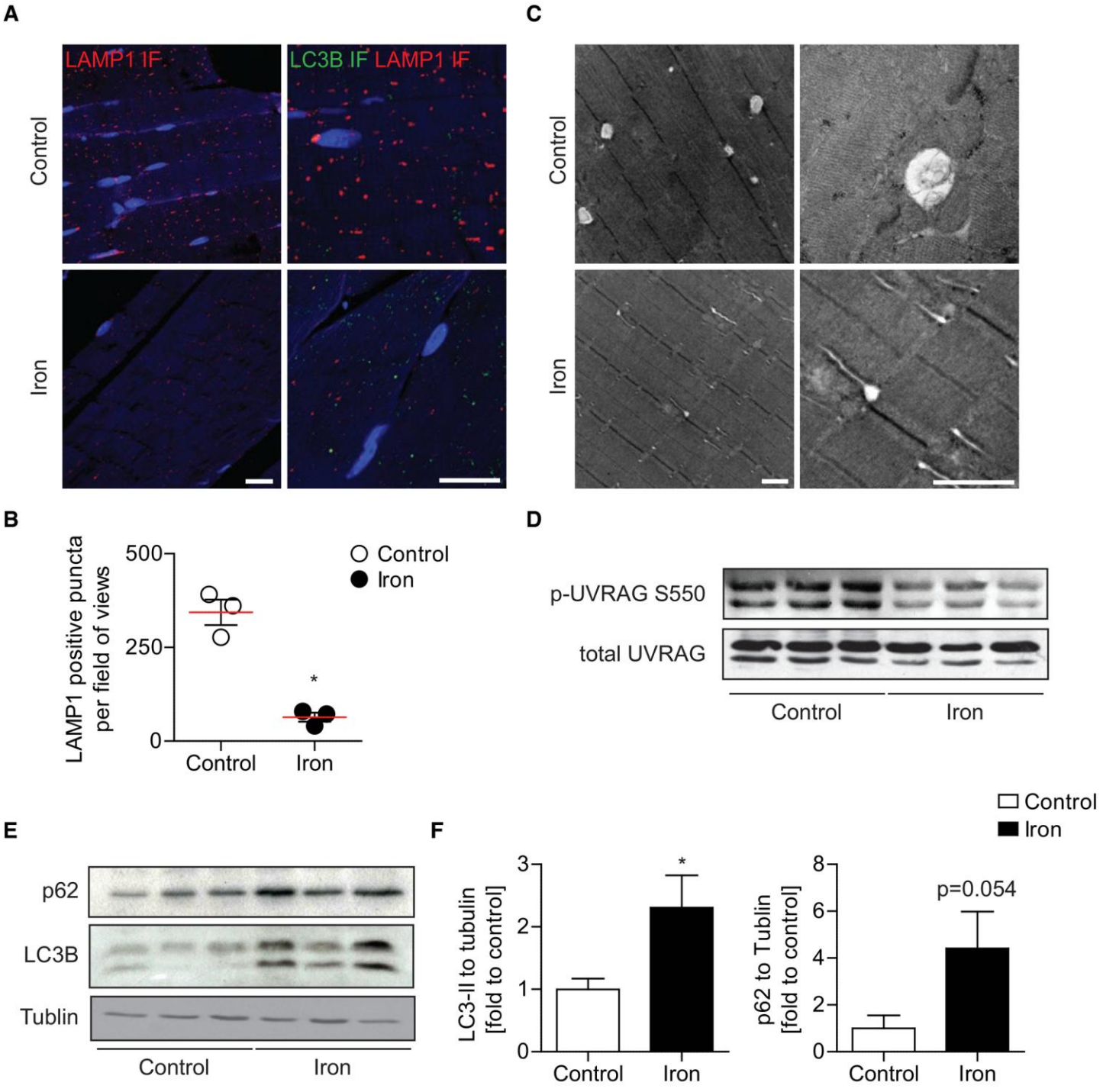
A
LAMP1 IF
LC3B IF LAMP1 IF
Control
Iron
C
Control
Iron
B
LAMP1 positive puncta per field of views
500
250
0
Control
Iron
*
Control
Iron
D
p-UVRAG S550
total UVRAG
Control
Iron
E
p62
LC3B
Tublin
Control
Iron
F
Control
Iron
LC3-II to tubulin [fold to control]
3
2
1
0
*
Control
Iron
p62 to Tublin [fold to control]
8
6
4
2
0
p=0.054
Control
Iron

Figure 7. Evidence of ALR defects in skeletal muscles after acute IO

A. Representative confocal microscope images of skeletal muscle tissue sections immuno-stained against LC3B (Alexa 647) and LAMP1 (Alexa 555) **B.** Quantification of lysosomes (LAMP1 puncta) in skeletal muscles 24 h after iron injections. *$P < 0.05$ (unpaired Student's *t*-test versus control). **C.** Representative TEM images of skeletal muscle 24 h after iron injections. **D.** Representative Western blot images of phospho-UVRAG S550 and total UVRAG in skeletal muscle 24 h after iron injections. **E, F.** Representative Western blot images and quantification of LC3-B and p62 to tubulin in skeletal muscles 24 h after iron injections. *$P < 0.05$ (unpaired Student's *t*-test versus control).

Data information: Results are presented as mean ± SEM. $n = 3$ males. Scale bar (confocal microscope) = 20 μm. Scale bar (electron microscope) = 500 nm.

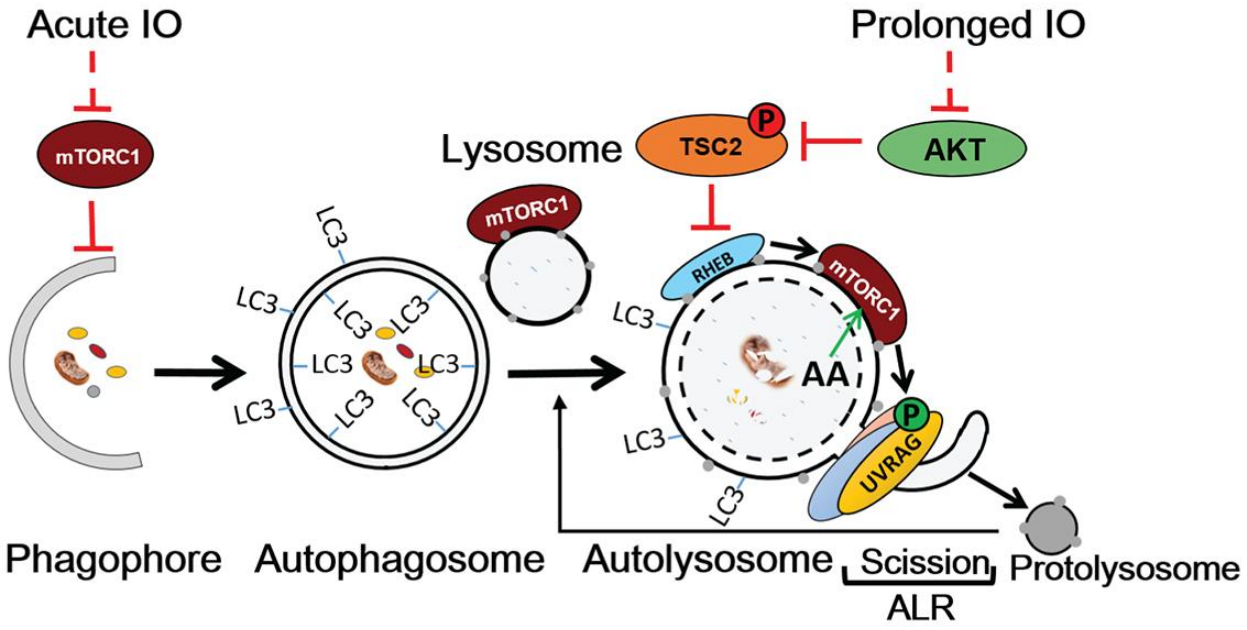

Figure 8. Schematic diagram of IO-mediated autophagy regulation

Working model of autophagy regulation by IO. Acute IO leads to inhibition of mTORC1 leading to autophagy induction. Prolonged IO prevents ALR-mediated production of new lysosomes through AKT-TSC-Rheb-mTORC1-UVRAG signaling defects. The lack of free lysosomes contributes to autophagy inhibition and insulin resistance in skeletal muscle.

3.5 Discussion

IO is a devastating and complex condition that most notably arises in individuals with beta thalassemia that require frequent blood transfusions or those with hereditary hemochromatosis, while IO in metabolic syndrome is also a common finding [10]. The pathophysiological mechanism underlying IO-induced diabetes is complicated as both insulin deficiency and insulin resistance contribute [8]. The causative relationship between IO and insulin secretion defects is well established [51], yet the precise mechanisms whereby iron can elicit insulin resistance are complicated and we believe that IO in skeletal muscle is underappreciated [13]. Here, we used an *in vitro* model using L6 cells and translated this to analysis of mouse skeletal muscle using an *in vivo* model of iron overload. In both, we observed that skeletal muscle insulin sensitivity was significantly compromised after IO. We found that preventing excess free iron levels in L6 cells using an iron chelator could prevent IO-induced insulin resistance and metabolic dysfunction, which is in keeping with the fact that clinical interventions to reduce free iron improved insulin sensitivity and can delay onset of T2D [11].

We and others have recently focused on the role of autophagy in regulation of metabolism at various levels [19]. For example, we have previously shown that stimulation of autophagy by adiponectin was of functional significance in improving insulin sensitivity and metabolism in skeletal muscle [19]. Interestingly, IO-induced insulin resistance has been described to involve reduced adiponectin expression in adipocytes. However, systematic IO did not always translate to insulin resistance because adipocytes could enhance iron excretion to avoid intracellular iron overload [55].

The relationship between IO and autophagy has been examined, where acute IO was observed to stimulate autophagy [56]. Indeed, this is in agreement with our own observations in that IO exposure

for up to 8 h stimulates autophagy. This increase in autophagy is likely the result of a compensatory cellular response upon detection of cellular stress. Acute IO activation of autophagy is also consistent with the observed rapid inhibition of mTORC1, the single most potent repressor of autophagy in mammals that responds to a large number of stressors including nutrient starvation and ER stress [58]. Yet, there are several problems with these conditions. First, acute IO does not reflect clinical reality of individuals that suffer from IO–chronic IO treatments and their pathophysiological effects are a more realistic case study. Second, initiation of autophagy is only the first step in a much more elaborate series of events that evolved to resolve stress and promote cell survival. Following autophagy, autophagosomes mature by fusing with lysosomes to degrade cargo and this is then followed by a third stage, whereby autolysosomal membranes are resorbed back into the endomembrane system, including reformation of lysosomes using a process now referred to as ALR. ALR is thus critical for cells to regain their degradative capacity and autophagic proficiency under prolonged stress. We now show for the first time that chronic IO causes autolysosomes to accumulate while depleting cells of free lysosomes, suggesting a defect in ALR.

Importantly, we have determined that IO prevents the reactivation of mTORC1 on autolysosomes, thereby causing a precipitous loss of a distinct lysosomal compartment. Normally, degradation of autophagic cargo locally stimulates mTORC1 on matured autolysosomes, even when the majority of mTORC1 remains inactive and is not bound to lysosomes. This localized reactivation of mTORC1 then promotes lysosomal reformation from the spent autolysosomes [38]. However, since IO prevents mTORC1 activation, lysosome reformation is impaired and lysosome numbers are depleted. Conversely, iron withdrawal restored mTORC1 activity, downstream UVRAG signaling, lysosomal numbers, and insulin signaling. Furthermore, forced activation of mTORC1 by expressing the constitutively active RHEB-GTPase not only prevented autophagosome

accumulation with minimal lysosomal loss, but also restored insulin sensitivity in cells exposed to IO. Together, these data strongly indicate that the block of mTORC1 activation on autolysosomes by IO is a contributor of insulin resistance.

Overall, our study adds important new knowledge on a novel molecular mechanisms contributing to insulin resistance in response to IO and presents the first *in vivo* model to show an ALR defect 27. Mechanistically, we observed that chronic IO led to a decrease in Akt-mediated repression of TSC2, resulting in a potent repression of RHEB and mTORC1, with consequent loss of ALR. Furthermore, our data indicate that mTOR-UVRAG-dependent lysosomal pool regeneration is an important contributor in maintaining autophagic flux and insulin sensitivity in skeletal muscle. Together, our data uncover a previously undocumented mechanism via which chronic IO limits autophagic capacity and leads to metabolic dysfunction. This observation may have implications in a wide range of disease states where cellular IO plays a pathogenic role.

3.6 Materials and Methods

Materials

The cell culture medium [α-minimal essential medium (α-MEM)], fetal bovine serum (FBS), and antibiotics/antimycotic solution were purchased from Wisent (St Bruno, QC, Canada). Cytochalasin B (Sigma) and human insulin (Humulin) were purchased from Eli Lilly (Toronto, ON, Canada), and deoxy-D-[2-3H] glucose was purchased from PerkinElmer (Woodbridge, ON, Canada). Ferrous Sulfate heptahydrates (FeSO4·7H2O, Cat#310077), Torin1 (Cat# 475991) Monoclonal Anti-Vinculin (Cat#V9131), and beta-actin antibody (Cat#A5441 clone AC-15) were purchased from Sigma-Aldrich (Ottawa, ON, Canada). AKT inhibitor MK-2206 was purchased from Selleck Chemicals. S6K (Cat#ab32529), LAMP1 (Cat#ab25630), and Alexa 647-conjugated

antibody (goat anti-rabbit, Cat#ab15007) were purchased from Abcam (Cambridge, MA, USA). LC3B (Cat#2775), GAPDH (Cat#2118), tubulin (Cat#2148) antibodies, and phospho-specific antibodies (phosphorylation sites) for AKT (T308, Cat#4056), phospho-S6K (T389, Cat#9234), phospho-ULK1 (S757, Cat#14202), mTOR (Cat#2983) phospho-mTOR (S2448, Cat#2971), TSC2 (Cat#4308T) phospho-TSC2 (T1462, Cat#3617T) phospho-AKT (Ser473 Cat#4060), total AKT (Cat#4691), horseradish peroxidase-conjugated secondary antibodies (anti-rabbit-IgG, Cat# #7074 and anti-mouse-IgG, Cat#7076) were purchased from Cell Signaling Technology (Beverly, MA, USA). UVRAG phospho-specific (S550, Cat# S307D) and UVRAG antibody (Cat# S323D) were provided from MRC PPU at The University of Dundee. Anti-transferrin receptor (Tfr1) monoclonal antibody (Cat#13-6800 clone H68.4), phospho-specific antibody for anti-IRS-1 (Y612, Cat#44-816G), Alexa 555-conjugated antibody (donkey anti-rat, Cat#A-21434), Lipofectamine 2000 (Cat# 11668019), and ProLong Gold (Cat#P36930) were purchased from Thermo Fisher Scientific (Burlington, ON, Canada). Anti-LC3B (Cat#PM036) and Anti-p62 (Cat# M162-3) were purchased from MBL. Anti-ferritin heavy chain (Cat#NBP1-31944) was purchased from Novus Biologicals. Anti-Myc (Cat# 9E10) was purchased from Alzforum. LAMP1 (Cat#sc-19992, Santa Cruz) antibody and iron-dextran dextran (a ferric hydroxide, $Fe(OH)^3$, complex with low molecular weight dextran, Cat#9004-66-4) were purchased from Santa Cruz Biotechnology Inc. VECTASHIELD Antifade Mounting Medium with DAPI (Cat# H-1200) was purchased from Vector Laboratories. Polyvinylidene difluoride membrane was from Bio-Rad Laboratories, Inc (Burlington, ON, Canada), and chemiluminescence reagent plus was from PerkinElmer (Boston, MA). Concanamycin A was purchased from BioShop Canada Inc. (Cat# FOL202, Burlington, ON, Canada). All other reagents and chemicals used were of the highest purity available.

Cell culture and generation of L6 cell line stably overexpressing gene of interest

L6 skeletal muscle cell line (ATCC® CRL-1458™ tested mycoplasma free) was grown to confluency in α-MEM supplemented with 10% [volume/volume (v/v)] FBS and 1% (v/v) antibiotic/antimycotic solution under a humidified atmosphere of 95% air and 5% CO_2 at 37°C. During treatment or iron withdrawal, the cells were switched to medium containing 0.5% (v/v) FBS and 1% (v/v) antibiotic/antimycotic. During iron treatment, ferrous iron stock, prepared by dissolving ferrous sulfate heptahydrate ($FeSO_4 \cdot 7H_2O$) in sterile distilled water at 10 mM, was dissolved in treatment medium at appropriate concentration. L6-GLUT4 cells stably transfected to overexpress myc-tagged GLUT4 were a gift from Dr Amira Klip, The Hospital for Sick Children, Toronto. IRE-CFP L6 cells stably transfected to overexpress IRE-CFP were a gift from Dr.s' James R Connor and Stephanie Patton, Penn State Hershey Medical Center, USA 62. eGFP-mCherry-LC3B, eGFP-mCherry-p62 stables, and myc-tagged RHEB Q64L mutant L6 cells were infected with lentivirus, and a stable polyclonal population was obtained through puromycin (1 µg/ml) selection for stable integration.

Determination of intracellular iron

Intracellular iron concentration was estimated by ferrozine-based assay as described previously [63]. Phen green SK (PGSK) diacetate dyes [64] were used to determine the degree of di-valent ions. Iron-specific probe-1 (IP-1) [29] was a kind gift from Dr Christopher J. Chang, University of California, Berkeley, and was used to determine labile iron levels in cells.

Gene expression analysis

Quantitative polymerase chain reaction (qPCR) was performed as previously described [19]. Total RNA was extracted with RNEasy Mini Kit (Qiagen, Toronto, Canada) and then converted to cDNA with GoScript Reverse Transcriptase (Promega). PCR cycle was performed with iTaq™ Universal

SYBR® green mixture (Bio-Rad) at following condition: 2 min at 95°C, followed by 40 cycles of 15 s each at 95°C, 60°C, 72°C. Relative gene expression levels were normalized to 18S rRNA. Primers used in this study are summarized in Table 1.

Table 1. Primers used in this study for PCR

Name	Kind	Sequence (5′–3′)
FTH	Forward	CTTTGCAACTTCGTCGCTCC
	Reverse	AGTCATCACGGTCAGGTTTCTTT
FTL	Forward	AGACCCTCACCTCTGTGACT
	Reverse	GGCGGTTACAAAGCTGCCTA
SLC40A1	Forward	CGTGCTATCTCCGGTTCCTC
	Reverse	TGTCAAGAGGAGGCCGTTTC
TFRC	Forward	AGCCAGATCAGCATTCTCTAACT
	Reverse	GCCTTCATGTTATTGTCGGCAT
18S rRNA	Forward	CCATAAACGATGCCGACTG
	Reverse	CGCTCCACCAACTAAGAAC

Western blotting

Lysates were prepared as we described before [66]. SDS–PAGE was performed, and proteins were transferred to PVDF membrane then incubated with blocking buffer (3% BSA or 5% skim milk in TBS-T), washed with TBS-T five times, and incubated with primary antibodies (1:1,000 in TBS-T 2% BSA) overnight at 4°C. Next, membranes were incubated in appropriate horseradish peroxidase-conjugated secondary antibody (1:10,000 in TBS-T 2% BSA or skim milk) for 1 h at room temperature. Quantitation of each specific protein band was determined by densitometric scanning with correction for the respective loading control.

Insulin sensitivity test

Glucose uptake was determined by measuring uptake of 2-deoxy-d-[^{3}H] glucose exactly as described previously [67]. L6-GLUT4 cells were incubated with insulin (10 and 100 nM) for 20 min after treatment with or without iron as described. Phosphorylation of IRS1 (Y612) and AKT (T308) was determined in cells incubated with insulin (10 or 100 nM) for 5 min after appropriate treatment.

Transmission electron microscope (TEM)

TEM was performed as described previously [66]. Briefly, samples were fixed in fixative (2% formaldehyde, 2% glutaaldehyde in 0.1 M sodium cacodylate buffer) for 2 h at room temperature. After washing three times with sodium cacodylate buffer, samples were fixed in 1% osmium tetroxide for 1 h at room temperature. After dehydration with ascending concentration of ethanol in series (50–100%), cells were embedded in Spurr's epoxy resin. Thin sections (60–80 nM) were cut with ultramicrotome and mounted on copper mesh grids. The sections were then contrasted with 1% uranyl acetate and lead citrate and examined with a FEI CM100 TEM and Kodak Megaplus Camera.

***In vitro* autophagy analysis**

Activity of the autophagy pathway was monitored by Western blot and immunofluorescence-based puncta quantification of LC3B. Flux assay was performed by measuring levels of LC3B-I and LC3B-II from cell lysates after appropriate treatment co-treated with lysosomal inhibitor (chloroquine, 30 μM). LC3B immunofluorescence was performed as described previously [32]. Briefly, cells were fixed, permeabilized, and blocked with PBS solution containing 1% BSA and 2% goat serum. After blocking, cells were incubated with blocking solution containing LC3B (Cat#PM036, MBL, conjugated with Cy3 Alexa Fluor 555 1:1,000) and mouse anti-LAMP1

(Cat#A11029, 1:500). Cells were incubated with anti-mouse Alexa Fluor 488 secondary antibody (Cat#ab25630, Thermo Fisher Scientific, 1:200) at room temperature for 1 h. After incubation, cells were mounted with DPAI after washes. Deconvoluted images were captured with an Apotome enabled Zeiss AxioObserver.Z1. For live cell imaging, L6 cells stably expressing eGFP-mCherry-LC3B or eGFP-mCherry-p62 were seeded into ibidi chambers and treated with iron ($FeSO_4$, 250 μM) or starvation medium (without amino acid). Treatments were carried out in FluorBright™ phenol red-free DMEM (Invitrogen) supplemented with GlutaMAX. Images were acquired and deconvolved using an environmental chamber control (DeltaVision Elite-Olympus IX-71 with FemtoJet Microinjector) microscopy.

Lysosome dynamics analysis

L6 cells were co-transfected with LAMP1-RFP and LC3-GFP using Lipofectamine 2000 as per manufacturer's specifications. Following 8 h of transfection, cells were incubated in treatment medium then imaged live. During live cell imaging, cells were maintained in an environment set to 5% CO_2 and 37°C. We used a Quorum Diskovery spinning disk confocal microscope system equipped with a Leica DMi8 microscope and connected to an Andor Zyla Megapixel sCMOS camera. Microscope and acquisition settings were controlled using Quorum Wave FX powered by MetaMorph software (Quorum Technologies, Guelph, ON). For time-lapse imaging and determination of lysosomal dynamics, images were acquired every 3 s for 3 min. For determination of lysosomal numbers, images were acquired along the z-plane at a defined interval of 0.3 μm.

For image analysis, lysosomal numbers were unbiasedly determined using particle detection tools in Volocity 6.3.0 software (PerkinElmer). Lysosomal numbers were determined in at least 15 cells per condition per experiment, where we repeated each experiment at least three independent times.

For lysosomal track analysis, movies were analyzed using particle detection tools in Imaris (Bitplane) image analysis software. Lysosome particles were defined as having a minimum of 0.5 μm in diameter and tracked using the software's autoregressive motion track analysis function. To minimize mis-tracking of particles, tracks were restricted to particles that moved a maximum distance of 1 μm between frames and with no more than a maximum gap distance of three frames. This analysis was completed for at least 6 cells per trial per condition with more than 100 tracks per cell. Track mean speed and displacement, which is defined as the distance between start and endpoints, were calculated.

Cathepsin activity assay

We used Magic Red Cathepsin L Kit (Bio-Rad Technologies, Cat# ICT941) and performed experiments as follows. After 24-h IO treatment, IO and control cells were incubated with 1× magic red cathepsin L reagent, concurrently or in the absence of 1 μM ConA, for 1 h, prior to live cell imaging. Using spinning disk confocal microscopy, confocal slices were acquired with a 0.3-micron interval between slices. For image analysis, the total magic red fluorescence for MR-positive puncta was determined and compared to the control counterpart.

Lysosomal β-glucosidase activity assay

L6 cells were plated on ibidi 8-well m-Slide (Ibidi, Cat# 80826) overnight and treated with iron ($FeSO_4$, 250 μM) for 24 h. Cells were then incubated in AMEM containing the β-glucosidase substrate (5 μM) for 1 h (Marker Gene Technologies, Cat# M2775). Then, cells were washed 3 times with PBS prior to the addition of Opti-Klear™ Live Cell Imaging Buffer. Images were acquired and deconvolved using an environmental chamber control (DeltaVision Elite-Olympus IX-71 with FemtoJet Microinjector) microscopy.

Cyto-ID autophagy detection assay

L6 cells were plated on ibidi 8-well m-Slide (Ibidi, Cat# 80826) overnight and treated with iron ($FeSO_4$, 250 μM). Cells were then incubated in AMEM without phenol red containing Cyto-ID autophagy detection stain (Enzo, ENZ-KIT175-0050) for 30 min with/without iron and then washed with PBS. Images were acquired and deconvolved using an environmental chamber control (DeltaVision Elite-Olympus IX-71 with FemtoJet Microinjector) microscopy.

Iron overload animals, glucose tolerance tests (GTT), and insulin tolerance tests (ITT)

Animal facilities met the guidelines of Canadian Council on Animal Cars, and the York University Animal Care Committee approved the experimental protocols. Animals were fed *ad libitum* on regular chow diet and kept in temperature and humidity control rooms (21 ± 2°C, 35–40%) with a daily 12:12-h light–dark cycle. Groups ($n = 6$) of 2-month-old C57/BL6 male mice were randomized into two groups and injected with iron-dextran intravenously (15 mg/kg, diluted in PBS to make 150 μl injection volume) three times at 2 h of interval or with only PBS as control. After 24 h postfirst injection, GTT and ITT were performed, without blinding, as described previously 68. For phosphorylation of insulin signaling molecule analysis, mice were injected with 4 units of insulin per kg before sacrifice.

Tissue immunofluorescence

Paraffin-embedded sections were deparaffinized and rehydrated with descending concentrations of ethanol and then brought into double distilled water. The antigens were retrieved in citrate buffer pH 6.0 in autoclave for 15 min. After three washes with PBS, sections then were permeabilized with Triton X-100 (0.3% Triton X-100 in PBS) and blocked with 2% BSA and 5% goat serum in PBS for 90 min. Sections were incubated with LAMP1 (Santa Cruz) and LC3B (MBL) at 1:100 in

2% BSA in PBS, followed by Alexa secondary antibody-conjugated fluorophores (Alexa 555 donkey anti-rat and Alexa 647 goat anti-rabbit). Sections were mounted on coverslips with ProLong Gold and VECTASHIELD antifade mounting medium with DAPI, and images were captured with Zeiss LSM 700. The number of LAMP1 puncta was determined by setting pre-set threshold "momentum" in ImageJ and counted the puncta (> 0.6 μm diameter, > 0.35 circularity) per field of views.

Statistical analysis

Data are expressed as mean ± standard error mean (SEM) from at least three separate experiments. The differences between groups were analyzed using Prism 5.0 (GraphPad Software Inc., San Diego, CA, USA) with one-way analysis of variance (ANOVA) followed by Student's *t*-test, with $P < 0.05$ considered as statistically significant. Quantification of endogenous lysosome and autophagosome number was performed using Perkin Elmer Volocity software for unbiased identification and quantification of objects. Vesicle numbers and individual vesicle sizes were identified from a minimum of nine representative cells, with a minimum of 40 vesicles per condition. Samples were compared using Student's *t*-test. Autophagosome mobility was determined by blinded vesicle tracking using a minimum of 11 time points to track an average of 10 autophagosomes per sample. Mean velocity was calculated for each autophagosome, and sample sets across multiple conditions were compared using Student's *t*-test.

Acknowledgements

GS acknowledges support from Canadian Institutes of Health Research (CIHR) and a Career Investigator Award from Heart & Stroke Foundation of Ontario. RCR also acknowledges support from CIHR (#PJT153034). JWSJ is a recipient of CIHR Frederick Banting and Charles Best

Canada Graduate Scholarship. We greatly appreciate Dr.s' James R Connor and Stephanie Patton, Penn State Hershey Medical Center for providing IRE-CFP reporter and Dr Christopher J. Chang, University of California Berkeley for providing IP-1 probe.

3.7 Supplementary Material

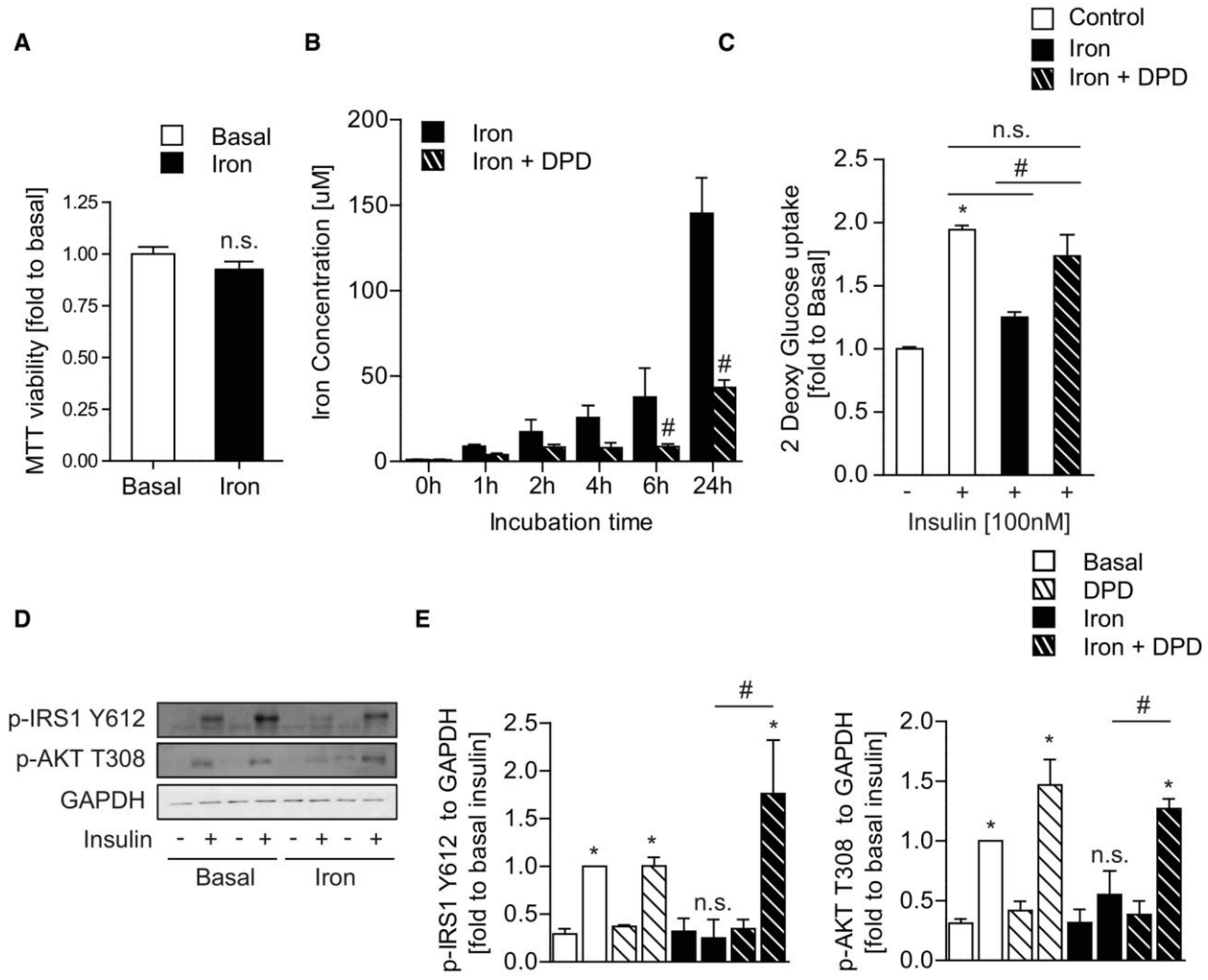

Figure EV1. Prevention of IO-induced insulin resistance in L6 cells with iron chelator A. MTT viability assay in L6 cells after iron treatment ($FeSO_4$, 250 µM) for 24 h. B. Time course measurement of intracellular iron concentration in L6 cells after iron treatment (250 µM) with iron chelator DPD (500 nM) for multiple time points. $^{\#}P < 0.05$ (unpaired Student's *t*-test versus iron at each time points). C. Glucose uptake of L6 cells with insulin stimulation (100 nM, 20 min) after iron treatment (250 µM, 24 h) with DPD (500 nM). $^{*}P < 0.05$, $^{\#}P < 0.05$ (one-way ANOVA test with multiple comparisons). D. Representative Western blot images of phosphor-IRS1 Y612, phosphor-AKT T308, and GAPDH expression. E. Quantification of phosphor-IRS1 Y612 over GAPDH and phosphor-AKT T308 over GAPDH in L6 cells with insulin stimulation (100 nM, 5 min) after iron treatment (250 µM, 24 h) with DPD (500 nM). $^{*}P < 0.05$ (unpaired Student's *t*-test versus basal without insulin), $^{\#}P < 0.05$ (unpaired Student's *t*-test versus iron with insulin).

Data information: All experiments were performed three times. Results are represented as mean ± SEM.

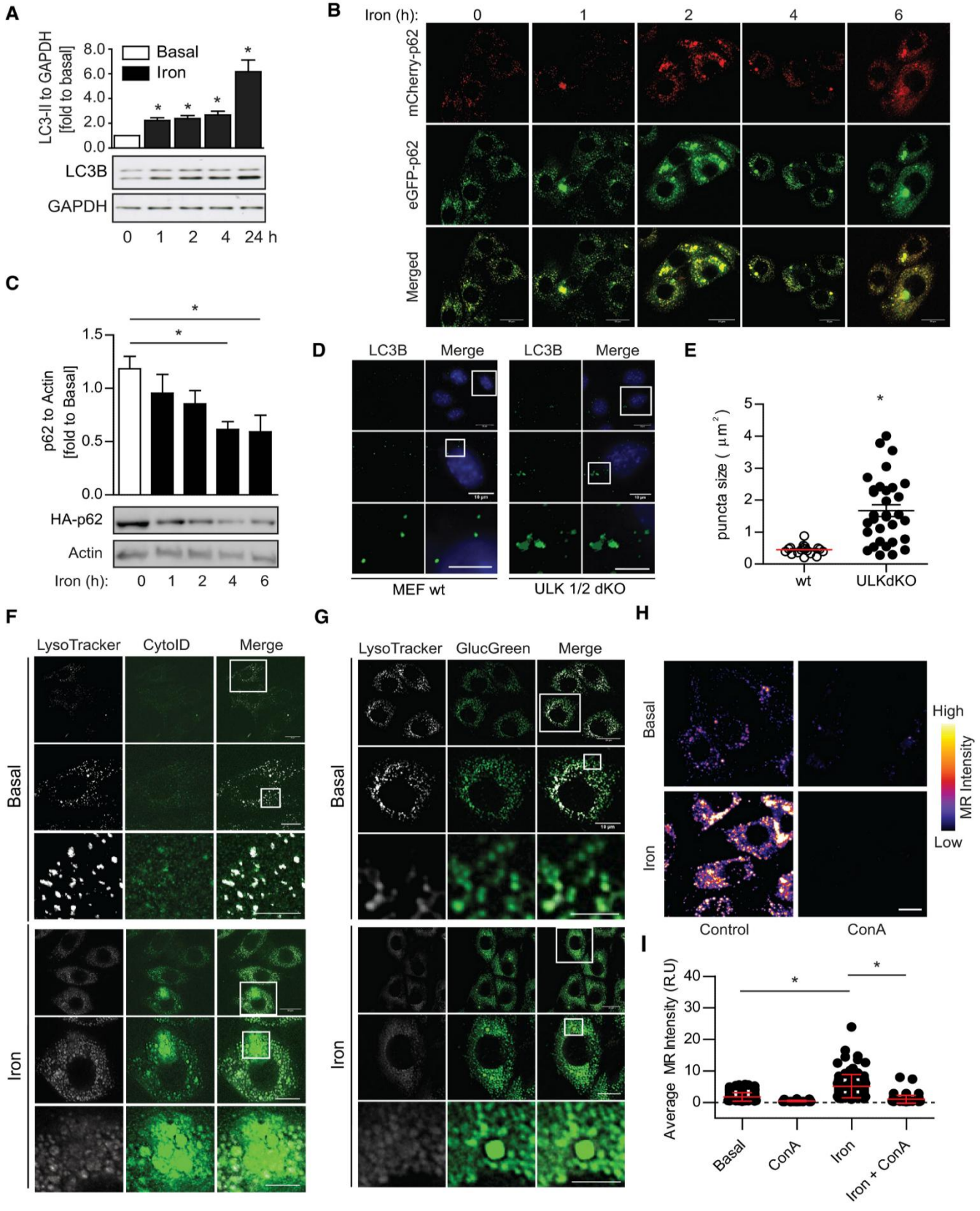
A
LC3-II to GAPDH [fold to basal]
Basal
Iron
LC3B
GAPDH
0 1 2 4 24 h
B
Iron (h): 0 1 2 4 6
mCherry-p62
eGFP-p62
Merged
C
p62 to Actin [fold to Basal]
HA-p62
Actin
Iron (h): 0 1 2 4 6
D
LC3B Merge LC3B Merge
MEF wt
ULK 1/2 dKO
E
puncta size (µm²)
wt
ULKdKO
F
LysoTracker CytoID Merge
Basal
Iron
G
LysoTracker GlucGreen Merge
Basal
Iron
H
Basal
Iron
High
MR Intensity
Low
Control
ConA
I
Average MR Intensity (R.U)
Basal
ConA
Iron
Iron + ConA

Figure EV2. Chronic IO resulted in accumulation of abnormal autophagosomes despite normal proteolytic activity

A. Representative Western blot images and quantification of LC3B-II to GAPDH in L6 cells after iron treatment ($FeSO_4$, 250 μM) for multiple time points. Experiments were performed three times. *$P < 0.05$ (multiple unpaired Student's *t*-test compared to basal). B. Representative epi-fluorescent images of p62 puncta in L6 cells stably expressing mCherry-eGFP p62, after iron treatment (250 μM) at time points indicated. C. Representative Western blot images and quantification of L6 transfected with HA-p62 after iron treatment (250 μM) at time points indicated. Experiments were performed three times. *$P < 0.05$ (multiple unpaired Student's *t*-test compared to 0 h of iron). D. Representative epi-fluorescent images of MEF cells (wild type, and ULK1 and ULK2 dKO) immuno-stained against LC3B. E. Quantification of LC3B puncta size from (D). Experiments were performed three times, and one representative experiment is presented here. *$P < 0.05$ (unpaired Student's *t*-test compared to wt). F. Representative epi-fluorescent images of autophagosomes (Cyto-ID) and lysosome (LysoTracker) in L6 cells after iron (FeSO4, 250 μM) for 24 h. G. Representative epi-fluorescent images of beta-glucosidase (GlucGreen) and lysosome (LysoTracker) in L6 cells after iron (FeSO4, 250 μM) for 24 h. H. Representative confocal microscope images of L6 cells pulsed with Magic Red L after iron treatment (250 μM, 24 h) with 1 μM concanamycin A. I. Quantification mean fluorescence intensity from magic red signals in 3D puncta in (H). Experiments were performed three times, and all biological and technical replicates are plotted here. *$P < 0.05$ (one-way ANOVA with multiple comparisons).

Data information: Data are expressed as means ± SD. Scale bar (B, H) = 20 μm. Scale bar (D, F, G) = 20, 10, and 5 μm.

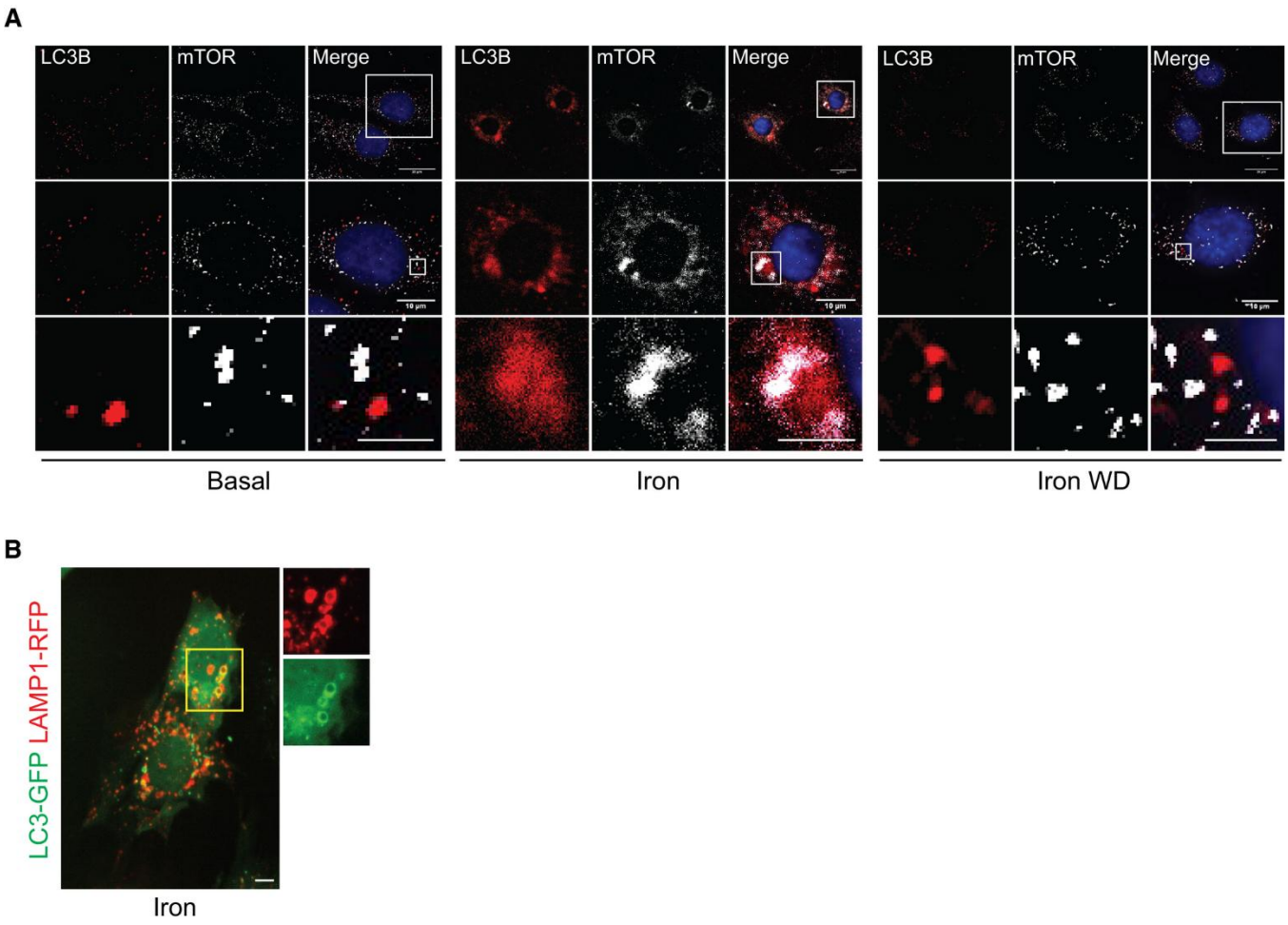

Figure EV4. Molecular mechanisms underlying iron-mediated mTOR suppression and restoration of lysosomal pools after iron withdrawal

A. Representative epi-fluorescent microscope images of L6 cells immuno-stained against LC3B and mTOR after iron treatment (250 μM, 24 h) followed by withdrawal for 4 h. B. Representative confocal images of L6 cells transfected with LC3-GFP and LAMP1-RFP after 24-h iron treatment (250 μM).

Data information: Scale bar (confocal microscope) = 10 μm and scale bar (epi-immunofluorescent microscope) = 20, 10, and 5 μm.

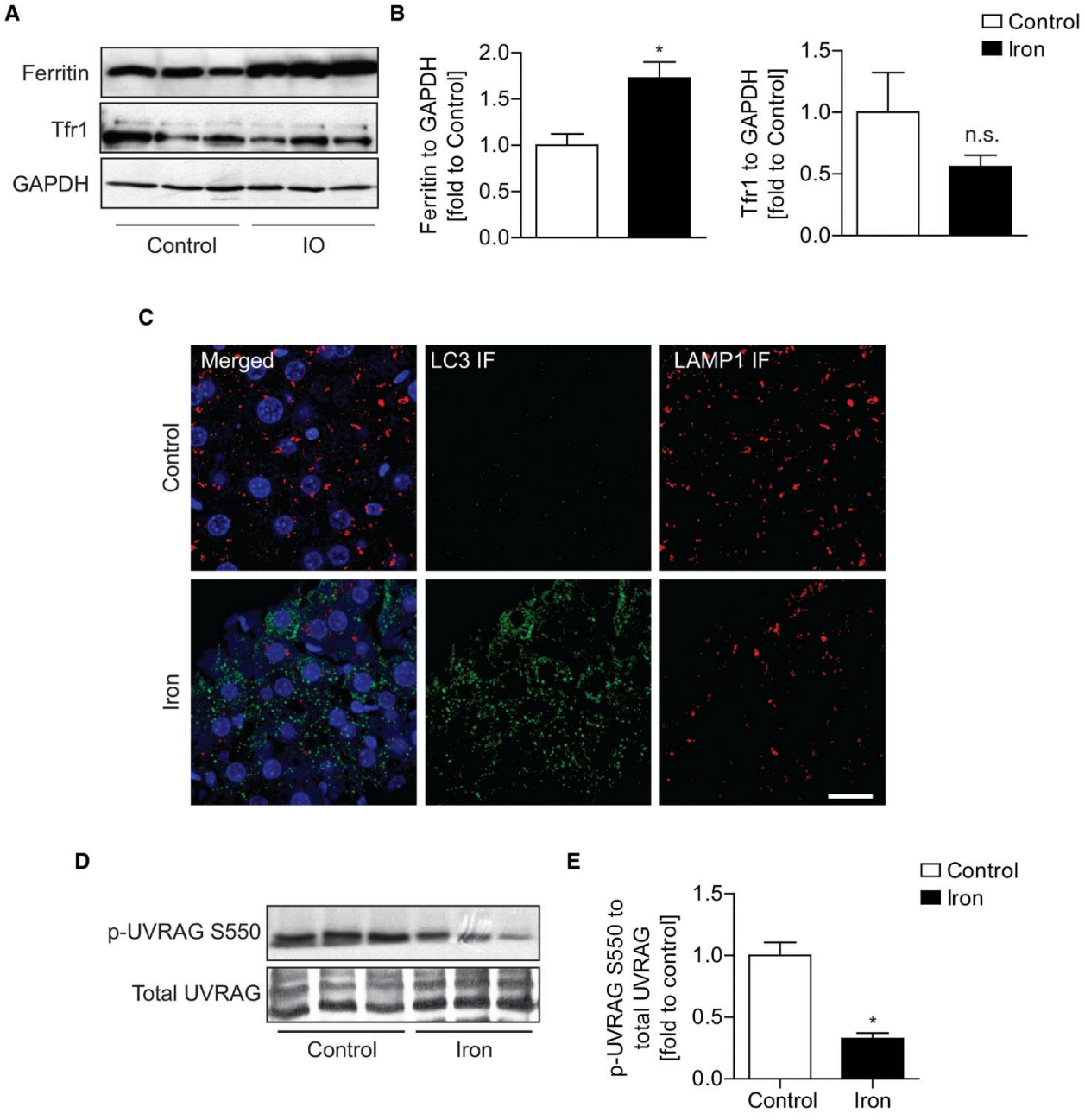

Figure EV5. ALR defects in liver after iron overload

A, B. Representative Western blot and quantification of ferritin and Tfr1 to GAPDH in liver 24 h after iron injections. $P < 0.05$ (unpaired Student's *t*-tests versus control). C. Confocal microscope images of liver tissue sections immuno-stained with against LC3B (Alex 647) and LAMP1 (Alexa 555). D, E. Representative Western blot images and quantification of phospho-UVRAG S550 to total UVRAG in liver 24 h after iron injections.

Data information: $n = 3$ males. Scale bar = 20 µm.

Movie EV1. Real time analysis of autophagosomes using LC3B-mCherry

Representative video of autophagosomes in L6 cells expressing mCherry-LC3B in Basal (Left) after amino acid-free media (Middle) or after iron treatment (250 μM, 24 h, Right). Treatments were carried out in phenol red-free DMEM buffered with GlutaMAX. Images were acquired every 15 sec for 15 min.

Movie EV2. Real time analysis of lysosomes using RFP-LAMP1

Representative videos of lysosomes in L6 cells expressing LAMP1-RFP after iron treatment (FeSO4, 250 μM) and withdrawal with or without Torin1 (200 nM). First Panel – Basal, Second Panel – Iron, Third Panel – Iron WD 4hr, Fourth Panel – Iron WD + Torin1 4hr. Images were acquired every 3 sec for 30 sec, movie showing 2 frames per second.

Find the video through this link https://doi.org/10.15252/embr.201947911

Chapter 4: The ER-phagy receptor FAM134B is targeted by *Salmonella* Typhimurium to promote infection

Damián Gatica[*], Reham M. Alsaadi[*], Rayan El Hamra, Boran Li, Rudolf Mueller, Makoto Miyazaki, Qiming Sun, Subash Sad & Ryan C. Russell

Co-First authors * These two authors contributed equally to this work

4.1 Author Contributions

D.G. and R.M.A. designed *in vitro* experiments. D.G. and R.M.A. performed *in vitro* experiments. D.G., R.M.A., R.EH., S.S. and R.R. designed mice experiments. D.G., R.M.A. and R.EH. performed mice experiments. R.M scored H&E samples. D.G., R.M.A. and R.R. wrote the manuscript. M.M provided *FAM134B* KO mice. B.L and Q.S performed Fam134B phosphorylation and acetylation experiments. All authors discussed the results and commented on the manuscript

The ER-phagy receptor FAM134B is targeted by *Salmonella* Typhimurium to promote infection

Damián Gatica[1*], Reham M. Alsaadi[1*], Rayan El Hamra[2], Boran Li[3], Rudolf Mueller[4], Makoto Miyazaki[5], Qiming Sun[3,6], Subash Sad[2] & Ryan C. Russell[1,7,8]

Affiliations

[1]Department of Cellular and Molecular Medicine, University of Ottawa, Ottawa, ON, Canada.

[2]Department of Biochemistry, Microbiology and Immunology, University of Ottawa, Ottawa, ON, Canada.

[3]International Institutes of Medicine, The Fourth Affiliated Hospital of Zhejiang University School of Medicine, Yiwu, Zhejiang, China.

[4]Department of Pathology and Laboratory Medicine, Faculty of Medicine, University of Ottawa, Ottawa, ON, Canada.

[5]Division of Renal Diseases and Hypertension, Department of Medicine, University of Colorado Denver, Aurora, CO, USA.

[6]Department of Biochemistry and Department of Cardiology of Second Affiliated Hospital Zhejiang University School of Medicine, Hangzhou, Zhejiang, China.

[7]Ottawa Institute of Systems Biology, University of Ottawa, Canada.

[8]University of Ottawa Centre for Infection, Immunity and Inflammation, Ottawa, ON, Canada.

*These authors contributed equally

Correspondence: ryan.russell@uottawa.ca

4.2 ABSTRACT

Macroautophagy/autophagy is a key catabolic-recycling pathway that can selectively target damaged organelles or invading pathogens for degradation. The selective autophagic degradation of the endoplasmic reticulum (hereafter referred to as ER-phagy) is a homeostatic mechanism, controlling ER size, the removal of misfolded protein aggregates, and organelle damage. ER-phagy can also be stimulated by pathogen infection. However, the link between ER-phagy and bacterial infection remains poorly understood, as are the mechanisms evolved by pathogens to escape the effects of ER-phagy. Here, we show that *Salmonella enterica* serovar Typhimurium inhibits ER-phagy by targeting the ER-phagy receptor FAM134B, leading to a pronounced increase in *Salmonella* burden after invasion. *Salmonella* prevents FAM134B oligomerization, which is required for efficient ER-phagy. FAM134B knock-out raises intracellular *Salmonella* number, while FAM134B activation reduces *Salmonella* burden. Additionally, we found that *Salmonella* targets FAM134B through the bacterial effector SopF to enhance intracellular survival through ER-phagy inhibition. Furthermore, FAM134B knock-out mice infected with *Salmonella* presented severe intestinal damage and increased bacterial burden. These results provide mechanistic insight into the interplay between ER-phagy and bacterial infection, highlighting a key role for FAM134B in innate immunity.

4.3 INTRODUCTION

Macroautophagy (hereafter autophagy) is an intracellular catabolic-recycling pathway that promotes survival in response to a diverse range of stress conditions including nutrient starvation or invasive pathogens[111]. Autophagic cargo can include proteins, lipids, damaged organelles, or even intracellular pathogens. These cytoplasmic components are sequestered inside double-membrane vesicles called autophagosomes. Fully formed autophagosomes then fuse with lysosomes leading to the degradation of the sequestered cargo by resident hydrolytic enzymes. The basic macromolecules obtained from cargo degradation are subsequently transported back to the cytoplasm for reutilization. Autophagy levels are regulated by several Atg (autophagy-related) proteins, involved in all steps of the autophagic process from initiation to lysosomal fusion[112]. Autophagosome cargo selection is often tightly regulated, specifically targeting damaged cellular components or invasive intracellular pathogens for degradation[113]. Selective autophagy is achieved by autophagy receptors that link the cargo targeted for degradation with the growing autophagosomal membrane. Autophagy receptors usually contain LC3-interacting regions (LIR), an evolutionary conserved sequence that binds to members of the Atg8/LC3/GABARAP family[114]. During autophagy initiation LC3 is lipidated and covalently bound to the growing autophagosomal membrane. Thus, by interacting with LC3, autophagy receptors selectively tether cargo to the sequestering autophagosome (Fig. 1A) [113,114]. The selective autophagic degradation of the endoplasmic reticulum (ER), termed ER-phagy, has been shown to be necessary to mitigate ER stress and maintain ER homeostasis. ER-phagy controls ER size and morphology, as well as inducing the degradation of misfolded protein aggregates that can be toxic for the cell[113,115]. Several ER-phagy cargo receptors have been described, including FAM134B[116] and TEX264[117,118], among others[115]. Recent reports have begun to

describe the different molecular mechanisms by which ER-phagy receptors are regulated in the promotion of ER-phagy[119–121]. The first ER-phagy receptor identified, FAM134B, is an ER transmembrane protein containing a reticulon-homology domain that allows it to sense and induce ER membrane curvature and budding through protein clustering[122,123]. FAM134B activity requires its oligomerization, which is highly regulated by post-translational modifications, including phosphorylation and acetylation, and is a requisite step in FAM134B-driven ER-phagy[119,120,124]. Interestingly, FAM134B has also been implicated in the cellular response against viral infection. FAM134B-dependent ER-phagy has been shown to limit SARS-COV-2, Ebola, Zika and dengue virus replication[125–128]. Moreover, multiple pathogens have developed strategies to inhibit ER-phagy by specifically hijacking or cleaving FAM134B[126,127,129]. Targeting FAM134B leads to ER remodeling, which is thought to benefit invading viruses, creating a favorable environment for replication[127,129]. However, the links between ER-phagy and bacterial infection; as well as the mechanisms pathogens have evolved to evade the effects of ER-phagy remain poorly understood. In this study, we identified a novel mechanism of bacterial-mediated inhibition of ER-phagy. Specifically, we found that *Salmonella enterica* serovar Typhimurium (*Salmonella*), inhibits ER-phagy by specifically targeting the activity of the ER-phagy receptor FAM134B, leading to a pronounced increase in *Salmonella* burden after invasion. *Salmonella* was chosen due to its well characterized intracellular growth cycle, membrane remodeling ability, capacity to avoid lysosomal/autophagic clearance, as well as continuing to be a major cause of foodborne infections worldwide[130,131]. We show that *Salmonella* infection prevents FAM134B oligomerization, which is required for efficient ER-phagy. Conversely, *Salmonella*-mediated ER-phagy blockage could be bypassed by promoting FAM134B oligomerization, which recovered ER-phagy levels. We provide evidence that *Salmonella* targets FAM134B

through the bacterial effector SopF, preventing oligomerization and ER-phagy activation. Furthermore*, in vivo* analysis of *FAM134B* knock-out (KO) mice infected with *Salmonella* revealed intestinal damage and increased bacterial levels in the spleen, intestine and feces. Our results provide new mechanistic insight into the interplay between ER-phagy and bacterial infection, highlighting a key role for FAM134B in innate immunity.

4.4 RESULTS

Salmonella Typhimurium infection blocks ER-phagy

To investigate the possible impact of *Salmonella* infection on ER-phagy, we generated a HEK293A cell line stably expressing a previously published doxycycline-inducible ER-phagy reporter containing an ER signal sequence, followed by the fluorescent proteins RFP and GFP, and the ER retention sequence KDEL (ss-RFP-GFP-KDEL)[117]. Upon doxycycline treatment and ER-phagy induction, the fluorescent ER-associated reporter is sequestered inside autophagosomes and cleaved upon lysosome fusion. Unlike GFP, RFP is relatively resistant to lysosomal pH and hydrolases[132]. As such, a ~25-KDa fragment corresponding to RFP can be detected by western blot upon activation of ER-phagy. Similarly, the same reporter can be used to measure ER-phagy by fluorescent microscopy due to the quenching of GFP fluorescence at lysosomal acidic pH (Fig. 1A). As a result, ER-phagy also can be monitored as an increase in RFP positive structures (lysosome associated ER-phagy probe) compared to the dual positive probe signal. We tested the reporter by activating ER-phagy through amino acid starvation[117] or Torin-1 (a potent autophagy inducer) treatment. As a negative control, we confirmed that ss-RFP-GFP-KDEL did not get cleaved in autophagy-deficient *FIP200* KO cells (Supp Fig. 1A).

Amino acid starvation for 6 hr is sufficient to induce ER-phagy. To determine if *Salmonella* infection impacted ER-phagy, we added *Salmonella* to the amino acid starvation media for the final 1 or 3 hrs of starvation. Infection with *Salmonella* for either 1 or 3 hr significantly reduced the production of the free RFP fragment when compared to 6 hr of amino acid starvation in the absence of *Salmonella* (Fig. 1B and 1C), indicating inhibition of ER-phagy upon infection. RFP processing was inhibited by *Salmonella* when normalized to either actin (Fig. 1C) or total ss-RFP-GFP-KDEL reporter (Supp Fig. 1B). We expanded our analysis of ER-phagy regulation by *Salmonella* in the HCT116 cell background, which were engineered to stably express ss-RFP-GFP-KDEL and observed a similar repression of ER-phagy (Supp Fig. 1C and Supp Fig. 1D). Moreover, both HEK293A and HCT116 cells expressing a HaloTag-based pulse-chase reporter for ER-phagy measurement[133], showed decreased ER-phagy levels upon *Salmonella* infection, further corroborating a role for *Salmonella* in repressing ER-phagy (Supp Fig. 1E and Supp Fig. 1F). Interestingly, *Salmonella* infection failed to block non-selective autophagy as shown by the degradation of p62/SQSTM1, a cargo receptor regularly used as an index for general autophagic degradation and LC3B-II production, the faster electrophoretic form of LC3B that is produce during autophagy initiation by LC3B lipidation[134,135] (Supp Fig. 1G and Supp Fig. 1H). Similarly, the general autophagy reporter mCherry-eGFP-LC3B[134], showed no significant differences (RFP puncta formation) between infected and non-infected cells during starvation (Supp Fig. 1I and Supp Fig. 1J). Furthermore, the commercial autophagy detection kit, CYTO-ID, confirmed that non-selective autophagy was not inhibited by *Salmonella* infection during starvation, suggesting *Salmonella* specifically targets ER-phagy (Supp Fig. 1K). Importantly, Bafilomycin A1 (BafA1) treatment, a potent inhibitor of autophagosome maturation and cargo degradation, completely blocked free RFP production when cells were starved in the presence of *Salmonella*, indicating

that *Salmonella* did not increase the turnover rate of autolysosomes (Supp Fig. 1L). The ss-RFP-GFP-KDEL probe can be used to visualize ER-phagy by fluorescence microscopy, where ER-phagy induction is observable through detection of RFP puncta formation. Infection with *Salmonella* resulted in a significant decrease in ER-phagy induction compared to cells that were not infected (Fig. 1D and 1E), which was consistent with our western blot analysis. Similar results were observed when we repeated the experiment using the ss-RFP-GFP-KDEL probe in HCT116 cells (Supp Fig. 1M and Supp Fig. 1N), and the HaloTag-based ER-phagy reporter in HEK293A and HCT116 (Supp Fig. 1O and Supp Fig. 1P). We next measured the protein levels of endogenous ER-phagy cargo receptors known to be involved in starvation-induced ER-phagy, namely *TEX264* and *FAM134B*. Because these receptors link the ER to the autophagosome membrane they are ultimately degraded making their protein levels inversely correlated with ER-phagy levels[116,117]. We measured the endogenous level of each receptor during ER-phagy inducing conditions in the absence and presence of *Salmonella* and found both TEX264 and FAM134B levels to be significantly higher upon infection, indicating that their degradation is blocked upon *Salmonella* infection (Fig. 1F and 1G). Conversely, non-selective p62/SQSTM1 autophagic degradation was similar between infected and non-infected samples. Similar results were observed when these experiments were repeated in HeLa cells (Supp Fig. 1Q). Additionally, *Salmonella* infection was also able to prevent the degradation of the ER-phagy receptors: FAM134A, FAM134C and RTN3L, further demonstrating the ability of *Salmonella* to block ER-phagy (Supp Fig. 1R and Fig. 1S). Collectively, these findings indicate that *Salmonella* infection specifically inhibits ER-phagy, but not non-selective autophagy.

Fig.1 *Salmonella* infection blocks ER-phagy

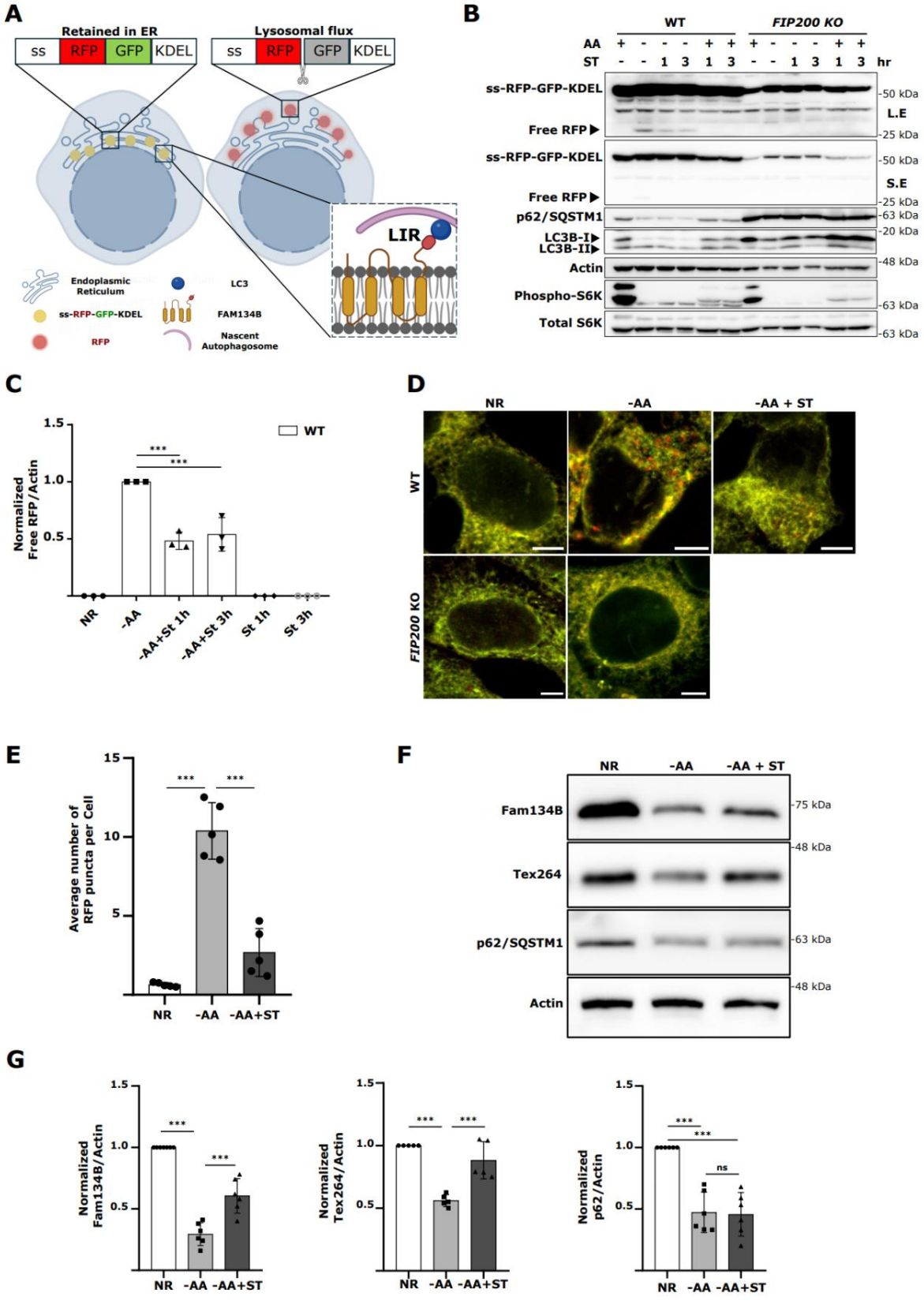

Fig. 1. *Salmonella* infection blocks ER-phagy.

A) Schematic for ER-phagy and the ss-RFP-GFP-KDEL probe. During ER-phagy, ER-bound FAM134B binds to LC3 family proteins through a LIR and is sequestered into nascent autophagosomes. ss-RFP-GFP-KDEL is processed by lysosomal hydrolases to generate a free RFP fragment. Lysosomal acidity quenches the GFP signal. LIR, LC3-interacting region; ss, signal sequence (Created with BioRender.com). **B)** WT and *FIP200* KO HEK293A cells stably expressing the ss-RFP-GFP-KDEL reporter were starved for AA for 6h; starved for 6h followed by ST infection for the final 1 or 3h in AA starvation media; or infected in nutrient rich media with ST for 1 or 3h. ER-phagy was measured by ss-RFP-GFP-KDEL processing. Non-selective autophagy activity was measured by LC3B lipidation and p62/SQSTM1 degradation. Phospho- and total S6K levels were determined to ascertain AA starvation. Actin was used as a loading control. AA, amino acids; ST, *Salmonella* Typhimurium; S.E, Short Exposure; L.E, Long Exposure. **C)** Normalized Free RFP-Actin ratio from WT cells in A). Error bars indicate the standard deviation of 3 independent experiments. ANOVA, ***P <0.001. NR, Nutrient Rich. **D)** Cells from B) were either AA starved for 6h or starved for 3h followed by ST infection for 3h in AA starvation media, fixed and imaged by confocal microscopy. Representative images are shown. ss-RFP-GFP-KDEL, yellow; Free RFP, red. Scale bar 5μm. **E)** Average number of RFP puncta per cell from D) were quantified. Error bars indicate the standard deviation of 5 independent experiments. The average number of RFP puncta was calculated from a minimum of 100 cells. ANOVA, ***P <0.001. **F)** HEK293A WT cells were AA starved for 2h or starved for 2h in the presence of ST. Fam134B, Tex264, p62/SQSTM1 and Actin levels were determined by western blot. **G)** Normalized Fam134B-Actin, Tex264-Actin and p62/SQSTM1 ratios from F) were quantified. Error bars indicate the standard deviation of at least 5 independent experiments. ANOVA, ***P <0.001, ns, no significance.

FAM134B is targeted by *Salmonella* to block ER-phagy

The ER-phagy receptor proteins FAM134B and TEX264 have been previously reported to be targeted by invasive pathogens to disrupt ER morphology and promote infection[129]. To investigate this possibility, we generated CRISPR KO cell lines of *FAM134B* and *TEX264* (Supp Fig. 2A). As expected, deletion of *FAM134B* and *TEX264* severely decreased ER-phagy (Fig 2A), which is in line with prior reports[117]. Consistent with our previous findings, WT cells infected with *Salmonella* showed a significant decrease in the levels of free RFP compared to uninfected cells during ER-phagy inducing conditions. However, *Salmonella* infection failed to show a significant difference in ER-phagy levels between infected and uninfected *FAM134B* KO cells. In contrast, *Salmonella* was still capable of repressing ER-phagy in *TEX264* KO cells (Fig. 2A and 2B). Immunofluorescence microscopy using the same experimental setup showed a dramatic decrease in RFP puncta formation when ER-phagy was induced in *Salmonella*-infected WT and *TEX264* KO cells. However, RFP puncta formation in *FAM134B* KO cells infected with *Salmonella* during ER-phagy induction failed to decrease to the same extent, displaying significant differences (Fig. 2C and 2D). To further analyze the requirement of FAM134B for Salmonella-mediated ER-phagy repression we created stable cell lines expressing an ER-phagy HALO reporter in WT and FAM134B KO cells. Using this reporter, we confirmed the inability of *Salmonella* to inhibit ER-phagy in the FAM134B KO background (Supp. Fig. 2B), consistent with the proteolytic cleavage of our GFP-RFP-KDEL reporter (Fig. 2A). These results suggest that *Salmonella* infection primarily targets FAM134B to inhibit ER-phagy.

Next, we sought to determine if *Salmonella*-mediated ER-phagy inhibition impacted intracellular bacterial viability. To this end, we performed a colony-forming unit (CFU) assay in WT, *FAM134B* KO, *TEX264* KO and *FAM134B* KO cells transfected with FAM134B WT. Analysis of *Salmonella*

viability at 4 hours post-infection revealed that *FAM134B* KO cells had significantly higher number of viable internalized bacteria, suggesting either a defect in the clearance of *Salmonella* or increased growth when compared to WT and *TEX264* KO cells. Furthermore, *FAM134B* KO cells reconstituted with *FAM134B* recovered similar levels of *Salmonella* viability as parental cells (Fig. 2E), indicating FAM134B, but not TEX264, is important for *Salmonella* growth and survival.

ER-phagy receptors couple the ER to the autophagosomal membrane through LIRs (Fig. 1A). We next sought to determine if the impact of FAM134B on *Salmonella* growth was due to ER-phagy induction or another uncharacterized autophagy-independent function. To this end, we transfected *FAM134B* KO cells with either FAM134B WT or FAM134B LIR mutant and performed the ER-phagy reporter RFP processing assay. Intriguingly, we observed no significant difference between infected and uninfected ER-phagy induced cells when the FAM134B LIR mutant was expressed. Conversely, cells expressing FAM134B WT showed a significant decreased in RFP production when infected with *Salmonella* (Fig. 2F and 2H). Consistent with our western blot analysis, we also observed that the decrease in the number of RFP puncta in the FAM134B LIR mutant cells triggered by *Salmonella* infection was not as pronounced as the one in infected cells expressing FAM134B WT (Fig. 2G and 2H). When we quantified *Salmonella* viability by CFU in HCT116 cells, results showed that the expression of the FAM134B LIR mutation resulted in a significant increase in the number of *Salmonella* compared to cells expressing FAM134B WT (Supp Fig. 2C). Together, these findings suggest that FAM134B plays a crucial role in limiting *Salmonella* burden and that this role is connected to FAM134B ability to induce ER-phagy.

Fig.2 FAM134B is targeted by *Salmonella* to block ER-phagy

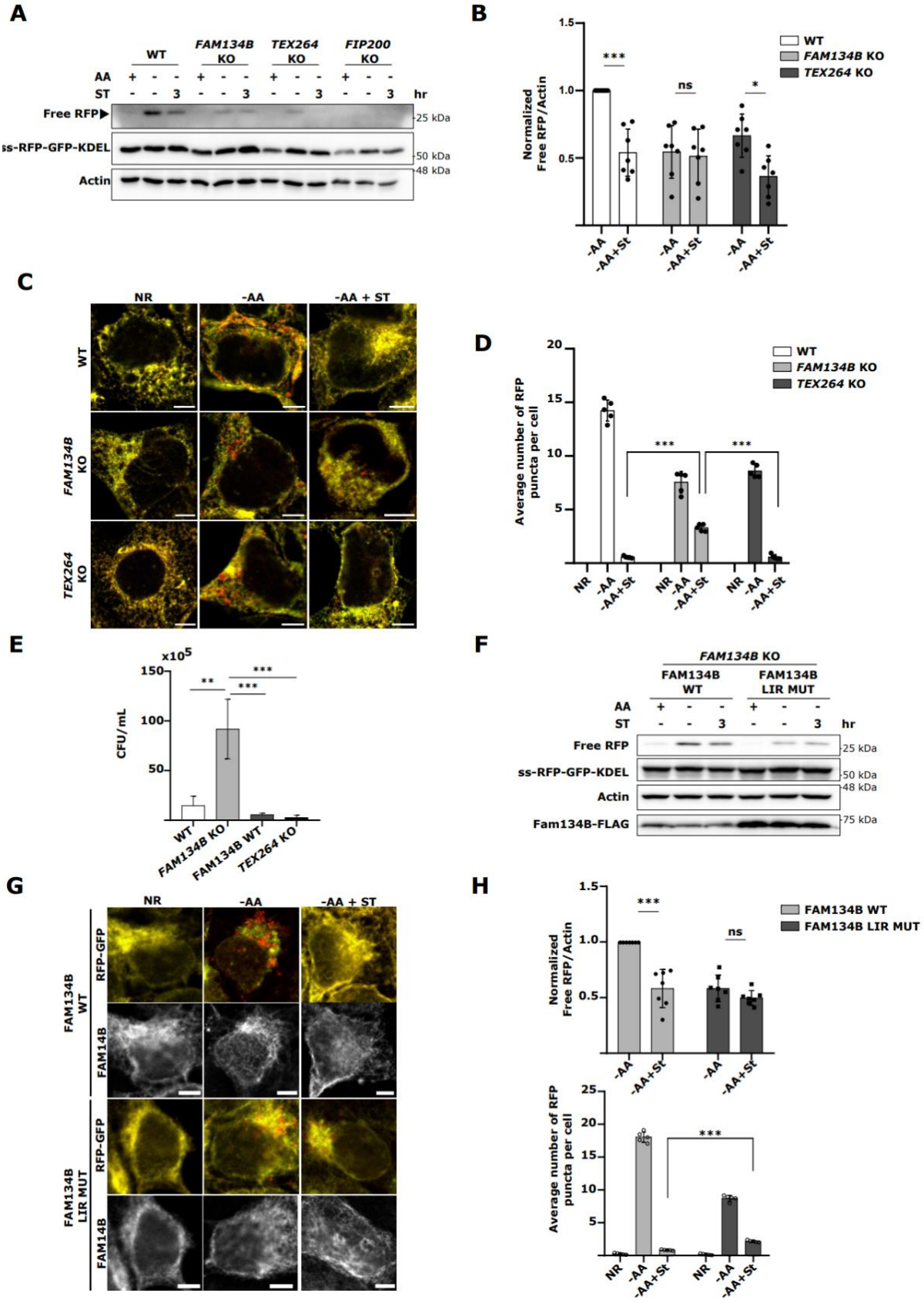

Fig. 2. FAM134B is targeted by Salmonella to block ER-phagy.

A) WT, *FAM134B* KO, *TEX264* KO and *FIP200* KO HEK293A cells stably expressing the ss-RFP-GFP-KDEL were either kept in nutrient rich media, starved for AA for 6h or starved for 3h followed by ST infection for 3h in AA starvation media. ER-phagy was measured by ss-RFP-GFP-KDEL processing. Actin was used as a loading control. AA, amino acids; ST, *Salmonella* Typhimurium. **B)** Normalized Free RFP-Actin ratio from cells in A). Error bars indicate the standard deviation of 7 independent experiments. ANOVA, *P <0.05; ***P <0.001; ns, no significance. **C)** Cells from A) were either AA starved for 6h, or AA starved for 3h, followed by ST infection for 3h in AA starvation media, fixed and imaged by confocal microscopy. NR, Nutrient Rich. Representative images are shown. ss-RFP-GFP-KDEL, yellow; Free RFP, red. Scale bar 5μm. **D)** Average number of RFP puncta per cell from C) were quantified. Error bars indicate the standard deviation of 5 independent experiments. The averages were calculated from a minimum of 100 cells. ANOVA, ***P <0.001. **E)** WT, *FAM134B* KO, *TEX264* KO and *FAM134B* KO cells transfected with WT FAM134B were infected with ST. Bacterial content was determined through a colony-forming unit (CFU). Error bars indicate standard deviation. ANOVA, **P <0.01; ***P <0.001. **F)** *FAM134B* KO cells transfected with either FAM134B WT or FAM134B LIR mutant were kept in nutrient rich media, starved for AA for 6h or starved for 3h followed by ST infection for 3h in AA starvation media. ER-phagy was measured by ss-RFP-GFP-KDEL processing. Actin was used as a loading control. **G)** Cells from F) were fixed and imaged by confocal microscopy. Representative images are shown. ss-RFP-GFP-KDEL, yellow; Free RFP, red; Fam134B, far red. Scale bar 5μm. **H)** Normalized Free RFP-Actin ratio from cells in F) and average number of RFP puncta per cell from G) were quantified. Error bars indicate the standard deviation of at least 5 independent experiments. The average number of RFP puncta was calculated from a minimum of 100 cells. ANOVA, ***P <0.001; ns, no significance.

FAM134B oligomerization is hindered by *Salmonella* infection

FAM134B promotes ER membrane scission and ER-phagy through its ability to oligomerize[119]. Therefore, we hypothesized that *Salmonella* infection might prevent ER-phagy by repressing FAM134B oligomerization. To test this hypothesis, FAM134B-FLAG was immunoprecipitated (IP) after 3 hr of ER-phagy induction in the presence and absence of *Salmonella* infection. Consistent with previous reports, FAM134B oligomers were relatively resistant to denatured conditions and are observed by western blot in a distinct, slow migrating band[119,124]. Notably, *Salmonella* infection significantly reduced the formation of FAM134B oligomers (Fig. 3A). Similar results were observed when we repeated the experiment in HCT116 cells (Supp Fig. 3A). Furthermore, amino acid starvation-induced FAM134B puncta formation was dramatically reduced by *Salmonella* infection, revealing *Salmonella* blocks ER membrane scission, which is driven by FAM134B oligomerization (Fig. 3B). These results indicate *Salmonella* may block ER-phagy by preventing the oligomerization of FAM134B. If *Salmonella* represses FAM134B by preventing oligomerization, then forcing FAM134B oligomerization would be predicted to bypass *Salmonella*-mediated ER-phagy reduction. To this end, we generated a FAM134B G216R mutant, a naturally occurring mutation that resides in FAM134B reticulon-homology domain and has been described to dramatically enhance FAM134B oligomerization[119,136]. We transfected either FAM134B WT or FAM134B G216R in *FAM134B* KO cells and measured ER-phagy through the RFP processing assay. As expected, cells transfected with FAM134B WT exhibited reduced ER-phagy under stimulated conditions when infected with *Salmonella* (Fig. 3C and 3D). However, cells transfected with FAM134B G216R showed no significant difference in ER-phagy rates in the presence or absence of *Salmonella*, indicating that *Salmonella* inhibits ER-phagy upstream, or at the level, of FAM134B activation. Analysis of ER-phagy by immunofluorescence under the same

conditions, showed that FAM134B G216R largely prevented ER-phagy repression by *Salmonella,* compared to FAM134B WT (Fig. 3E and 3F). Additionally, *Salmonella* infection failed to decrease FAM134B G216R oligomerization (Supp Fig. 3B), showing a dramatic increase in self-interaction and oligomerization as previously reported[119]. Together, these experiments support a model in which *Salmonella* regulates ER-phagy through repression of FAM134B activity.

Fig.3 FAM134B oligomerization is hindered by *Salmonella* infection

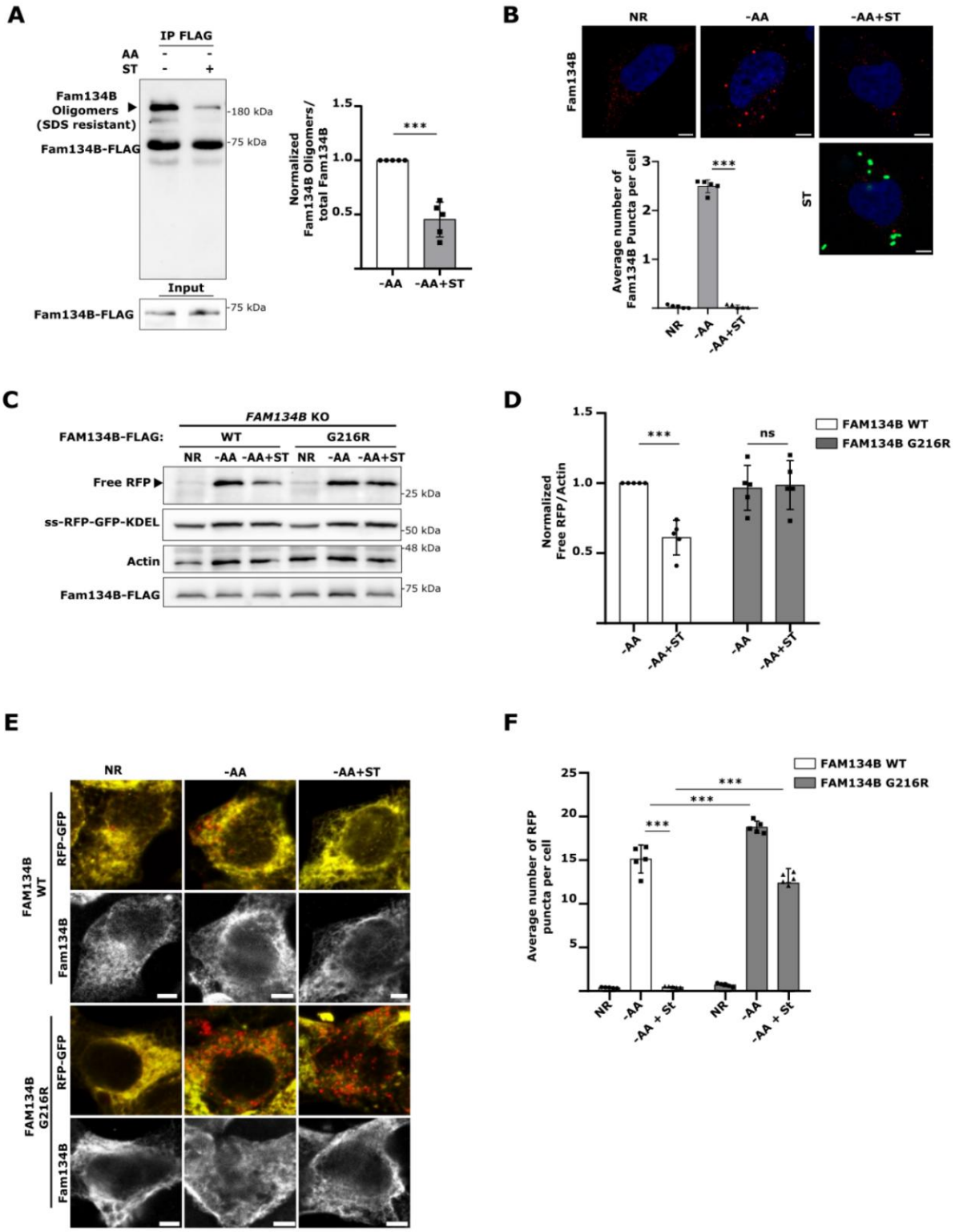

Fig. 3. FAM134B oligomerization is hindered by Salmonella infection.

A) *FAM134B* KO HEK293A cells transfected with FAM134B-FLAG were starved for AA for 3h in the absence or presence of ST. FLAG was immunoprecipitated. Error bars indicate the standard deviation of 5 independent experiments. Student's t-test, *** P <0.001. AA, amino acids; ST, *Salmonella* Typhimurium. **B)** WT cells were incubated with BafA1 and starved for AA for 3h in the presence or absence of ST. Fam134B puncta formation was observed by confocal microscopy. NR, Nutrient Rich; BafA1, Bafilomycin A1. Error bars indicate standard deviation of 5 independent experiments. The average number of Fam134B puncta was calculated from a minimum of 100 cells. Representative images are shown. Fam134B, red; DAPI, blue; ST, green. Scale bar 5μm. ANOVA, *** P <0.001. **C)** *FAM134B* KO cells were transfected with either FAM134B WT or FAM134B G216R and starved for AA for 6h or starved for 3h, followed by ST infection for 3h in AA starvation media. ER-phagy was measured by ss-RFP-GFP-KDEL processing. Actin was used as a loading control. **D)** Normalized Free RFP-Actin ratio from cells in C). Error bars indicate the standard deviation of 5 independent experiments. ANOVA, ***P <0.001; ns, no significance. **E)** *FAM134B* KO were transfected with either FAM134B WT or G216R and starved for AA for 6h or starved for 3h followed by ST infection for 3h in AA starvation media. Representative images are shown. ss-RFP-GFP-KDEL, yellow; Free RFP, red; Fam134B, far red. Scale bar 5μm. **F)** Average number of RFP puncta per cell from E) were quantified. Error bars indicate standard deviation of 5 independent experiments. The average number of RFP punctuation was calculated from a minimum of 100 cells. ANOVA, ***P <0.001.

The *Salmonella* effector SopF blocks ER-phagy

In order to promote invasion and replication, *Salmonella* expresses two type-III secretion systems, which deliver multiple bacterial effectors into the host cells[137]. We hypothesized that one of these effectors might be involved in *Salmonella*-mediated ER-phagy inhibition. To test our hypothesis, we repeated the ss-RFP-GFP-KDEL processing assay infecting them with different *Salmonella* effector mutants. Among the mutants tested, *Salmonella* defective for the phosphoinositide-binding effector SopF showed the most complete and consistent loss of ER-phagy regulation (Supp Fig. 4A). Analysis of ER-phagy by western blot and immunofluorescence in our reporter cells showed that SopF-deficient *Salmonella* was unable to supress ER-phagy compared to WT *Salmonella* infected controls under stimulated conditions (Fig. 4A-D). Together, these experiments indicate that SopF is necessary for *Salmonella*-induced ER-phagy repression. Next, we sought to determine if the expression of the SopF effector was sufficient to inhibit ER-phagy. To this end, ER-phagy reporter cells were transfected with FLAG-SopF or control vector. We observed by western blot, that SopF expression was sufficient to inhibit ER-phagy under stimulated conditions (Fig. 4E and 4F). Consistently, RFP puncta formation was significantly decreased in cells transfected with HA-SopF compared to control cells (Supp Fig. 4B and Supp Fig. 4C). Furthermore, SopF expression dramatically blocked endogenous Fam134B degradation by ER-phagy under stimulated conditions (Supp Fig. 4D). Together, these data indicate the bacterial effector SopF is required for *Salmonella* to inhibit ER-phagy.

Because forcing FAM134B oligomerization with the G216R mutant could bypass *Salmonella*-mediated ER-phagy blockage, we sought to determine if SopF effects on ER-phagy could also be prevented by FAM134B G216R. Indeed, *FAM134B* KO cells co-expressing FLAG-SopF and FAM134B G216R were able to significantly induce ER-phagy when stimulated compared to cells

transfected with FLAG-SopF and FAM134B WT (Fig. 4G and 4H). These data suggest *Salmonella* targets FAM134B oligomerization through SopF.

Recently, the crystal structure of SopF was solved revealing it to be a member of the ADP-ribosyltransferase superfamily[138]. Indeed, SopF has been shown to catalyze the transfer of ADP-ribose from nicotinamide adenine dinucleotide (NAD^+) to the v-ATPase subunit ATP6V0C leading to the inhibition of bacterial autophagy, but not general autophagy or other types of selective autophagy[138,139]. To test if SopF could directly interact with and target FAM134B, we co-immunoprecipitated FLAG-SopF and endogenous Fam134B, detecting a possibly transient interaction between both proteins (Fig. 4I). To further validate FAM134B and SopF interaction, we performed a TurboID assay, which relies on biotin-based proximity labeling and can detect transient interactions more reliably than co-IP. Briefly, SopF was tagged with a more promiscuous form of BirA, an *Escherichia coli*-derived biotin ligase. After incubation with biotin, proteins in the near vicinity of the TurboID-tagged SopF become biotinylated, enabling their identification after streptavidin pull-down[140]. We observed that FAM134B was dramatically enriched after streptavidin pull-down when TurboID-SopF was expressed compared to the TurboID control, indicating SopF comes in close proximity to FAM134B (Fig. 4J).

SopF mutations preventing its binding to the N-ribose (E325A) or the nicotinamide (Y224A, Y240A) group of NAD^+ largely blocked SopF ADP-ribosylation activity[138]. Consistently, SopF Y240A failed to prevent ER-phagy activation as observed by a significant increase in RFP production compared to SopF WT. (Fig. 4K and 4L). Additionally, SopF mutants E325A and Y224A also showed increased ER-phagy compared to SopF WT (Supp Fig. 4E and Supp Fig. 4F). Moreover, expression of SopF WT, but not the ADP-ribosylation mutant SopF Y240A, reduced the formation of FAM134B oligomers (Supp Fig. 4G). To test if SopF could ADP-ribosylate

FAM134B we used a pan-ADP-ribose binding reagent capable of detecting both mono and poly-ADP ribosylation. A band was observed when FAM134B was IP in the presence of SopF, which was absent in the control IP, suggesting SopF may directly ADP-ribosylate FAM134B (Fig. 4M). Recent studies have reported the importance of FAM134B acetylation at Lys160 and phosphorylation at residues Ser149, Ser151 and Ser153 in promoting its oligomerization and ER-phagy activation[119,120]. We hypothesized that one of the ways *Salmonella* could inhibit FAM134B oligomerization was by preventing these post-translational modifications. Mass spectrometry analysis of FAM134B in the absence of SopF, showed phosphorylation in Ser151, which was not detected when SopF was co-expressed (Supp Fig. 4H). Consistently, *Salmonella* infection significantly decreased both FAM134B Ser151 phosphorylation and Lys160 acetylation, in both nutrient rich and starvation conditions (Fig. 4O and 4P), indicating *Salmonella* directly targets FAM134B regulation and its ability to oligomerize. Further studies will be required to determine if *Salmonella*-mediated inhibition of FAM134B oligomerization is driven by SopF directly ADP-ribosylating FAM134B or upstream regulators. Together these results indicate that SopF ADP-ribosylation activity is required for ER-phagy inhibition.

Fig.4 The *Salmonella* effector SopF blocks ER-phagy

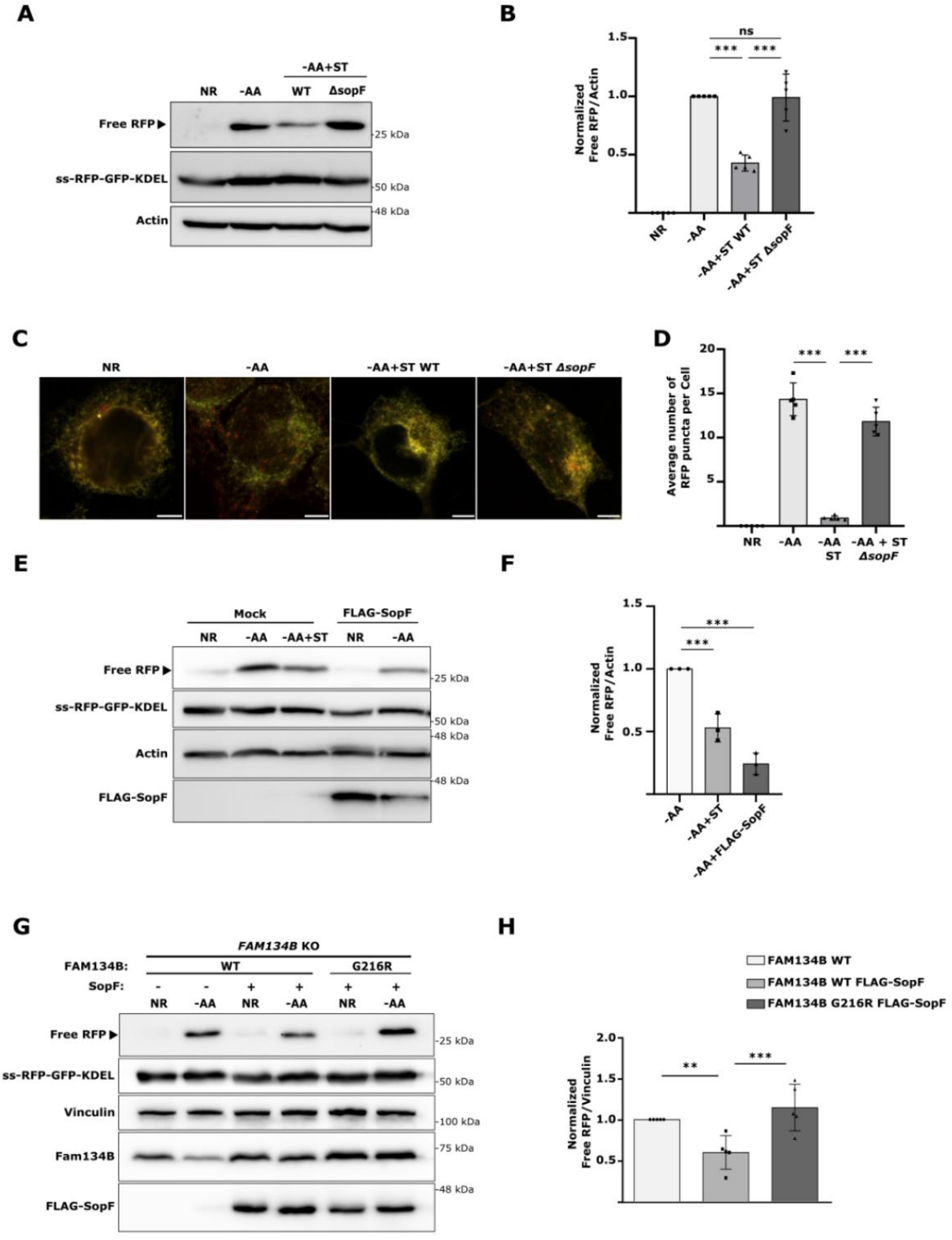

Fig.4 The *Salmonella* effector SopF blocks ER-phagy

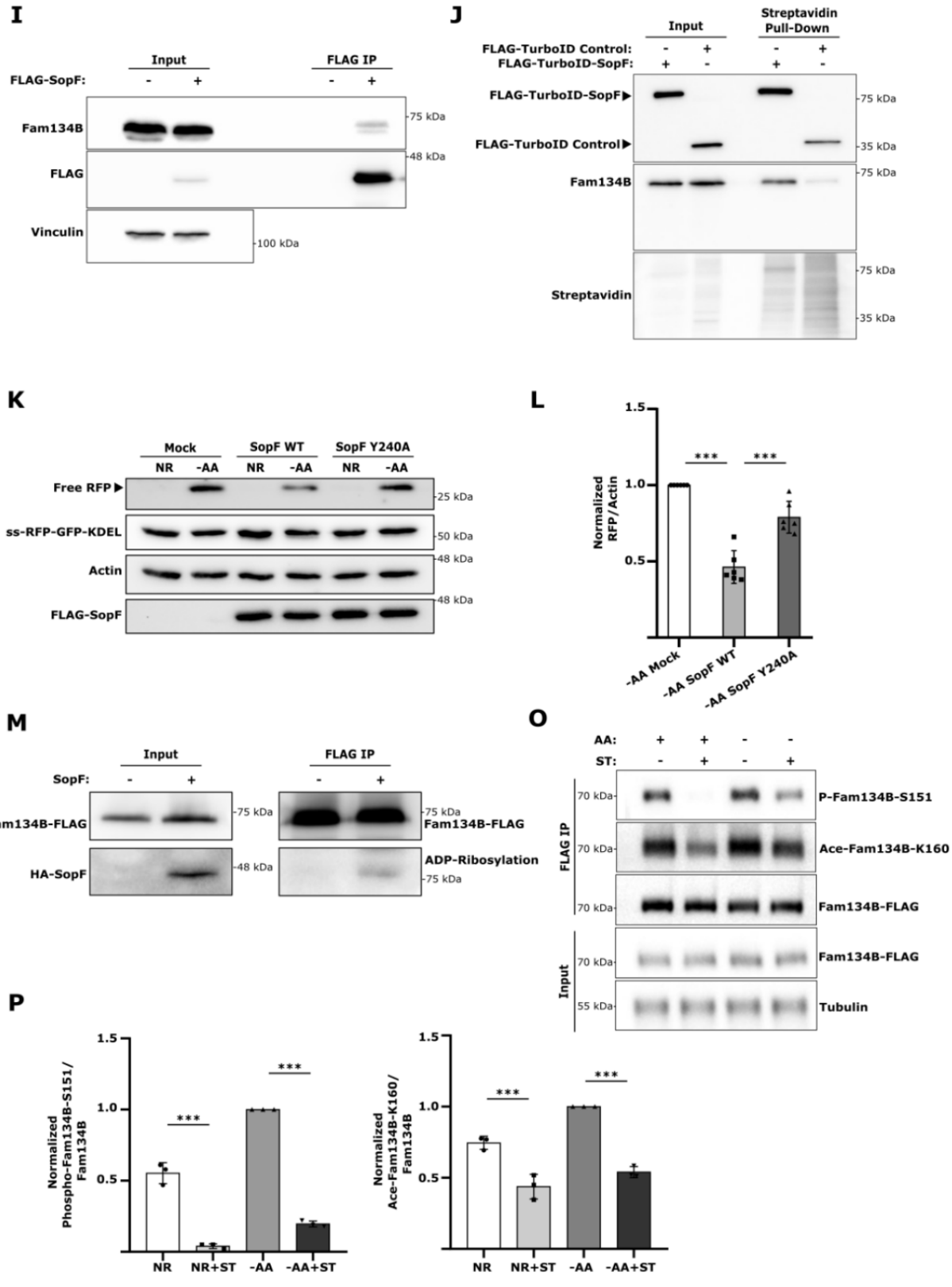

Fig. 4. The *Salmonella* effector SopF blocks ER-phagy.

A) WT HEK293A cells stably expressing the ss-RFP-GFP-KDEL reporter were starved for AA for 6h or starved for 3h followed by infection with ST WT or ST *ΔsopF* for 3h in AA starvation media. ER-phagy was measured by ss-RFP-GFP-KDEL processing. Actin was used as a loading control. NR, Nutrient Rich; AA, amino acids; ST, *Salmonella* Typhimurium. **B)** Normalized Free RFP-Actin ratio from cells in A). Error bars indicate the standard deviation of 5 independent experiments. ANOVA, ***P <0.001; ns, no significance. **C)** WT HEK293A cells stably expressing the ss-RFP-GFP-KDEL reporter were either AA starved for 6h or AA starved for 3h followed by ST WT or ST *ΔsopF* infection for 3h in starvation media, fixed and imaged by confocal microscopy. Representative images are shown. ss-RFP-GFP-KDEL, yellow; Free RFP, red. Scale bar 5μm. **D)** Average number of RFP puncta per cell from C) were quantified. Error bars indicate standard deviation of 5 independent experiments. The average number of RFP punctuation was calculated from a minimum of 100 cells. ANOVA, ***P <0.001. **E)** WT cells from A) transfected with either FLAG-SopF or a mock plasmid were starved for AA for 6h or starved for 3h followed by infection with ST WT for 3h in AA starvation media. ER-phagy was measured by ss-RFP-GFP-KDEL processing. Actin was used as a loading control. **F)** Normalized Free RFP-Actin ratio from cells in E). Error bars indicate the standard deviation of 3 independent experiments. ANOVA, ***P <0.001. **G)** HEK293A *FAM134B* KO cells stably expressing the ss- RFP-GFP-KDEL reporter were transfected with combinations of FAM134B WT, FAM134B G216R and FLAG-SopF and then starved for AA for 6h. Vinculin was used as loading control. **H)** Normalized Free RFP- Vinculin ratio from cells in G). Error bars indicate the standard deviation of 5 independent experiments. ANOVA, **P <0.01; ***P <0.001. **I)** HEK293A WT cells were transfected with FLAG-SopF or a mock plasmid. FLAG-SopF was immunoprecipitated. **J)** WT HEK293A cells were transfected with either FLAG-TurboID- SopF or FLAG-TurboID control plasmid. Cells were incubated with 50 μM Biotin for 1h and subjected to streptavidin pull-down. **K)** WT HEK293A cells stably expressing the ss-RFP-GFP-KDEL reporter were transfected with either FLAG-SopF WT, FLAG-SopF Y240A or a mock plasmid and starved for AA for 6h. ER-phagy was measured by ss-RFP-GFP-KDEL processing. Actin was used as a loading control. **L)**Normalized Free RFP-Actin ratio from cells in K). Error bars indicate the standard deviation of 6 independent experiments. ANOVA, ***P <0.001. **M)** *FAM134B* KO cells were transfected with FAM134B- FLAG and either HA-SopF or a mock plasmid and FLAG was immunoprecipitated. ADP-ribosylation was detected with a pan-ADP ribose binding reagent. **O)** HeLa cells transfected with FAM134B-FLAG were starved for 3h or infected with ST for 3h in starvation media. FLAG was immunoprecipitated. Fam134B Ser151 phosphorylation and Lys160 acetylation were determined using specific antibodies. Tubulin was used as loading control. **P)** Normalized Phospho Fam134B-S151-Total

Fam134B and Ace-Fam134B-K160- Total Fam134B ratios from cells in O). Error bars indicate the standard deviation of 3 independent experiments. ANOVA, ***P <0.001.

FAM134B restricts *Salmonella* growth

To better understand the nature of FAM134B-mediated resistance to intracellular *Salmonella,* we next looked at the factors that could contribute to the *FAM134B* KO defect, such as bacteria vesicle escape, clearance, and growth. First, we infected WT and *FAM134B* KO cells with GFP *Salmonella* and quantified growth post-invasion for 4 hrs. To distinguish between external and internalized *Salmonella*, cells were stained with a LPS antibody before permeabilization, allowing selective labelling and exclusion of external bacteria in our quantifications. We observed a similar level of bacterial internalization in both WT and *FAM134B* KO at 1 hr (Fig. 5A), indicating similar levels of infection rate. Interestingly, we observed a significant difference in growth rate between WT and *FAM134B* KO beginning at 2 hr post infection that persisted through the remaining time points. Escape from *Salmonella*-containing vesicles (SCV) is known to increase the growth rate of intracellular *Salmonella*, which is significantly higher in the cytosol. However, SCV escape in WT cells typically occurs well after 4 hrs post infection[141] and results in the growth of rod-shaped *Salmonella* that are more spread out than those growing in the SCV. Given the early timepoint of divergence in growth rates and the morphology of internalized *Salmonella,* it is highly unlikely that *FAM134B* KO defects are a result of early escape from the SCV. Nevertheless, we quantified the amount of cytosolic *Salmonella* compared to the total population using a chloroquine resistance CFU assay. Chloroquine accumulates in high concentration within endosomes, preferentially targeting vacuolar, rather than cytosolic *Salmonella,* rendering SCV-containing *Salmonella* transcriptionally inactive and non-replicative[141]. Consistent with other studies, we observed that

cytosolic *Salmonella* accounted for 10% of total bacteria in infected WT cells at similar time points[141] (Supp. Fig. 5A). However there was no significant difference in cytosolic *Salmonella* between infected WT and *FAM134B* KO cells, indicating FAM134B is not involved in *Salmonella* escape from SCVs (Supp. Fig. 5A). We next sought to measure the impact of FAM134B on autophagic bacterial clearance, termed xenophagy. To estimate the relative contribution of FAM134B in *Salmonella* clearance compared to other forms of autophagy, we performed a CFU assay in WT and *FAM134B* KO cells treated with the VPS34 inhibitor, VPS34-IN1. The class-III phosphatidylinositol-3-phosphate kinase complex, which is formed by the catalytic subunit PIK3C3/VPS34, among others, plays an essential role in autophagy activation[142], thus, VPS34 inhibition blocks general autophagy[134]. As expected, inhibiting VPS34 dramatically increased *Salmonella* levels in both WT and *FAM134B* KO cells. However, VPS34-IN1-treated *FAM134B* KO cells showed a significant increase in *Salmonella* burden compared to treated WT cells, suggesting FAM134B may have an additional role in preventing *Salmonella* growth, not directly related to xenophagy (Supp. Fig. 5B). Autophagosomal degradation of *Salmonella* is mediated by LC3 recruitment to bacteria and autophagy-deficient cells have been shown to be more permissive for *Salmonella* growth[143]. However, the impact of ER-phagy in *Salmonella* clearance is unclear. Strikingly, *FAM134B* KO cells contained less LC3B-positive *Salmonella* compared to WT cells, suggesting a role for FAM134B and ER-phagy in *Salmonella* clearance (Fig. 5B and 5C). LC3B targeting to *Salmonella* is modulated by various xenophagy adaptors such as TBK1, which is involved in phosphorylating different xenophagy receptors and recruiting them to the surface of *Salmonella* for degradation[144]. Interestingly, we found no significant difference in TBK1 recruitment to *Salmonella* in WT and *FAM134B* KO cells (Supp Fig. 5C and Supp Fig. 5D),

suggesting FAM134B effects on *Salmonella* replication might be either downstream of TBK1, or not directly related to xenophagy.

To determine if SopF is required for the suppression of LC3-positive puncta in *FAM134B* KO cells, we quantified the localization of LC3B to SopF-deficient *Salmonella.* We observed the previously reported increase of LC3B colocalization to *ΔsopF Salmonella* compared to WT *Salmonella* in our control cells[145]. However, SopF deletion exerted no significant difference in LC3B colocalization in *FAM134B* KO cells (Fig. 5D and 5E). Similarly, SopF overexpression significantly increased WT *Salmonella* levels in control cells, while overexpression of SopF in *FAM134B* KO cells showed no significant difference in *Salmonella* viability compared to mock transfected *FAM134B* KO cells (Fig. 5F), further indicating that SopF effects on *Salmonella* growth are linked to FAM134B. Moreover, it reinforces our working model that SopF is inhibiting ER-phagy to influence ER morphology and promote intracellular *Salmonella* survival. This hypothesis was further corroborated by electron microscopy images showing increased ER area in cells stably expressing SopF compared to control cells (Supp. Fig. 5E), indicating SopF-mediated inhibition of ER-phagy reconfigures ER morphology. The mechanisms that specifically link FAM134B-dependent ER-phagy to xenophagy are unclear at this time, however, these results suggest an additional, yet undiscovered, pathway linking FAM134B to *Salmonella* restriction.

Fig.5 FAM134B restricts *Salmonella* growth

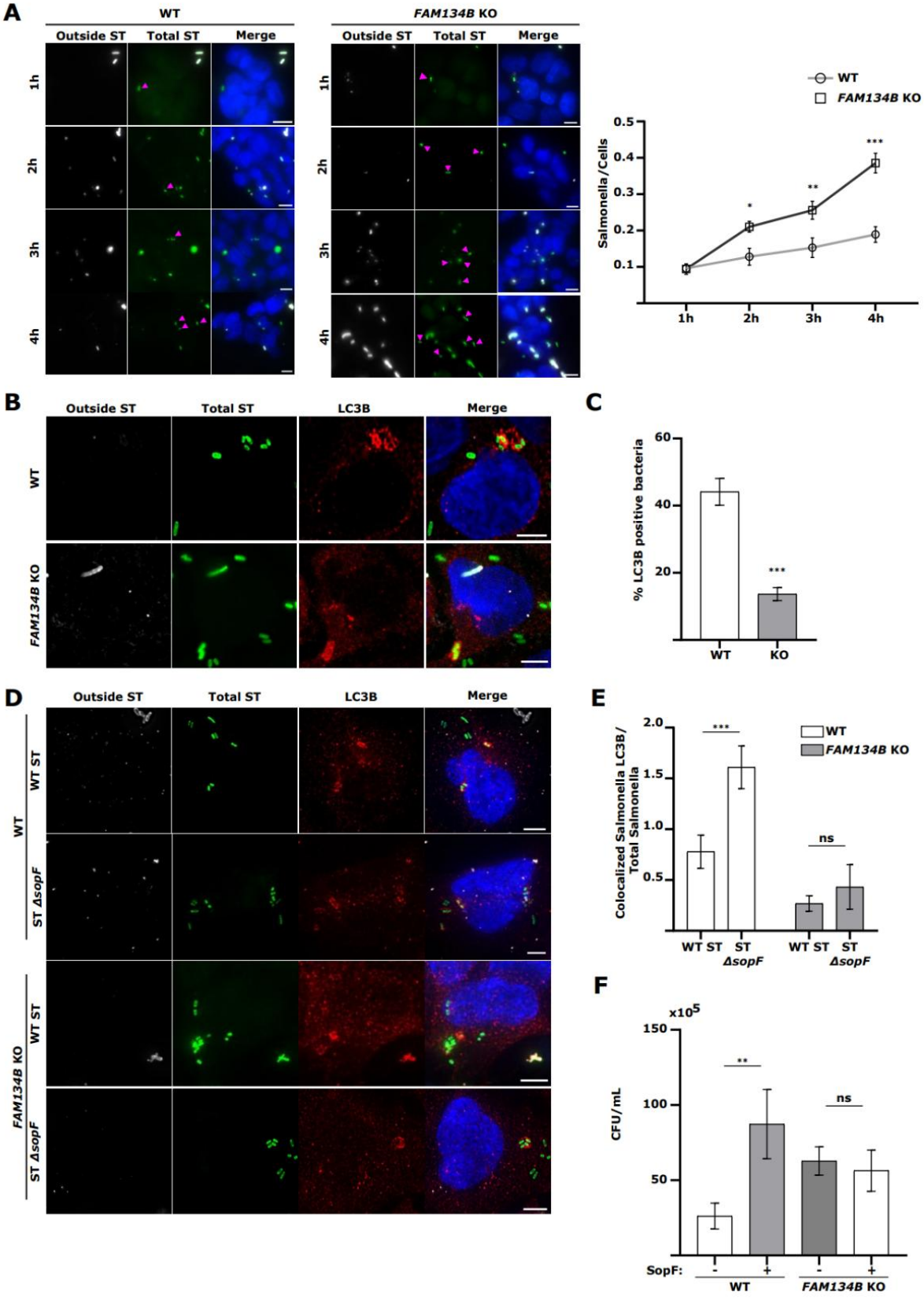

Fig. 5. FAM134B restricts *Salmonella* growth.

A) WT and *FAM134B* KO HEK293A cells were infected with ST for 1h followed by Gentamicin wash-off. Cells were fixed at indicated time points. ST, *Salmonella* Typhimurium. Representative images are shown. ST, green; LPS, far red; DAPI; blue. Scale bar 10µm. Error bars indicate standard deviation. The number of ST were calculated from a minimum of 100 cells. ANOVA, *P <0.05; **P <0.01; ***P <0.001. **B)** HEK293A WT and *FAM134B* KO cells were infected for 1h. Autophagic capture of ST was analyzed by immunostaining for LPS and LC3B**.** Representative images are shown. ST, green; LC3B, red; LPS, far red; DAPI; blue. Scale bar 5µm. **C)** Percentage of ST colocalizing with LC3B in WT and *FAM134B* KO cells from B). Error bars indicate standard deviation. The percentage of colocalization was calculated from a minimum of 100 cells. Student's t test, ***P <0.001. **D)** HEK293A WT and *FAM134B* KO cells were infected with either ST WT or ST *ΔsopF* for 1h. Autophagic capture of ST was analyzed by immunostaining for LPS and LC3B**.** Representative images are shown. ST, green; LC3B, red; LPS, far red; DAPI; blue. Scale bar 5µm. **E)** The ratio between the number of ST colocalizing with LC3B and total internalized ST from D) is presented. Error bars indicate standard deviation. LC3B-ST colocalization was calculated from a minimum of 100 cells. . ANOVA, ***P <0.001; ns, no significance. **F)** HEK293A WT and *FAM134B* KO were transfected with either FLAG-SopF or a mock plasmid followed by WT ST infection. Bacterial content was determined through colony forming unit (CFU). Error bars indicate standard deviation. ANOVA, **P <0.01; ns, no significance.

Infected *FAM134B* KO mice are more susceptible to *Salmonella* infection.

We next sought to determine the pathophysiological effects of *Salmonella*-mediated inhibition of ER-phagy *in vivo*. To this end, we performed oral gavage *Salmonella* infection of WT and *FAM134B* KO mice[146] and analyzed bacterial burden and intestinal damage 5 days post infection. Histochemical analysis of hematoxylin and eosin (H&E) stained intestine samples of infected WT mice presented mucosa and submucosa infiltration, along with occasional damage (Fig. 6A). However, infected *FAM134B* KO mice showed severe wall, mucosa and submucosa infiltration, as well as marked necrotic damage, fibrin formation and edema. Following H&E, mucosa and submucosa samples were stained to detect *Salmonella* levels, which showed a significant increase in bacterial burden in *FAM134B* KO compared to WT cells (Fig. 6B and 6C). These results are consistent with our *in vitro* data, highlighting FAM134B role in restricting *Salmonella* growth. Infections were repeated as described above and WT and *FAM134B* KO *Salmonella* load was measured by CFU in feces, spleen, and intestine. Consistent with immunofluorescence analysis, we observed significantly higher levels of *Salmonella* in the tissue and feces of *FAM134B* KO mice (Fig. 6D, 6E and 6F). We next tried to determine if our previous results extended to primary macrophages, key agents involved in the innate and adaptive immune response against *Salmonella* infection. Thus, we measured FAM134B-mediated ER membrane scission in starved bone marrow derived macrophages (BMDM) obtained from WT mice that were infected with either *Salmonella* WT or *ΔsopF*. As expected, ER-phagy activation induced FAM134B puncta formation, which was significantly blocked by *Salmonella* WT, but not SopF defective *Salmonella* (Fig. 6G and 6H), recapitulating our results in endothelial cells. Finally, BMDM obtained from *FAM134B* KO mice displayed significantly more *Salmonella* than WT BMDM after infection (Fig. 6I), further underlining the importance of FAM134B in anti-bacterial response in multiple tissues and cell

types. Overall, our results indicate that FAM134B is an important factor in controlling bacterial infection *in vivo*.

Fig.6 Infected *FAM134B* KO mice are more susceptible to *Salmonella* infection.

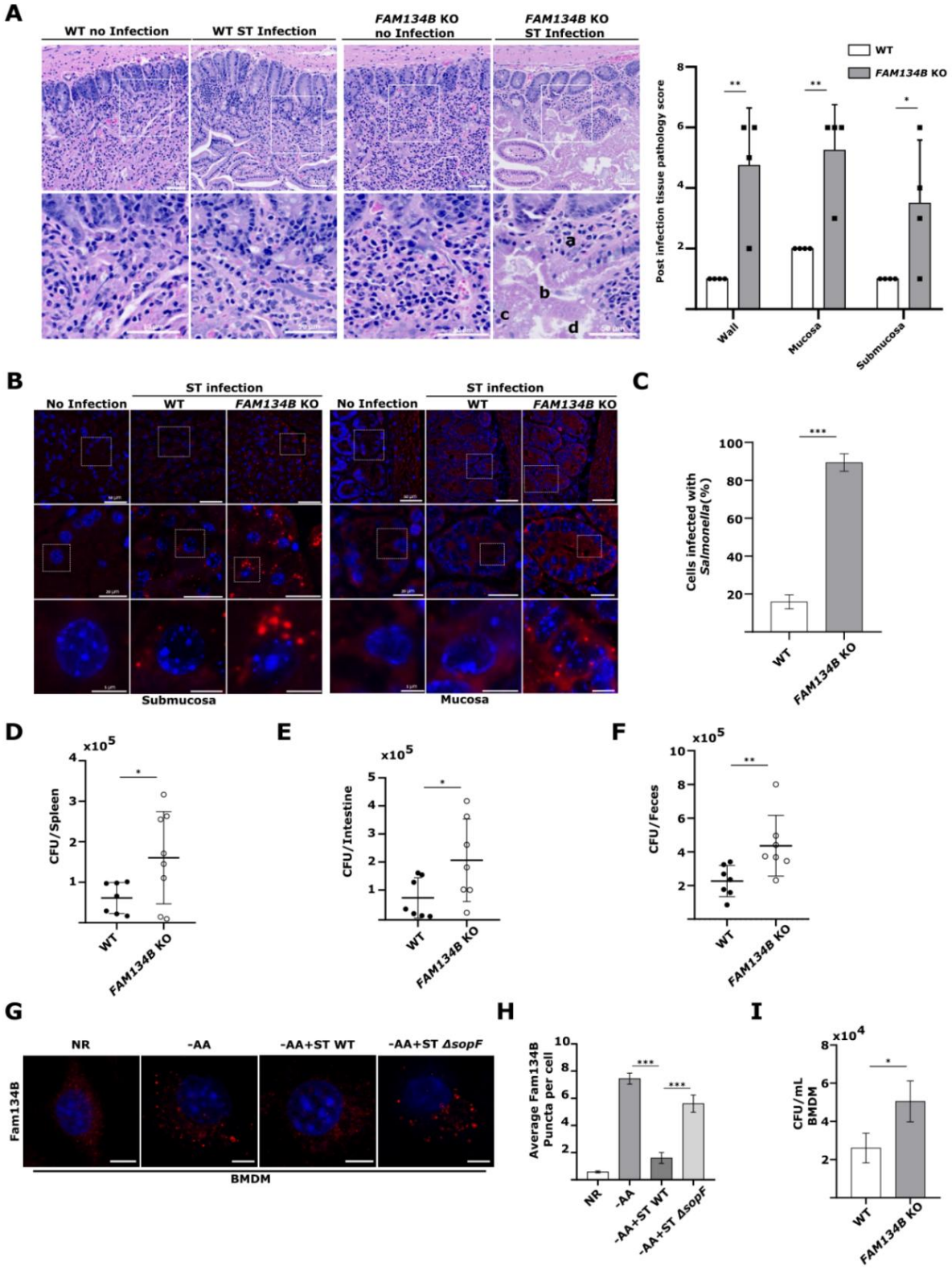

Fig. 6. Infected *FAM134B* KO mice are more susceptible to *Salmonella* infection.

A) WT and *FAM134B* KO C57BL/6J mice were infected with WT GFP ST through oral gavage and after 5 days, their small intestine was fixed and stained with H&E. (a) infiltration, (b) necrosis, (c) fibrosis, and (d) edema. Pathology scores of post infected tissues are presented. Error bars indicate standard deviation. ANOVA, *P <0.05; **P <0.01. ST, *Salmonella* Typhimurium. Scale bar 50μm. **B)** WT and *FAM134B* KO mice small intestine samples from A) were stained with DAPI and GFP to detect ST. ST, Red; DAPI, Blue. Scale bar: 5, 20 and 50 μm. **C)** The number of cells infected with ST from B) were quantified. Error bars indicate standard deviation, ST infection was calculated from a minimum of 350 cells. Student's t test, ***P <0.001. **D, E and F)** WT and *FAM134B* KO mice were infected with ST through oral gavage and after 5 days their spleen, whole intestine and feces were collected. Bacterial content was determined through colony- forming unit (CFU). Error bars indicate standard deviation. Student's t test, *P <0.05; **P <0.01. **G)** BMDM, bone marrow derived macrophages from WT mice were kept in NR media, AA starved for 2 hr or starve for 1 hr followed by ST WT or ST *ΔsopF* infection in starvation media for an additional 1 hr. Starved samples were treated with BafA1. BMDM were then fixed and imaged by confocal microscopy. Representative images are shown. NR, Nutrient Rich; AA, amino acids, BafA1, Bafilomycin A1. Scale bar 5 μm. **H)** Average number of Fam134B puncta per cell from G) were quantified. Error bars indicate the standard deviation. Average Fam134B puncta formation was calculated from a minimum of 100 cells. ANOVA, ***P <0.001. **I)** BMDM from WT and *FAM134B* KO mice were infected with *ΔinvA* ST. Bacterial content was determined through colony-forming unit (CFU). Error bars indicate standard deviation. Student's t test, *P <0.05.

4.5 DISCUSSION

The ER is a dynamic and complex intracellular organelle with several critical functions involved in maintaining cell homeostasis and adapting to stress response[147]. The selective autophagic degradation of the ER, ER-phagy, aims to restore ER homeostasis through the degradation of portions of the ER and in turn regulate the size and morphology of the organelle. Recently, several studies have begun to uncover the link between ER-phagy and intracellular invasive pathogens. Here, we describe a novel mechanism by which the intracellular pathogen *Salmonella enterica* serovar Typhimurium specifically prevents the protein receptor FAM134B oligomerization in order to block ER-phagy and increase bacterial viability after infection (Fig. 7).

We determined that *Salmonella* specifically targets FAM134B, but not TEX264, to block ER-phagy and increase bacterial viability, which was intrinsically linked to FAM134B ability to induce ER-phagy. A previous report highlighted how invasive bacteria capitalize on transforming the ER morphology to improve their viability. Upon *Legionella pneumophila* infection, multiple ER regulatory proteins, including FAM134A, FAM134B, FAM134C, RTN4 and TEX264, are subject to phosphoribosyl-linked ubiquitination, triggering ER remodeling and membrane recruitment to bacterial containing vacuoles[129]. Further studies will be required to determine if other members of the FAM134 family or other proteins involved in the regulation of ER morphology and stability are also targeted by *Salmonella*.

We also identified that *Salmonella*-mediated ER-phagy blockage is linked to the bacterial effector SopF, specifically its ADP-ribosylation activity. Previously identified as an anti-bacterial autophagy inhibitor, SopF specifically disrupts the interaction between v-ATPase and ATG16L1 by ADP-ribosylating the v-ATPase subunit ATP6V0C[138,139]. In these experiments SopF was shown to inhibit anti-bacterial autophagy, but not canonical autophagy. However, ER-phagy was not

tested[139]. Thus, it is likely that SopF can ADP-ribosylate multiple targets to both prevent *Salmonella* clearance and promote *Salmonella* growth. Interestingly, SopF-mediated ER-phagy blockage could be bypassed by expressing FAM134B G216R mutant, which promotes FAM134B oligomerization. Conversely, *Salmonella* infection decreased both FAM134B Ser151 phosphorylation and K160 acetylation, which positively regulate oligomerization; and mass spectrometry analysis confirmed SopF expression resulted in undetectable FAM134B Ser151 phosphorylation. However, mass spectrometry failed to measure K160 acetylation and ADP-ribosylation in both the presence and absence of SopF, possibly due to a paucity of protease sites and low peptide coverage for some areas of the protein. Thus, it is possible that SopF prevents FAM134B oligomerization by directly ADP-ribosylating FAM134B or indirectly by targeting upstream regulators of FAM134B involved in the formation of multi-protein clusters required for ER-phagy[148].

Finally, our *in vivo* results demonstrated the physiological importance of FAM134B in innate immunity. Infected *FAM134B* KO mice presented increased necrotic damage compared to infected WT mice. Additionally, *Salmonella* burden was increased in the spleen, intestine and feces of *FAM134B* deficient mice, as well as infected BMDMs, suggesting a yet uncharacterized but important role for FAM134B in the innate response against invading pathogens. Altogether, our data uncover a previously undiscovered mechanism by which *Salmonella* seeks to promote bacterial viability by targeting FAM134B-mediated ER-phagy and transform the host environment to suit their growth needs. We believe this study raises several important questions including the interplay between SopF targets in controlling *Salmonella* viability and the general ability of FAM134B-dependent restriction for other intracellular bacteria.

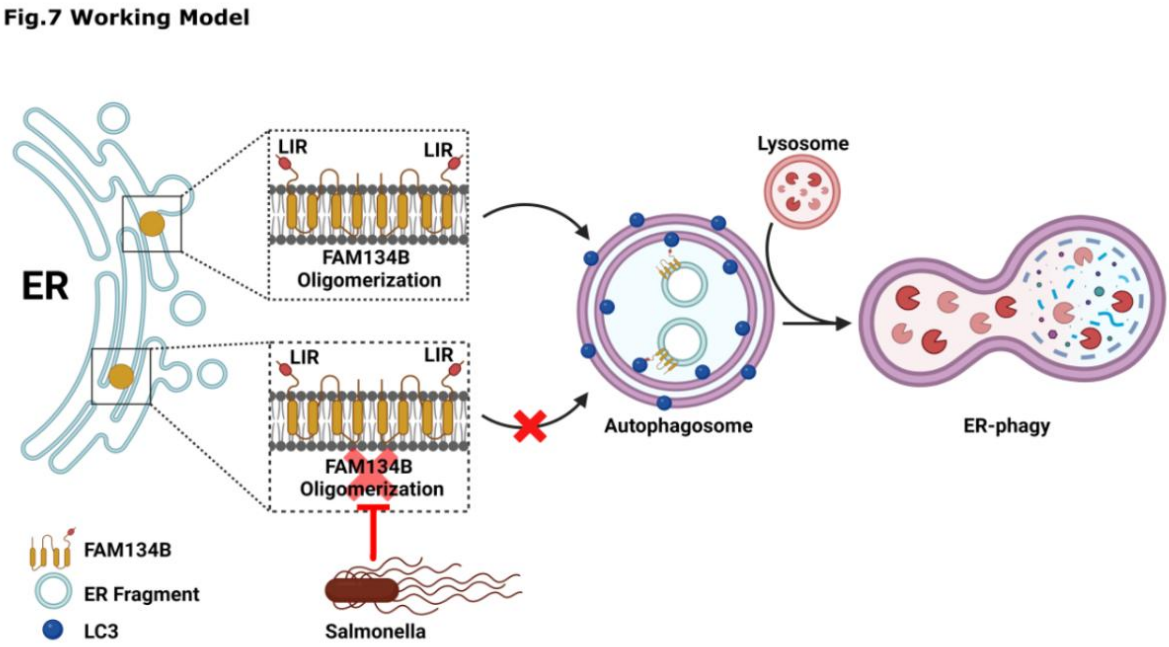

Chapter 1 Fig. 7. Model

Fam134B oligomerization leads to membrane scission, Fam134B LIR binds to LC3-family bound isolation membranes that form autophagosomes and triggers ER remodelling and degradation by ER-phagy. *Salmonella* infection blocks Fam134B oligomerization via the bacterial effector SopF, hindering ER-phagy induction, which in turn promotes *Salmonella* viability.

4.6 MATERIAL AND METHODS

Antibodies and reagents

HA-HRP (Cat#2999), Fam134B (Cat#83414), and phospho-S6K T389 (Cat#9234) antibodies were obtained from Cell Signaling Technology. Anti-LC3B (Cat#PM036 for immunofluorescence) antibody was purchased from MBL. Pan-ADP-ribose binding reagent (MABE1016), Beta-actin (Cat#A5441 clone AC-15) and Vinculin (Cat#V9131), Fam134C (Cat#HPA016492) antibodies, as well as doxycycline hyclate (Cat#24390-14-5), Chloroquine (Cat#C6628-25G) and VPS34 inhibitor VPS34-IN1 (Cat#1383716-33-3) were obtained from Sigma. DYKDDDDK Epitope Tag (Cat#NBP1-06712 for WB), anti-Tex264 (Cat#NBP1-89866) and LC3/MAP1LC3B (Cat#NB100-2220 for western blot) antibodies were purchased from Novus Biologicals. Anti-LPS FITC (Cat#sc-52223) and TBK1 (Cat#SC-398366) antibodies were purchased from Santa Cruz Biotechnology. LPS (Cat#ab128709), and Anti-S6K (Cat#ab32529) were obtained from Abcam. Anti-RFP (Cat#600-401-379) was obtained from Cedarlane. Anti-p62 (Cat#GP62-C) was purchased from Progen. Anti-Tex264 (Cat#25858-1-AP), Fam134A (Cat#24650-1-AP) and anti-Tubulin (Cat#66362-1-Ig) were purchased from Proteintech. Bafilomycin A1 was obtained from Tocris (Cat#133410U). Digitonin (Cat#10188-874) was obtained from VWR. Alexa Fluor 647 (Mouse Cat#A21235, Rabbit Cat#A21244), Alexa Fluor 568 (Cat#A11036), HA tag monoclonal antibody (Cat#26183), Streptavidin-HRP (Cat#21130) and Reticulon 3 poly-clonal antibody (Cat#A302-860A) were purchased from Thermo-Fisher. Anti-phospho-Fam134B-Ser151 and anti-Ace-Fam134B-Lys160 are not commercially available and have been previously described[119,120]. Anti-HALOTag® Monoclonal Antibody (Cat#G9211) and HALOTag® TMR Ligand (Cat#G8252) were purchased from Promega.

Cell culture

HEK293A, HCT116 and HeLa cell lines were cultured in DMEM supplemented with 10% bovine calf serum (VWR Life Science Seradigm). Amino acid starvation medium was prepared based on the Gibco standard recipe, omitting all amino acids without the addition of non-essential amino acids and substitution with dialyzed FBS (Invitrogen). Doxycycline treatment of cells stably expressing ER-phagy probe was performed as previously described[117].

Transfection

Transfections were performed using polyethylenimine (PEI, medistore uOttawa) or Polyjet DNA transfection reagent (Cat#SL100688) from FroggaBio. The samples were analyzed 48–72 h post-transfection.

Generation of knock-out cell lines using CRISPR/Cas9

FAM134B and *TEX264* KO lines were generated in the HEK293A and HCT116 background utilizing CRISPR/Cas9 using primers that were previously described[117]. *FIP200* KO HEK293A cell line was generated using guide RNA sequence AGAGTGTGTACCTACAGTGC.

Generation of stable cell lines

WT and KO clones were infected with lentiviruses carrying ss-RFP-GFP-KDEL as previously described[117]. Similarly, cell lines stably expressing HALO-mGFP-KDEL were generated as previously described[133].

Plasmids

Plasmids pEGFP-C1-SopF (#137734), pCW57-CMV-ssRFP-GFP-KDEL (#128257), pMRX-IB-HaloTag7-mGFP-KDEL (#184904**)** and pMRX-INU-FLAG-FAM134B (#128260) were obtained

from Addgene. SopF cDNA from pEGFP-C1-SopF was subcloned into FLAG-pcDNA to generate FLAG-SOPF plasmids. FAM134B cDNA from pMRX-INU-FLAG-FAM134B was subcloned into c-FLAG-pcDNA to generate FAM134B-FLAG plasmids. All constructs were generated using fast-cloning as previously described[149]. SopF cDNA from pEGFP-C1-SopF was cloned using Gibson assembly into pFLAG-TurboID C1 to generate pFLAG-TurboID-SopF. pFLAG-TurboID C1 was a gift from Dr. Laura Trinkle.

Site-directed mutagenesis

Primers used for making FAM134B LIR mutation

Mutation	Forward	Reverse
FAM134B LIR	GATGACGCTGCAGCAGCTGACCA GTCAGAGCTGGATCAAATTGAGA GTGAATTGGGACT	TCAGCTGCTGCAGCGTCATCA CCTTCTTCAGTGTCTGTGTCCT CTTCTGGGATGGG
FAM134B G216R	CATTCCTAGGGTTATACTCAGCTAT CTACTGTTACTGTGTGCATT	TGAGTATAACCCTAGGAATGTA ACTTCCCAAGATCGTAAAAAA TGTG
SopF E325A	TTATATAGCGGCTCATATTCATGGT GATGTATGTTTATTCAGAG	ATATGAGCCGCTATATAATTCC CTTCATAGCCTTTACCA
Sopf Y224A	CCAATTGCTGCTGCACTGGACTTT CTGAACGGTG	GCAGCAGCAATTGGTCTGCTT GTAGTGCTAAAAGTTCT
Sopf Y240A	GGAGGTGCCAGCGCCGCTGGGAA ATCATTTTTG	CGCTGGCACCTCCATTTTCAC CGTTCAGAAAGTCC

Site-directed mutagenesis was performed as previously described[150]. Specificity of mutagenesis was analyzed by direct sequencing.

Bacterial strains

Wild-type and *ΔinvA* (SL1344) *Salmonella* enterica serovar Typhimurium strains were a gift from Dr. Subash Sad (University of Ottawa). *Salmonella ΔsopF*, *ΔpipB2* and *ΔspiC* strain (SL1344) and others were a gift from Dr. John Brumell (University of Toronto). Bacteria were grown in Luria-Bertani (LB) broth (Fisher).

Bacterial infection

Salmonella was grown in 4 ml of LB broth at 37°C at 250 rpm. Overnight cultures of *Salmonella* were diluted 30-fold and allowed to grow until reaching an OD_{600} of 1.5, followed by centrifugation of 10,000 *g* for 2 min, and the resulting pellet was resuspended in 1 ml of phosphate-buffered saline (PBS). Bacterial stock was then diluted to multiplicity of infection (MOI) of 180 in DMEM supplied with 10% heat-inactivated bovine calf serum for infection or amino acid starvation media. Cells cultured in antibiotic-free medium were infected with *Salmonella* infection and maintained at 37°C in a 5% CO2 environment for the specified duration. Prior to analysis, cells were washed once with PBS and lysed directly using 1x denaturing SDS sample buffer.

Western blot and immunoprecipitation

Whole-cell lysates were prepared by direct lysis with 1x SDS sample buffer, followed by boiling for 10 minutes at 95°C and resolved by SDS–PAGE. Immunoprecipitation cells were harvested in mild lysis buffer (MLB) containing 10 mM Tris pH 7.5, 10 mM EDTA, 100 mM NaCl, 50 mM NaF, and 1% NP-40, supplemented with protease and phosphatase inhibitor cocktails (including

EDTA from APExBIO). The lysates were then centrifuged at maximum speed for 10 minutes to remove cell debris. Anti-FLAG affinity gel beads (Sigma) were washed once with MLB and then incubated with cell lysates for 1.5 hours, followed by a single wash with MLB containing inhibitors and four quick washes with MLB alone. The beads were subsequently boiled in a 1x denaturing sample buffer for 10 minutes before being resolved by SDS–PAGE. Imaging was conducted using the ChemiDoc™ Touch imaging system (Bio-Rad).

Immunofluorescence

Cells were seeded onto IBIDI-treated coverslips and allowed to adhere overnight. Following treatments for *Salmonella* infection MOI of 70 was used for IF experiments, cells were fixed in 4% paraformaldehyde in PBS for 15 minutes and then permeabilized with 50 μg/ml digitonin in PBS for 10 minutes at room temperature. Subsequently, cells were blocked using a blocking buffer (1% BSA and 2% serum in PBS) for 45 minutes, followed by incubation with primary antibodies in the same buffer for 1 hour at room temperature. After incubation, samples were washed three times in PBS and once in blocking buffer before being incubated in secondary antibodies for 1 hour at room temperature. Slides were washed three times in PBS, stained with DAPI, and mounted. Imaging was conducted using a Zeiss LSM 800 AxioObserver Z1 Confocal Microscope. For staining bacterial localization (inside/outside), cells were first incubated with an anti-LPS antibody for 1hr and followed by secondary antibody incubation for 1hr in a blocking buffer before permeabilization. This was followed by three PBS washes between steps. Confocal microscopy images were analyzed using an automated protocol implemented in ImageJ software to minimize bias. The same protocol was consistently applied to each field of view and across all samples. An average of seven unique fields of view from representative experiments were selected for quantification.

Cyto-ID Autophagy Detection Kit assay

Cells were seeded onto ibidi 8 well μ-Slides (Ibidi, cat. 80826) and allowed to adhere overnight. Subsequently, cells were subjected to amino acid starvation with or without *Salmonella* infection. Following treatment, cells were incubated in DMEM without phenol red containing Cyto-ID autophagy detection stain (Enzo, ENZ-KIT175-0050) for 30 minutes, then washed with PBS and re-incubated with either complete DMEM without phenol red or amino acid media. Images were acquired and deconvolved using an inverted epifluorescent Zeiss AxioObserver.Z1 microscope.

Biotin-based proximity labeling TurboID assay

Transfected cells with either FLAG-TurboID-SopF or FLAG-TurboID control were incubated with 50μM biotin (Sigma, B4639) for 1 hour. Cells were then rinsed with PBS and lysed with high salt RIPA buffer (50 mM Tris pH 7.5, 500 mM NaCl, 1% NP-40, 0.5% deoxycholate), supplemented with protease and phosphatase inhibitor cocktails (including EDTA from APExBIO). Lysates were centrifugated at maximum speed for 10 minutes at 4°C and the supernatant was transferred to a new tube and diluted with an equal volume of no salt RIPA buffer (50 mM Tris pH 7.5, 1% NP-40, 0.5% deoxycholate). Diluted samples were incubated with Streptavidin-agarose beads (Thermo Fischer, 20359) for 4 hours at 4°C. Beads were then pelleted at 1000 RPM for 2 minutes, washed 3 times with 250 mM salt RIPA buffer and eluted by adding a bead equivalent volume of 2% SDS with 30 mM biotin, vortexed and incubated at 95°C for 10 min.

Colony-forming unit assay

Cell lines

Cells were infected with *Salmonella* at a multiplicity of infection (MOI) of 180 for 1 hour. Subsequently, the infected cells were rinsed three times and treated with media containing 100

μg/ml Gentamicin for 0.5 hours, followed by a 4-hour incubation with media containing 50 μg/ml Gentamicin. After incubation, the samples were washed three times with PBS and then lysed using CFU buffer (0.1% Triton X-100 and 0.01% SDS in PBS). The lysates obtained were subjected to serial dilution (1:50, 1:75, and 1:100) and plated onto LB agar plates containing Streptomycin. The plates were incubated at 37°C for 16–18 h, and the colonies were counted to determine the number of CFU.

Colony-forming unit assay

BMDM

Salmonella ΔinvA was used to quantify intracellular bacterial burden without the issue of cell death acting as a confounding variable. C57BL/6J WT and *FAM134B* KO BMDMs were seeded in triplicate at a density of 300,000 cells per well. *Salmonella ΔinvA* was cultured overnight at 37°C with shaking at 250 RPM in 5 mL of LB broth containing 100 μg/mL streptomycin. The following day, the optical density at 600 nm reached ~2.3, which represents a concentration of $9.2x10^9$ CFU/mL. *Salmonella ΔinvA* was then centrifuged at 9,500 RPM for 5 minutes. The resulting pellet was resuspended in 1 mL of R8 medium. 100 uL of resuspended *Salmonella ΔinvA* was added to 650 μL of PBS and 250 μL of normal mouse serum (Jackson ImmunoResearch Laboratories) in a 15 mL Falcon tube to facilitate bacterial opsonization. This was incubated with shaking at 37°C and 210 RPM for 25 minutes. Following incubation, the opsonized bacteria was centrifuged, washed twice with PBS, and resuspended in R8 medium.

Salmonella ΔinvA was then added to BMDMs at an MOI of 10. Next, the plate was centrifuged at 800 x g for 5 minutes and incubated at 37°C for 25 minutes. After the incubation, the cells were washed twice with PBS containing 50 μg/mL of gentamicin and incubated with R8 medium containing 50 ug/mL of gentamicin. After 1.5 hours, the media was replaced with R8 medium

containing a reduced concentration of gentamicin (10 μg/mL). Intracellular bacterial replication was quantified by lysing the BMDMs at desired time points using 300 μL of 1% Triton-X lysis buffer. Serial dilutions of the lysates were plated on LB agar containing 100 μg/mL streptomycin to quantify bacterial burden. Plates were incubated overnight at 37°C and CFU was counted the following day.

Immunohistochemistry staining

Samples were rinsed three times with PBS, treated with 3% H_2O_2 (in PBS) for 10 min, and washed three times with PBS. Blocked with protein block serum-free (catalog no. X0909 Dako) for 2 h, stained with primary antibody overnight at 4 °C (GFP 1:150 catalog no. Sigma #G1544), washed three times with PBS, incubated with secondary antibody (Alexa Fluor 555 anti-rabbit, catalog no. A31572, 1:1,000) for 1 h, washed once with PBS, stained with DAPI (2 mg ml−1, Roche Diagnostics) for 10 min, washed three times with PBS and cover slip-mounted with Fluoromount-G mounting solution (Invitrogen, 00-4958-02). All treatments were done at room temperature unless otherwise stated. Images were acquired using a Zeiss LSM 800 AxioObserver Z1 Confocal Microscope.

***In vivo* experiments**

WT and *FAM134B* KO C57BL/6J mice were subjected to a 3-hour fast from both food and water prior to the oral administration of 20 mg of streptomycin (Millipore Sigma) dissolved in 100 μL of ddH2O. 2 hours following the streptomycin treatment, food and water were reintroduced to the mice. The following day, mice were again fasted from food and water for 3 hours prior to receiving an oral dose of WT GFP *Salmonella* (1×10^8 CFU) in 100 μL of saline per mouse. Food and water were reintroduced 2 hours after the infection.

5 days post-infection, small intestines were harvested and fixed in 10% formalin for 2 days, then rinsed 3 times with 30% sucrose. The samples were then dehydrated and paraffin-embedded, sectioned into 4 μm thick slices and mounted onto glass microscope slides. Prior to staining, samples were rehydrated and deparaffinized. Antigen-retrieval for both groups was performed in pH 9.0 EDTA solution, at 110°C for 12 minutes in a microwave processor (Histo5, Milestone).

For CFU assays, five days post mice infection, desired organs were collected and homogenized using frosted glass slides (Fisherbrand) and filtered through a 70 μm cell strainer. The filtered spleen cells were centrifuged at 500 x g for 5 minutes and resuspended in 10 mL R8 medium (RPMI 1640 media (Gibco, Thermo-Fisher Scientific Inc) supplemented with 8% FBS (Gibco) and 55 μM 2-mercaptoethanol (Gibco). Appropriate serial dilutions were made in PBS and 100 uL aliquots were plated onto LB agar plates containing 100 ug/mL of streptomycin. Plates were incubated overnight at 37°C and CFU were counted the following day.

Mass-Spectrometry

Two 15 cm plates expressing FAM134B-FLAG and either HA-SOPF or mock plasmid cultured to 90-100% confluency were starved for amino acids for 1 h and subjected to immunoprecipitation. Beads were eluted with 100 μL Glycine 0.1M pH3 for 10 min with constant rocking and immediately neutralized with 10 uL 0.5M Tris-HCl pH 7.4 1.5M NaCl. Elutes were subjected to mass spectrometry analysis to identify post-translational modifications. TCEP [Tris(2-carboxyethyl)phosphine hydrochloride; Thermo Fisher Scientific] was added to the samples to a final concentration of 10mM. Samples were vortexed for 1 h at 37°C. Chloroacetamide (Sigma-Aldrich) was added for alkylation to a final concentration of 55 mM. Samples were vortexed for another hour at 37°C. One microgram of trypsin was added, and digestion was performed for 8 h at 37°C. Samples were dried down and solubilized in 5% ACN-4% formic acid (FA). The samples

were loaded on a 1.5 ul pre-column (Optimize Technologies, Oregon City, OR). Peptides were separated on a home-made reversed-phase column (150-µm i.d. by 200 mm) with a 56-min gradient from 10 to 30% ACN-0.2% FA and a 600-nl/min flow rate on a Easy nLC-1200 connected to a Exploris 480 (Thermo Fisher Scientific, San Jose, CA). Each full MS spectrum acquired at a resolution of 120,000 was followed by tandem-MS (MS-MS) spectra acquisition on the most abundant multiply charged precursor ions for 3s. Tandem-MS experiments were performed using higher energy collision dissociation (HCD) at a collision energy of 34%. The data were processed using PEAKS X Pro (Bioinformatics Solutions, Waterloo, ON) and a Uniprot database. Mass tolerances on precursor and fragment ions were 10 ppm and 0.01 Da, respectively. Fixed modification was carbamidomethyl (C). Variable selected posttranslational modifications were acetylation (N-ter), oxidation (M), deamidation (NQ), phosphorylation (STY). The data were visualized with Scaffold 5.0 (protein threshold, 99%, with at least 2 peptides identified and a false-discovery rate [FDR] of 1% for peptides).

Transmission Electron Microscopy

HEK293A cells were treated with the indicated treatments and fixed overnight in electron microscopy-grade 4% paraformaldehyde (EMS Cat#15713-s) and 3.5% glutaldehyde. To prepare the samples for electron microscopy, the cells were washed in PBS to eliminate the antifreeze solution. The samples are then treated with a mixture of 1.5% potassium ferrocyanide and 2% osmium tetroxide for 1 hour, followed by a ddH2O wash. Next, the cells undergo a 20 mins incubation in 10mg/mL TCH solution, another ddH2O wash, and a 30 mins treatment with 2% osmium tetroxide, followed by a final ddH2O rinse. The cells then undergo sequential 2 mins dehydration in increasing concentrations of ethanol, followed by 5 mins final dehydration in propylene oxide. The samples were then transferred to pans containing Durcupan resin and left

overnight until the samples sank. The following day, the samples are sandwiched between Aclar sheets coated with a thin resin layer and cured in a 55°C oven for 3 days. Finally, the samples are sectioned to 70nm thickness using an ultramicrotome with a diamond knife, mounted on 300-mesh copper grids (EMS cat #G300-Cu), and imaged using a Jeol JEM1400-Flash electron microscope at 80kV, with magnifications of 8000X and 15kX.

Generation of murine bone marrow-derived macrophages

WT and *FAM134B* KO C57BL/6J mice were euthanized following the guidelines set by the Canadian Council on Animal Care (CCAC). Bone marrow was harvested from the femur, tibia, and hip bones. The isolated bone marrow cells were plated onto petri dishes (Fisherbrand) that had been pre-coated with 5 ng/mL of macrophage colony-stimulating factor (BioLegend). The cells were then cultured in RPMI 1640 medium supplemented with 8% fetal bovine serum (Gibco) and 50μg/mL of gentamicin (Gibco). After a 7-day incubation at 37°C and 5% CO2, the bone marrow-derived macrophages were collected for subsequent experiments.

Statistical analysis

Error bars for western blot analysis represent the standard deviation between densitometry data collected using ImageJ software from at least three unique biological experiments. Statistical analyses were performed using GraphPad Prism 8. Statistical significance was determined using either Student's t-test or ANOVA. Differences with a P value <0.05 or lower were considered significant. significant. *$p<0.05$, **$p<0.01$, ***$p<0.001$. The number of independent experiments (n), statistical measurements tests utilized, dispersion of measurements, and significance are described in the figure legends. Sample sizing for cellular imaging was chosen to be the minimum

number of independent experiments required for statistically significant results and are described in figure legends.

Ethics compliance

All procedures involving mice were conducted at the University of Ottawa animal facility, adhering strictly to the guidelines established by the Canadian Council on Animal Care (CCAC). The University of Ottawa Animal Care Committee approved all experimental protocols.

Acknowledgements

We would like to thank Dr. John Brumell for sharing *Salmonella* mutants. We would also like to thank Karyn King for providing *FIP200* KO cell lines and Dr. Rudolf Mueller for scoring H&E staining. A big thank you to Zaida Ticas, Marjan Khalili and Mufida Alazzabi from the Louise Pelletier HCF at the University of Ottawa for all their help.

We would like to acknowledge the assistance of StemCore Laboratories Genomics Core Facility, OHRI, University of Ottawa (RRID:SCR_012601). The authors must acknowledge the Cell Biology and Image Acquisition Core (RRID: SCR_021845) funded by the University of Ottawa, Ottawa, Natural Sciences and Engineering Research Council of Canada, and the Canada Foundation for Innovation. We gratefully acknowledge the IHC tissue samples processing services provided by the Louise Pelletier HCF (RRID: SCR_021737) at the University of Ottawa. The authors acknowledge the Electron Microscopy Core (RRID: SCR_025398) funded by the University of Ottawa, Brain-Heart Interconnectome (BHI) via Canadian First Research Excellence Fund (CFREF). Finally, proteomics analyses were performed by the Center for Advanced Proteomics Analyses, a Node of the Canadian Genomic Innovation Network that is supported by the Canadian Government through Genome Canada.

This work was supported by the Canadian Institutes of Health Research (CIHR), funding reference number 181799 (D.G) & 376756 (R.C.R), 153034 (R.C.R), and Natural Sciences and Engineering Research Council of Canada #2023-05587 (R.C.R). R.M.A received support from the Ottawa Institute of System Biology and the Centre for Infection, Immunity and Inflammation.

Declaration of Interests

The authors declare no competing interests.

4.7 Supplementary Material

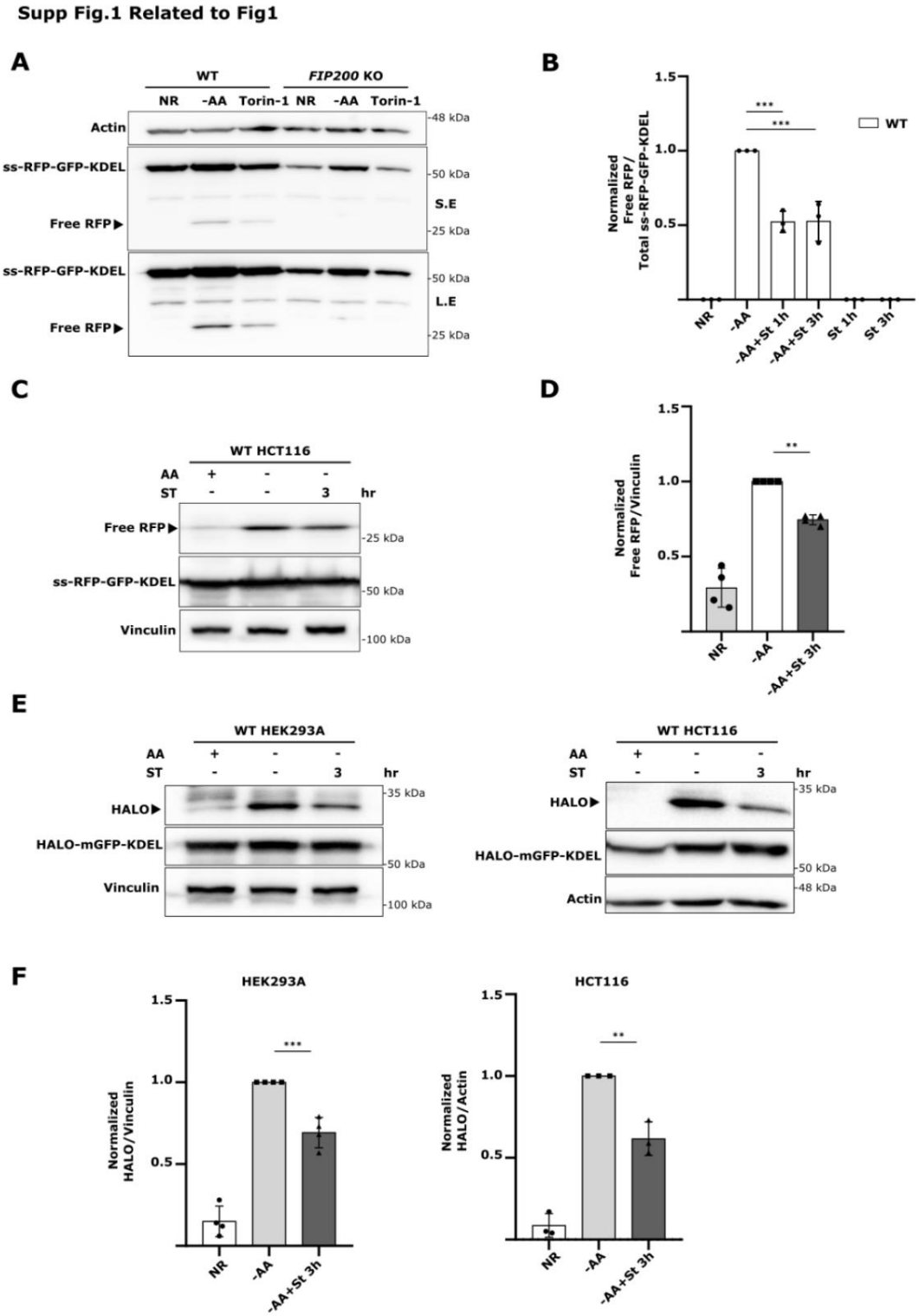

Supp Fig.1 Related to Fig1

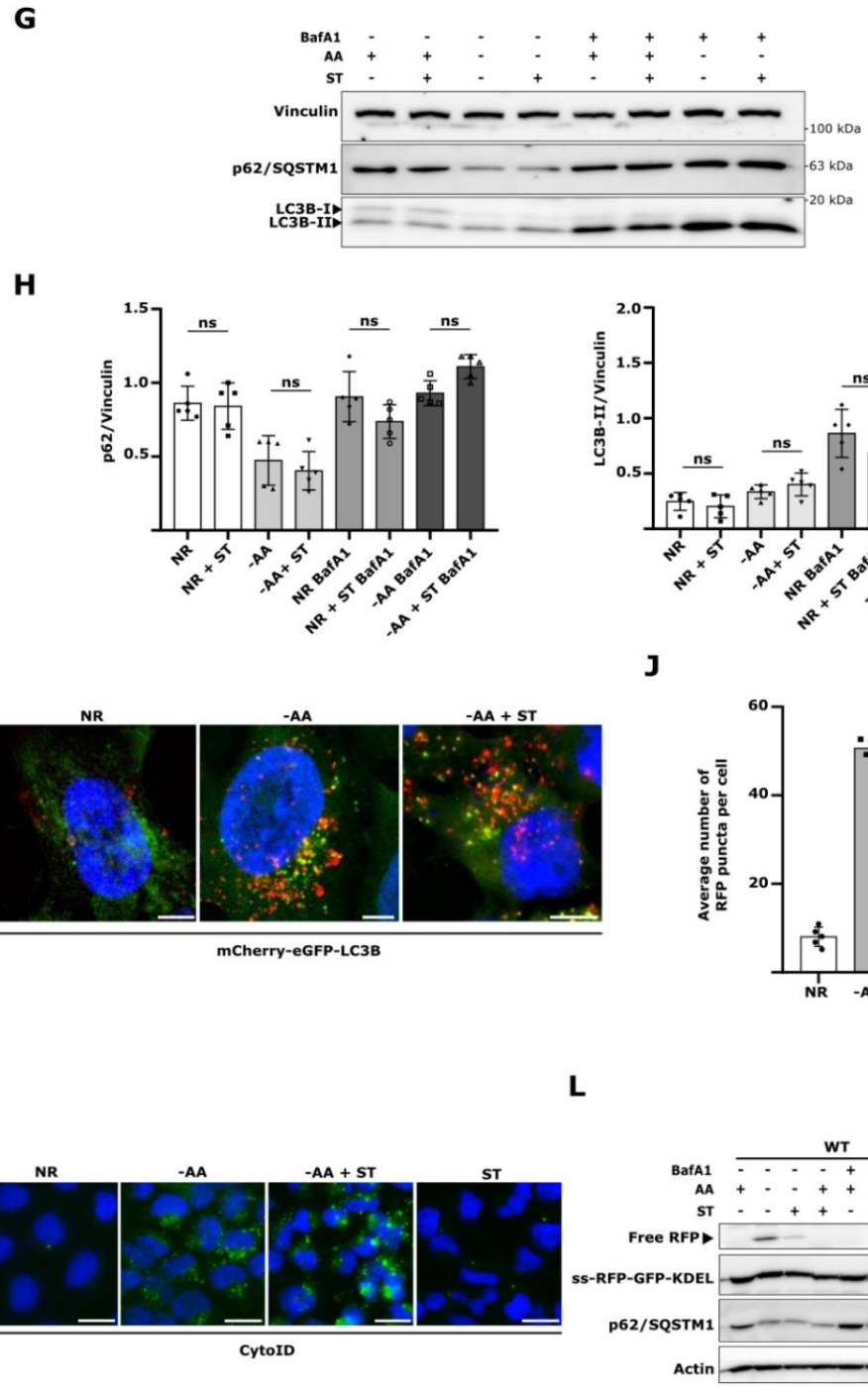

Supp Fig.1 Related to Fig1

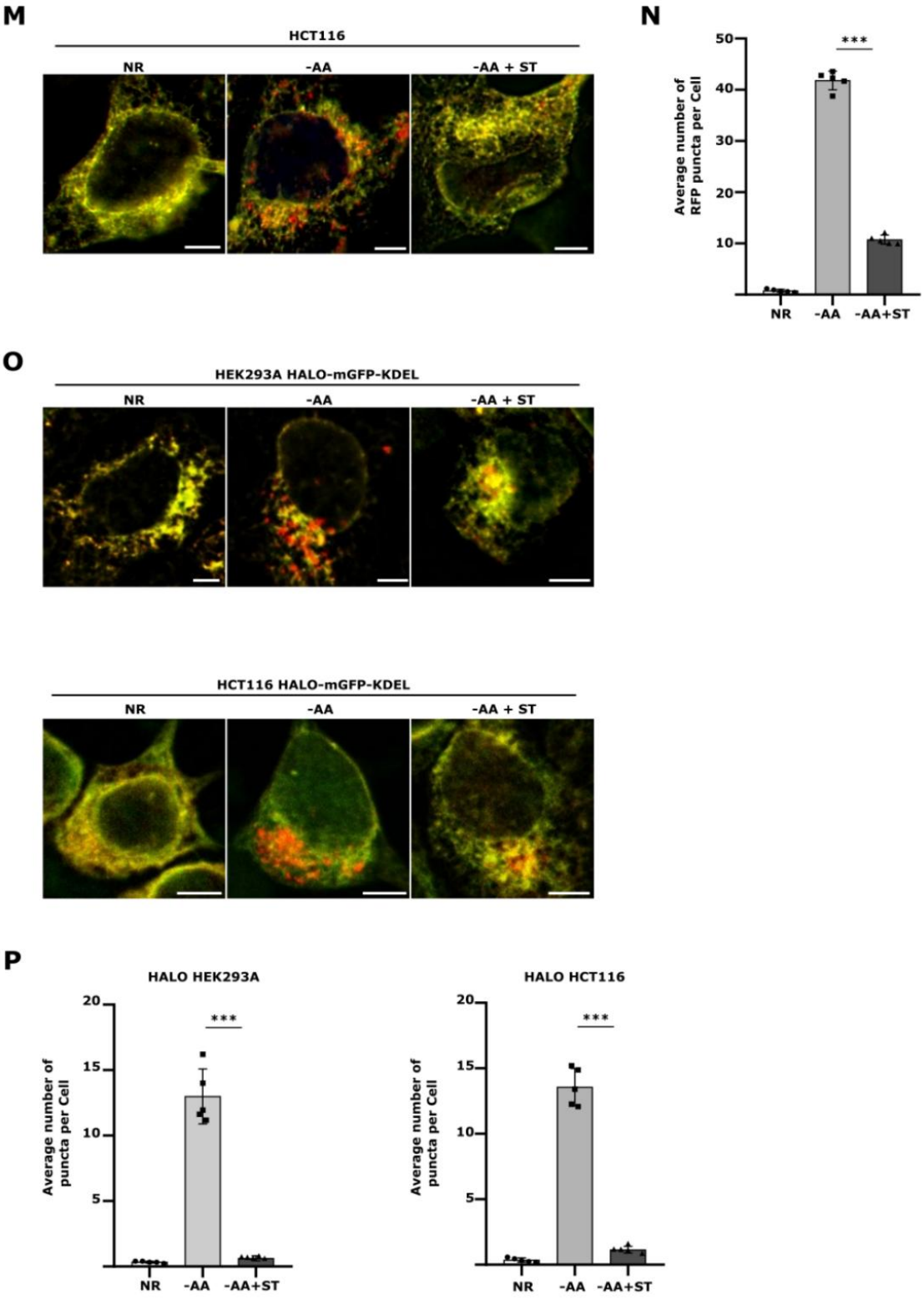

Supp Fig.1 Related to Fig1

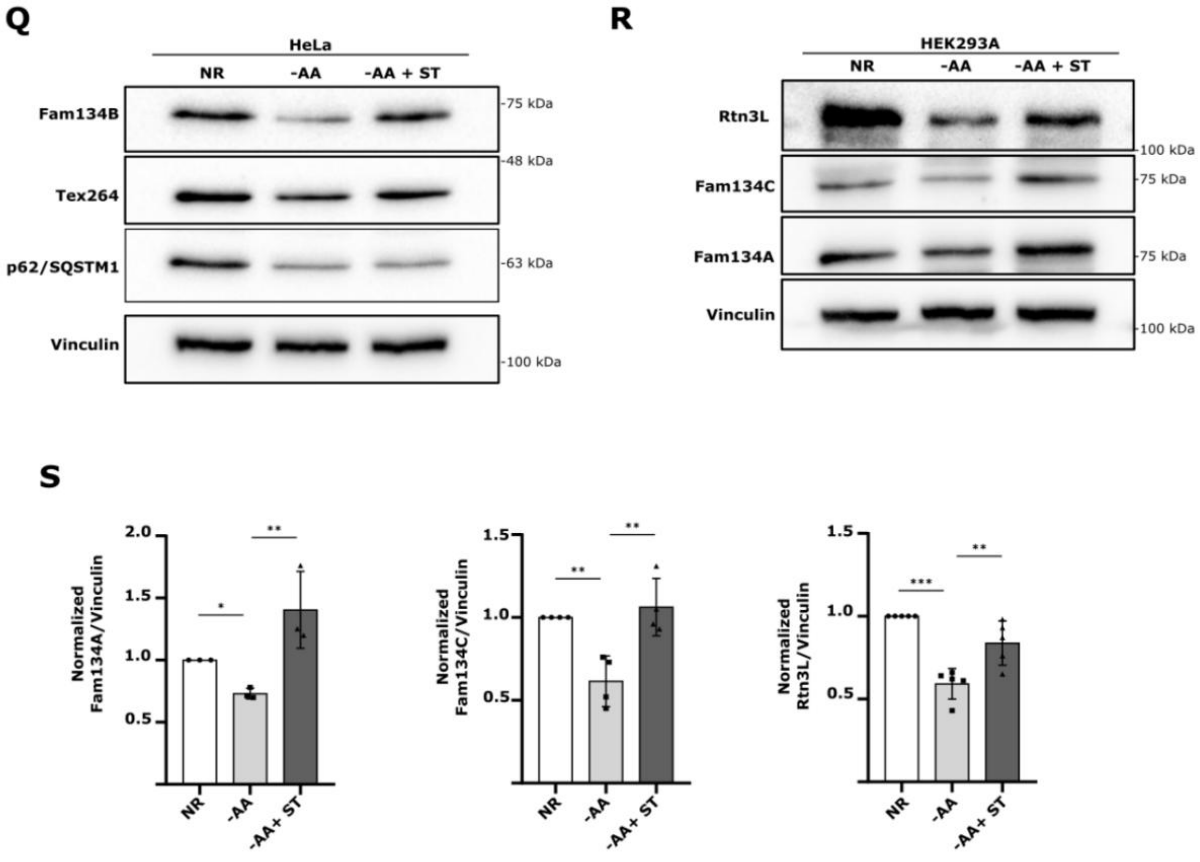

Supplementary Fig. 1. Related to Figure 1.

A) ER-phagy measurement example by ss-RFP-GFP-KDEL processing. WT and FIP200 KO HEK293A cells stably expressing the ss-RFP-GFP-KDEL reporter were either starved for AA or treated with Torin 1 for 6h. ER-phagy was measured by ss-RFP-GFP-KDEL processing. Actin was used as a loading control. NR, Nutrient Rich; AA, Amino Acids; S.E, Short Exposure; L.E, Long Exposure. B) Normalized Free RFP-Total ss-RFP-GFP- KDEL ratio from WT cells in Fig. 1A. Error bars indicate the standard deviation of 3 independent experiments. ANOVA, ***P <0.001. ST, Salmonella Typhimurium. C) WT HCT116 cells stably expressing the ss-RFP-GFP-KDEL reporter were starved for AA for 6h or starved for 6h followed by ST infection for the final 3h in AA starvation media. ER-phagy was measured by ss-RFP-GFP-KDEL processing. Vinculin was used as a loading control. D) Normalized Free RFP-Vinculin ratio from C). Error bars indicate the standard deviation of 4 independent experiments. ANOVA, **P <0.01. E) WT HEK293A and HCT116 cells stably expressing HaloTag (Halo)-mGFP-KDEL were pulse-labeled for 20 min with 100 nM tetramethylrhodamine-conjugated ligand in nutrient-rich media and either kept in NR, starved for AA for 6h or starved for 6h followed by ST infection for the final 3h in AA starvation media. ER-phagy was measured by the Halo-based processing assay. F) Normalized HALO-Vinculin and HALO-Actin ratios from HEK293A and HCT116 cells, respectively in E). Error bars indicate the standard deviation of at least 3 independent experiments. ANOVA, **P<0.01; ***P <0.001. G) WT HEK293A were either kept in NR or starved for 2h in combination with ST infection and/or BafA1. Vinculin was used as a loading control. BafA1, Bafilomycin A1. H) p62-Vinculin and LC3B-II-Vinculin ratios from G). Error bars indicate the standard deviation of 5 independent experiments. ANOVA. ns, no significance. I) WT HEK293A cells stably expressing the general autophagy reporter mCherry-eGFP-LC3B were starved for 6 h or starved for 3h followed by ST infection for 3h in AA starvation media. Representative images are shown. mCherry-eGFP- LC3B, yellow; Free mCherry, red; DAPI, blue. Scale bars, 5 μm. J) Average number of RFP puncta per cell from I). Error bars indicate standard deviation of 5 independent experiments. Average RFP puncta formation was calculated from a minimum of 100 cells. ANOVA. ns, no significance. K) WT HEK293A cells were either kept in NR, starved for AA in the absence or presence of ST or infected with ST in NR conditions. Non-selective autophagy was measured by CytoID. Autophagic vacuoles, green; Hoechst, blue. L) HEK293A WT and FIP200 KO cells stably expressing the ss-RFP-GFP-KDEL reporter were starved for AA for 6h in the presence or absence of BafA1 or starved for 3h followed by ST infection for 3h in AA starvation media with or without BafA1. ER-phagy was measured by ss-RFP-GFP-KDEL processing. Non-selective autophagy activity was measured by p62/SQSTM1

degradation. Actin was used as a loading control. M) WT HCT116 cells stably expressing the ss-RFP-GFP-KDEL reporter were starved for AA for 6h or starved for 3h followed by ST infection for 3h in AA starvation media. Representative images are shown. Scale bar 5 μm. N) Average number of RFP puncta per cell from M). Error bars indicate standard deviation of 5 independent experiments. Average RFP puncta formation was calculated from a minimum of 100 cells. ANOVA, ***P <0.001. O) WT HEK293A and HCT116 cells stably expressing HaloTag (Halo) mGFP-KDEL were pulse- labeled for 20 min with 100 nM tetramethylrhodamine-conjugated ligand in NR media and either kept in NR, starved for AA for 6h or starved for 6h followed by ST infection for the final 3h in AA starvation media. Representative images are shown. Ligand-Halo-mGFP-KDEL, yellow; ligand-Halo, red. Scale bar 5 μm. P) Average number of puncta per cell from O). Error bars indicate standard deviation of 5 independent experiments. Average puncta formation was calculated from a minimum of 100 cells. ANOVA, ***P <0.001. Q) WT HeLa cells were AA starved for 2h or starved for 2h in the presence of ST. Vinculin was used as a loading control. R) WT HEK293A cells were AA starved for 2h or starved for 2h in the presence of ST. Vinculin was used as a loading control. S) Normalized Fam134A-Vinculin, Fam134C-Vinculin and Rtn3L-Vinculin ratios from R) were quantified. Error bars indicate the standard deviation of at least 3 independent experiments. ANOVA, *P<0.05, **P<0.01, ***P <0.001.

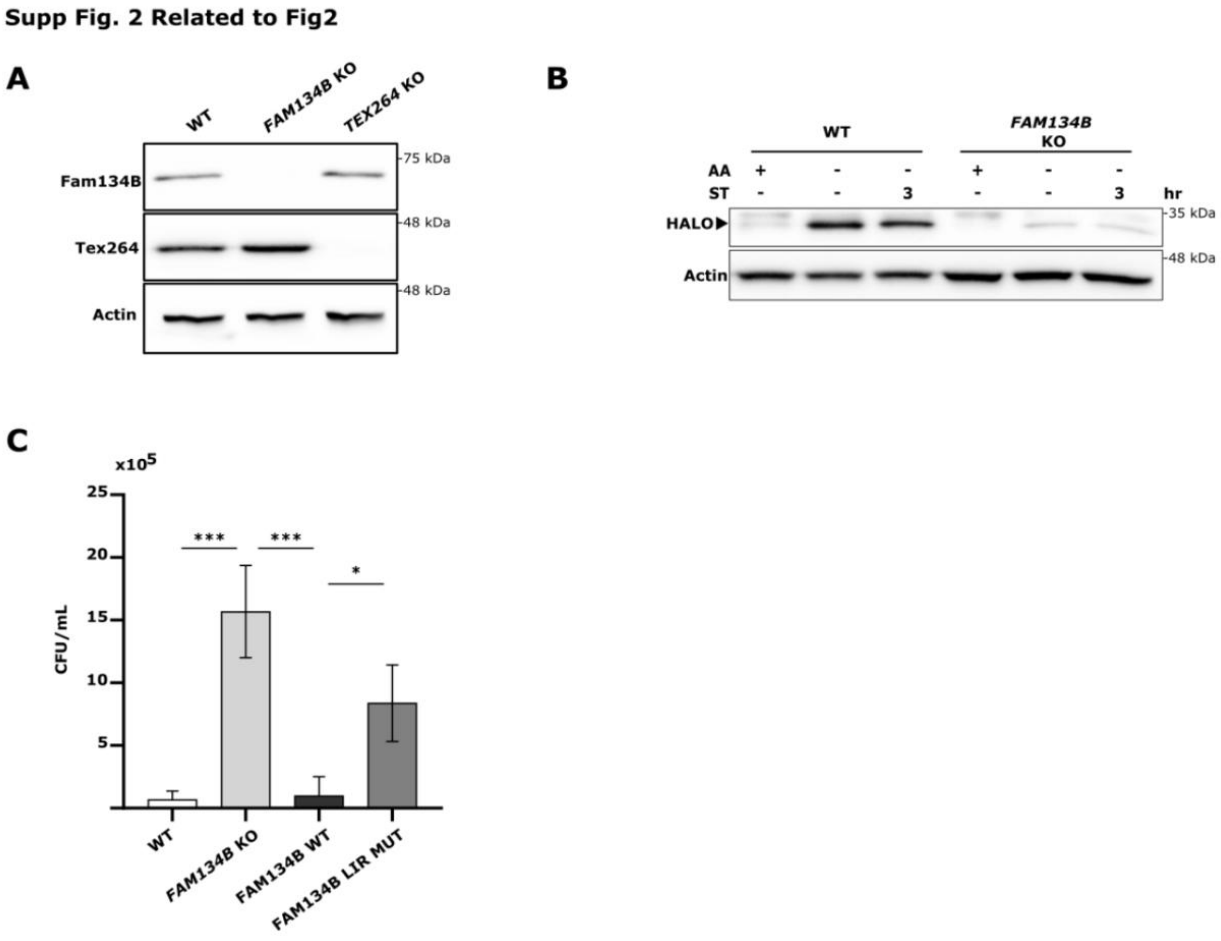

Supplementary Fig. 2. Related to Figure 2.

A) Fam134B, Tex264 and Actin levels were determined by western blot in HEK293A WT, *FAM134B* KO and *TEX264* KO cells **B)** HEK293A WT and *FAM134B* KO cells stably expressing HaloTag (Halo)-mGFP-KDEL were pulse-labeled for 20 min with 100 nM tetramethylrhodamine-conjugated ligand in nutrient-rich media and either starved for AA for 6h or starved for 6h followed by ST infection for the final 3h in AA starvation media. ST, *Salmonella* Typhimurium. **C)** HCT116 WT and *FAM134B* KO cells transfected with either FAM134B WT, FAM134B LIR mutant or a mock plasmid were infected with ST. Bacterial content was determined through colony-forming unit (CFU). Error bars indicate standard deviation. ANOVA, *P <0.05; ***P <0.001.

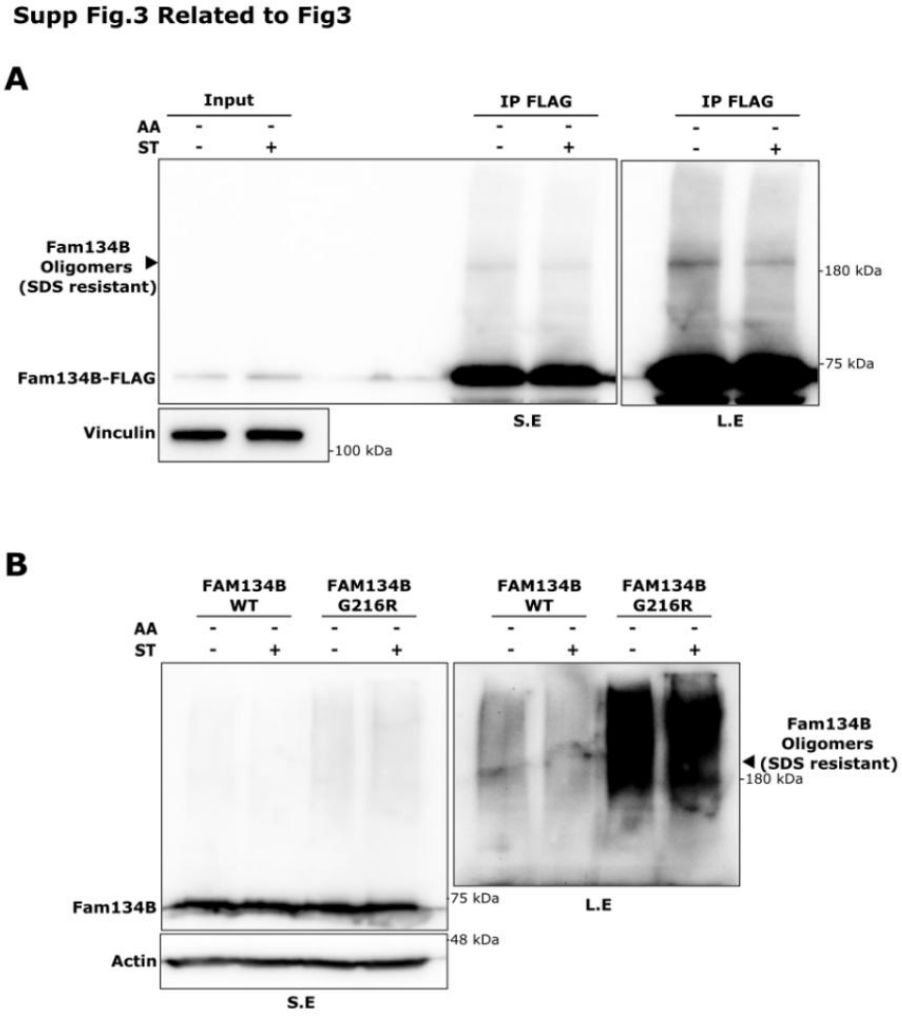

Supplementary Fig. 3. Related to Figure 3.

A) HCT116 *FAM134B* KO cells transfected with FAM134B-FLAG were starved for AA for 3h in the absence or presence of ST. FLAG was immunoprecipitated. Vinculin was used as a loading control. AA, amino acids; ST, *Salmonella* Thypimurium. S.E, Short Exposure; L.E, Long Exposure. **B)** HEK293A expressing FAM134B WT or FAM134B G216R were starved for AA for 3h in the absence or presence of ST. Actin was used a loading control.

Supp Fig. 4 Related to Fig4

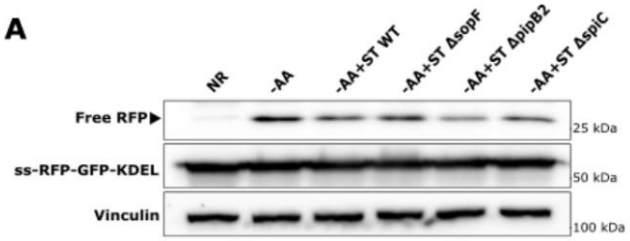

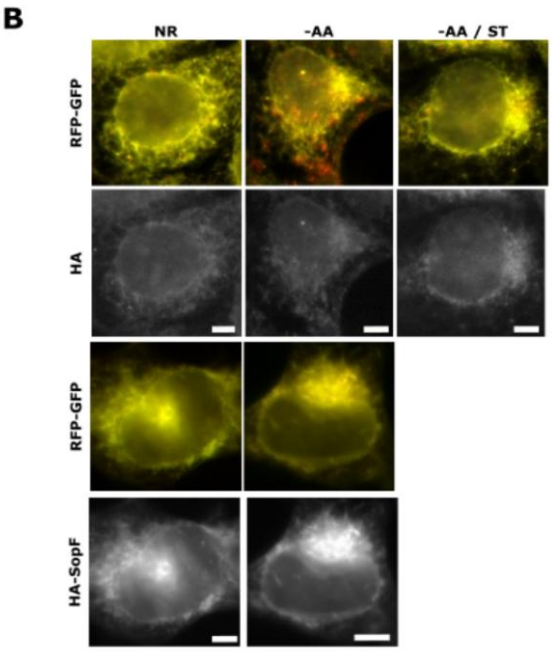

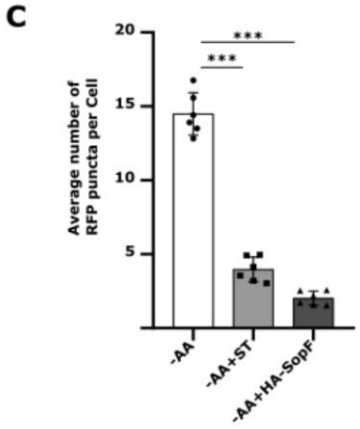

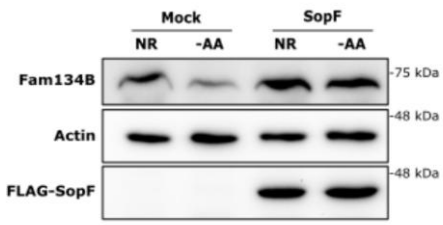

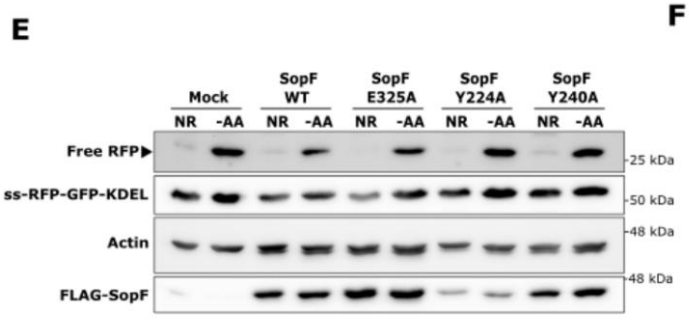

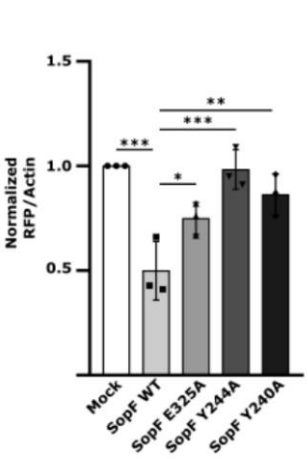

Supp Fig. 4 Related to Fig4

G

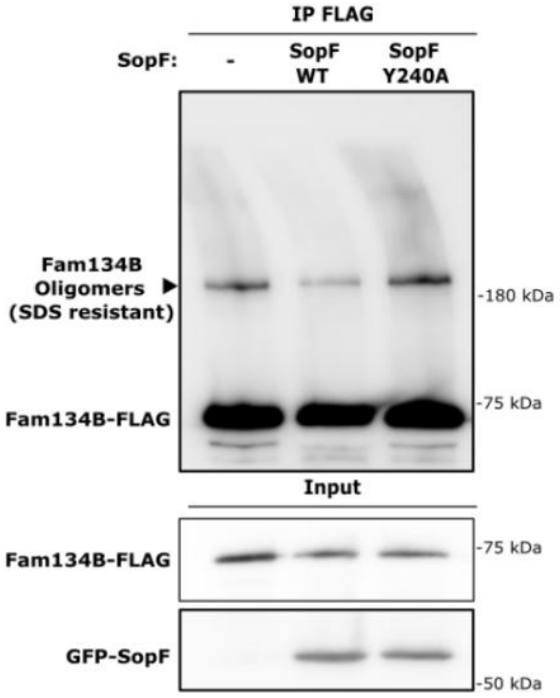

H

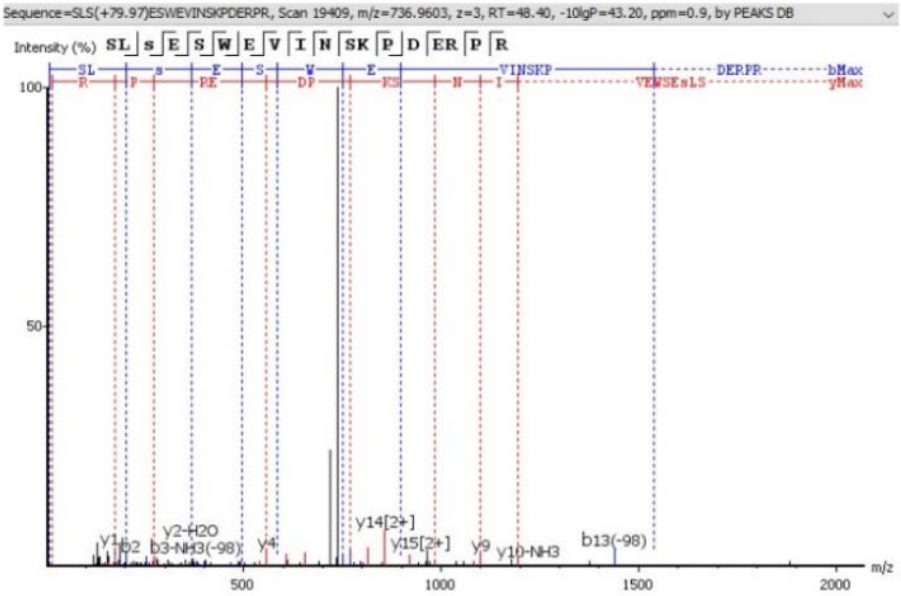

Supplementary Fig. 4. Related to Figure 4

A) Some of the mutants tested. WT HEK293A cells stably expressing ss-RFP-GFP-KDEL were starved for AA for 6h or starved for 3h followed by ST WT, *Δ*sopF, *Δ*pipB2 or *Δ*spiC infection for 3h in AA starvation media. Vinculin was used as a loading control. ST, *Salmonella* Typhimurium; NR, nutrient rich; AA, amino acids. **B)** WT HEK293 cells stably expressing ss-RFP-GFP-KDEL were transfected with HA-SOPF or a mock plasmid and starved for AA for 6h. Representative images are shown. ss-RFP-GFP-KDEL, yellow; Free RFP, red; HA, far red. Scale bar, 5 μm. **C)** Average number of RFP puncta per cell from B). Error bars indicate standard deviation of 6 independent experiments. Average puncta formation was calculated from a minimum of 100 cells. ANOVA, ***P <0.001. **D)** WT HEK293A cells expressing FLAG-SopF or a mock plasmid were AA starved for 2h. Fam134B, Actin and FLAG-SopF levels were determined by western blot. **E)** WT HEK293A cells stably expressing ss-RFP-GFP-KDEL were transfected with either FLAG-SopF WT, E325A, Y224A, Y240A or a mock plasmid and then starved for AA for 6h. ER-phagy was measured by ss- RFP-GFP-KDEL processing. Actin was used as a loading control. **F)** Normalized RFP-Actin ratio from E). Error bars indicate the standard deviation of 3 independent experiments. ANOVA, *P<0.05; **P<0.01; ***P <0.001. **G)** *FAM134B* KO cells transfected with FAM134B-FLAG and either GFP-SopF WT, GFP-SopF Y240A or a mock plasmid were starved for AA for 3h. FLAG was immunoprecipitated. **H)** Mass spectrometry analysis shows FAM134B phosphorylation at Serine 151 in WT cells but not SopF-expressing cells.

Supp Fig.5 Related to Fig.5

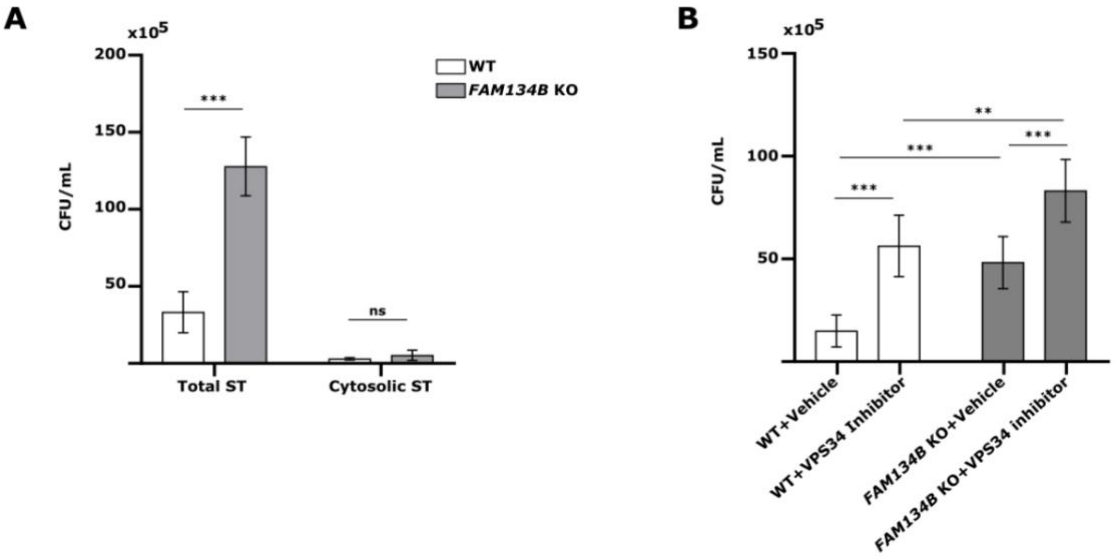

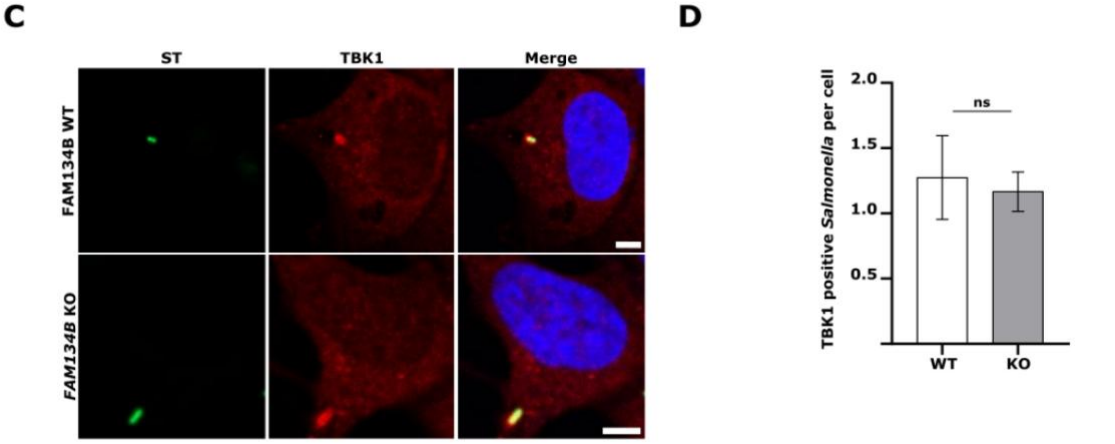

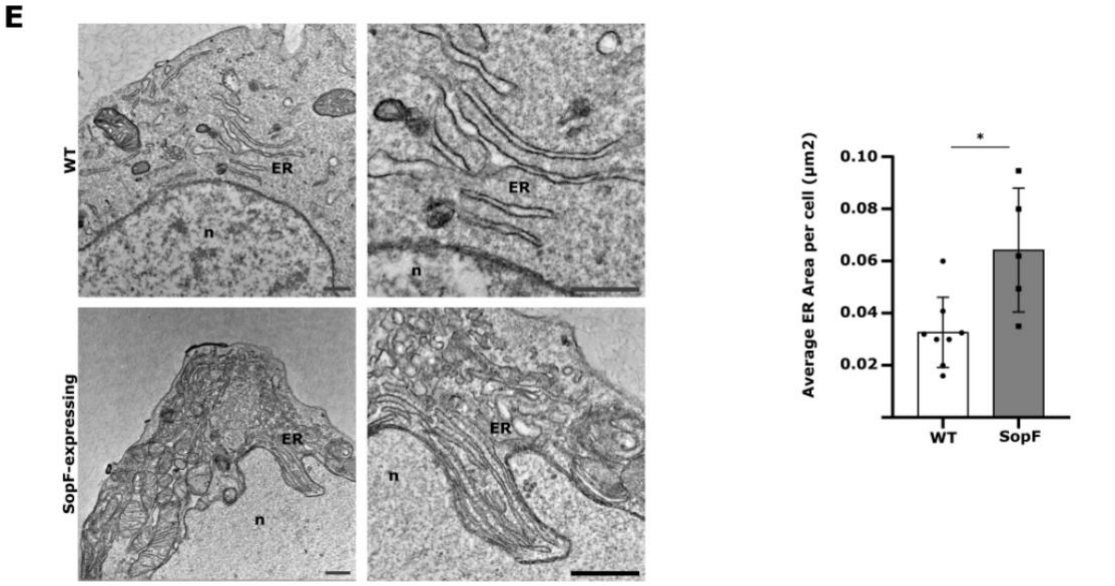

Supplementary Fig. 5. Related to Figure 5

A) WT HEK293A were infected with WT ST and the total and cytosolic ST content was determined through colony forming unit (CFU). Error bars indicate standard deviation. ANOVA, ***P <0.001; ns, no significance. ST, *Salmonella* Typhimurium. **B)** WT HCT116 were infected with WT ST in the presence and absence of the VPS34 inhibitor, VPS34-IN1. ST content was determined through CFU. Error bars indicate standard deviation. ANOVA, **P<0.01; ***P <0.001. **C)** HEK293A WT and *FAM134B* KO cells were infected with ST for 1h, fixed and imaged by confocal microscopy. Representative images are shown. ST, green; TBK1, red; DAPI, blue. Scale bar 5 μm. **D)** Number of TBK1 positive ST per cell from C). Error bars indicate standard deviation. Number of TBK1 positive ST was calculated from a minimum of 100 cells. Student's t-test; ns, no significance. **E)** Representative transition electron microscopy images of HEK293A WT and SopF-expressing cells. Nucleus, n; Endoplasmic Reticulum; ER. Scale bar, 0.5 μm. Average ER area per cell is represented. Error bars indicate standard deviation. A minimum of 5 cells were analyzed for each condition. Student's t-test; *P<0.05.

Chapter 5: General Discussion

5.1 An antibody for analysis of autophagy induction

The characterization of pATG16L1^{278} as a marker for autophagy provided a new tool for researchers studying autophagy-related events. The phospho-protein based readout not only circumvents the limitations existing autophagy markers such as LC3B and p62, it also serves as a marker of early stage autophagosomes. pATG16L1^{278} is directly linked to the ULK1 complex and mTORC1 signaling pathway, which control autophagy initiation. ULK1, a serine/threonine kinase, is inhibited by mTORC1 under nutrient-rich conditions and activated during stress to promote autophagy[16,151]. Earlier work has shown that ULK1 phosphorylation of multiple downstream ATG proteins is essential for autophagy initiation[12,13]. The discovery of pATG16L1^{278} as a downstream target of ULK1 provides a new molecular link between ULK1 activation and the recruitment of autophagy machinery to nascent autophagosomes.

The study also addresses the limitations of widely used autophagy markers, such as LC3B and p62. LC3B, particularly its lipidated form (LC3B-II), has been a gold standard for monitoring autophagy due to its association with autophagosomal membranes[152,153]. However, disruptions of the autophagy pathway can also lead to LC3B-II accumulation, leading to potentially false interpretation of autophagy[154]. Similarly, p62, an autophagy adapter protein, is degraded during autophagy, but its levels can be influenced by transcriptional regulation and stress-induced changes, complicating its use as a reliable marker[155,156]. pATG16L1^{278} is free of those caveats, since it is specific to newly forming autophagosomes and unaffected by late-stage autophagy blocks. Thus, pATG16L1^{278} offers a more accurate representation of autophagic than the more

traditionally used markers. Additionally, in systems where LC3-II and p62 measurement are difficult, pATG16L1^{278} provide an alternative method for autophagy readout.

Advanced imaging techniques were employed in this study, including high-resolution confocal microscopy and electron microscopy, to validate the localization of pATG16L1^{278} to nascent autophagosomes. This approach is consistent with previous studies that have used similar techniques to visualize autophagosome formation and dynamics[157,158]. For example, Koyama-Honda et al. utilized live-cell imaging to track the recruitment of ATG proteins to autophagosome formation sites, providing insights into the temporal and spatial regulation of autophagy[158]. This study builds on the work by demonstrating that pATG16L1^{278} is specifically associated with expanding autophagosomal membranes, validating its property to be used as a marker for nascent autophagosomes.

The findings of this study have significant implications autophagy-related research, as autophagy dysregulation have been linked to multiple human health conditions, such as neurodegenerative disorders, cancer, and metabolic diseases. For instance, in neurodegenerative diseases like Alzheimer's and Parkinson's, impaired autophagy has been linked to the accumulation of toxic protein aggregates[159]. The ability to monitor autophagy induction specifically, without the confounding effects of impaired autophagosome clearance, could provide new insights into the role of autophagy in these conditions. Similarly, in cancer, autophagy plays a dual role, acting as both a tumor suppressor and a survival mechanism for cancer cells under stress[160]. The use of pATG16L1^{278} as a marker could help clarify the role of autophagy in tumor progression and response to therapy. Looking ahead, the study opens several avenues for future research. One promising direction is the exploration of other phosphorylation sites on ATG16L1 and their potential roles in regulating autophagy. High-throughput mass spectrometry data suggest that other

serine and threonine residues in the same region as S278 may also be phosphorylated, raising the possibility of additional regulatory mechanisms[161]. Investigating these sites could provide a more comprehensive understanding of how ATG16L1 and other autophagy-related proteins are regulated during autophagy initiation.

Lastly, pATG16L1^{278} based readouts can be combined with traditional methods including LC3B and p62 analysis to provide a more holistic view of autophagy flux. While pATG16L1^{278} is specific to autophagy induction, combining its analysis with markers that reflect later stages of autophagy (e.g., autophagosome-lysosome fusion) could help distinguish between different phases of the autophagy process. This would be particularly valuable in complex experimental systems, such as *in vivo* models or patient samples, where autophagy dynamics may vary widely. In summary, the study on pATG16L1^{278} represents a significant advancement in the field of autophagy research. By providing a tool that is specific to autophagy induction and unaffected by late-stage blocks, it addresses key limitations of existing markers and offers new opportunities for studying autophagy in health and disease. The findings build on and complement previous research on ULK1, mTORC1, and autophagy markers like LC3B and p62, while also opening new avenues for future investigation. There are some limitations of using pATG16L1^{278} as the sole marker for monitoring autophagy. For example, in paper 2 we were mainly interested in a process that occurred during late stage autophagy, while in paper 3 we were more interested in monitoring selective autophagy (ERphagy) rather than general autophagy. In both cases, pATG16L1^{278} was not the best tool for the autophagy analysis of interest. As the field continues to explore the complex regulation of autophagy, tools like pATG16L1^{278} will be invaluable for gaining deeper insights into this critical cellular process.

5.2 Iron overload inhibits late stage autophagy flux leading to insulin resistance

Our investigation has provided mechanistic insights on how iron overload (IO) could lead to insulin resistance and metabolic syndrome through the perturbation of autophagy signaling. Specifically, we found that IO inhibited mTORC1-UVRAG signaling and autophagy through impairment of the autophagic-lysosome regeneration (ALR) process. This novel discovery adds to a growing body of evidence linking IO to metabolic dysfunction and metabolic syndrome. For instance, previous studies have demonstrated that IO exacerbates oxidative stress and mitochondrial dysfunction, which are key contributors to insulin resistance and beta-cell dysfunction in diabetes[162,163]. Elevated iron levels caused by IO can generate reactive oxygen species (ROS), resulting in damage to cellular components such as proteins, lipids, and DNA, leading to impaired insulin signaling and glucose metabolism. Additionally, IO has also been shown to disrupt adipocyte function, resulting in reduced adiponectin secretion and further exacerbating insulin resistance[164].

The role of autophagy in metabolic regulation is increasingly being investigated in recent studies. For instance, it has been demonstrated that adiponectin-stimulated autophagy enhances insulin sensitivity and metabolic function in skeletal muscle. While IO-induced insulin resistance has been linked to reduced adiponectin expression in adipocytes, suggesting inhibition of autophagy as a mechanism through which IO leads to insulin resistance[165]. However, we have found that acute IO can stimulate autophagy, as we observed autophagy activation within 8 hours of IO exposure. This response is likely a compensatory mechanism to cellular stress. Acute IO also rapidly inhibits mTORC1, a key regulatory kinase that normally represses autophagy. However, acute IO does not reflect the chronic IO seen in clinical settings, which we have found to inhibit autophagy instead. This was a consequence of chronic inhibition of mTOCR1 signaling, which inhibited the ALR

pathway crucial for recycling autolysosomal membranes and restoring cellular degradative capacity and autophagic function. Normally, mTORC1 is locally reactivated on mature autolysosomes, promoting lysosomal reformation. However, chronic IO disrupted this process, impairing lysosome regeneration and significantly reduced lysosome numbers. Additionally, forced activation of mTORC1 via constitutively active RHEB-GTPase prevented autophagosome accumulation, minimized lysosomal loss, and restored insulin sensitivity in IO-exposed cells. These findings strongly suggest that IO-induced inhibition of autophagy contributes to insulin resistance.

In summary, our study provides novel insights into the molecular mechanisms underlying IO-induced insulin resistance and presents the first *in vivo* model demonstrating an ALR defect. Mechanistically, chronic IO reduces Akt-mediated repression of TSC2, leading to RHEB and mTORC1 inhibition and subsequent ALR impairment. Our data also highlight the importance of mTOR-UVRAG-dependent lysosomal pool regeneration in maintaining autophagic flux and insulin sensitivity in skeletal muscle. These findings reveal a previously unrecognized mechanism by which chronic IO disrupts autophagy and contributes to metabolic dysfunction, with potential implications for various diseases where cellular IO plays a pathogenic role.

5.3 The ER-phagy receptor FAM134B is targeted by *Salmonella* Typhimurium to promote infection

This study builds on a growing body of research that highlighted the critical role of FAM134B in ER-phagy and its involvement in cellular defense mechanisms against various pathogens. FAM134B, an ER-phagy receptor, has previously been implicated in the degradation of damaged ER and the regulation of ER homeostasis. Additionally, FAM134B also have well known antiviral functions, with studies demonstrating that FAM134B-dependent ER-phagy limits the replication

of viruses such as SARS-CoV-2, Ebola, Zika, and dengue[166,167, 168]. For example, during Ebola virus infection, FAM134B has been shown to restrict viral replication by promoting the degradation of viral components through ER-phagy[169]. Similarly, Zika and dengue viruses subvert FAM134B-mediated ER-phagy by cleaving the receptor, thereby evading cellular defense mechanisms[169]. Collectively, these studies underscore the importance of FAM134B in the cellular response to viral infections and provide a foundation for understanding its role in bacterial infections, as explored in this study.

Intracellular pathogens manipulate ER morphology and, in general, autophagy pathways to promote their survival. For instance, *Legionella pneumophila*, another intracellular bacterium, has been shown to exploit ER-phagy receptors, including FAM134B and TEX264, to remodel the ER and create a favorable environment for replication[170]. *Legionella* achieves this by inducing phosphoribosyl-linked ubiquitination of ER-phagy receptors, which triggers ER remodeling and membrane recruitment to bacterial-containing vacuoles[170]. This is a clear parallel to the findings of the current study, where *Salmonella Typhimurium* targets FAM134B to inhibit ER-phagy and promote bacterial survival. The convergent nature of bacterial manipulation ER-phagy receptors shows that this may be a common mode of strategy employed by intracellular pathogens to evade host defenses and establish infection.

We identified SopF as the key *Salmonella* effector for ER-phagy modulation. Similarly, SopF has previously been identified as an inhibitor of xenophagy, a selective autophagy pathway that targets intracellular bacteria for degradation. Specifically, SopF disrupts the interaction between the v-ATPase and ATG16L1 by ADP-ribosylating the v-ATPase subunit ATP6V0C, thereby inhibiting xenophagy[171]. We have extended these findings by demonstrating that SopF also inhibits ER-phagy by targeting FAM134B, highlighting the versatility of SopF in disrupting multiple

autophagy pathways. The dual inhibition of both xenophagy and ER-phagy by SopF suggests that *Salmonella* employs a multi-faceted approach to evade host defenses, further emphasizing the complexity of host-pathogen interactions.

The activity of ER-phagy receptors is regulated through post-translational modifications. For example, TEX264, another ER-phagy receptor, has been shown to require phosphorylation by casein kinase 2 (CK2) for efficient interaction with ATG8 proteins and the induction of ER-phagy[172]. Similarly, FAM134B oligomerization is regulated by phosphorylation and acetylation, both are critical for its function in ER membrane scission and ER-phagy[173,174]. We showed that *Salmonella* infection reduced FAM134B phosphorylation and acetylation, thereby inhibiting its oligomerization and ER-phagy activity. Further highlighting the importance of these regulatory post-translational modifications, and how pathogens could work to exploit these regulatory controls for their own benefit.

The ability of *Salmonella* to avoid lysosomal degradation and manipulate host membrane trafficking pathways has been extensively studied[175,176]. By demonstrating that *Salmonella* also targets ER-phagy to promote its survival, we have revealed another angle of the complex pathogen-host interplay. Importantly, this finding further strengthens the role of autophagy in host defense against invasive bacteria. Previous studies have already demonstrated autophagy-deficient cells are more permissive for *Salmonella* growth, highlighting the importance of autophagy in controlling bacterial infections [177].

The interplay between ER-phagy and other selective autophagy pathways, such as xenophagy, is an area of growing interest. Xenophagy, which targets intracellular pathogens for degradation, is mediated by the recruitment of autophagy receptors such as NDP52 and TBK1 to the bacteria[178]. Our findings hint at a possible link between ER-phagy and xenophagy, as FAM134B-deficient

cells showed reduced LC3B recruitment to *Salmonella*, suggesting that ER-phagy may play a role in bacterial clearance. This opens up new avenues for research into the coordination of different autophagy pathways during bacterial infection and how pathogens may exploit these interactions to evade host defenses.

FAM134B and its regulatory partners emerged from our study as potential therapeutic targets for intra-cellular bacterial clearance. We found that promoting FAM134B oligomerization bypassed *Salmonella*-mediated ER-phagy inhibition, suggesting that small molecules or peptides that enhance FAM134B activity could be developed as potential therapeutics. There exist similar ongoing efforts to modulate autophagy for the treatment of infectious diseases and other conditions[179,180]. For example, pharmacological activation of autophagy has been explored as a strategy to enhance the clearance of intracellular pathogens such as *Mycobacterium tuberculosis* and *Listeria monocytogenes*[179,180]. Our study adds to this body of work by identifying FAM134B as a potential target for therapeutic intervention in *Salmonella* infections.

In conclusion, our study identified novel roles of ER-phagy in cellular defense against *Salmonella*, and how *Salmonella* seeks to exploit the system through manipulating the ER-phagy receptor FAM134B. The identification of Salmonella effector protein SopF as a key effector that inhibited both ER-phagy and xenophagy highlighted the complexity of host-pathogen interactions and opened new avenues for research into the co-operative interplay between different branches of the autophagy pathways. Future research should focus on elucidating the molecular mechanisms of SopF-FAM134B interaction, exploring the role of FAM134B in regulating non-ER-phagy autophagy pathways, and investigating its potential as a therapeutic target for bacterial infections.

5.4 Conclusion

In conclusion, the three studies featured in this thesis significantly advanced our understanding of autophagy, each from a unique aspect, featuring better autophagy measurement, regulation by iron metabolism, and host-pathogen interplay in ER-phagy. The first study demonstrated pATG16L1^{278} as a novel marker for autophagy induction, overcoming limitations of traditional markers and offered potential for new insights into early autophagosome formation, providing a great alternative tool for autophagy researchers across disciplines. The second study revealed how iron overload induced insulin resistance through autophagy defects, particularly via mTORC1-UVRAG signaling, emphasizing the need for further research into chronic iron overload models and tissue-specific responses. It also highlighted potential therapeutic strategies targeting defects in autophagy and iron metabolism. The third study elucidated the role of FAM134B in ER-phagy and its manipulation by pathogens like *Salmonella Typhimurium*, demonstrating how bacterial effectors such as SopF could disrupt host autophagy pathways. These findings deepened our understanding of host-pathogen interactions and suggested new therapeutic avenues for enhancing bacterial clearance. Collectively, these studies underscore the importance of autophagy-related pathways in health and disease, paving the way for future research and clinical applications aimed at addressing metabolic disorders, infections, and other autophagy-related conditions.

Appendix I

References Cited

Citation of Chapter 1 and Chapter 5

1. Duve, C. de & Wattiaux, R. Functions of Lysosomes. *Annu. Rev. Physiol.* **28**, 435–492 (1966).
2. Smith, R. E. & Farquhar, M. G. Lysosome function in the regulation of the secretory process in cells of the anterior pituitary gland. *J. Cell Biol.* **31**, 319–347 (1966).
3. Matsuura, A., Tsukada, M., Wada, Y. & Ohsumi, Y. Apg1p, a novel protein kinase required for the autophagic process in Saccharomyces cerevisiae. *Gene* **192**, 245–250 (1997).
4. Tsukada, M. & Ohsumi, Y. Isolation and characterization of autophagy-defective mutants of Saccharomyces cerevisiae. *FEBS Lett.* **333**, 169–174 (1993).
5. Mizushima, N., Sugita, H., Yoshimori, T. & Ohsumi, Y. A new protein conjugation system in human. The counterpart of the yeast Apg12p conjugation system essential for autophagy. *J. Biol. Chem.* **273**, 33889–33892 (1998).
6. Klionsky, D. J. The molecular machinery of autophagy: unanswered questions. *J. Cell Sci.* **118**, 7–18 (2005).
7. Kaushik, S. & Cuervo, A. M. Chaperone-mediated autophagy: a unique way to enter the lysosome world. *Trends Cell Biol.* **22**, 407–417 (2012).
8. Abounit, K., Scarabelli, T. M. & McCauley, R. B. Autophagy in mammalian cells. *World J. Biol. Chem.* **3**, 1–6 (2012).
9. Mizushima, N. & Komatsu, M. Autophagy: renovation of cells and tissues. *Cell* **147**, 728–741 (2011).
10. Lim, J. & Yue, Z. Neuronal aggregates: formation, clearance, and spreading. *Dev. Cell* **32**, 491–501 (2015).
11. Anding, A. L. & Baehrecke, E. H. Cleaning House: Selective Autophagy of Organelles. *Dev. Cell* **41**, 10–22 (2017).
12. Hosokawa, N. *et al.* Nutrient-dependent mTORC1 association with the ULK1-Atg13-FIP200 complex required for autophagy. *Mol. Biol. Cell* **20**, 1981–1991 (2009).
13. Jung, C. H. *et al.* ULK-Atg13-FIP200 complexes mediate mTOR signaling to the autophagy machinery. *Mol. Biol. Cell* **20**, 1992–2003 (2009).
14. Suzuki, H., Osawa, T., Fujioka, Y. & Noda, N. N. Structural biology of the core autophagy machinery. *Curr. Opin. Struct. Biol.* **43**, 10–17 (2017).

15. Wong, P.-M., Puente, C., Ganley, I. G. & Jiang, X. The ULK1 complex: sensing nutrient signals for autophagy activation. *Autophagy* **9**, 124–137 (2013).
16. Russell, R. C. *et al.* ULK1 induces autophagy by phosphorylating Beclin-1 and activating VPS34 lipid kinase. *Nat. Cell Biol.* **15**, 741–750 (2013).
17. Park, J.-M. *et al.* The ULK1 complex mediates MTORC1 signaling to the autophagy initiation machinery via binding and phosphorylating ATG14. *Autophagy* **12**, 547–564 (2016).
18. Itakura, E. & Mizushima, N. Characterization of autophagosome formation site by a hierarchical analysis of mammalian Atg proteins. *Autophagy* **6**, 764–776 (2010).
19. Yuan, H.-X., Russell, R. C. & Guan, K.-L. Regulation of PIK3C3/VPS34 complexes by MTOR in nutrient stress-induced autophagy. *Autophagy* **9**, 1983–1995 (2013).
20. Dooley, H. C. *et al.* WIPI2 links LC3 conjugation with PI3P, autophagosome formation, and pathogen clearance by recruiting Atg12-5-16L1. *Mol. Cell* **55**, 238–252 (2014).
21. Fujita, N. *et al.* The Atg16L complex specifies the site of LC3 lipidation for membrane biogenesis in autophagy. *Mol. Biol. Cell* **19**, 2092–2100 (2008).
22. Tanida, I., Ueno, T. & Kominami, E. LC3 conjugation system in mammalian autophagy. *Int. J. Biochem. Cell Biol.* **36**, 2503–2518 (2004).
23. Nair, U. *et al.* A role for Atg8-PE deconjugation in autophagosome biogenesis. *Autophagy* **8**, 780–793 (2012).
24. Mortimore, G. E. & Schworer, C. M. Induction of autophagy by amino-acid deprivation in perfused rat liver. *Nature* **270**, 174–176 (1977).
25. Yang, H. *et al.* mTOR kinase structure, mechanism and regulation. *Nature* **497**, 217–223 (2013).
26. Wan, W. *et al.* mTORC1-Regulated and HUWE1-Mediated WIPI2 Degradation Controls Autophagy Flux. *Mol. Cell* **72**, 303-315.e6 (2018).
27. Munson, M. J. *et al.* mTOR activates the VPS34-UVRAG complex to regulate autolysosomal tubulation and cell survival. *EMBO J.* **34**, 2272–2290 (2015).
28. Hardie, D. G., Carling, D. & Gamblin, S. J. AMP-activated protein kinase: also regulated by ADP? *Trends Biochem. Sci.* **36**, 470–477 (2011).
29. Hawley, S. A. *et al.* Complexes between the LKB1 tumor suppressor, STRAD alpha/beta and MO25 alpha/beta are upstream kinases in the AMP-activated protein kinase cascade. *J. Biol.* **2**, 28 (2003).
30. Shaw, R. J. *et al.* The tumor suppressor LKB1 kinase directly activates AMP-activated kinase and regulates apoptosis in response to energy stress. *Proc. Natl. Acad. Sci. U. S. A.* **101**, 3329–3335 (2004).
31. Xiao, B. *et al.* Structure of mammalian AMPK and its regulation by ADP. *Nature* **472**, 230–233 (2011).

32. Oakhill, J. S. *et al.* AMPK is a direct adenylate charge-regulated protein kinase. *Science* **332**, 1433–1435 (2011).
33. Gwinn, D. M. *et al.* AMPK phosphorylation of raptor mediates a metabolic checkpoint. *Mol. Cell* **30**, 214–226 (2008).
34. Kalender, A. *et al.* Metformin, independent of AMPK, inhibits mTORC1 in a rag GTPase-dependent manner. *Cell Metab.* **11**, 390–401 (2010).
35. Egan, D. F. *et al.* Phosphorylation of ULK1 (hATG1) by AMP-activated protein kinase connects energy sensing to mitophagy. *Science* **331**, 456–461 (2011).
36. Kim, J., Kundu, M., Viollet, B. & Guan, K.-L. AMPK and mTOR regulate autophagy through direct phosphorylation of Ulk1. *Nat. Cell Biol.* **13**, 132–141 (2011).
37. Yamamoto, H. *et al.* Atg9 vesicles are an important membrane source during early steps of autophagosome formation. *J. Cell Biol.* **198**, 219–233 (2012).
38. Dunn, W. A. Studies on the mechanisms of autophagy: formation of the autophagic vacuole. *J. Cell Biol.* **110**, 1923–1933 (1990).
39. Hailey, D. W. *et al.* Mitochondria supply membranes for autophagosome biogenesis during starvation. *Cell* **141**, 656–667 (2010).
40. Søreng, K. *et al.* SNX18 regulates ATG9A trafficking from recycling endosomes by recruiting Dynamin-2. *EMBO Rep.* **19**, e44837 (2018).
41. Pattingre, S. *et al.* Bcl-2 antiapoptotic proteins inhibit Beclin 1-dependent autophagy. *Cell* **122**, 927–939 (2005).
42. Fan, W., Nassiri, A. & Zhong, Q. Autophagosome targeting and membrane curvature sensing by Barkor/Atg14(L). *Proc. Natl. Acad. Sci. U. S. A.* **108**, 7769–7774 (2011).
43. Di Bartolomeo, S. *et al.* The dynamic interaction of AMBRA1 with the dynein motor complex regulates mammalian autophagy. *J. Cell Biol.* **191**, 155–168 (2010).
44. Hosokawa, N. *et al.* Atg101, a novel mammalian autophagy protein interacting with Atg13. *Autophagy* **5**, 973–979 (2009).
45. Lystad, A. H. *et al.* Distinct functions of ATG16L1 isoforms in membrane binding and LC3B lipidation in autophagy-related processes. *Nat. Cell Biol.* **21**, 372–383 (2019).
46. Melia, T. J., Lystad, A. H. & Simonsen, A. Autophagosome biogenesis: From membrane growth to closure. *J. Cell Biol.* **219**, e202002085 (2020).
47. Itakura, E., Kishi-Itakura, C. & Mizushima, N. The hairpin-type tail-anchored SNARE syntaxin 17 targets to autophagosomes for fusion with endosomes/lysosomes. *Cell* **151**, 1256–1269 (2012).
48. Bjørkøy, G. *et al.* p62/SQSTM1 forms protein aggregates degraded by autophagy and has a protective effect on huntingtin-induced cell death. *J. Cell Biol.* **171**, 603–614 (2005).
49. Dikic, I., Wakatsuki, S. & Walters, K. J. Ubiquitin-binding domains - from structures to functions. *Nat. Rev. Mol. Cell Biol.* **10**, 659–671 (2009).

50. Pankiv, S. *et al.* p62/SQSTM1 binds directly to Atg8/LC3 to facilitate degradation of ubiquitinated protein aggregates by autophagy. *J. Biol. Chem.* **282**, 24131–24145 (2007).
51. Ichimura, Y. *et al.* Structural basis for sorting mechanism of p62 in selective autophagy. *J. Biol. Chem.* **283**, 22847–22857 (2008).
52. Johansen, T. & Lamark, T. Selective autophagy mediated by autophagic adapter proteins. *Autophagy* **7**, 279–296 (2011).
53. Orhon, I. & Reggiori, F. Assays to Monitor Autophagy Progression in Cell Cultures. *Cells* **6**, 20 (2017).
54. Mizushima, N. The ATG conjugation systems in autophagy. *Curr. Opin. Cell Biol.* **63**, 1–10 (2020).
55. Zhang, Z., Singh, R. & Aschner, M. Methods for the Detection of Autophagy in Mammalian Cells. *Curr. Protoc. Toxicol.* **69**, 20.12.1-20.12.26 (2016).
56. Mizushima, N. & Yoshimori, T. How to interpret LC3 immunoblotting. *Autophagy* **3**, 542–545 (2007).
57. Sánchez-Martín, P. & Komatsu, M. p62/SQSTM1 - steering the cell through health and disease. *J. Cell Sci.* **131**, jcs222836 (2018).
58. BenYounès, A. *et al.* A fluorescence-microscopic and cytofluorometric system for monitoring the turnover of the autophagic substrate p62/SQSTM1. *Autophagy* **7**, 883–891 (2011).
59. Guo, S. *et al.* A rapid and high content assay that measures cyto-ID-stained autophagic compartments and estimates autophagy flux with potential clinical applications. *Autophagy* **11**, 560–572 (2015).
60. Zhou, C. *et al.* Monitoring autophagic flux by an improved tandem fluorescent-tagged LC3 (mTagRFP-mWasabi-LC3) reveals that high-dose rapamycin impairs autophagic flux in cancer cells. *Autophagy* **8**, 1215–1226 (2012).
61. Novak, I. *et al.* Nix is a selective autophagy receptor for mitochondrial clearance. *EMBO Rep.* **11**, 45–51 (2010).
62. Bernales, S., McDonald, K. L. & Walter, P. Autophagy counterbalances endoplasmic reticulum expansion during the unfolded protein response. *PLoS Biol.* **4**, e423 (2006).
63. Dupont, N. *et al.* Shigella phagocytic vacuolar membrane remnants participate in the cellular response to pathogen invasion and are regulated by autophagy. *Cell Host Microbe* **6**, 137–149 (2009).
64. Zheng, Y. T. *et al.* The adaptor protein p62/SQSTM1 targets invading bacteria to the autophagy pathway. *J. Immunol. Baltim. Md 1950* **183**, 5909–5916 (2009).
65. Rubinsztein, D. C. The roles of intracellular protein-degradation pathways in neurodegeneration. *Nature* **443**, 780–786 (2006).

66. Takeshige, K., Baba, M., Tsuboi, S., Noda, T. & Ohsumi, Y. Autophagy in yeast demonstrated with proteinase-deficient mutants and conditions for its induction. *J. Cell Biol.* **119**, 301–311 (1992).
67. Ashford, T. P. & Porter, K. R. Cytoplasmic components in hepatic cell lysosomes. *J. Cell Biol.* **12**, 198–202 (1962).
68. Novikoff, A. B. & Essner, E. Cytolysomes and mitochondrial degeneration. *J. Cell Biol.* **15**, 140–146 (1962).
69. Deosaran, E. *et al.* NBR1 acts as an autophagy receptor for peroxisomes. *J. Cell Sci.* **126**, 939–952 (2013).
70. Thurston, T. L. M., Wandel, M. P., von Muhlinen, N., Foeglein, A. & Randow, F. Galectin 8 targets damaged vesicles for autophagy to defend cells against bacterial invasion. *Nature* **482**, 414–418 (2012).
71. Vainshtein, A. & Grumati, P. Selective Autophagy by Close Encounters of the Ubiquitin Kind. *Cells* **9**, 2349 (2020).
72. Johansen, T. & Lamark, T. Selective Autophagy: ATG8 Family Proteins, LIR Motifs and Cargo Receptors. *J. Mol. Biol.* **432**, 80–103 (2020).
73. Heo, J.-M., Ordureau, A., Paulo, J. A., Rinehart, J. & Harper, J. W. The PINK1-PARKIN Mitochondrial Ubiquitylation Pathway Drives a Program of OPTN/NDP52 Recruitment and TBK1 Activation to Promote Mitophagy. *Mol. Cell* **60**, 7–20 (2015).
74. Moore, A. S. & Holzbaur, E. L. F. Dynamic recruitment and activation of ALS-associated TBK1 with its target optineurin are required for efficient mitophagy. *Proc. Natl. Acad. Sci. U. S. A.* **113**, E3349-3358 (2016).
75. Richter, B. *et al.* Phosphorylation of OPTN by TBK1 enhances its binding to Ub chains and promotes selective autophagy of damaged mitochondria. *Proc. Natl. Acad. Sci. U. S. A.* **113**, 4039–4044 (2016).
76. Khaminets, A., Behl, C. & Dikic, I. Ubiquitin-Dependent And Independent Signals In Selective Autophagy. *Trends Cell Biol.* **26**, 6–16 (2016).
77. Randow, F. & Youle, R. J. Self and nonself: how autophagy targets mitochondria and bacteria. *Cell Host Microbe* **15**, 403–411 (2014).
78. Shahnazari, S. & Brumell, J. H. Mechanisms and consequences of bacterial targeting by the autophagy pathway. *Curr. Opin. Microbiol.* **14**, 68–75 (2011).
79. Rich, K. A., Burkett, C. & Webster, P. Cytoplasmic bacteria can be targets for autophagy. *Cell. Microbiol.* **5**, 455–468 (2003).
80. Nakagawa, I. *et al.* Autophagy defends cells against invading group A Streptococcus. *Science* **306**, 1037–1040 (2004).
81. Gutierrez, M. G. *et al.* Autophagy is a defense mechanism inhibiting BCG and Mycobacterium tuberculosis survival in infected macrophages. *Cell* **119**, 753–766 (2004).

82. Ogawa, M. *et al.* Escape of intracellular Shigella from autophagy. *Science* **307**, 727–731 (2005).
83. Dortet, L. *et al.* Recruitment of the major vault protein by InlK: a Listeria monocytogenes strategy to avoid autophagy. *PLoS Pathog.* **7**, e1002168 (2011).
84. Yoshikawa, Y. *et al.* Listeria monocytogenes ActA-mediated escape from autophagic recognition. *Nat. Cell Biol.* **11**, 1233–1240 (2009).
85. Chargui, A. *et al.* Subversion of autophagy in adherent invasive Escherichia coli-infected neutrophils induces inflammation and cell death. *PloS One* **7**, e51727 (2012).
86. Fagone, P. & Jackowski, S. Membrane phospholipid synthesis and endoplasmic reticulum function. *J. Lipid Res.* **50 Suppl**, S311-316 (2009).
87. Rapoport, T. A. Protein translocation across the eukaryotic endoplasmic reticulum and bacterial plasma membranes. *Nature* **450**, 663–669 (2007).
88. Reid, D. W. & Nicchitta, C. V. Diversity and selectivity in mRNA translation on the endoplasmic reticulum. *Nat. Rev. Mol. Cell Biol.* **16**, 221–231 (2015).
89. Chen, S., Novick, P. & Ferro-Novick, S. ER structure and function. *Curr. Opin. Cell Biol.* **25**, 428–433 (2013).
90. Wilkinson, S. ER-phagy: shaping up and destressing the endoplasmic reticulum. *FEBS J.* **286**, 2645–2663 (2019).
91. Loi, M., Fregno, I., Guerra, C. & Molinari, M. Eat it right: ER-phagy and recovER-phagy. *Biochem. Soc. Trans.* **46**, 699–706 (2018).
92. Song, S., Tan, J., Miao, Y. & Zhang, Q. Crosstalk of ER stress-mediated autophagy and ER-phagy: Involvement of UPR and the core autophagy machinery. *J. Cell. Physiol.* **233**, 3867–3874 (2018).
93. Oakes, S. A. & Papa, F. R. The role of endoplasmic reticulum stress in human pathology. *Annu. Rev. Pathol.* **10**, 173–194 (2015).
94. Yang, M. *et al.* ER-Phagy: A New Regulator of ER Homeostasis. *Front. Cell Dev. Biol.* **9**, 684526 (2021).
95. Grumati, P., Dikic, I. & Stolz, A. ER-phagy at a glance. *J. Cell Sci.* **131**, jcs217364 (2018).
96. Bhaskara, R. M. *et al.* Curvature induction and membrane remodeling by FAM134B reticulon homology domain assist selective ER-phagy. *Nat. Commun.* **10**, 2370 (2019).
97. Cai, M. *et al.* FAM134B promotes adipogenesis by increasing vesicular activity in porcine and 3T3-L1 adipocytes. *Biol. Chem.* **400**, 523–532 (2019).
98. Cai, M. *et al.* FAM134B promotes adipogenesis by increasing vesicular activity in porcine and 3T3-L1 adipocytes. *Biol. Chem.* **400**, 523–532 (2019).
99. Liao, Y., Duan, B., Zhang, Y., Zhang, X. & Xia, B. Excessive ER-phagy mediated by the autophagy receptor FAM134B results in ER stress, the unfolded protein response, and cell death in HeLa cells. *J. Biol. Chem.* **294**, 20009–20023 (2019).

100. Yun, C. W. & Lee, S. H. The Roles of Autophagy in Cancer. *Int. J. Mol. Sci.* **19**, 3466 (2018).
101. Fujikake, N., Shin, M. & Shimizu, S. Association Between Autophagy and Neurodegenerative Diseases. *Front. Neurosci.* **12**, 255 (2018).
102. Gustafsson, A. B. & Gottlieb, R. A. Autophagy in ischemic heart disease. *Circ. Res.* **104**, 150–158 (2009).
103. Ye, X., Zhou, X.-J. & Zhang, H. Exploring the Role of Autophagy-Related Gene 5 (ATG5) Yields Important Insights Into Autophagy in Autoimmune/Autoinflammatory Diseases. *Front. Immunol.* **9**, 2334 (2018).
104. Huang, P. L. A comprehensive definition for metabolic syndrome. *Dis. Model. Mech.* **2**, 231–237 (2009).
105. Kitada, M. & Koya, D. Autophagy in metabolic disease and ageing. *Nat. Rev. Endocrinol.* **17**, 647–661 (2021).
106. Freeman, A. M., Acevedo, L. A. & Pennings, N. Insulin Resistance. in *StatPearls* (StatPearls Publishing, Treasure Island (FL), 2025).
107. He, B. *et al.* Spatial regulation of glucose and lipid metabolism by hepatic insulin signaling. *Cell Metab.* S1550-4131(25)00207–4 (2025) doi:10.1016/j.cmet.2025.03.015.
108. Kim, S., Eun, H. S. & Jo, E.-K. Roles of Autophagy-Related Genes in the Pathogenesis of Inflammatory Bowel Disease. *Cells* **8**, 77 (2019).
109. Patel, K. K. & Stappenbeck, T. S. Autophagy and intestinal homeostasis. *Annu. Rev. Physiol.* **75**, 241–262 (2013).
110. Khalili, L., Park, G., Nagpal, R. & Salazar, G. The Role of Akkermansia muciniphila on Improving Gut and Metabolic Health Modulation: A Meta-Analysis of Preclinical Mouse Model Studies. *Microorganisms* **12**, 1627 (2024).
111. Yang, Z. & Klionsky, D. J. Eaten alive: a history of macroautophagy. *Nat. Cell Biol.* **12**, 814–822 (2010).
112. Feng, Y., He, D., Yao, Z. & Klionsky, D. J. The machinery of macroautophagy. *Cell Res.* **24**, 24–41 (2014).
113. Gatica, D., Lahiri, V. & Klionsky, D. J. Cargo recognition and degradation by selective autophagy. *Nat. Cell Biol.* **20**, 233–242 (2018).
114. Klionsky, D. J. & Schulman, B. A. Dynamic regulation of macroautophagy by distinctive ubiquitin-like proteins. *Nat. Struct. Mol. Biol.* **21**, 336–345 (2014).
115. Chino, H. & Mizushima, N. ER-Phagy: Quality and Quantity Control of the Endoplasmic Reticulum by Autophagy. *Cold Spring Harb. Perspect. Biol.* **15**, a041256 (2023).
116. Khaminets, A. *et al.* Regulation of endoplasmic reticulum turnover by selective autophagy. *Nature* **522**, 354–358 (2015).

117. Chino, H., Hatta, T., Natsume, T. & Mizushima, N. Intrinsically Disordered Protein TEX264 Mediates ER-phagy. *Mol. Cell* **74**, 909-921.e6 (2019).
118. An, H. *et al.* TEX264 Is an Endoplasmic Reticulum-Resident ATG8-Interacting Protein Critical for ER Remodeling during Nutrient Stress. *Mol. Cell* **74**, 891-908.e10 (2019).
119. Jiang, X. *et al.* FAM134B oligomerization drives endoplasmic reticulum membrane scission for ER-phagy. *EMBO J.* **39**, e102608 (2020).
120. Wang, X. *et al.* A regulatory circuit comprising the CBP and SIRT7 regulates FAM134B-mediated ER-phagy. *J. Cell Biol.* **222**, e202201068 (2023).
121. Chino, H. *et al.* Phosphorylation by casein kinase 2 enhances the interaction between ER-phagy receptor TEX264 and ATG8 proteins. *EMBO Rep.* **23**, e54801 (2022).
122. Bhaskara, R. M. *et al.* Curvature induction and membrane remodeling by FAM134B reticulon homology domain assist selective ER-phagy. *Nat. Commun.* **10**, 2370 (2019).
123. Siggel, M., Bhaskara, R. M., Moesser, M. K., D Ikić, I. & Hummer, G. FAM134B-RHD Protein Clustering Drives Spontaneous Budding of Asymmetric Membranes. *J. Phys. Chem. Lett.* **12**, 1926–1931 (2021).
124. González, A. *et al.* Ubiquitination regulates ER-phagy and remodelling of endoplasmic reticulum. *Nature* **618**, 394–401 (2023).
125. Chiramel, A. I., Dougherty, J. D., Nair, V., Robertson, S. J. & Best, S. M. FAM134B, the Selective Autophagy Receptor for Endoplasmic Reticulum Turnover, Inhibits Replication of Ebola Virus Strains Makona and Mayinga. *J. Infect. Dis.* **214**, S319–S325 (2016).
126. Lennemann, N. J. & Coyne, C. B. Dengue and Zika viruses subvert reticulophagy by NS2B3-mediated cleavage of FAM134B. *Autophagy* **13**, 322–332 (2017).
127. Tan, X. *et al.* Coronavirus subverts ER-phagy by hijacking FAM134B and ATL3 into p62 condensates to facilitate viral replication. *Cell Rep.* **42**, 112286 (2023).
128. Zhang, L. *et al.* AMFR-mediated Flavivirus NS2A ubiquitination subverts ER-phagy to augment viral pathogenicity. *Nat. Commun.* **15**, 9578 (2024).
129. Shin, D. *et al.* Regulation of Phosphoribosyl-Linked Serine Ubiquitination by Deubiquitinases DupA and DupB. *Mol. Cell* **77**, 164-179.e6 (2020).
130. Sher, A. A., Mustafa, B. E., Grady, S. C., Gardiner, J. C. & Saeed, A. M. Outbreaks of foodborne Salmonella enteritidis in the United States between 1990 and 2015: An analysis of epidemiological and spatial-temporal trends. *Int. J. Infect. Dis. IJID Off. Publ. Int. Soc. Infect. Dis.* **105**, 54–61 (2021).
131. Bakowski, M. A., Braun, V. & Brumell, J. H. Salmonella-containing vacuoles: directing traffic and nesting to grow. *Traffic Cph. Den.* **9**, 2022–2031 (2008).
132. Katayama, H., Yamamoto, A., Mizushima, N., Yoshimori, T. & Miyawaki, A. GFP-like proteins stably accumulate in lysosomes. *Cell Struct. Funct.* **33**, 1–12 (2008).

133. Yim, W. W.-Y., Yamamoto, H. & Mizushima, N. A pulse-chasable reporter processing assay for mammalian autophagic flux with HaloTag. *eLife* **11**, e78923 (2022).
134. Klionsky, D. J. *et al.* Guidelines for the use and interpretation of assays for monitoring autophagy (4th edition)1. *Autophagy* **17**, 1–382 (2021).
135. Ichimura, Y. *et al.* A ubiquitin-like system mediates protein lipidation. *Nature* **408**, 488–492 (2000).
136. Davidson, G. L. *et al.* Frequency of mutations in the genes associated with hereditary sensory and autonomic neuropathy in a UK cohort. *J. Neurol.* **259**, 1673–1685 (2012).
137. LaRock, D. L., Chaudhary, A. & Miller, S. I. Salmonellae interactions with host processes. *Nat. Rev. Microbiol.* **13**, 191–205 (2015).
138. Xu, Y. *et al.* ARF GTPases activate Salmonella effector SopF to ADP-ribosylate host V-ATPase and inhibit endomembrane damage-induced autophagy. *Nat. Struct. Mol. Biol.* **29**, 67–77 (2022).
139. Xu, Y. *et al.* A Bacterial Effector Reveals the V-ATPase-ATG16L1 Axis that Initiates Xenophagy. *Cell* **178**, 552-566.e20 (2019).
140. Trinkle-Mulcahy, L. Recent advances in proximity-based labeling methods for interactome mapping. *F1000Research* **8**, F1000 Faculty Rev-135 (2019).
141. Knodler, L. A., Nair, V. & Steele-Mortimer, O. Quantitative assessment of cytosolic Salmonella in epithelial cells. *PloS One* **9**, e84681 (2014).
142. Gatica, D., Chiong, M., Lavandero, S. & Klionsky, D. J. The role of autophagy in cardiovascular pathology. *Cardiovasc. Res.* **118**, 934–950 (2022).
143. Birmingham, C. L., Smith, A. C., Bakowski, M. A., Yoshimori, T. & Brumell, J. H. Autophagy controls Salmonella infection in response to damage to the Salmonella-containing vacuole. *J. Biol. Chem.* **281**, 11374–11383 (2006).
144. Thurston, T. L. M., Ryzhakov, G., Bloor, S., von Muhlinen, N. & Randow, F. The TBK1 adaptor and autophagy receptor NDP52 restricts the proliferation of ubiquitin-coated bacteria. *Nat. Immunol.* **10**, 1215–1221 (2009).
145. Lau, N. *et al.* SopF, a phosphoinositide binding effector, promotes the stability of the nascent Salmonella-containing vacuole. *PLoS Pathog.* **15**, e1007959 (2019).
146. Kohno, S., Shiozaki, Y., Keenan, A. L., Miyazaki-Anzai, S. & Miyazaki, M. An N-terminal-truncated isoform of FAM134B (FAM134B-2) regulates starvation-induced hepatic selective ER-phagy. *Life Sci. Alliance* **2**, e201900340 (2019).
147. Bravo, R. *et al.* Endoplasmic reticulum and the unfolded protein response: dynamics and metabolic integration. *Int. Rev. Cell Mol. Biol.* **301**, 215–290 (2013).
148. Foronda, H. *et al.* Heteromeric clusters of ubiquitinated ER-shaping proteins drive ER-phagy. *Nature* **618**, 402–410 (2023).
149. Li, C. *et al.* FastCloning: a highly simplified, purification-free, sequence- and ligation-independent PCR cloning method. *BMC Biotechnol.* **11**, 92 (2011).

150. Liu, H. & Naismith, J. H. An efficient one-step site-directed deletion, insertion, single and multiple-site plasmid mutagenesis protocol. *BMC Biotechnol.* **8**, 91 (2008).
151. Ganley, I. G. *et al.* ULK1.ATG13.FIP200 complex mediates mTOR signaling and is essential for autophagy. *J. Biol. Chem.* **284**, 12297–12305 (2009).
152. Kabeya, Y. *et al.* LC3, a mammalian homologue of yeast Apg8p, is localized in autophagosome membranes after processing. *EMBO J.* **19**, 5720–5728 (2000).
153. Klionsky, D. J. *et al.* Guidelines for the use and interpretation of assays for monitoring autophagy (4th edition)1. *Autophagy* **17**, 1–382 (2021).
154. Mizushima, N., Yoshimori, T. & Levine, B. Methods in mammalian autophagy research. *Cell* **140**, 313–326 (2010).
155. Jain, A. *et al.* p62/SQSTM1 is a target gene for transcription factor NRF2 and creates a positive feedback loop by inducing antioxidant response element-driven gene transcription. *J. Biol. Chem.* **285**, 22576–22591 (2010).
156. Sahani, M. H., Itakura, E. & Mizushima, N. Expression of the autophagy substrate SQSTM1/p62 is restored during prolonged starvation depending on transcriptional upregulation and autophagy-derived amino acids. *Autophagy* **10**, 431–441 (2014).
157. Ylä-Anttila, P., Vihinen, H., Jokitalo, E. & Eskelinen, E.-L. 3D tomography reveals connections between the phagophore and endoplasmic reticulum. *Autophagy* **5**, 1180–1185 (2009).
158. Koyama-Honda, I., Itakura, E., Fujiwara, T. K. & Mizushima, N. Temporal analysis of recruitment of mammalian ATG proteins to the autophagosome formation site. *Autophagy* **9**, 1491–1499 (2013).
159. Nixon, R. A. The role of autophagy in neurodegenerative disease. *Nat. Med.* **19**, 983–997 (2013).
160. White, E. Deconvoluting the context-dependent role for autophagy in cancer. *Nat. Rev. Cancer* **12**, 401–410 (2012).
161. Alsaadi, R. M. *et al.* ULK1-mediated phosphorylation of ATG16L1 promotes xenophagy, but destabilizes the ATG16L1 Crohn's mutant. *EMBO Rep.* **20**, e46885 (2019).
162. Luc, K., Schramm-Luc, A., Guzik, T. J. & Mikolajczyk, T. P. Oxidative stress and inflammatory markers in prediabetes and diabetes. *J. Physiol. Pharmacol. Off. J. Pol. Physiol. Soc.* **70**, (2019).
163. Harrison, A. V., Lorenzo, F. R. & McClain, D. A. Iron and the Pathophysiology of Diabetes. *Annu. Rev. Physiol.* **85**, 339–362 (2023).
164. Gabrielsen, J. S. *et al.* Adipocyte iron regulates adiponectin and insulin sensitivity. *J. Clin. Invest.* **122**, 3529–3540 (2012).
165. Liu, Y. *et al.* Adiponectin stimulates autophagy and reduces oxidative stress to enhance insulin sensitivity during high-fat diet feeding in mice. *Diabetes* **64**, 36–48 (2015).

166. Chiramel, A. I., Dougherty, J. D., Nair, V., Robertson, S. J. & Best, S. M. FAM134B, the Selective Autophagy Receptor for Endoplasmic Reticulum Turnover, Inhibits Replication of Ebola Virus Strains Makona and Mayinga. *J. Infect. Dis.* **214**, S319–S325 (2016).
167. Lennemann, N. J. & Coyne, C. B. Dengue and Zika viruses subvert reticulophagy by NS2B3-mediated cleavage of FAM134B. *Autophagy* **13**, 322–332 (2017).
168. Tan, X. *et al.* Coronavirus subverts ER-phagy by hijacking FAM134B and ATL3 into p62 condensates to facilitate viral replication. *Cell Rep.* **42**, 112286 (2023).
169. Guan, K. *et al.* MiR-142-5p/FAM134B Axis Manipulates ER-Phagy to Control PRRSV Replication. *Front. Immunol.* **13**, 842077 (2022).
170. Kawabata, M. *et al.* Legionella hijacks the host Golgi-to-ER retrograde pathway for the association of Legionella-containing vacuole with the ER. *PLoS Pathog.* **17**, e1009437 (2021).
171. Xu, Y. *et al.* A Bacterial Effector Reveals the V-ATPase-ATG16L1 Axis that Initiates Xenophagy. *Cell* **178**, 552-566.e20 (2019).
172. Chino, H. *et al.* Phosphorylation by casein kinase 2 enhances the interaction between ER-phagy receptor TEX264 and ATG8 proteins. *EMBO Rep.* **23**, e54801 (2022).
173. Jiang, X. *et al.* FAM134B oligomerization drives endoplasmic reticulum membrane scission for ER-phagy. *EMBO J.* **39**, e102608 (2020).
174. Wang, X. *et al.* A regulatory circuit comprising the CBP and SIRT7 regulates FAM134B-mediated ER-phagy. *J. Cell Biol.* **222**, e202201068 (2023).
175. Sindhwani, A. *et al.* Salmonella exploits the host endolysosomal tethering factor HOPS complex to promote its intravacuolar replication. *PLoS Pathog.* **13**, e1006700 (2017).
176. Eswarappa, S. M., Negi, V. D., Chakraborty, S., Chandrasekhar Sagar, B. K. & Chakravortty, D. Division of the Salmonella-containing vacuole and depletion of acidic lysosomes in Salmonella-infected host cells are novel strategies of Salmonella enterica to avoid lysosomes. *Infect. Immun.* **78**, 68–79 (2010).
177. Benjamin, J. L., Sumpter, R., Levine, B. & Hooper, L. V. Intestinal epithelial autophagy is essential for host defense against invasive bacteria. *Cell Host Microbe* **13**, 723–734 (2013).
178. Sharma, V., Verma, S., Seranova, E., Sarkar, S. & Kumar, D. Selective Autophagy and Xenophagy in Infection and Disease. *Front. Cell Dev. Biol.* **6**, 147 (2018).
179. Bradfute, S. B. *et al.* Autophagy as an immune effector against tuberculosis. *Curr. Opin. Microbiol.* **16**, 355–365 (2013).
180. Kim, Y. S., Silwal, P., Kim, S. Y., Yoshimori, T. & Jo, E.-K. Autophagy-activating strategies to promote innate defense against mycobacteria. *Exp. Mol. Med.* **51**, 1–10 (2019).

Citation of Chapter 2

1. Parzych, K. R. & Klionsky, D. J. An overview of autophagy: morphology, mechanism, and regulation. Antioxid. Redox Signal. 20, 460–473 (2014).
2. Russell, R. C., Yuan, H. X. & Guan, K. L. Autophagy regulation by nutrient signaling. Cell Res. 24, 42–57 (2014).
3. Kuma, A. et al. Te role of autophagy during the early neonatal starvation period. Nature 432, 1032–1036 (2004).
4. Mizushima, N., Yoshimori, T. & Ohsumi, Y. Te role of Atg proteins in autophagosome formation. Annu. Rev. Cell Dev. Biol. 27, 107–132 (2011).
5. Mercer, C. A., Kaliappan, A. & Dennis, P. B. A novel, human Atg13 binding protein, Atg101, interacts with ULK1 and is essential for macroautophagy. Autophagy 5, 649–662 (2009).
6. Suzuki, H., Kaizuka, T., Mizushima, N. & Noda, N. N. Structure of the Atg101–Atg13 complex reveals essential roles of Atg101 in autophagy initiation. Nat. Struct. Mol. Biol. 22, 572–580 (2015).
7. Hara, T. et al. FIP200, a ULK-interacting protein, is required for autophagosome formation in mammalian cells. J. Cell Biol. 181,497–510 (2008).
8. Ganley, I. G. et al. ULK1.ATG13.FIP200 complex mediates mTOR signaling and is essential for autophagy. J. Biol. Chem. 284, 12297–12305 (2009).
9. Hosokawa, N. et al. Nutrient-dependent mTORC1 association with the ULK1–Atg13–FIP200 complex required for autophagy. Mol. Biol. Cell 20,1981–1991 (2009).
10. Jung, C. H. et al. ULK-Atg13-FIP200 complexes mediate mTOR signaling to the autophagy machinery. Mol. Biol. Cell 20,1992–2003 (2009).
11. Lee, E. J. & Tournier, C. Te requirement of uncoordinated 51-like kinase1 (ULK1) and ULK2 in the regulation of autophagy. Autophagy 7,689–695 (2011).
12. Gammoh, N., Florey, O., Overholtzer, M. & Jiang, X. Interaction between FIP200 and ATG16L1 distinguishes ULK1 complex-dependent and-independent autophagy. Nat. Struct. Mol. Biol. 20, 144–149 (2013).
13. Nishimura, T. et al. FIP200 regulates targeting of Atg16L1 to the isolation membrane. EMBO Rep. 14, 284–291 (2013).

14. Fujita, N. et al. Te Atg16L complex specifes the site of LC3 lipidation for membrane biogenesis in autophagy. Mol. Biol. Cell 19, 2092–2100 (2008).
15. Wu, J. et al. Molecular cloning and characterization of rat LC3A and LC3B—two novel markers of autophagosome. Biochem. Biophys. Res.Commun. 339, 437–442 (2006).
16. Kabeya, Y. et al. LC3, a mammalian homologue of yeast Apg8p, is localized in autophagosome membranes afer processing. EMBO J. 19, 5720–5728 (2000).
17. Kimura, S., Fujita, N., Noda, T. & Yoshimori, T. Monitoring autophagy in mammalian cultured cells through the dynamics of LC3. Methods Enzymol. 452,1–12 (2009).
18. Klionsky, D. J. et al. Guidelines for the use and interpretation of assays for monitoring autophagy. Autophagy 12, 1–222 (2016).
19. Jain, A. et al. p62/SQSTM1 is a target gene for transcription factor NRF2 and creates a positive feedback loop by inducing antioxidant response elementdriven gene transcription. J. Biol. Chem. 285, 22576–22591 (2010).
20. Fujita, K. & Srinivasula, S. M. TLR4-mediated autophagy in macrophages is a p62-dependent type of selective autophagy of aggresome-like induced structures (ALIS). Autophagy 7, 552–554 (2011).
21. Salminen, A. et al. Emerging role of p62/sequestosome-1 in the pathogenesis of Alzheimer's disease. Prog. Neurobiol. 96, 87–95 (2012).
22. Jiang, X. et al. VPS34 stimulation of p62 phosphorylation for cancer progression. Oncogene 36, 6850–6862 (2017).
23. Clausen, T. H. et al. p62/SQSTM1 and ALFY interact to facilitate the formation of p62 bodies/ALIS and their degradation by autophagy. Autophagy 6, 330–344 (2010).
24. Kirkin, V., Lamark, T., Johansen, T. & Dikic, I. NBR1 cooperates with p62 in selective autophagy of ubiquitinated targets. Autophagy 5, 732–733 (2009).
25. Shi, J. et al. NBR1 is dispensable for PARK2-mediated mitophagy regardless of the presence or absence of SQSTM1. Cell Death Dis. 6, e1943 (2015).
26. Yla-Anttila, P., Vihinen, H., Jokitalo, E. & Eskelinen, E. L. Monitoring autophagy by electron microscopy in mammalian cells. Methods Enzymol. 452,143–164 (2009).
27. Roberts, E. A. & Deretic, V. Autophagic proteolysis of long-lived proteins in non-liver cells. Methods Mol. Biol. 445, 111–117 (2008).

28. Ueno, T. et al. Autolysosomal membrane-associated betaine homocysteine methyltransferase. Limited degradation fragment of a sequestered cytosolic enzyme monitoring autophagy. J. Biol. Chem. 274, 15222–15229 (1999).
29. Warnes, G. Flow cytometric assays for the study of autophagy. Methods 82, 21–28 (2015).
30. Guo, S. et al. A rapid and high content assay that measures cyto-ID-stained autophagic compartments and estimates autophagy fux with potential clinical applications. Autophagy 11, 560–572 (2015).
31. Alsaadi, R. M. et al. ULK1-mediated phosphorylation of ATG16L1 promotes xenophagy, but destabilizes the ATG16L1 Crohn's mutant. EMBO Rep. 20,e46885 (2019).
32. Diamanti, M. A. et al. IKKα controls ATG16L1 degradation to prevent ER stress during infammation. J. Exp. Med 214, 423–437 (2017).
33. Koyama-Honda, I., Itakura, E., Fujiwara, T. K. & Mizushima, N. Temporal analysis of recruitment of mammalian ATG proteins to the autophagosome formation site. Autophagy 9, 1491–1499 (2013).
34. Nguyen, T. N. et al. Atg8 family LC3/GABARAP proteins are crucial for autophagosome–lysosome fusion but not autophagosome formation during PINK1/Parkin mitophagy and starvation. J. Cell Biol. 215, 857–874 (2016).
35. Komatsu, M. et al. Homeostatic levels of p62 control cytoplasmic inclusion body formation in autophagy-defcient mice. Cell 131,1149–1163 (2007).
36. Sahani, M. H., Itakura, E. & Mizushima, N. Expression of the autophagy substrate SQSTM1/p62 is restored during prolonged starvation depending on transcriptional upregulation and autophagy-derived amino acids. Autophagy 10, 431–441 (2014).
37. Mizushima, N., Yamamoto, A., Matsui, M., Yoshimori, T. & Ohsumi, Y. In vivo analysis of autophagy in response to nutrient starvation using transgenic mice expressing a fuorescent autophagosome marker. Mol. Biol. Cell 15,1101–1111 (2004).
38. Rosenfeldt, M. T., Nixon, C., Liu, E., Mah, L. Y. & Ryan, K. M. Analysis of macroautophagy by immunohistochemistry. Autophagy 8, 963–969 (2012).
39. Xi, Y. et al. Knockout of Atg5 delays the maturation and reduces the survival of adult-generated neurons in the hippocampus. Cell Death Dis. 7, e2127 (2016).

Citation of Chapter 3

1. Evstatiev R, Gasche C (2012) Iron sensing and signalling. Gut 61:933 – 952
2. Wang J, Pantopoulos K (2011) Regulation of cellular iron metabolism.Biochem J 434: 365 – 381
3. Zimmermann MB, Hurrell RF (2007) Nutritional iron deficiency. Lancet370: 511 – 520
4. Hentze MW, Muckenthaler MU, Galy B, Camaschella C (2010)Two to tango: regulation of Mammalian iron metabolism. Cell 142:24 – 3
5. Pantopoulos K, Porwal SK, Tartakoff A, Devireddy L (2012) Mechanismsof mammalian iron homeostasis. Biochemistry 51: 5705 – 5724
6. Sebastiani G, Pantopoulos K (2011) Disorders associated with systemicor local iron overload: from pathophysiology to clinical practice. Metal-lomics 3: 971 – 986
7. Brissot P, Ropert M, Le Lan C, Loreal O (2012) Non-transferrin boundiron: a key role in iron overload and iron toxicity. Biochem Biophys Acta1820: 403 – 410
8. Simcox JA, McClain DA (2013) Iron and diabetes risk. Cell Metab 17:329 – 341
9. Zhuang T, Han H, Yang Z (2014) Iron, oxidative stress and gestational diabetes. Nutrients 6: 3968–3980
10. McClain DA, Abraham D, Rogers J, Brady R, Gault P, Ajioka R, Kushner JP (2006) High prevalence of abnormal glucose homeostasis secondary to decreased insulin secretion in individuals with hereditary haemochromatosis. Diabetologia 49: 1661–1669
11. Wongjaikam S, Kumfu S, Chattipakorn SC, Fucharoen S, Chattipakorn N (2015) Current and future treatment strategies for iron overload cardiomyopathy. Eur J Pharmacol 765: 86–93
12. Rajpathak SN, Crandall JP, Wylie-Rosett J, Kabat GC, Rohan TE, Hu FB (2009) The role of iron in type 2 diabetes in humans. Biochem Biophys Acta 1790: 671–681
13. Datz C, Felder TK, Niederseer D, Aigner E (2013) Iron homeostasis in the metabolic syndrome. Eur J Clin Invest 43: 215–224
14. Fernandez-Real JM, Lopez-Bermejo A, Ricart W (2002) Cross-talk between iron metabolism and diabetes. Diabetes 51: 2348–2354
15. Bofill C, Joven J, Bages J, Vilella E, Sans T, Cavalle P, Miralles R, Llobet J, Camps J (1994) Response to repeated phlebotomies in patients with non-insulin-dependent diabetes mellitus. Metabolism 43: 614–620

16. Abraham D, Rogers J, Gault P, Kushner JP, McClain DA (2006) Increased insulin secretory capacity but decreased insulin sensitivity after correction of iron overload by phlebotomy in hereditary haemochromatosis. Diabetologia 49: 2546–2551
17. Cooksey RC, Jones D, Gabrielsen S, Huang J, Simcox JA, Luo B, Soesanto Y, Rienhoff H, Abel ED, McClain DA (2010) Dietary iron restriction or iron chelation protects from diabetes and loss of beta-cell function in the obese (ob/ob lep-/-) mouse. Am J Physiol Endocrinol Metab 298: E1236–E1243
18. Galaris D, Pantopoulos K (2008) Oxidative stress and iron homeostasis: mechanistic and health aspects. Crit Rev Clin Lab Sci 45: 1–23
19. Liu Y, Palanivel R, Rai E, Park M, Gabor TV, Scheid MP, Xu A, Sweeney G (2015) Adiponectin stimulates autophagy and reduces oxidative stress to enhance insulin sensitivity during high-fat diet feeding in mice. Diabetes 64: 36–48
20. Mizushima N, Komatsu M (2011) Autophagy: renovation of cells and tissues. Cell 147: 728–741
21. Yang JS, Lu CC, Kuo SC, Hsu YM, Tsai SC, Chen SY, Chen YT, Lin YJ, Huang YC, Chen CJ et al (2017)Autophagy and its link to type II diabetes mellitus. BioMedicine 7: 8
22. Sarparanta J, Garcia-Macia M, Singh R (2017) Autophagy and mitochondria in obesity and type 2 diabetes. Curr Diabetes Rev 13: 352–369
23. Zheng Q, Zhao Y, Guo J, Zhao S, Fei C, Xiao C, Wu D, Wu L, Li X, Chang C (2018) Iron overload promotes mitochondrial fragmentation in mesenchymal stromal cells from myelodysplastic syndrome patients through activation of the AMPK/MFF/Drp1 pathway. Cell Death Dis 9: 515
24. Watson A, Lipina C, McArdle HJ, Taylor PM, Hundal HS (2016) Iron depletion suppresses mTORC1-directed signalling in intestinal Caco-2 cells via induction of REDD1. Cell Signal 28: 412–424
25. Egan D, Kim J, Shaw RJ, Guan KL (2011) The autophagy initiating kinase ULK1 is regulated via opposing phosphorylation by AMPK and mTOR. Autophagy 7: 643–644
26. Kim J, Kundu M, Viollet B, Guan KL (2011) AMPK and mTOR regulate autophagy through direct phosphorylation of Ulk1. Nat Cell Biol 13: 132–141
27. Chen Y, Yu L (2018) Development of research into autophagic lysosome reformation. Mol Cells 41: 45–49

28. Xu G, Ahn J, Chang S, Eguchi M, Ogier A, Han S, Park Y, Shim C, Jang Y, Yang B et al (2012) Lipocalin-2 induces cardiomyocyte apoptosis by increasing intracellular iron accumulation. J Biol Chem 287: 4808–4817
29. Au-Yeung HY, Chan J, Chantarojsiri T, Chang CJ (2013) Molecular imaging of labile iron(II) pools in living cells with a turn-on fluorescent probe. J Am Chem Soc 135: 15165–15173
30. Varghese J, James J, Vaulont S, McKie A, Jacob M (2018) Increased intracellular iron in mouse primary hepatocytes in vitro causes activation of the Akt pathway but decreases its response to insulin. Biochim Biophys Acta Gen Subj 1862: 1870–1882
31. Kimura S, Noda T, Yoshimori T (2007) Dissection of the autophagosome maturation process by a novel reporter protein, tandem fluorescent-tagged LC3. Autophagy 3: 452–460
32. Russell RC, Tian Y, Yuan H, Park HW, Chang YY, Kim J, Kim H, Neufeld TP, Dillin A, Guan KL (2013) ULK1 induces autophagy by phosphorylating Beclin-1 and activating VPS34 lipid kinase. Nat Cell Biol 15: 741–750
33. Hara T, Takamura A, Kishi C, Iemura S, Natsume T, Guan JL, Mizushima N (2008) FIP200, a ULK-interacting protein, is required for autophagosome formation in mammalian cells. J Cell Biol 181: 497–510 34. Matsunaga K, Saitoh T, Tabata K, Omori H, Satoh T, Kurotori N, Maejima I, Shirahama-Noda K, Ichimura T, Isobe T et al (2009) Two Beclin 1-binding proteins, Atg14L and Rubicon, reciprocally regulate autophagy at different stages. Nat Cell Biol 11: 385–396
34. Zhang Y, Xu M, Xia M, Li X, Boini KM, Wang M, Gulbins E, Ratz PH, Li PL (2014) Defective autophagosome trafficking contributes to impaired autophagic flux in coronary arterial myocytes lacking CD38 gene. Cardiovasc Res 102: 68–78]
35. Kao JK, Wang SC, Ho LW, Huang SW, Chang SH, Yang RC, Ke YY, Wu CY, Wang JY, Shieh JJ (2016) Chronic iron overload results in impaired bacterial killing of THP-1 derived macrophage through the inhibition of lysosomal acidification. PLoS One 11: e0156713
36. Yu L, McPhee CK, Zheng L, Mardones GA, Rong Y, Peng J, Mi N, Zhao Y, Liu Z, Wan F et al (2010) Termination of autophagy and reformation of lysosomes regulated by mTOR. Nature 465: 942–946

37. Munson MJ, Allen GF, Toth R, Campbell DG, Lucocq JM, Ganley IG (2015) mTOR activates the VPS34-UVRAG complex to regulate autolysosomal tubulation and cell survival. EMBO J 34: 2272–2290
38. Parmar N, Tamanoi F (2010) Rheb G-proteins and the activation of mTORC1. Enzymes 27: 39–56
39. Li Y, Inoki K, Guan KL (2004) Biochemical and functional characterizations of small GTPase Rheb and TSC2 GAP activity. Mol Cell Biol 24: 7965–7975
40. Fernandez-Real JM, Penarroja G, Castro A, Garcia-Bragado F, Hernandez-Aguado I, Ricart W (2002) Blood letting in high-ferritin type 2 diabetes: effects on insulin sensitivity and beta-cell function. Diabetes 51: 1000–1004
41. Chiang GG, Abraham RT (2005) Phosphorylation of mammalian target of rapamycin (mTOR) at Ser-2448 is mediated by p70S6 kinase. J Biol Chem 280: 25485–25490
42. Holz MK, Blenis J (2005) Identification of S6 kinase 1 as a novel mammalian target of rapamycin (mTOR)-phosphorylating kinase. J Biol Chem 280: 26089–26093 [DOI] [PubMed] [Google Scholar]
43. Inoki K, Li Y, Xu T, Guan KL (2003) Rheb GTPase is a direct target of TSC2 GAP activity and regulates mTOR signaling. Genes Dev 17: 1829–1834
44. Inoki K, Li Y, Zhu T, Wu J, Guan KL (2002) TSC2 is phosphorylated and inhibited by Akt and suppresses mTOR signalling. Nat Cell Biol 4: 648–657
45. Thoreen CC, Kang SA, Chang JW, Liu Q, Zhang J, Gao Y, Reichling LJ, Sim T, Sabatini DM, Gray NS (2009) An ATP-competitive mammalian target of rapamycin inhibitor reveals rapamycin-resistant functions of mTORC1. J Biol Chem 284: 8023–8032
46. Liu Q, Chang JW, Wang J, Kang SA, Thoreen CC, Markhard A, Hur W, Zhang J, Sim T, Sabatini DM et al (2010) Discovery of 1-(4-(4-propionylpiperazin-1-yl)-3-(trifluoromethyl)phenyl)-9-(quinolin-3-yl)benz o[h][1,6]naphthyridin-2(1H)-one as a highly potent, selective mammalian target of rapamycin (mTOR) inhibitor for the treatment of cancer. J Med Chem 53: 7146–7155
47. Martin LE, Bates CM, Beresford CR, Donaldson JD, McDonald FF, Dunlop D, Sheard P, London E, Twigg GD (1955) The pharmacology of an iron-dextran intramuscular haematinic. Br J Pharmacol Chemother 10: 375–382

48. Italia K, Colah R, Ghosh K (2015) Experimental animal model to study iron overload and iron chelation and review of other such models. Blood Cells Mol Dis 55: 194–199
49. Heming N, Letteron P, Driss F, Millot S, El Benna J, Tourret J, Denamur E, Montravers P, Beaumont C, Lasocki S (2012) Efficacy and toxicity of intravenous iron in a mouse model of critical care anemia*. Crit Care Med 40: 2141–2148
50. Cooksey RC, Jouihan HA, Ajioka RS, Hazel MW, Jones DL, Kushner JP, McClain DA (2004) Oxidative stress, beta-cell apoptosis, and decreased insulin secretory capacity in mouse models of hemochromatosis. Endocrinology 145: 5305–5312
51. Chen W, Huang FW, de Renshaw TB, Andrews NC (2011) Skeletal muscle hemojuvelin is dispensable for systemic iron homeostasis. Blood 117: 6319–6325
52. Xu A, Sweeney G (2015) Emerging role of autophagy in mediating widespread actions of ADIPOQ/adiponectin. Autophagy 11: 723–724
53. Ahlstrom P, Rai E, Chakma S, Cho HH, Rengasamy P, Sweeney G (2017) Adiponectin improves insulin sensitivity via activation of autophagic flux. J Mol Endocrinol 59: 339–350
54. Gabrielsen JS, Gao Y, Simcox JA, Huang J, Thorup D, Jones D, Cooksey RC, Gabrielsen D, Adams TD, Hunt SC et al (2012) Adipocyte iron regulates adiponectin and insulin sensitivity. J Clin Investig 122: 3529–3540
55. Cen WJ, Feng Y, Li SS, Huang LW, Zhang T, Zhang W, Kong WD, Jiang JW (2017) Iron overload induces G1 phase arrest and autophagy in murine preosteoblast cells. J Cell Physiol 233: 6779–6789
56. Chen G, Jing CH, Liu PP, Ruan D, Wang L (2013) Induction of autophagic cell death in the rat brain caused by iron. Am J Med Sci 345: 369–374
57. Russell RC, Yuan HX, Guan KL (2014) Autophagy regulation by nutrient signaling. Cell Res 24: 42–57
58. Ganley IG, du Lam H, Wang J, Ding X, Chen S, Jiang X (2009) ULK1.ATG13.FIP200 complex mediates mTOR signaling and is essential for autophagy. J Biol Chem 284: 12297–12305
59. Jung CH, Jun CB, Ro SH, Kim YM, Otto NM, Cao J, Kundu M, Kim DH (2009) ULK-Atg13-FIP200 complexes mediate mTOR signaling to the autophagy machinery. Mol Biol Cell 20: 1992–2003

60. Hosokawa N, Hara T, Kaizuka T, Kishi C, Takamura A, Miura Y, Iemura S, Natsume T, Takehana K, Yamada N et al (2009) Nutrient-dependent mTORC1 association with the ULK1-Atg13-FIP200 complex required for autophagy. Mol Biol Cell 20: 1981–1991
61. Henderson RJ, Patton SM, Connor JR (2005) Development of a fluorescent reporter to assess iron regulatory protein activity in living cells. Biochem Biophys Acta 1743: 162–168
62. Riemer J, Hoepken HH, Czerwinska H, Robinson SR, Dringen R (2004) Colorimetric ferrozine-based assay for the quantitation of iron in cultured cells. Anal Biochem 331: 370–375
63. Esposito BP, Epsztejn S, Breuer W, Cabantchik ZI (2002) A review of fluorescence methods for assessing labile iron in cells and biological fluids. Anal Biochem 304: 1–18
64. Aron AT, Reeves AG, Chang CJ (2018) Activity-based sensing fluorescent probes for iron in biological systems. Curr Opin Chem Biol 43: 113–118
65. Jahng JW, Turdi S, Kovacevic V, Dadson K, Li RK, Sweeney G (2015) Pressure overload-induced cardiac dysfunction in aged male adiponectin knockout mice is associated with autophagy deficiency. Endocrinology 156: 2667–2677
66. Palanivel R, Maida A, Liu Y, Sweeney G (2006) Regulation of insulin signalling, glucose uptake and metabolism in rat skeletal muscle cells upon prolonged exposure to resistin. Diabetologia 49: 183–190
67. Liu Q, Zhang J, Xu Y, Huang Y, Wu C (2013) Effect of carvedilol on cardiomyocyte apoptosis in a rat model of myocardial infarction: a role for toll-like receptor 4. Indian J Pharmacol 45: 458–463

Citation of Chapter 4

1. Yang, Z. & Klionsky, D. J. Eaten alive: a history of macroautophagy. Nat. Cell Biol. 12, 814–822 (2010).

2. Feng, Y., He, D., Yao, Z. & Klionsky, D. J. The machinery of macroautophagy. Cell Res. 24, 24–41 (2014).

3. Gatica, D., Lahiri, V. & Klionsky, D. J. Cargo recognition and degradation by selective autophagy. Nat. Cell Biol. 20, 233–242 (2018).

4. Klionsky, D. J. & Schulman, B. A. Dynamic regulation of macroautophagy by distinctive ubiquitin-like proteins. Nat. Struct. Mol. Biol. 21, 336–345 (2014).

5. Chino, H. & Mizushima, N. ER-Phagy: Quality and Quantity Control of the Endoplasmic Reticulum by Autophagy. Cold Spring Harb. Perspect. Biol. 15, a041256 (2023).

6. Khaminets, A. et al. Regulation of endoplasmic reticulum turnover by selective autophagy. Nature 522, 354–358 (2015).

7. Chino, H., Hatta, T., Natsume, T. & Mizushima, N. Intrinsically Disordered Protein TEX264 Mediates ER-phagy. Mol. Cell 74, 909-921.e6 (2019).

8. An, H. et al. TEX264 Is an Endoplasmic Reticulum-Resident ATG8-Interacting Protein Critical for ER Remodeling during Nutrient Stress. Mol. Cell 74, 891-908.e10 (2019).

9. Jiang, X. et al. FAM134B oligomerization drives endoplasmic reticulum membrane scission for ER-phagy. EMBO J. 39, e102608 (2020).

10. Wang, X. et al. A regulatory circuit comprising the CBP and SIRT7 regulates FAM134B-mediated ER-phagy. J. Cell Biol. 222, e202201068 (2023).

11. Chino, H. et al. Phosphorylation by casein kinase 2 enhances the interaction between ER-phagy receptor TEX264 and ATG8 proteins. EMBO Rep. 23, e54801 (2022).

12. Bhaskara, R. M. et al. Curvature induction and membrane remodeling by FAM134B reticulon homology domain assist selective ER-phagy. Nat. Commun. 10, 2370 (2019).

13. Siggel, M., Bhaskara, R. M., Moesser, M. K., D Ikić, I. & Hummer, G. FAM134B-RHD Protein Clustering Drives Spontaneous Budding of Asymmetric Membranes. J. Phys. Chem. Lett. 12, 1926–1931 (2021).

14. González, A. et al. Ubiquitination regulates ER-phagy and remodelling of endoplasmic reticulum. Nature 618, 394–401 (2023).

15. Chiramel, A. I., Dougherty, J. D., Nair, V., Robertson, S. J. & Best, S. M. FAM134B, the Selective Autophagy Receptor for Endoplasmic Reticulum Turnover, Inhibits Replication of Ebola Virus Strains Makona and Mayinga. J. Infect. Dis. 214, S319–S325 (2016).

16. Lennemann, N. J. & Coyne, C. B. Dengue and Zika viruses subvert reticulophagy by NS2B3-mediated cleavage of FAM134B. Autophagy 13, 322–332 (2017).

17. Tan, X. et al. Coronavirus subverts ER-phagy by hijacking FAM134B and ATL3 into p62 condensates to facilitate viral replication. Cell Rep. 42, 112286 (2023).

18. Zhang, L. et al. AMFR-mediated Flavivirus NS2A ubiquitination subverts ER-phagy to augment viral pathogenicity. Nat. Commun. 15, 9578 (2024).

19. Shin, D. et al. Regulation of Phosphoribosyl-Linked Serine Ubiquitination by Deubiquitinases DupA and DupB. Mol. Cell 77, 164-179.e6 (2020).

20. Sher, A. A., Mustafa, B. E., Grady, S. C., Gardiner, J. C. & Saeed, A. M. Outbreaks of foodborne Salmonella enteritidis in the United States between 1990 and 2015: An analysis of epidemiological and spatial-temporal trends. Int. J. Infect. Dis. IJID Off. Publ. Int. Soc. Infect. Dis. 105, 54–61 (2021).

21. Bakowski, M. A., Braun, V. & Brumell, J. H. Salmonella-containing vacuoles: directing traffic and nesting to grow. Traffic Cph. Den. 9, 2022–2031 (2008).

22. Katayama, H., Yamamoto, A., Mizushima, N., Yoshimori, T. & Miyawaki, A. GFP-like proteins stably accumulate in lysosomes. Cell Struct. Funct. 33, 1–12 (2008).

23. Yim, W. W.-Y., Yamamoto, H. & Mizushima, N. A pulse-chasable reporter processing assay for mammalian autophagic flux with HaloTag. eLife 11, e78923 (2022).

24. Klionsky, D. J. et al. Guidelines for the use and interpretation of assays for monitoring autophagy (4th edition)1. Autophagy 17, 1–382 (2021).

25. Ichimura, Y. et al. A ubiquitin-like system mediates protein lipidation. Nature 408, 488–492 (2000).

26. Davidson, G. L. et al. Frequency of mutations in the genes associated with hereditary sensory and autonomic neuropathy in a UK cohort. J. Neurol. 259, 1673–1685 (2012).

27. LaRock, D. L., Chaudhary, A. & Miller, S. I. Salmonellae interactions with host processes. Nat. Rev. Microbiol. 13, 191–205 (2015).

28. Xu, Y. et al. ARF GTPases activate Salmonella effector SopF to ADP-ribosylate host V-ATPase and inhibit endomembrane damage-induced autophagy. Nat. Struct. Mol. Biol. 29, 67–77 (2022).

29. Xu, Y. et al. A Bacterial Effector Reveals the V-ATPase-ATG16L1 Axis that Initiates Xenophagy. Cell 178, 552-566.e20 (2019).

30. Trinkle-Mulcahy, L. Recent advances in proximity-based labeling methods for interactome mapping. F1000Research 8, F1000 Faculty Rev-135 (2019).

31. Knodler, L. A., Nair, V. & Steele-Mortimer, O. Quantitative assessment of cytosolic Salmonella in epithelial cells. PloS One 9, e84681 (2014).

32. Gatica, D., Chiong, M., Lavandero, S. & Klionsky, D. J. The role of autophagy in cardiovascular pathology. Cardiovasc. Res. 118, 934–950 (2022).

33. Birmingham, C. L., Smith, A. C., Bakowski, M. A., Yoshimori, T. & Brumell, J. H. Autophagy controls Salmonella infection in response to damage to the Salmonella-containing vacuole. J. Biol. Chem. 281, 11374–11383 (2006).

34. Thurston, T. L. M., Ryzhakov, G., Bloor, S., von Muhlinen, N. & Randow, F. The TBK1 adaptor and autophagy receptor NDP52 restricts the proliferation of ubiquitin-coated bacteria. Nat. Immunol. 10, 1215–1221 (2009).

35. Lau, N. et al. SopF, a phosphoinositide binding effector, promotes the stability of the nascent Salmonella-containing vacuole. PLoS Pathog. 15, e1007959 (2019).

36. Kohno, S., Shiozaki, Y., Keenan, A. L., Miyazaki-Anzai, S. & Miyazaki, M. An N-terminal-truncated isoform of FAM134B (FAM134B-2) regulates starvation-induced hepatic selective ER-phagy. Life Sci. Alliance 2, e201900340 (2019).

37. Bravo, R. et al. Endoplasmic reticulum and the unfolded protein response: dynamics and metabolic integration. Int. Rev. Cell Mol. Biol. 301, 215–290 (2013).

38. Foronda, H. et al. Heteromeric clusters of ubiquitinated ER-shaping proteins drive ER-phagy. Nature 618, 402–410 (2023).

39. Li, C. et al. FastCloning: a highly simplified, purification-free, sequence- and ligation-independent PCR cloning method. BMC Biotechnol. 11, 92 (2011).

40. Liu, H. & Naismith, J. H. An efficient one-step site-directed deletion, insertion, single and multiple-site plasmid mutagenesis protocol. BMC Biotechnol. 8, 91 (2008).

Appendix II

Permission to reprint published manuscripts

1. Tian, W., **Alsaadi, R.**, Guo, Z. et al. An antibody for analysis of autophagy induction. Nat Methods 17, 232–239 (2020). https://doi.org/10.1038/s41592-019-0661-y

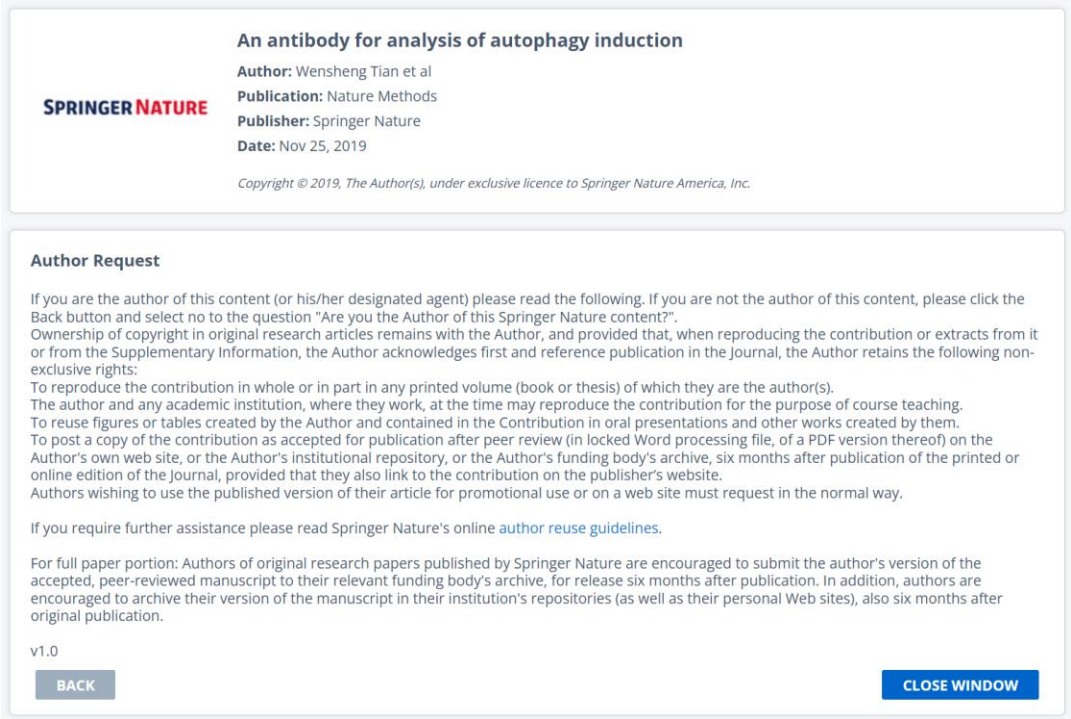

SPRINGER NATURE

An antibody for analysis of autophagy induction

Author: Wensheng Tian et al
Publication: Nature Methods
Publisher: Springer Nature
Date: Nov 25, 2019

Copyright © 2019, The Author(s), under exclusive licence to Springer Nature America, Inc.

Author Request

If you are the author of this content (or his/her designated agent) please read the following. If you are not the author of this content, please click the Back button and select no to the question "Are you the Author of this Springer Nature content?".
Ownership of copyright in original research articles remains with the Author, and provided that, when reproducing the contribution or extracts from it or from the Supplementary Information, the Author acknowledges first and reference publication in the Journal, the Author retains the following non-exclusive rights:
To reproduce the contribution in whole or in part in any printed volume (book or thesis) of which they are the author(s).
The author and any academic institution, where they work, at the time may reproduce the contribution for the purpose of course teaching.
To reuse figures or tables created by the Author and contained in the Contribution in oral presentations and other works created by them.
To post a copy of the contribution as accepted for publication after peer review (in locked Word processing file, of a PDF version thereof) on the Author's own web site, or the Author's institutional repository, or the Author's funding body's archive, six months after publication of the printed or online edition of the Journal, provided that they also link to the contribution on the publisher's website.
Authors wishing to use the published version of their article for promotional use or on a web site must request in the normal way.

If you require further assistance please read Springer Nature's online author reuse guidelines.

For full paper portion: Authors of original research papers published by Springer Nature are encouraged to submit the author's version of the accepted, peer-reviewed manuscript to their relevant funding body's archive, for release six months after publication. In addition, authors are encouraged to archive their version of the manuscript in their institution's repositories (as well as their personal Web sites), also six months after original publication.

v1.0

BACK CLOSE WINDOW

2. Jahng JWS, **Alsaadi R. M**, Palanivel R, Song E, Hipolito VEB, Sung HK, Botelho RJ, Russell RC, Sweeney G. (2019). Iron overload inhibits late stage autophagic flux leading to insulin resistance. EMBO Reports, https://doi.org/10.15252/embr.201947911.

EMBO reports

Publication type: e-Journal
Article: Iron overload inhibits late stage autophagic flux leading to insulin resistance

ISSN: 1469-3178
Publication Year: 2000 - Present
Publisher: OXFORD UNIVERSITY PRESS
Language: English

Country: United Kingdom of Great Britain and Northern Ireland
Rightsholder: Springer Nature BV
URL: http://onlinelibrary.wiley.com/journal/10.1002/(ISSN)1469-3178
Authors: European Molecular Biology Organization.; Oxford University Press.; HighWire Press.

View less details

3. Damián Gatica, **Reham M. Alsaadi**, Rayan El Hamra, Boran Li, Rudolf Mueller, Makoto Miyazaki, Qiming Sun, Subash Sad, Ryan C. Russell. The ER-phagy receptor FAM134B is targeted by Salmonella Typhimurium to promote infection.

- DOI: 10.1038/s41467-025-58035-7